

✓  
**EPR OF SPIN LABELS AND PROBES IN  
REVERSE MICELLAR MEDIA : LINESHAPE  
STUDIES AND CONSTRUCTION OF A  
SPECTROMETER INTERFACE**

*A Thesis Submitted*  
in Partial Fulfilment of the Requirements  
for the Degree of  
**DOCTOR OF PHILOSOPHY**

*by*  
**U. ILANGOVAN**

Acc. No. A117872

*to the*  
**DEPARTMENT OF CHEMISTRY  
INDIAN INSTITUTE OF TECHNOLOGY KANPUR**  
**NOVEMBER, 1993**

*to the downtrodden society*

*for shedding blood each and every day*

*to build this country*

MANKIND TAKES UP ONLY SUCH PROBLEMS AS IT CAN SOLVE

- KARL MARX

## STATEMENT

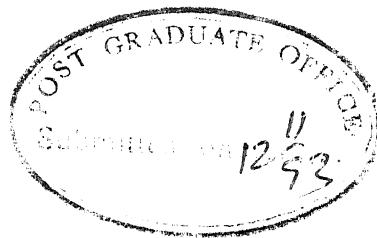
I hereby declare that the work embodied in this thesis entitled, 'EPR OF SPIN LABELS AND PROBES IN REVERSE MICELLAR MEDIA : LINESHAPE STUDIES AND CONSTRUCTION OF A SPECTROMETER INTERFACE' is the result of investigations carried out by me in the Department of Chemistry, Indian Institute of Technology Kanpur, India, under the supervision of Professor P. Raghunathan.

In keeping with scientific tradition, wherever work done by others has been utilized, due acknowledgement has been made.

  
U. Ilangovan

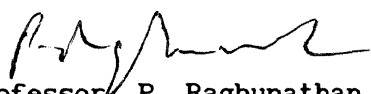
Kanpur  
November, 1993





## CERTIFICATE I

Certified that the work presented in this thesis entitled, 'EPR OF SPIN LABELS AND PROBES IN REVERSE MICELLAR MEDIA : LINESHAPE STUDIES AND CONSTRUCTION OF A SPECTROMETER INTERFACE' by *Mr. U. Ilangovan* has been carried out under my supervision and has not been submitted elsewhere for a degree.

  
( Professor P. Raghunathan )  
Thesis Supervisor  
Department of Chemistry  
I.I.T. Kanpur

Kanpur  
November, 1993

DEPARTMENT OF CHEMISTRY  
INDIAN INSTITUTE OF TECHNOLOGY KANPUR, INDIA

CERTIFICATE II

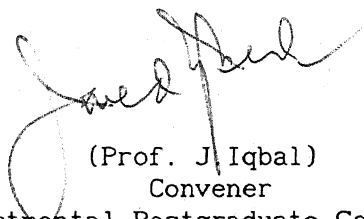
This is to certify that *Mr. U. Ilangovan* satisfactorily completed all the courses required for the Ph.D. degree program. The courses include :

Chm 505	Principles of Organic Chemistry
Chm 521	Chemical Binding
Chm 524	Modern Physical Methods in Chemistry
Chm 525	Principles of Physical Chemistry
Chm 545	Principles of Inorganic Chemistry
Chm 626	Solid State Chemistry
Chm 800	General Seminar
Chm 801	Special Seminar
Chm 900	Ph.D. Thesis

*Mr. U. Ilangovan* was admitted to the candidacy for the Ph.D. degree in October 1987 after he successfully completed the written and oral qualifying examinations.



(Prof. P.K. Ghosh)  
Head  
Department of Chemistry  
I.I.T. Kanpur



(Prof. J. Iqbal)  
Convener  
Departmental Postgraduate Committee  
I I T Kanpur

A special word of thanks to Chitra Manoravi, Andal Ramesh, Sheela Tharmaraj and Mrs. Ponnusamy for their kind hospitality and care.

I also thank Mr. Dinesh Kannaugia for providing help in all my EPR recordings and B. P. Pant for neat typing.

Last but not least, I wish to thank my appa, amma, thatha and mama Mr. Karmegam for their constant encouragement and patience.

-Ilangoan-

## SYNOPSIS

Surfactants, i.e., surface active compounds, aggregate in non-polar solvents and have the peculiar property of solubilizing large quantities of water. The resulting clear isotropic solutions are referred to as reverse micelles, which consist of at least three distinct compartments; an internal aqueous microphase (water pool), the external organic phase, and the surfactant layer that separates the two phases. The nature of the above-mentioned aqueous microphases has been observed in recent years to be quite different from that of ordinary bulk water and the determination of their size, which is normally controlled by the  $[H_2O]$  to [surfactant] ratio (R), has received much attention. The reverse micelles are rapidly gaining importance because they can be used to solubilize biopolymers such as enzymes, nucleic acid and bacteria in 'apolar solvents' and to investigate their physicochemical properties in the presence of limited amounts of water. More interestingly, reverse micelles are known to act like micro reactors in which guest molecules solubilized in the water pools exhibit remarkable activity.

Interesting questions often arise, bearing on the structural organization of the surfactant layer at the interface between the internal water pool and the external organic phase, and the dynamical properties of molecules present in different compartments of reverse micelles, including the inter-compartmental exchange of these molecules. These questions could be well answered by the choice of appropriate techniques. EPR spin labeling is a versatile technique that lends itself well to the physicochemical characterization of the compartmental structure of reverse micelles. These spin labels can be suitably designed and synthesized so that they can reside in a particular compartment without perturbing the environment and report the relevant informa-

tion. In the literature, the potential of the EPR spin labeling technique has been investigated and reported for different reverse micellar systems containing synthetic surfactants. Although some other techniques such as NMR, UV-visible, IR, have been widely used to characterize the egg-yolk lecithin (EYL) reverse micelles, EPR spin labeling has not been adequately utilized to our knowledge.

The main focus of this thesis, then, is egg-yolk lecithin (Phosphatidylcholine or PC), which is also one of the most commonly found glycerophospholipids constituting the bulk of phospholipid content in animal cells and bacterial membranes. In our study, reverse micelles of lecithin have been formed with cyclohexane and water. In addition, reverse micelles of synthetic surfactants (Cetyl trimethylammonium bromide (CTAB), Aerosol OT (AOT)) have also been studied and reported. We have given particular importance to EPR studies of different nitroxide spin labels, and to a  $\text{VO}^{2+}$  paramagnetic probe. As a part of this thesis, details of instrumentation for the computer interfacing of our Varian E-109 EPR spectrometer are also reported.

In chapter 1, after a brief review of such topics as the source and structure of phospholipids, existence of reverse micellar structures in biological membranes, and the importance of reverse micellar 'water pool', we move on to survey the generally used experimental methodologies for probing reverse micelles, which include scattering techniques, physical methods and spectroscopic techniques. This is followed by details regarding the application of electron paramagnetic resonance (EPR) spectroscopy for probing micellar structure. The chapter ends with a detailed survey of EPR studies on reverse micelles reported to-date.

Chapter 2 describes our EPR studies of reverse micelles using some nitroxide spin labels. The reverse micellar system chosen for this work is

lecithin/cyclohexane/H<sub>2</sub>O. Spin labels used are (1) potassium iminoxide xanthogenate (PIX) (2) spin labeled sodium hexyl sulfate (SL-SHS) and (3) 5-doxyl stearic acid (5-DSA). The basic theory of EPR of nitroxide radical, as well as the effect of motion of spin labels on the EPR spectra, are discussed. Conventional methods often used in the literature to calculate the motional correlation time ( $\tau$ ) are then reviewed. The dependence of (1) the width of the high field line which is sensitive to the motion of the spin label, (2) <sup>14</sup>N hyperfine splitting values (3)  $\tau$  and (4) anisotropic parameters on the size of reverse micellar water pools have been determined and discussed in detail. Further results of this chapter are the following : (i) a two-site model has been applied to the lecithin reverse micelles containing PIX spin label; (ii) the exchange of SL-SHS among different environments has been treated qualitatively; and (iii) variation of order parameter with 'R' of the reverse micelles has been explored using 5-DSA.

Chapter 3 describes the effect of temperature and cosurfactant on the EPR spectra of lecithin/cyclohexane/H<sub>2</sub>O reverse micelles. The cosurfactant and spin label used in this work are cholesterol and Tempol (2-hydroxy Tempo), respectively.

In chapter 4, our EPR studies of paramagnetic metal ion probe in reverse micelles containing cationic, anionic and zwitterionic surfactants are presented. VOSO<sub>4</sub> has been used as EPR spin probe in CTAB, AOT and EYL reverse micelles. The chapter begins with essential background material on the EPR spectroscopy of VO<sup>2+</sup> and the effects of various possible motional modes of VO<sup>2+</sup> on EPR spectral profiles. In our work, the VO<sup>2+</sup> ion exhibits different EPR lineshapes, especially at low water content, in the presence of cationic, anionic and zwitterionic surfactants. Appropriate rationalization has been given for the dynamical behavior of VO<sup>2+</sup> on the basis of electrostatic

interaction with the polar head groups of surfactants chosen to form reverse micelles. Our detailed study leads to the finding that the location of  $\text{VO}^{2+}$  spin probe in reverse micelles is strongly influenced by the ionic nature of the surfactant head group and by the size of the water pools of the reverse micelles. The dynamics of  $\text{VO}^{2+}$  in the water pools has been investigated using EPR linewidth analysis, correlation time and microviscosity measurements. The dependence of these dynamical parameters on water content also been determined and discussed.

Chapter 5 embodies the development of novel computational procedures for analyzing nitroxide lineshapes in the 'fast' and 'slow' reorientational limits. The computational procedure developed by us for the 'slow motional spectra' is reported in the *first part* of this chapter. After introducing the theory in detail we proceed to show how this simple and (computationally) fast algorithm was developed. Full justification is given for our choice of the 'systematic sampling' technique to reduce the error. Towards the end of this *first part*, we demonstrate how only 25 sampling points ( $\cos\theta$  values in the range 0-1) are sufficient to achieve convergence. The *second part* of this chapter describes the development of another computer program which expedites our lineshape analysis of EPR spectra of nitroxide spin labels undergoing fast motion. This program enables us to estimate the contributions of motional (Lorentzian) and inhomogeneous (Gaussian) broadening mechanisms to the total experimental linewidths. The total theoretical lineshapes computed by convoluting the inhomogeneous Gaussian lineshape having width of  $\Delta B_{\text{inh}}^0$  over the motional Lorentzian lineshape having width  $\Delta B_M(\tau)$  is in good agreement with the corresponding experimental lineshapes. Accurate values of fast motional correlation times ( $\tau$ ) have also been computed and compared with those obtained from conventional methods.

Chapter 6 describes the construction of a **PC-EPR** spectrometer interface which has enabled us to have a very useful 'data acquisition system' (**DAS**) during the course of our experiments. This chapter starts with a note about the advantages of a computer interface and a survey of existing interfacing methods for **EPR** spectrometers. Emphasis has been given to the hardware features of interfacing, which in our work comprise an IBM-compatible **PC-AT**, an acquisition card, and an adapter circuit. The significant role of the adapter circuit in assuring hardware compatibility between **PC**, acquisition card (custom built) and **EPR** spectrometer is explained. As regards software, we have written two 'assembly language' programs. These programs not only establish proper communication ('handshake') between the **PC** and **EPR** spectrometer but also enable us to acquire digital data and to record the spectrum on our X-Y recorder. The chapter concludes by highlighting the salient features of our **DAS**.

Chapter 7 contains the overall summary of the main findings of this investigation and some suggestions of further prospects in this area.

The Appendix contains listings of various programs (Fortran and assembly language) developed in Chapters 5 and 6.



## LIST OF CONTENTS

	Page
LIST OF FIGURES	xvi
LIST OF TABLES	xxi
CHAPTER 1      GENERAL INTRODUCTION	1
1.1      Reverse Micelles	1
1.2      Phospholipids : Source and Structure	3
1.3      Lipid Polymorphism	6
1.4      Existence of Reverse Micellar Structures in Biological Membranes	6
1.5      Thermodynamics and Phase Diagrams	8
1.6      Reverse Micellar 'Water Pool'	11
1.7      Experimental Methods Used to Probe Reverse Micelles	12
1.8      Survey of EPR, ENDOR and ESEM studies on reverse micelles	19
REFERENCES	42
CHAPTER 2      EPR OF NITROXIDE SPIN LABELS IN LECITHIN REVERSE MICELLES	50
2.1      Introduction	50
2.2      Theory of EPR Spectroscopy of Nitroxide Spin Labels	51
2.2.1      Nitroxide Spin Label in Oriented Crystals	52
2.2.2      Nitroxide Spin Label in Non-oriented Systems	56
2.2.3      Nitroxide Spin Labels in Solution	56
2.2.4      Effect of Motion on the EPR Spectra of Nitroxide Solutions	58
2.2.5      Determination of $\tau$ from the Lineshape	61
2.3      Experimental Details	65

2.3.1	Materials	65
2.3.2	Sample Preparations	67
2.3.3	EPR Spectrometry	68
2.4	Results and Discussion	68
2.4.1	EPR Studies of PIX in Lecithin Reverse Micelles	69
2.4.1.1	EYL/Cyclohexane/H <sub>2</sub> O(PIX)	71
2.4.1.2	EYL/Cyclohexane(PIX)/H <sub>2</sub> O	75
2.4.2	EPR Studies of SL-SHS in the Water Pools of EYL/Cyclohexane/H <sub>2</sub> O Reverse Micelles	83
2.4.3	EPR Studies of 5-Doxyl Stearic Acid in EYL/Cyclohexane/H <sub>2</sub> O Reverse Micelles	94
2.5	Conclusions	100
	REFERENCES	101
CHAPTER 3	DYNAMICS OF SPIN LABELS INCORPORATED EYL/CYCLO- HEXANE/H <sub>2</sub> O REVERSE MICELLES :EFFECTS OF TEMPERATURE AND CHOLESTEROL ADDITION	103
3.1	Introduction	103
3.2	Experimental Details	104
3.3	Results and Discussion	105
3.3.1	Effect of Cholesterol on the Dynamics of 'TEMPOL' Incorporated in EYL/Cyclohexane/H <sub>2</sub> O Reverse Micelles	105
3.3.2	Effect of Cholesterol on the Dynamics of SL-SHS Incorporated in EYL/Cyclohexane/H <sub>2</sub> O Reverse Micelles	111
3.3.3	Effect of Temperature on the EPR Spectral Profiles of TEMPOL in EYL/Cyclohexane/H <sub>2</sub> O Reverse Micelles	114
3.4	Conclusions	116
	REFERENCES	118

CHAPTER 4	EPR STUDIES OF THE $\text{VO}^{2+}$ PROBE IN REVERSE MICELLES CONTAINING CATIONIC, ANIONIC, AND ZWITTERIONIC SURFACTANTS	119
4.1	Introduction	119
4.2	EPR Spectroscopy of Vanadyl Ion	120
4.2.1	Effect of Motion on the EPR Spectral Profiles of $\text{VO}^{2+}$	124
4.3	Experimental Details	126
4.3.1	Materials	126
4.3.2	Sample Preparations	128
4.3.3	EPR Spectrometry	129
4.4	Results and Discussion	131
4.4.1	EPR Studies of $\text{VOSO}_4$ in Reverse Micelles Containing Cationic Surfactants	131
4.4.2	EPR Studies of $\text{VOSO}_4$ in Reverse Micelles Containing Anionic Surfactants	150
4.4.3	EPR Studies of $\text{VOSO}_4$ in Reverse Micelles Containing Zwitterionic Surfactants	162
4.5	Conclusions	164
	REFERENCES	166
CHAPTER 5	DEVELOPMENT OF NOVEL COMPUTATIONAL PROCEDURES FOR ANALYZING NITROXIDE EPR LINESHAPES	168
5.1	Introduction	168
5.2	Timescale of Nitroxide EPR Spectroscopy	169
5.3	Types of Lineshapes and Effect of Motion on EPR Spectral Profiles	171
5.4	Theory and Computational Procedure Used to Simulate the Lineshapes of Nitroxide Spin Labels Undergoing Slow Motion	173
5.4.1	Theory	175
5.4.2	Computational Procedure	183

5.4.3.	Discussion	187
5.5	Theory and Computational Procedure Used to Simulate The Lineshapes of Nitroxide Spin Labels Undergoing Fast Motion	188
5.5.1	Theory	192
5.5.2	Computational Procedure	194
5.5.3	Discussion	198
5.6	Conclusions	201
	REFERENCES	204
CHAPTER 6	CONSTRUCTION OF A PC-EPR SPECTROMETER INTERFACE	206
6.1	Motivation	206
6.2	Advantages of Interfacing a Computer	208
6.3	Survey of Existing Interfacing Methods for EPR Spectrometer	214
6.4	Design Criteria	215
6.5	Hardware	217
6.5.1	Specifications	217
6.5.1.1	The IBM-Compatible PC-AT	217
6.5.1.2	Acquisition Card	218
6.5.1.3	Adapter Circuit	218
6.5.1.4	EPR Jack J007	220
6.5.2	Functional Details of the Hardware	220
6.5.2.1	Acquisition Card	220
6.5.2.2	Adapter Circuit	224
6.6	Software	225
6.6.1	ACQN.ASM	226
6.6.1.1	Functions of Subroutines	226
6.6.2	RECR.ASM	228
6.6.2.1	Function of Subroutine	228

6.6.3	DSPL.ASM	230
6.6.4	HEX.FOR	230
6.7	Self Test on Hardware and Software	230
6.9	Working details of Software	231
6.8	Improvement in Software	233
6.10	Salient Features of our Data Acquisition System (DAS)	234
6.11	Performance and Discussion	235
6.12	Conclusions	244
	REFERENCES	245
CHAPTER 7	SUMMARY AND FURTHER PROSPECTS	247
APPENDIX I		
APPENDIX II		
APPENDIX III		
APPENDIX IV		

## LIST OF FIGURES

		Page
Fig. 1.1	The Singer and Nicholson 'fluid mosaic' model of a biomembrane.	4
Fig. 1.2	General Chemical structures of (a) sphingophospholipids (b) glycerophospholipids and (c) main classes of glycerophospholipids with their common names.	5
Fig. 1.3	The 'metamorphic mosaic' model of biological membranes.	9
Fig. 2.1	(a) Nitroxide coordinate system,	53
	(b)-(d) X-band EPR spectra with the magnetic field along each axis of a rigidly oriented nitroxide,	53
	(e) EPR spectral response of a collection of randomly oriented nitroxides in the absence of motion	53
Fig. 2.2	(a) Energy levels and transitions for a nitroxide in high magnetic fields.	59
	(b) X-band EPR spectrum of the TEMPO nitroxide spin label in aqueous solution.	59
Fig. 2.3	X-Band EPR spectra of nitroxide (1) dissolved in ethylene glycol at (a) 298 K (b) 248 K (c) 193 K (d) 123 K	60
Fig. 2.4	Room Temperature EPR spectra of PIX and SL-SHS in pure solvents (water and cyclohexane).	70
Fig. 2.5	X-band EPR spectra of EYL/Cyclohexane/H <sub>2</sub> O(PIX) reverse micelles as a function of water content 'R'.	72
Fig. 2.6	Isotropic <sup>14</sup> N hyperfine splitting constant $a_N$ (mT) of EYL/cyclohexane/H <sub>2</sub> O(PIX) reverse micelles as a function of 'R'	73
Fig. 2.7	Ratio of the relative amplitudes of low-field <sup>14</sup> N hyperfine line to the central-field line, $h_{+1}/h_0$ vs 'R' for EYL/cyclohexane/H <sub>2</sub> O(PIX) reverse micelles.	76
Fig. 2.8	Ratio of relative amplitudes of central-field line to high-field line against 'R' for EYL/cyclohexane/H <sub>2</sub> O(PIX) system.	77

	Fig. 2.9	Variation of rotational correlation times, $\tau_B$ (from Eq. 2.36) and $\tau_c$ (from Eq. 2.37), as functions of 'R' for EYL/cyclohexane/H <sub>2</sub> O(PIX) system.	78
	Fig. 2.10	EPR spectra of EYL/cyclohexane(PIX)/H <sub>2</sub> O as a function of 'R'.	79
	Fig. 2.11	Variation of the fraction of bound water in EYL/cyclohexane/H <sub>2</sub> O reverse micelles as a function of 'R'.	84
	Fig. 2.12	EPR spectra of SL-SHS, in EYL/cyclohexane/H <sub>2</sub> O reverse micelles (R = 1-6 cases)	85
	Fig. 2.13	EPR spectra of SL-SHS, in EYL/cyclohexane/H <sub>2</sub> O reverse micelles (R = 7 to 16 cases)	86
CHAPTER	Fig. 2.14	Variation of the ratio of amplitudes of central-field line to low-field EPR lines of EYL/cyclohexane/H <sub>2</sub> O (SL-SHS) system for different 'R' values.	88
APPENDIX			
APPENDIX	Fig. 2.15	Variation of the ratio of amplitudes of central-field line to high-field EPR lines as a function of 'R'.	89
APPENDIX			
APPENDIX	Fig. 2.16	Isotropic <sup>14</sup> N hyperfine coupling constant $a_N$ (mT) of SL-SHS in EYL/cyclohexane/H <sub>2</sub> O, as a function of 'R'.	91
	Fig. 2.17	R-values dependence of $\tau_B$ (from Eq. 2.36) and $\tau_c$ , of SL-SHS in EYL/cyclohexane/H <sub>2</sub> O system.	92
	Fig. 2.18	EPR spectra of 5-DSA in EYL/cyclohexane/H <sub>2</sub> O reverse micelles for values of R between 0 and 6.	95
	Fig. 2.19	EPR spectra of 5-DSA in EYL/cyclohexane/H <sub>2</sub> O reverse micelles for values of R between 8 and 16.	96
	Fig. 2.20	Order parameter variation of 5-DSA in EYL/ cyclo hexane/H <sub>2</sub> O reverse micelles as a function of 'R'.	99

Fig. 3.2	Ratio of the relative amplitudes of central-field $^{14}\text{N}$ hyperfine line to the low-field line, $h_0/h_{-1}$ vs 'R' for (i) EYL/cholesterol/cyclohexane/ $\text{H}_2\text{O}$ (TEMPOL) (ii) EYL/cyclohexane/ $\text{H}_2\text{O}$ (TEMPOL) reverse micelles.	108
Fig. 3.3	Variation of rotational correlation times of TEMPOL as a function of 'R' in (i) cholesterol added system (ii) cholesterol free system.	109
Fig. 3.4	EPR spectra of SL-SHS in EYL/cholesterol/cyclohexane/ $\text{H}_2\text{O}$ reverse micelles as a function of 'R'.	112
Fig. 3.5	Temperature dependent EPR spectra of TEMPOL in EYL/cyclohexane/ $\text{H}_2\text{O}$ reverse micelles as a function of 'R'.	115
Fig. 4.1	Isotropic X-band EPR spectrum of the pentaquo vanadyl(IV) ion in room temperature aqueous solution	122
Fig. 4.2	Rigid-limit X-band EPR spectrum of the pentaquo vanadyl(IV) ion in frozen (77 K) aqueous solution	123
Fig. 4.3	X-band EPR spectrum of $\text{VO}(\text{acac})_2$ in toluene at 193 K intermediate motional region	125
Fig. 4.4	EPR spectra of $\text{VO}^{2+}$ ion in CTAB/ $\text{CHCl}_3$ -Octane/ $\text{H}_2\text{O}$ reverse micelles for $R = 0.5$ to $2.0$ .	133
Fig. 4.5	EPR spectra of $\text{VO}^{2+}$ ion in CTAB/ $\text{CHCl}_3$ -Octane/ $\text{H}_2\text{O}$ reverse micelles for $R = 3.0$ to $10.0$ .	134
Fig. 4.6	Dependence of the $m_1$ -dependent $\text{VO}^{2+}$ EPR linewidths on the water pool size ( $\propto R$ ) of CTAB reverse micelles.	141
Fig. 4.7	Dependence of the $\text{VO}^{2+}$ EPR linewidths on $m_1$ for various 'R' values.	142
Fig. 4.8	Dependence of $\text{VO}^{2+}$ rotational correlation times on 'R' in CTAB reverse micelles.	145
Fig. 4.9	Variation of microviscosity of the water pools of CTAB reverse micelles with size of the pools ( $\propto R$ ).	146
Fig. 4.10	X-band EPR of $\text{VO}^{2+}$ in AOT/isooctane/ $\text{H}_2\text{O}$ reverse micelles for $R = 1$ to $4$ .	151
Fig. 4.11	X-band EPR of $\text{VO}^{2+}$ in AOT/isooctane/ $\text{H}_2\text{O}$ reverse micelles for $R = 6$ to $20$ .	152



6.6.3	DSPL.ASM	230
6.6.4	HEX.FOR	230
6.7	Self Test on Hardware and Software	230
6.9	Working details of Software	231
6.8	Improvement in Software	233
6.10	Salient Features of our Data Acquisition System (DAS)	234
6.11	Performance and Discussion	235
6.12	Conclusions	244
	REFERENCES	245
CHAPTER 7	SUMMARY AND FURTHER PROSPECTS	247
APPENDIX I		
APPENDIX II		
APPENDIX III		
APPENDIX IV		

Fig. 6.5	Spectral subtraction by computer.	213
Fig. 6.6	Block diagram of EPR data acquisition system (DAS).	216
Fig. 6.7	Layout of the acquisition card.	219
Fig. 6.8	Circuit diagram of the adapter circuit.	221
Fig. 6.9	Wave forms as a result of self test.	232
Fig. 6.10	(a) EPR spectrum obtained for 5-doxylstearic acid in lecithin reverse micelles with single scan.	236
	(b) EPR spectrum obtained for 5-doxylstearic acid in lecithin reverse micelles with No. of scans = 10.	236
Fig. 6.11	(a) EPR spectrum obtained for 5-doxylstearic acid in lecithin reverse micelles with single scan.	238
	(b) EPR spectrum obtained for 5-doxylstearic acid in lecithin reverse micelles with No. of scans = 10.	238
Fig. 6.12	(a) EPR spectrum obtained for 5-doxylstearic acid in lecithin reverse micelles with single scan.	239
	(b) EPR spectrum obtained for 5-doxylstearic acid in lecithin reverse micelles with No. of scans = 10.	239
Fig. 6.13	(a) EPR spectrum obtained for 5-doxylstearic acid in lecithin reverse micelles without using DAS.	240
	(b) EPR spectrum obtained for 5-doxylstearic acid in lecithin reverse micelles with No. of scans = 15. (computer plots)	240
Fig. 6.14	(a) EPR spectrum obtained for 5-doxylstearic acid in lecithin reverse micelles with No. of scans = 40, recording time = 30 s and attenuation = 4. (recorded using X-Y recorder).	242
	(b) EPR spectrum obtained for 5-doxylstearic acid in lecithin reverse micelles with No. of scans = 40, recording time = 30 s and attenuation = 8. (recorded using X-Y recorder).	242
Fig. 6.15	(a) EPR spectrum obtained for 5-doxylstearic acid in lecithin reverse micelles with No. of scans = 40, recording time = 120 s and attenuation = 4. (recorded using X-Y recorder).	243
	(b) EPR spectrum obtained for 5-doxylstearic acid in lecithin reverse micelles with No. of scans = 40, recording time = 120 s and attenuation = 80. (recorded using X-Y recorder).	243

# LIST OF TABLES

		Page
Table 2.1	Spectroscopic splitting factor (g-factor) and hyperfine coupling constant (a) for different spin labels in different solvents at room temperature.	69
Table 2.2	Experimental parameters measured from EPR spectra of EYL/Cyclohexane/H <sub>2</sub> O(PIX)	74
Table 2.3	Experimental parameters derived from EYL/Cyclohexane(PIX)/H <sub>2</sub> O reverse micelles	80
Table 2.4	Anisotropic parameters and correlation time of PIX in EYL/Cyclohexane(PIX)/H <sub>2</sub> O reverse micelles.	81
Table 2.5	Experimental parameters measured from EPR spectra of EYL/Cyclohexane/H <sub>2</sub> O(SL-SHS) reverse micelles	87
Table 2.6	Spectral parameters of 5-DSA in EYL reverse micelles	97
Table 4.1	Composition of CTAB/CHCl <sub>3</sub> -n-octane/water reverse micelles	130
Table 4.2	Composition of AOT/iso-octane/water reverse micelles	130
Table 4.3	Composition of lecithin/cyclohexane/water reverse micelles	131
Table 4.4	Anisotropic EPR spectroscopic parameters calculated from frozen samples	137
Table 4.5	Linewidths of the component hyperfine lines of VO <sup>2+</sup> ion in CTAB reverse micelles	139

Table 4.6	Least-squares parameters used in Eq. 4.2	140
Table 4.7	Rotational correlation times of $\text{VO}^{2+}$ in CTAB reverse micelles	144
Table 4.8	Microviscosities of water pools of various sizes in CTAB reverse micelles, probed by $\text{VO}^{2+}$	147
Table 4.9	Quantitative data on $\text{AOT}/\text{H}_2\text{O}(\text{VO}^{2+})$ reverse micelles at various 'R'	154
Table 4.10	Component hyperfine Linewidths of $\text{VO}^{2+}$ in $\text{AOT}/\text{iso-octane}/\text{H}_2\text{O}$ reverse micelles	155
Table 4.11	Least-squares parameters used in Eq. 4.2	157
Table 4.12	Dynamical parameters of $\text{VO}^{2+}$ in AOT reverse micelles	160
Table 5.1	Input parameters used in the program	200
Table 5.2	Various spectral parameters derived using our computer program	202
Table 6.1	Details of the connections between the EPR J007 jack and the interfaces	223
Table 6.2	Parameters used to acquire spectra shown in Fig. 6.10 to 6.13 using our DAS	241
Table 6.3	Parameters used for recording spectra shown in Figs. 6.14 and 6.15	244

# CHAPTER 1

## GENERAL INTRODUCTION

### 1.1 Reverse Micelles

Surfactants, i.e., surface active compounds, are amphiphilic molecules that aggregate in solution when their concentration exceeds a minimal value known as the 'critical micelle concentration' (CMC). Reverse micelles are the aggregates of surfactants (such as Aerosol OT(AOT), Cetyltrimethylammonium bromide(CTAB), Sodium dodecyl sulfate(SDS), Dodecylammonium propionate(DAP), Phosphatidylcholine etc.,) in nonpolar media.<sup>1,2</sup> Reverse micelles can be formed both in the presence and in the absence of solubilized water. However, if the medium is completely water free, there is no well defined CMC and the aggregates formed are very small and polydisperse.<sup>3</sup> For instance, the close packing of the surfactant polar heads of the extensively studied surfactant, AOT, leaves an empty volume in the center of the micellar core (radius 4.4 Å for icosahedral packing<sup>4</sup>) which can only be filled with hydration (or bound) water. Such reverse micellar structures are capable of solubilizing a large amount of water and several other polar solvents, e.g., glycerol and formamide, forming in the case of water the so-called 'water pool'.<sup>5</sup>

In reverse micelles, the polar 'head' groups of surfactant molecules are concentrated in the interior of the aggregate and directed towards the water pool while their hydrophobic 'tail' structures protrude into, and are surrounded by, the bulk nonpolar solvent. The surfactant dissolved in the organic phase is found to reduce the interfacial tension between water and the organic phase, which is a prerequisite for forming reverse micelles. These

aggregates are thermodynamically stable, homogeneous and optically transparent.

Because of the water core's peculiar properties, reverse micelles have attracted special attention over the past twenty years. This is illustrated by the growing number of reviews on surfactant aggregation and micellization in nonpolar solvents,<sup>2,6</sup> the application of various analytical methods in the study of reverse micelles,<sup>7-9</sup> the study of solubilization,<sup>10-12</sup> catalysis and enzymatic reactions in reverse micelles<sup>9,10,13-15</sup> and the application of reverse micelles for protein separation using liquid-liquid extraction.<sup>16,17</sup> Also, these multicomponent structures provide a model for processes in biomembranes<sup>18</sup> including transbilayer transport<sup>19</sup> and fusion.<sup>20</sup> While there is a considerable accumulation of experimental results regarding these aggregated systems, the information is nevertheless incomplete for an unambiguous quantitative interpretation of micellar behaviour. In particular, much work is needed for a full understanding of (i) the dynamic behaviour of reverse micelles, (ii) the kinetics of their formation, (iii) their catalytic effects, and (iv) the solubilization of other molecules by the aggregates. The experimental and theoretical results accumulated on reverse micelles till recently are summarized in published monographs<sup>9,21-27</sup> and review articles.<sup>28,29</sup> The references given here are merely meant to be representative, and do not imply a complete coverage of the many studies which have been published.

Since phospholipid is the mostly studied surfactant in this thesis, we shall first briefly summarize the general structure of phospholipids and their different aggregated forms, the possible biological relevance of reverse micelles, their thermodynamics and phase diagrams, and the wide variety of methods (physical and chemical) used to characterize/probe reverse micellar structures. We shall then make a fairly detailed review of the literature on the EPR studies of reverse micelles.

## 1.2 Phospholipids : Source and Structure

Membranes play a key role in cell biology. They control cell life by modulating transport and exchange processes between endocellular (inside) and exocellular (outside) compartments, and are involved in biosynthesis, energy transduction, information transmission, and cell recognition.<sup>30-33</sup> The basic structure of a cell membrane is a bilayer lamellar sheet, approximately 4-5 nm thick comprising polar and neutral lipids and proteins that are embedded in the bilayer (integral) and bound at the surface (peripheral). The Singer and Nicholson<sup>34</sup> fluid mosaic model of a membrane structure is given in Fig. 1.1.

Phospholipids are the primary structural components of all biological membranes. These are polar lipids containing phosphoric acid as mono- or di-ester.<sup>35</sup> The natural phospholipids are classified into two main groups,<sup>31,36,37</sup> namely,

- (i) **Sphingophospholipids** : These are derived from sphingosine. Their general formula is given in Fig. 1.2(a), where R represents a hydrophilic group and R' an acyl group. The most common sphingophospholipid is sphingomyelin, where the R group is  $-\text{CH}_2\overset{+}{\text{CH}}_2\text{N}(\text{CH}_3)_3$ .
- (ii) **Glycerophospholipids** : These are derived from glycerol, and have glycerol as a backbone with one or two O-acyl or O-alkyl, or O-(1-alkenyl) chains attached at positions one and two and phosphate at position three. Their general chemical structure is given in Fig. 1.2(b). The R' and R'' groups are mostly derived from fatty acids, generally unbranched and with an even number of carbon atoms. Fig. 1.2(c) shows the main R groups found in natural membranes and their corresponding common names.

Although the two classes of phospholipids mentioned above are different in terms of structure and function, they are both amphipaths. Further

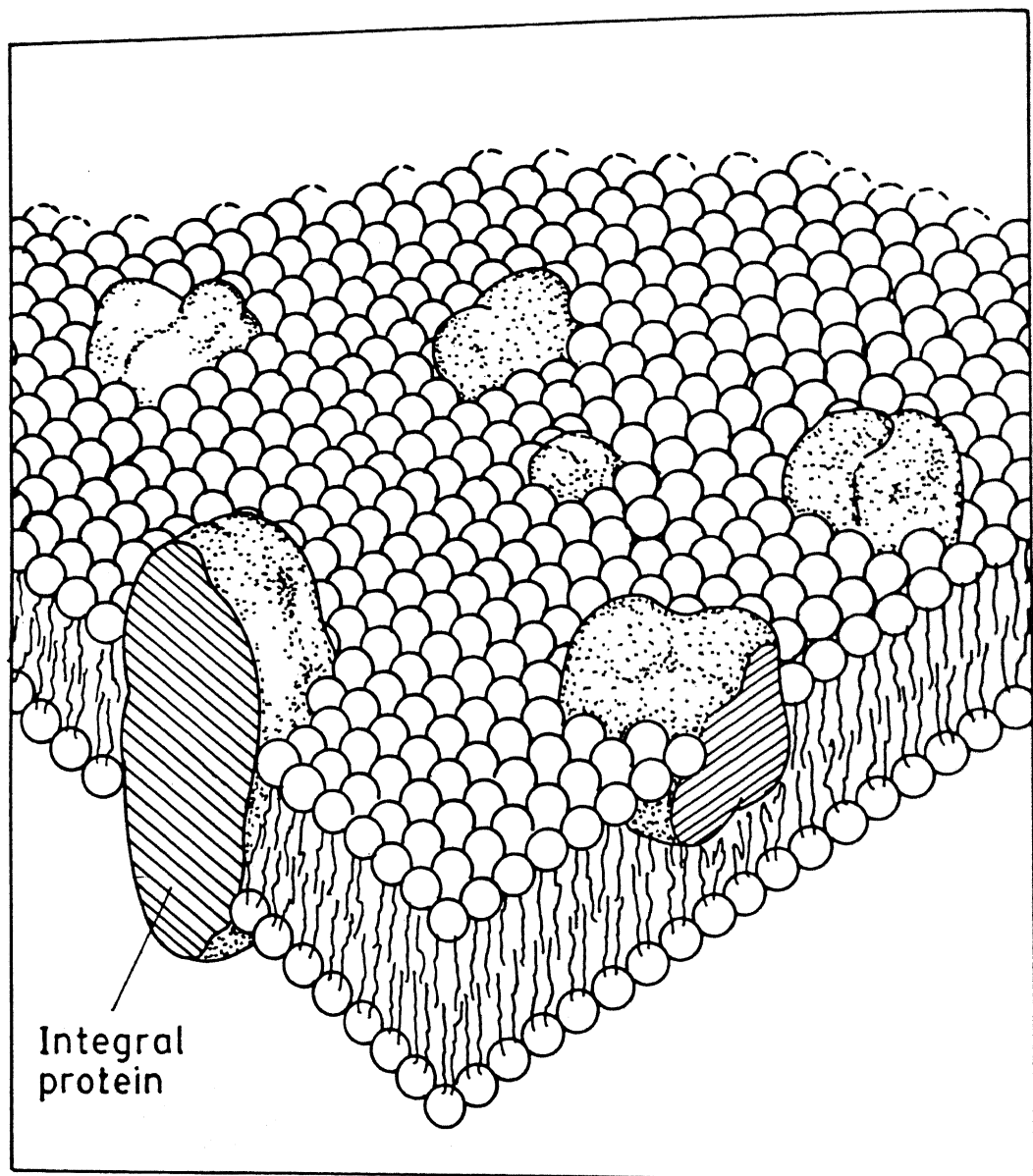


Fig. 1.1 The Singer and Nicholson 'fluid mosaic' model of a biomembrane (Adapted from ref. 34).



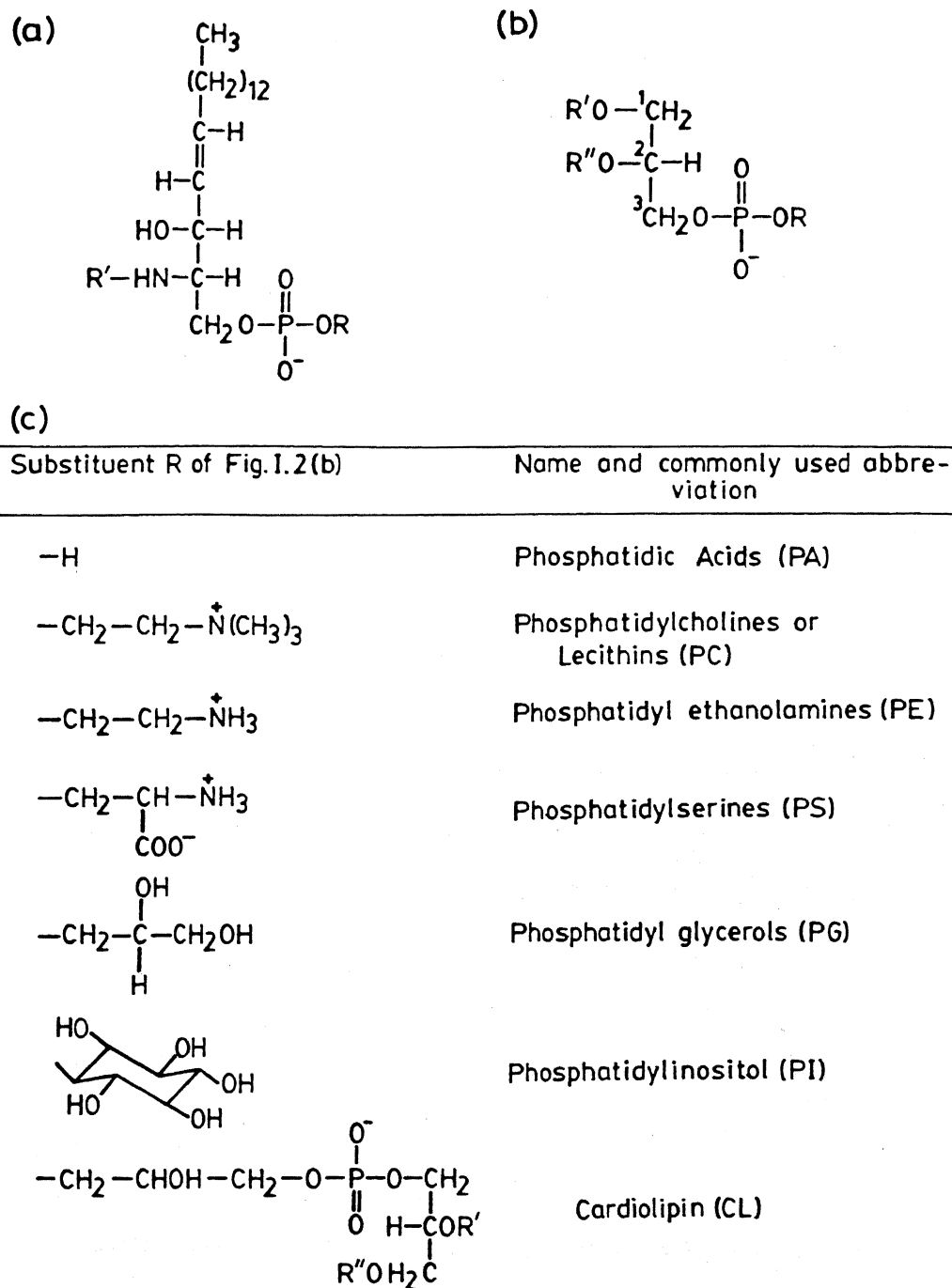


Fig. 1.2 General Chemical structures of (a) sphingo-phospholipids (b) glycerophospholipids and (c) main classes of glycerophospholipids with their common names.

details are given below about glycerophospholipids only, since these are the most commonly found membrane lipids<sup>33</sup> and also since these appear exclusively in phospholipid based reverse micelles. In our thesis, we shall use the word 'phospholipid' to indicate a glycerophospholipid, unless we specify otherwise.

### 1.3 Lipid Polymorphism

Phospholipids are seldom molecularly dispersed in solution. As amphipathic molecules, phospholipids have a great tendency to aggregate and, like fatty acids, to form more than one structurally different phase in the crystalline (solid) state as well as in aqueous dispersions. This property is referred as polymorphism.<sup>38</sup> Various structures have been mainly established by X-ray diffraction<sup>39,40</sup>, electron microscopy<sup>41</sup> and magnetic resonance.<sup>9,42</sup>

The most common phases of phospholipids in water<sup>35,39,43</sup> are given in Table 1.1. In the Table, L indicates a one-dimensional lamellar lattice, H, P and Q represent hexagonal two-dimensional, rectangular two-dimensional and cubic lattices, respectively. The Greek letters  $\alpha$ ,  $\beta$ ,  $\beta'$  and  $\alpha\beta$  indicate various conformations of the hydrocarbon chains.




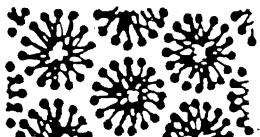

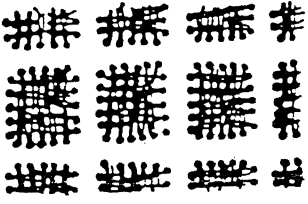
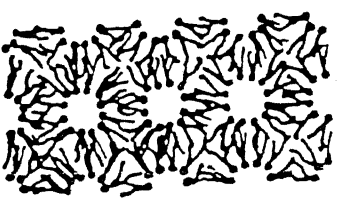
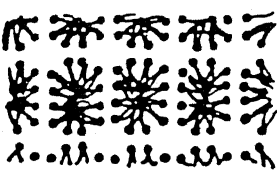

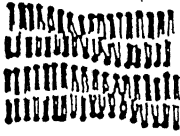

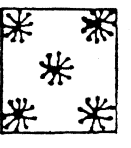
Reverse micelles, the subject of this thesis, belong to  $H_{II-\alpha}$  (reversed two-dimensional hexagonal type),  $P_{II-\alpha}$  (reversed two-dimensional tetragonal type) and  $Q_{\alpha}$  (reversed three-dimensional cubic type) containing a water core in an organic environment.

### 1.4 Existence of Reverse Micellar Structures in Biological Membranes

Although the existence of non-bilayer structures in biological membranes is by no means established conclusively, the existence of reverse micelles of membrane proteins and phospholipids in organic solvents is established.<sup>44</sup> The possibility of reverse micellar dynamic intermediates<sup>45-47</sup>

Table 1.1

The most common phases of phospholipids in water

Type of Packing	Structure <sup>†</sup>		
Coherent double-layers of molecules separated by water; lamellar one-dimensional array	 L	 $L_{\beta}$	 $L_{\beta}'$
Rod-like aggregates with organic core ( $H_{I-\alpha}$ ) and aqueous core ( $H_{II-\alpha}$ ); hexagonal two-dimensional array	 $H_{I-\alpha}$	 $H_{II-\alpha}$	
Rod-like aggregates with organic core ( $P_{I-\alpha}$ ) and aqueous core ( $P_{II-\alpha}$ ); tetragonal two-dimensional array	 $P_{I-\alpha}$	 $P_{II-\alpha}$	
Rod-like aggregates with organic core in aqueous environment; rectangular two-dimensional array	 $P_{III-\alpha}$		
Rippled double layers of molecules separated by water; lamellar two-dimensional array	 $P_{\beta}'$	 $P_{\alpha\beta}$	
Rod-like aggregates with aqueous core ( $Q_{\alpha}$ ) and organic core ( $Q_{I-\alpha}$ ); cubic three-dimensional array	 $Q_{\alpha}$	 $Q_{I-\alpha}$	

<sup>†</sup> adapted from refs. 29, 39a, 43 and 58.

8

occurring in membrane-membrane interactions and fusion processes and their roles have been analyzed.<sup>47-51</sup> These and the studies on lipid polymorphism led to a new fundamental insight into the physical properties and functional roles of lipids in membranes. A new understanding of biomembranes necessitated a revision of the well-known 'fluid mosaic' model. The new model proposed by Cullis et al.,<sup>52,53</sup> called the 'metamorphic mosaic' model, reproduced in Fig. 1.3, includes possible processes which involve reverse micellar structures such as exo- and endocytosis membrane fusion, movement of lipids across the bilayer, transport of ions across the bilayer and perhaps many other processes yet undetected.

### 1.5 Thermodynamics and Phase Diagrams

Amphipathic or amphiphilic molecules aggregate in nonpolar solvents predominantly due to dipole-dipole and ion pair interactions<sup>54</sup> and also due to a decrease in the overall free energy of the system. The hydrophobic effect of these molecules provides the driving force for aggregation and the repulsion between head groups limits the size of the aggregated structure. The nature of solvent (its polarity, dielectric constant, etc.) also plays a role in the aggregation behaviour of surfactants.

The thermodynamic principles of amphiphilic self-aggregation and the geometric aspects of the phenomenon have been well discussed.<sup>33,55-59</sup> Israelachvili and coworkers<sup>55</sup> discuss these in terms of a parameter called 'critical packing parameter',<sup>57,58</sup> which is associated with the thermodynamic characteristics of the amphiphile. The enthalpy and entropy changes of aggregation of potassium benzene sulfonate in heptane<sup>60</sup> ( $\Delta H = -79.5 \text{ kJ mol}^{-1}$ ;  $\Delta S = -62.8 \text{ JK}^{-1} \text{ mol}^{-1}$ ) suggest that the association energy for reverse micelles is mainly of enthalpic rather than entropic origin, as in the case of aqueous

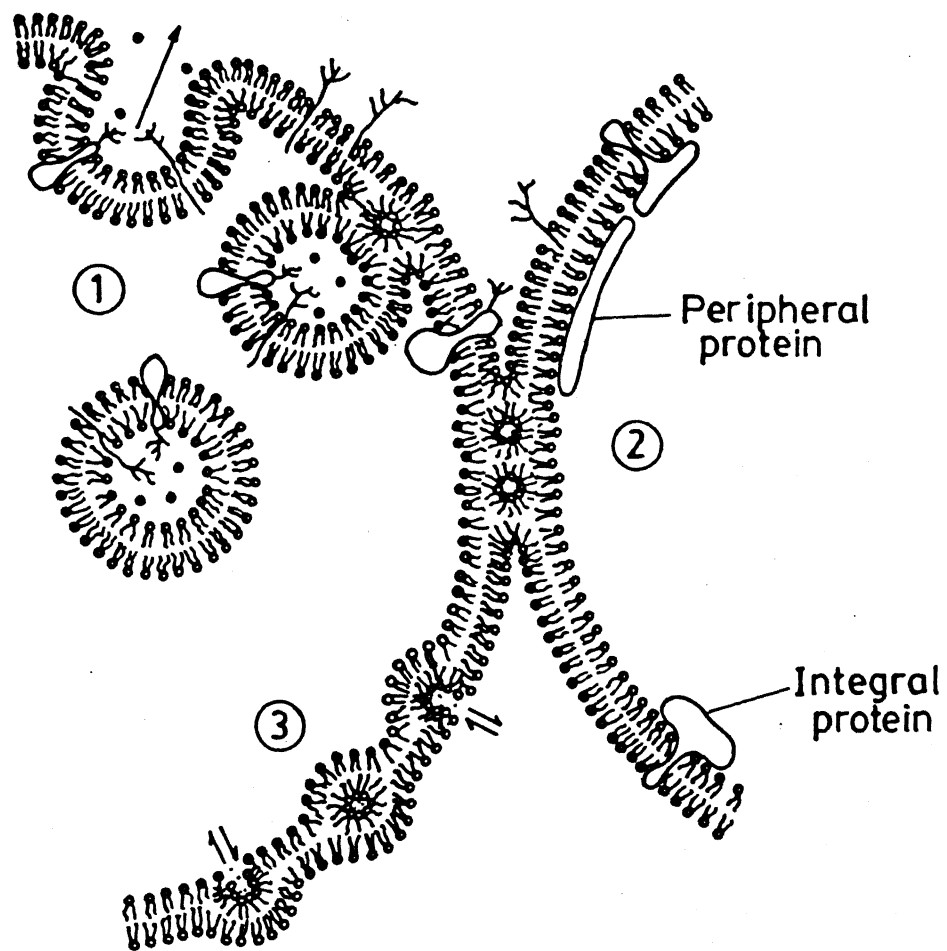


Fig. 1.3 The 'metamorphic' mosaic' model of biological membranes (taken from ref.(53)). Regions (1) and (3) show the involvement of reverse micellar as reverse cylinder-structural intermediates in an exocytotic fusion process and transbilayer molecular-transport process, respectively. Region (2) shows the possible existence of reverse cylinder structure at interbilayer tight junctions.

micelles.

The thermodynamics of amphiphile aggregation in polar and nonpolar solvents is usually discussed in terms of CMC. Three basic models<sup>61-63</sup> have been used for the thermodynamic treatment of micellization, namely, (i) pseudophase, (ii) single step equilibrium, or (iii) mass action law and multistep equilibrium. The first model is frequently used in NMR studies of micelles.<sup>63</sup> Giomini et al.<sup>64</sup> used the mass action law model for finding out the CMC and other thermodynamic parameters of lecithin/benzene/water reverse micelles. Although these theories can in principle be applied to phospholipid aggregates, much progress has not been made due to the following two reasons : (i) The cooperativity of reverse micellar formation is much smaller<sup>65</sup> compared with that of normal micelles. When the aggregation number is small, the change in physical properties with increasing concentration of the surfactant is gradual and, therefore, a well-defined CMC can seldom be identified.<sup>54b,65</sup> (ii) Since minute amounts of water are invariably present in the organic solvent, these systems should be considered as ternary, and the CMC would then lose its significance as it changes with the amount of water.<sup>2</sup>

Despite such a lack of a clear-cut concept of CMC for reverse micelles, 'CMC' values have been determined for many surfactants in nonpolar solvents.<sup>2,64,66-68</sup> Another way of understanding the thermodynamic properties of these systems would be through the construction of ternary phase diagrams. To the best of our knowledge, only two reports have been published on lecithin-based reverse micelles.<sup>69,92</sup> Shervani et al.<sup>92</sup> have studied lecithin-based reverse micelles in benzene, cyclohexane, n-octane and n-dodecane, in the presence and absence of cholesterol.

The role of water in the formation of reverse micelles has also received considerable attention. Previous study<sup>4</sup> has shown that, in general,

water is a prerequisite to promote the aggregation of amphiphilic surfactants to reverse micelles and that part of the water present serves as 'gluing' agent between the polar head groups of the surfactant monomers in the core of the reverse micellar aggregates. However, Yu et al.<sup>70</sup> reported recently from dynamic and static light scattering studies on sodium bis(2-ethylhexyl) phosphate in n-hexane that water is not a prerequisite for reversed micellization, in contrast with earlier reports; instead, the view has been taken that water can function as an antimicellization agent.<sup>70</sup>

### 1.6 Reverse Micellar 'Water Pool'

Much importance attaches to the physico-chemical studies of water in reverse micelles because of its rather peculiar chemical and physical properties<sup>71-74</sup> which differ from those of normal water, especially at low water-to-surfactant ratios. For instance, it has been found by various spectroscopic and other physical methods that reverse micellar water exhibits much higher viscosities,<sup>75-78</sup> lower mobilities,<sup>78-80</sup> varied polarity,<sup>81-91</sup> and dielectric constant,<sup>113</sup> varied pH<sup>82</sup> and hydrogen bonding<sup>72</sup> and low freezing point.<sup>74</sup>

Considerable studies have also been conducted on the interaction of water with the polar head groups of phospholipids.<sup>1,78,83-85</sup> However, the conclusions of some of these studies<sup>83</sup> are often contradictory or tentative.

Reverse micelles are not rigid but dynamic entities. They can collide freely in the hydrocarbon solution which leads to the exchange of water pools. The dynamics of the exchange of water in reverse micelles and biological systems can be described by qualitative and quantitative models. Qualitative models assume that water molecules exist in two or more environments, with one of these environments being that of pure water. The simplest case would be a

two-state model classifying the water molecules as 'bound' and 'bulk'.<sup>86,87</sup> This was later extended to a three-state model,<sup>88-91</sup> the states in question being described as follows.

**Type I : "bulk Water" or "Free Water"** - the rotational and translational motions of these water molecules are not appreciably altered compared to normal water, with  $\tau_R$ , the rotational correlation time, being  $\sim 10^{-12}$  s.

**Type II : "bound water"** - the rotational motion, freezing point, etc. of these water molecules are significantly hindered by interactions with the polar head group of surfactants, leading to  $\tau_R$  values of  $\sim 10^{-9}$  s.

**Type III : "trapped water" or "irrotationally bound water"** (this term, however, does not exclude translational or exchange mechanisms); these water molecules are essentially "trapped" or "site bound" to the surfactant or to the macromolecules, with  $\tau_R \sim 10^{-5}$  to  $10^{-7}$  s.

Quantitative estimation of these types of water has also been made. Koenig and Schillinger<sup>88b</sup> estimated Type III water from the magnitude of NMR spin-lattice relaxation time ( $T_1$ ) dispersion. Type II water can be directly estimated from freezing experiments, and the remaining water is to be considered as Type I or bulk water. Although previous studies have led to a reasonably consistent picture of the mobility and organization of water in the 'water pool', there still exists the necessity for obtaining true (or at least reliable) values for the physical properties of the aqueous core of reverse micelles by using a variety of techniques.

### 1.7 Experimental Methods Used to Probe Reverse Micelles

Various experimental methods have been used to characterize the reverse micelles. Most of these methods are used to probe the compartmentalized, polar microenvironment, the 'water pool', while a few of them are used to



get some macroscopic information such as bulk viscosity .

We may broadly categorize the experimental methods into three groups, namely, (i) scattering techniques, (ii) physical methods, (iii) spectroscopic techniques. These may be further understood as follows.

#### (i) Scattering Techniques

Scattering techniques provide macroscopic structural information about reverse micelles, the three most frequently used techniques being light scattering (LS), small-angle neutron scattering (SANS) and small-angle X-ray scattering (SAXS).

Light scattering essentially probes the Brownian motion of particles. Static and dynamic light scattering<sup>98</sup> (also known as quasi-elastic light scattering or photon correlation spectroscopy) have been used to determine the size and translational diffusion coefficients of droplets, to measure intermicellar interactions of reverse micelles and to investigate protein encapsulation in reverse micelles. A good review of these studies has been published.<sup>26</sup>

Light scattering studies of egg lecithin reverse micelles in benzene, carbon tetrachloride ( $\text{CCl}_4$ ) and cyclohexane were reported from our laboratory.<sup>76</sup> These studies reveal the presence of homodisperse aggregates in benzene and  $\text{CCl}_4$  and anisotropic tubular structures in cyclohexane.

The small angle neutron scattering (SANS) technique gives more detailed information on size and size distributions of reverse micelles, due to the fact that the neutron scattering vector has a large range ( $0.02\text{--}0.2 \text{ \AA}^{-1}$ ). This can also be used to study the effect of additives in the reverse micelles.<sup>93</sup> Translational motion of reverse micelles can be monitored by using a quasi-elastic, incoherent neutron scattering method.<sup>94</sup> Several comprehensive reports of SANS studies in micellar and microemulsion systems have been published.<sup>26,95,98,99</sup>

A SAXS experiment determines the so-called 'radius of gyration', which is related to the polar core radius of reverse micelles. These can be used to probe the change (increase or decrease) in size of the polar core in the presence of additives or solubilized enzymes.<sup>96</sup>

### (ii) Physical Methods

A variety of physical methods have been used to probe reverse micelles, namely, (a) viscosity measurement, (b) electrical conductivity, (c) electron microscopy, to name the more important ones. All these techniques have been used on egg-lecithin reverse micelles in three different solvents in our laboratory earlier.<sup>76</sup> The major results of these studies are : the reverse micelles contain dispersed water in small spherical droplets surrounded by a phospholipid layer; the electrolyte (KCl solution) added for measuring specific conductivity is contained in discrete water pools that are formed in the interior of the reverse micelles; the cyclohexane system at water-to-surfactant mole ratio of 5-6 exhibits an elongated tubular structure containing aqueous canals.

### (iii) Spectroscopic techniques

A wide variety of spectroscopic techniques may be used to probe the water pool, organic bulk phase and surfactant to get dynamic or motional information of the system.

The selection of a particular technique depends on the type of physical property in which one is interested. The motional frequencies of different parts of the lipids occur in the range of  $10^{-6} - 10^{+14} \text{ s}^{-1}$ , i.e., spanning a time-scale of 20 orders of magnitude. We note that some techniques yield a static picture since the molecular motions are 'slow' relative to the measurement while others see a time averaged picture of molecules which move between different environments very rapidly relative to the measurement time.

The fact that Magnetic Resonance (EPR,NMR) can probe a reasonably wide range of molecular motions makes this method an important tool for motional studies.

The time scale of a particular motion being studied vis-a-vis the time scale of the technique being used for the measurement are worth a further emphasis. Consider a general case which could apply equally well to an EPR, fluorescence, or  $^2\text{H}$ -NMR measurement of a molecular probe. All three spectroscopic techniques are sensitive to the orientation of the molecule with respect to an axis system defined in the laboratory. For example, in  $^2\text{H}$ -NMR, the observed spectrum is sensitive to the orientation of C-D, O-D or other bond in relation to the externally applied magnetic field. In EPR, the situation is similar, where the spectrum is sensitive to the orientation of the N-O (nitroxide) bond present in most commonly used probes, with respect to the applied magnetic field. In fluorescence spectroscopy, the measured polarization of the emitted light is dependent on the orientation of the molecular transition dipole moment with respect to the direction defined by the polarizer used to make the measurements. Some further elaboration of these techniques is given below :

**(a) Optical Spectroscopy** (UV-visible, fluorescence, IR, Raman and circular dichroism).<sup>26,28,93,97</sup>

In most of these experiments, some probe molecules are entrapped in either the water pool or the organic phase of micelles, and conclusions are derived from the observed trend of properties such as polarity, hydrogen bonding, mobility, vibrational motion of a bond in a molecule, protein conformation, activities of solubilized enzymes, etc.

To give but one example, using the nitrate ion as a probe and monitoring the  $n \rightarrow \pi^*$  band in the UV range in egg lecithin based reverse

micelles in benzene, carbon tetrachloride and cyclohexane,<sup>81</sup> it has been found that the effective polarity of the water pool is lower than that of bulk water. This result is substantiated by the fluorescence emission spectra of the same three systems,<sup>81</sup> using 8-anilinonaphthalene sulfonic acid (ANSA) as a probe. In the cyclohexane system, this technique suggested the possible presence of a liquid crystalline phase when the water-to-surfactant ratio was six. Near-IR spectra of the same systems<sup>81</sup> give two absorption bands : one at about 1890 nm corresponding to water-dispersed in the organic phase and the other band over a range of 1930-1960 nm corresponding to the water solubilized in the reverse micellar interior. From this study, it is also estimated that only about 0.05% (V/V) of total water is present in the bulk solvent.

Other spectroscopic techniques, used to a lesser extent to characterize the water-pools of reverse micelles, are (a) time-domain dielectric spectroscopy,<sup>100</sup> (b) positron annihilation spectroscopy,<sup>101</sup> (c) photon correlation spectroscopy,<sup>102</sup> and (d) perturbed angular correlation spectroscopy.<sup>103</sup> However, these shall not be further described here.

## (b) Magnetic Resonance Techniques

### Nuclear Magnetic Resonance (NMR)

Since all nuclei with nonzero nuclear spin quantum number are NMR 'active', useful information can be obtained from virtually all components of the reverse micelle. This essentially eliminates the need for using a molecule which may be 'invasive' and change the physico-chemical properties of the system.

The NMR parameters are of two kinds. The first kind consists of steady state parameters (the chemical shift ( $\delta$ ) and scalar (J), dipolar, and quadrupolar coupling constants) which are related to the molecular structure of

the system under study; they give information about the chemical environment of the observed nucleus and about its stereochemical relationship with other nuclei in close spatial proximity. The second kind includes dynamic parameters (the longitudinal or spin-lattice relaxation time ( $T_1$ ) and the transverse or spin-spin relaxation time ( $T_2$ )) which are related to the motional characteristics of the nuclear spin system.

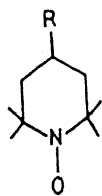
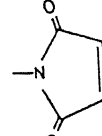
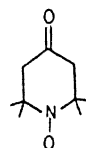
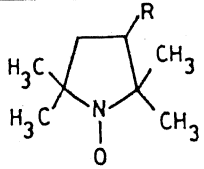
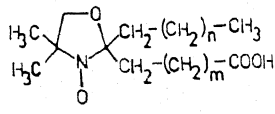
The following information can be obtained from NMR studies on reverse micelles:<sup>26,28,29</sup> aggregation numbers and exchange rates of different components of the system, extent of hydration of the polar head group, properties and activities of the solute solubilised in different phases, macroscopic self-diffusion of a molecule and segmental motions, conformations and order parameters of surfactant molecules, etc.

Systematic studies have been carried out in our laboratory on egg-lecithin based reverse micelles<sup>76,78,81,85</sup> in benzene,  $\text{CCl}_4$  and cyclohexane using extensively,  $^1\text{H}$ ,  $^{31}\text{P}$  and  $^{13}\text{C}$  NMR and to a limited extent  $^2\text{H}$  and water proton diffusion coefficient measurements. A survey of the available literature on NMR studies of reverse micelles has been given elsewhere.<sup>104</sup>

### Electron Paramagnetic Resonance (EPR)

EPR spectroscopy is one of the most promising and extremely useful techniques for the study of reverse micelles. Since the generally used biomolecules, surfactants, solvents and water are not paramagnetic in nature, to carry out EPR investigations we have to necessarily incorporate some specific probes which are likely to be very sensitive to environmental changes. These are called 'spin labels'. The advantage with spin labels is that they can be designed and synthesized according to our requirement. The generally used spin labels are listed in Table 1.2.

TABLE 1.2 The generally used EPR spin labels

	Spin label	Name
I	 <p>a) R = -H</p> <p>b) R = -OH</p> <p>c) R = -NH-CO-CH<sub>2</sub>I</p> <p>d) R = </p> <p>e) R = -NH<sub>2</sub></p>	<p>TEMPO derivative</p> <p>(2,2,6,6-tetramethyl piperidin-1-yloxy)</p> <p>TEMPO</p> <p>TEMPOL (4-hydroxy-TEMPO)</p> <p>4-iodoacetamido-TEMPO</p> <p>4-maleimido-TEMPO</p> <p>4-amino-TEMPO</p>
II		<p>TEMPONE</p> <p>(2,2,6,6-tetramethyl piperidin-4-one-1-yloxy)</p>
III	 <p>a) R = -CONH<sub>2</sub></p> <p>b) R = -OH</p> <p>c) R = -COO<sup>-</sup></p>	<p>PROXYL derivative</p> <p>(2,2,5,5-tetramethyl pyrrolidin-1-yloxy)</p> <p>3-carbonyl-PROXYL</p> <p>3-hydroxy-PROXYL</p> <p>3-carboxy-PROXYL</p>
IV	 <p>a) m = 2 &amp; n = 9</p> <p>b) m = 4 &amp; n = 7</p> <p>c) m = 7 &amp; n = 4</p> <p>d) m = 9 &amp; n = 2</p>	<p>DOXYL derivative</p> <p>(4,4-dimethyl oxazolidin-1-yloxy)</p> <p>5-doxyl stearic acid</p> <p>7-doxyl stearic acid</p> <p>9-doxyl stearic acid</p> <p>12-doxyl stearic acid</p>

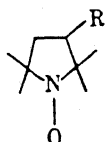
**Physio-chemical results deduced from EPR :** Dealing as it does with the electron spin, EPR explores much shorter timescales than its nuclear spin counterpart, NMR.<sup>105</sup> EPR is sensitive to exchange processes in the time domain ( $10^{-6}$ - $10^{-4}$  s) where the exchange of surfactant monomers and guest molecules between spherical aggregates and the bulk solution is to be expected.<sup>106-109</sup> In micellar solutions of exclusively spin labeled surfactant (SL-surfactant) molecules, above the CMC, two overlapping EPR-signals are expected if the exchange rate between micelles and dispersion media is sufficiently slow : one signal corresponds to the SL-surfactant monomers in bulk solutions, while the other, a spin exchange broadened signal, is due to the SL-surfactant molecules within the micelles.<sup>110</sup>

These spin label probes also yield information about the dynamics of rotation of the probe,<sup>110,111</sup> and polarity of the environment as revealed by the hyperfine splitting constants<sup>127</sup> and order parameters.<sup>127</sup>

#### 1.8 Survey of EPR, ENDOR and ESEM studies on reverse micelles

Not much work has been done, using EPR as a tool, on the reverse micellar water pool. This is evident from the miniscule literature of around thirty papers available in this area to date. A brief review has been published recently.<sup>112</sup>

The first pioneering EPR study on spin labels incorporated in reverse micelles was carried out by Menger.<sup>113</sup> AOT/heptane/water system was used in this study. The spin labels used were :



R = CONH<sub>2</sub>  
R = OH  
R = COO<sup>-</sup>

Changes in the nitrogen hyperfine splitting constants ( $a_N$ ) and linewidth parameters of all these three spin labels were investigated as a function of the water content. As the pool size diminished, the hyperfine coupling constants decreased from that characteristic of water to that characteristic of heptane. Since the  $a_N$  values indicated that the local environment of spin label at low R was heptane-like, the two possible sites for spin labels were (1) the heptane phase, (2) the heptane-water interface. Considering the inability of the spin labels to partition and dissolve into the heptane, it was concluded that the likely site was the heptane-water interface. The increase in line broadening with diminishing pool size was explained by the fact that the contraction of the pool must 'squeeze' the spin label from the pool interior onto the interface. In this region the spin label experienced a slight restriction in mobility which could be due to the viscosity of the interface and due to the nitroxide groups immersing themselves in the heptane. The high field peak of the carboxylate spin label split into two when  $R = 10.3$ , i.e., signals from the probe molecules in the water pools and the interface were observed separately. This was because of the slow exchange of the labels. The non-ionic spin labels, however, did not show spectral distortion by virtue of a rapidly exchanging environment.

Lim and Fendler<sup>114</sup> made a detailed study of three different compartments of dodecylammonium propionate(DAP)/benzene/H<sub>2</sub>O reverse micellar system using specially chosen anionic, cationic and neutral EPR spin probes. The neutral probe, somewhat soluble in the organic solvent (benzene), exchanged among the environments provided by the reverse micelles. The exchange frequency was found to be  $\geq 6 \times 10^6$  s. Conversely, both the charged spin probes favorably partitioned into water and their EPR data provided information on the micro environments of these probes. The anionic radical was likely to be



anchored at the water-hydrocarbon interface with polar carboxylate group intruding into the surfactant solubilized water pools. The cationic radical, however, was shown to be situated in a less polar region corresponding to that occupied by the ammonium head group of the surfactant. The 'microviscosities' reported by the charged probes increased initially with increasing water content, until maxima were reached at 0.4 M cosolubilised water concentration, when free water molecules began to appear. Important conclusions reached from these results were, (i) that different environments were preferred by the surfactant cation head group and its counter ion, and (ii) more than one type of bound water molecule was present. The rate of quenching of the anionic radical by phenylhydrazine remained unaffected by micellar DAP but that by sodium ascorbate decreased if the concentration of the quencher was taken to be that dissolved in the surfactant solubilised water pools. It is of interest to note that the increase in nitrogen hyperfine coupling constants was significant for the anionic probe and moderate for the cationic probe as the water content increased; the coupling constants stayed virtually unchanged in the case of the neutral probes.

Kumar and Balasubramanian<sup>115</sup> used 2,4-dinitro-diphenyl hydrazone of 2,2,6,6-tetramethylpiperidiny-1-oxy spin probe to study the structural features of Triton X-100/1-hexanol/H<sub>2</sub>O microemulsions. They adopted Yoshioka's method<sup>116</sup> to monitor the dynamics of the non polar end of the surfactant. Absorption studies of the same probe in the reverse micellar systems<sup>115</sup> revealed that the polar molecule had been positioned close to the alkyl phenyl ether end of the ethylene oxide chain of the Triton X-100. The correlation time calculated from the EPR spectra increased with increase in the water content. In the initial region (0-1%) this was significant. In the region of 1-3 % water, a drop in the  $\tau_R$  values indicated a greater mobility of the probe near

the non polar region of the surfactant. Again, in the region beyond 3%, an increase in the  $\tau_R$  showed that mobility was reduced due to hydration of the surfactant extended up to the ether end of the ethylene oxide chain. These results were completely in agreement with  $T_2$  values of -OH and  $-\text{CH}_2-\text{CH}_2-\text{O}$  protons of Triton X-100 obtained from NMR.

Yoshioka<sup>117</sup> carried out a variable temperature study on TEMPONE (2,2,6,6-tetramethylpiperidine-4-one-1-oxy) spin probe incorporated in AOT reverse micelles. It was observed that the presence of a large amount of water led to phase separation when the temperature was lowered below 18° C and that the water was not frozen even at -33° C. Also, the micellar size was not changed. The small changes in  $a_N$  values and intensity ratios of low field line to the high field line showed that the probe was not present in the water pool; instead, the probe was present in the shell especially when the reverse micelles were having low water content. This explained why the probe did not feel the polarity of water in the pool. Two-site exchange model was the basis for the interpretation of these spectra at lower temperatures. The two sites were the polar and nonpolar parts of the reverse micelles. This exchange model suggested that the environment in the shell was nonpolar like heptane. The fraction of probes located at the polar and nonpolar sites were calculated to be  $f_{\text{polar}} = 0.31$  and  $f_{\text{nonpolar}} = 0.69$ . The probability ( $P_{\text{SW}}$ ) for the exchange between two sites was also calculated at various temperatures in the reverse micelle. There was a linear dependence of  $\log(P_{\text{SW}})$  on reciprocal temperature and the activation energy for the exchange process was calculated to be 7.5 kcal mol<sup>-1</sup>.

Based on EPR lineshape simulations, Yoshioka et al.<sup>118</sup> proposed a model for the positional exchange of the spin probes in the reverse micelles. Simulations were done based on a modified Bloch equation. The assumed two-phase

model suggested the presence of two types of probes, one mobile and the other bound or immobile.

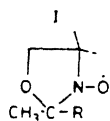
Gandin et al.<sup>119</sup> examined the effect of oxygen diffusion in the water pools of AOT/heptane/H<sub>2</sub>O reverse micelles with the help of Fremy's salt (sodium salt of peroxyaminedisulfonate, PADS). The ratios of the intensity of the high field and central nitrogen hyperfine lines, which reflected the mobility of the probe in different environments, decreased with decreasing R. When the 'R' values were varied from 9.8 to 6.55 this effect was prominent. This result, indicating the mobile and immobile water present in the reverse micelles, was in agreement with other spectroscopic methods. The <sup>14</sup>N hyperfine linewidths of Fremy's salt in aerated ( $W_{\text{air}}$ ), deoxygenated ( $W_a$ ) and oxygen saturated ( $W_{\text{oxygen}}$ ) reverse micellar solutions showed independent linear relationships with water content or R value. The decreasing order of the broadening was  $W_{\text{oxygen}} > W_{\text{air}} > W_a$ . The ratio between the line broadening due to oxygen spin exchange in aerated solution (air) and that in oxygen saturated solution was around 0.2. There was a linear dependence in the broadening due to oxygen as a function of varying amount of water. Line broadening effects due to O<sub>2</sub>, as a function of R values were then related to the collision frequency of nitroxides with oxygen.<sup>119</sup> Finally, the 'diffusion coefficient - concentration product' was related to the radius of the aqueous core, and it was shown that the diffusion coefficient concentration product increased linearly with radius of the water droplet (from 12 to 43 Å). The concentration of the oxygen present in the micelles was shown to be 0.75 times that of the bulk water concentrations which was  $2 \times 10^{-4}$  M. The average number of oxygen molecules present in a water bubble could be calculated from this value. This was  $\leq 1$ , depending on R, indicating that the oxygen molecule essentially came from the organic phase.

Brüggeller<sup>120</sup> used CuCl<sub>2</sub> as an EPR spin probe to examine the

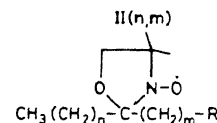
possibility of ice formation in water/oil(w/o) microemulsions. In this study, microemulsions of cationic, anionic and nonionic surfactants as well as the detergentless system were investigated and the influence of co-surfactants also examined. In the detergentless w/o microemulsion (n-hexane/2-propanol/0.1M  $\text{CuCl}_2$ -water) ice formation was not observed even at 173 K.  $\text{Cu}(\text{H}_2\text{O})_2^{2+}$  in the system felt an isotropic liquid environment near 313 K. A decrease in mobility of the spin probe due to interaction of  $\text{Cu}^{2+}$  with 2-propanol was revealed by the EPR spectra recorded at room temperature. As the system was cooled down, rigid limit spectra were observed at 173 K SDS/1-butanol/toluene/0.1  $\text{CuCl}_2$ -water system. All these spectra were reversible with temperature. The triton X-100/1-butanol/cyclohexane/0.1 M  $\text{CuCl}_2$ -water system behaved slightly differently. At 233 K, a typical combination spectrum of an isotropic component (centered at about 3020 Gauss) and an anisotropic one (centered at about 3130 Gauss) was obtained. Comparison of EPR spectra of CTACl/1-hexanol/ $\text{H}_2\text{O}$  and SDS/1-octanol/ $\text{H}_2\text{O}$  gave interesting results during slow cooling. While the cationic system (CTACl) was not affected by slow cooling, in the anionic system ice formation was observed at 248 K. The 'rigid limit' spectrum was not observed by this slow cooling process. Rather, the system had to be quenched at liquid nitrogen temperature in order to get 'rigid limit' spectrum of SDS/1-octanol/ $\text{H}_2\text{O}$ . Finally, when short chain alcohol was present, even without surfactant, ice formation was not observed. This was due to the solubility of these alcohols in water, which then act as cryoprotecting agents. In the system containing 1-octanol, which did not take up water present in the system, the cooling process was different. This was due to the presence of free and bound water.

In 1986, Eicke et.al.<sup>121</sup> investigated the exchange kinetics of surfactants in AOT/isooctane/water microemulsion using EPR spectroscopy. The

spinlabels used in the study are shown below.



- a)  $R = -(\text{CH}_2)_4-\text{CH}_3$   
 b)  $-R = -\text{CH}_2-\text{CH}_2-\text{CH}(\text{CH}_3)_2$



- a)  $R = -\text{OH}$   
 b)  $R = -\text{SO}_3\text{Na}$

Anisotropy in the EPR spectrum of II(0,4)b was more compared with II(0,4)a which was in turn more than in Ia (numbers in parentheses indicating n and m values, respectively). The  $^{14}\text{N}$  hyperfine splitting constant of water insoluble compounds such as Ia and Ib did not vary with increase of water content (weak R dependence), while the water soluble spin labels showed a strong R dependence. The peak height ratio of the central to the high field line ( $h_0/h_{-1}$ ) showed strong R dependence as far as the EPR spectra of II(0,4)b and II(0,4)a were concerned, which indicated a slow rotational motion of the radical when R was small (up to 6) and fast motion when R was high (above 6). Up to about  $R = 6$  water in the aggregated system was in the bound state in the primary hydration shell of AOT. Above  $R = 6$ , the compound, II(0,4)b (hydrocarbon-insoluble), became less rigid with increasing amounts of solubilised water. The penetration of spin label II(0,4)a, indicated by the kink at about  $R = 12$  in the plot of  $h_0/h_{-1}$  versus R, was also an indication of appearance of free water. Anisotropy in the bound water region was explained on the basis of already proposed<sup>122a-b</sup> viscous water shell model.

In the case of I(a) or I(b) the  $h_0/h_{-1}$  values were very close to those observed for freely tumbling nitroxides in nonviscous liquids.<sup>121</sup> Exchange of II(a) between hydrocarbon and water phases was revealed in the EPR spectrum (splitting of high field line). Variation of the linewidth of the high field lines with varying R showed isotherms which passed through minima. The

exchange processes within the aqueous nanometer-sized droplets (i.e., nanodroplets) were investigated using detailed line-width analysis and rate constants for exchange were evaluated by considering the experimental line-width ( $1/T_2$ ) as a sum of natural linewidth ( $1/T_{2,0}$ ) and linewidth contribution of the exchange processes ( $1/T_{2,ex}$ ). The exchange line-width increased with the increase in temperature due to the increase of exchange rate. Rate constants of the forward and backward reaction of the exchange processes followed an increasing trend with increasing temperature at constant R, and a decreasing trend at a constant temperature with increasing R. Activation energies for the forward and backward reaction also followed an increasing trend with increasing R. The difference between these two values at a given R (i.e., transition enthalpy ( $\Delta H$ ) of the label between two solubilizations) passed through a pronounced maximum with increasing R. The transition entropy ( $\Delta S$ ) also followed the same pattern. The steep rise in the  $\Delta S$  and  $\Delta H$  values with increasing water pool size was because of the increasingly favorable tendency of the amphiphilic label to exchange between monolayers and water. This exchange process was inhibited when the size of the water pool was small (bound water region), and facilitated when it was large (free water region).

Fremy's salt was used as a spin probe in the AOT/toluene/water and DAP/toluene/water systems to carry out EPR and ENDOR studies in 1986 (Janzen et al).<sup>123</sup> The  $^{14}\text{N}$  hyperfine splitting constants obtained from EPR spectra of Fremy's salt in DAP reverse micelles was greater than that in DAP solution which in turn was greater than  $^{14}\text{N}$  hyperfine splitting constants of Fremy's salt in aqueous solution. This showed the difference in the polarity of the water present in the above system. EPR linewidths were monitored as the temperature was decreased from 310 K. Line-broadening was exhibited even after the freezing point, which is markedly different from the 'bulk water' property.

Intensity ratio measurements reflected the slower rotational diffusion of the spin probe in reverse micellar water.

As the sensitivity of the EPR linewidth to changes in temperature was rather poor,  $^{14}\text{N}$  ENDOR was used in this work,<sup>123</sup> and the intensity of the  $m_I = 0$  line was monitored as a function of temperature in reverse micelles and in bulk water. ENDOR studies of the reverse micelles showed that the temperature for the optimum ENDOR signal was different from that in water. Freezing of bulk aqueous solutions was observed before the optimum ENDOR condition. The optimum rotational correlation time ( $\tau_R^{\text{opt}}$ ) was shown to be  $1.4 \times 10^{-10}$  s. The viscosity data obtained from these  $\tau_R^{\text{opt}}$  were 2.2 cP for DAP reverse micelles at 317 K (c.f. 0.61 cP for bulk water at 317 K). The AOT reverse micelles showed 2.3 cP for  $\tau_R^{\text{opt}}$  at 325 K (c.f. 0.53 cP for bulk water at 325 K).

Proton ENDOR spectra of organic radical anions (from lumiflavin, riboflavin, FMN and FAD) were first reported by Kurreck et al.<sup>124a-b</sup> Reverse micelles provided a good environment for the abovementioned organic radical anions for getting ENDOR signals; Such studies were otherwise impossible in aqueous solution.

In a later work, Janzen et al.<sup>125</sup> have carried out EPR studies on Fremy's salt in AOT/Heptane/water systems. This probe is known to occupy only the water pools of the reverse micelles, because of its insolubility in dry organic solvents even in the presence of AOT. The line width increased with the decrease of water content. Broadening was observed in the high field EPR lines of Fremy's salt when the water pool was very small. However, it was also concluded that the Fremy's salt was not suitable to probe the change in the polarity of the water pools. Standard expressions were used for calculating rotational correlation times. The 'R' dependent  $\tau_R$  showed a marked increase between  $R = 10$  to  $R = 2$ . The viscosities calculated from Stokes-Einstein

equation also followed a similar pattern of correlational times.

In 1988, Okazaki and Toriyama<sup>126</sup> used reverse micelle as a medium to resolve the  $^{33}\text{S}$ ,  $^{17}\text{O}$  and  $^{15}\text{N}$  satellite EPR lines of Fremy's salt. In reverse micelles, a high concentration of Fremy's salt gave a spin-exchange-free and dipolar-broadening-free EPR spectrum, which was the main advantage, claimed by the authors, for carrying out this work. Considerable line narrowing was achieved in the EPR spectrum when AOT/isooctane/ $\text{H}_2\text{O}$  was used as a medium instead of water. The line narrowing was due to the inhibition of spin exchange and of the dipole-dipole interaction between the radicals solubilised in the water pools of the reverse micelles. Even at high concentration of Fremy's salt ( $3.3 \times 10^{-2} \text{ M}$ ) no line broadening occurred; instead, quartet hyperfine signals due to the  $^{33}\text{S}$  isotope and sextet hyperfine signals due to the  $^{17}\text{O}$  isotope of  $\text{SO}_3$  group at their natural abundances were observed. Increased modulation width and higher microwave power yielded  $^{33}\text{S}$  satellite line of Fremy's salt containing  $^{15}\text{N}$  nucleus. The hyperfine splittings for  $^{33}\text{S}$  and  $^{17}\text{O}$  in  $\text{SO}_3$  group and  $^{15}\text{N}$  and  $^{17}\text{O}$  in  $\text{NO}$  group were  $1.282 \pm 0.01 \text{ G}$ ,  $0.537 \pm 0.01 \text{ G}$ ,  $18.35 \pm 0.05 \text{ G}$  and  $20.55 \pm 0.2 \text{ G}$ , respectively. In addition, 9 out of the 18 satellite lines due to the  $^{17}\text{O}$  nucleus of nitroxyl group were resolved at natural abundance. Inhibition of spin exchange in the reverse micelle was interpreted as follows. For an estimated content of 200 water molecules per water pool in the reverse micelle, each molecule of Fremy's salt would be distributed among 28 water pools. The thick wall made up of surfactant molecules around the water phase would inhibit the inter radical interactions, i.e., spin exchange and dipole-dipole interaction, provided that the life span of the micellar particle was long enough. The suppression of the line broadening due to molecular oxygen was also explained in the same manner: since the solubility of atmospheric oxygen in water was about  $0.3 \text{ mM}$  at  $20^\circ \text{ C}$ , the



probability that one oxygen molecule could become solubilised in the water pool in which a Fremy's salt molecule was already solubilized was very small ( $4 \times 10^{-5}$ ), thereby making any linewidth considerations negligible. When the concentration of surfactant was low, however, the probability of oxygen solubility would be high, and consequently lines would be broadened due to interradsical interaction.

Haering et al,<sup>127</sup> in their detailed study, have characterized different compartments of AOT/isooctane/H<sub>2</sub>O reverse micellar system using the EPR spin labeling technique. Probes having different chemical structure and amphiphilic character have been used in this work. These probes were n-doxyl stearates ( $n = 5, 6, 7, 9, 10, 16$ ), 4-[(N,N-dimethyl-N-hexadecyl) ammonio]-2,2,6,6-tetramethylpiperidine-1-oxyl iodide (CAT 16), tempopalmitate, tempocholine and DSTA. The order parameter of the reverse micelles labeled with n-doxylstearates, increased with water content, reaching a plateau at about  $R = 30$ . With further water addition, <sup>14</sup>N hyperfine splitting constant also increased, for AOT reverse micelles labeled with different n-doxylstearates except 16-doxylstearates. This indicated that the local environment of the probe became more polar as  $R$  increased. The change in  $a_N$  was more pronounced the closer the doxyl group was to the COO<sup>-</sup> group. This could be due to molecular and segmental motion of the n-doxylstearate molecule. In the case of 16-doxylstearates labeled AOT reverse micelles, since the spin group was far removed from AOT-water interface (i.e., totally in isooctane bulk phase), there was no change in the  $a_N$  values. The AOT reverse micelles labeled with DSTA and tempocholine behaved similarly. The  $a_N$  values increased continuously with increasing  $R$ ; furthermore, with decreasing  $R$ , the linewidth increased for both spin labels. This result indicated that the preferred location of these labels was AOT-water interface with nitroxide group penetrating into hydrocarbon

region. The line broadening might be caused by weak immobilization of the spin label due to its orientation at the interface. The exchange frequency between the site and bulk water pool was estimated to be about  $10^7 \text{ s}^{-1}$ . The EPR spectra<sup>127</sup> further confirmed the anisotropic rotation of the spin label molecules about an axis that is parallel to the N-O bond or the X principal axis. With decreasing R the  $a_N$  values also decreased for CAT 16 labeled reverse micelles. The dependence of the  $^{14}\text{N}$  hyperfine splitting constant of CAT 16 on R confirmed that the nitroxide group oriented at the interface, as was the case with DSTA and tempocholine.

The AOT reverse micelles were characterised<sup>127</sup> with the above-mentioned spin probes by keeping R as constant (R=50). EPR spectra of different n-doxylstearates were monitored at constant R (say 50). Up to 9-doxylstearate the EPR spectra were characteristic of rapid but anisotropic motion. The spectrum of 16-doxylstearate was almost isotropic, while the  $^{14}\text{N}$  lineshape of the 10-doxylstearate spectrum was more anisotropic. Further, the pH of the water pools of AOT was determined as 7.7 using 5-doxylstearate. The order parameter and hyperfine (isotropic) splitting showed an increasing trend with increase of pH of the water pools. It was found that order parameter profile of AOT reverse micelles was distinctly different from that of normal egg LPC micelles.

Okazaki and Toriyama<sup>128</sup> have described how the dissolved spin probe 2,2,5,5-tetramethylpyrrolidine- $\text{d}_{15}$ -1-oxyl changes its position with pH and temperature in reverse micellar environment. An approximately 2.0 G difference in the  $^{14}\text{N}$  hyperfine coupling constants between acidic pH and basic pH was observed, which is totally contrary to the fact that  $^{14}\text{N}$  hyperfine coupling of the spin probe in bulk water does not show any dependence on pH. At intermediate pH values, EPR spectra contained both the 'acid type' and 'basic type'

components. The ratio of these two components (i.e., A/B) decreased with increasing pH. Line width analysis showed that the spin probe experienced two different environment at a constant R and different pH.<sup>128</sup> Probable sites for these acidic and basic types of probes (abbreviated as AH and A<sup>-</sup>) are the peripheral and central regions of the water pool, respectively. When the temperature was increased, the acidic form also increased. The ratio A/B decreased with increasing 'pool size'. Based on these studies (pH dependence, temperature dependence, line width analysis and hyperfine coupling constant values), a model has been proposed for this system.<sup>128</sup> According to this model, when the water content exceeds the amount needed for the solvations of ionic groups of surfactant, the excess water is stored at the center of the pool (as bulk water). It solubilises ionic species such as A<sup>-</sup> (basic form). When a proton is received by this species microsystem AH (acid form) is formed. To stabilize this 'form' the molecule AH changes its position in such a way that the 'nitroxyl group' protrudes into the non polar alkyl part of AOT shell, and the 'carbonyl group' prefers to stay in the water phase (but not in the core water). The probability that the water pool loses the proton depends on acid base equilibrium constant ( $K_a$ ) of the spin probe, which is in turn dependent on the radius of water pool and the temperature. The smaller the size, or higher the temperature, the smaller the  $K_a$  and higher the ratio of AH/A<sup>-</sup>.

Hauser et al<sup>129</sup> spin labelled the AOT/isooctane/water reverse micelles using CAT16 and carried out EPR studies. In view of the insoluble nature of the spin probe in isooctane, it was assumed (in line with previous studies) that CAT16 was incorporated at the AOT-water interface. In terms of this model, the contributions to the EPR spectrum from the exchange of CAT16 between different compartments of the AOT reverse micelles could be ruled out and the dynamics could be evaluated in terms of effective rotational correla-

tion time ( $\tau_R$ ). Effective correlation times were derived from the standard expression in the fast motion limit.<sup>129</sup> Comparisons of  $\tau_R$  values of the micelle-tumbling and probe-tumbling at different R values showed that, at low R values, the spin label was dominated by the overall tumbling of the AOT reverse micelles. With the increase of R,  $\tau_R$  decreased markedly up to R=10, after which the value levelled off. A model was proposed to explain this behavior whereby the probe experienced two different environments. The observed  $\tau_R$  was the sum of the contribution from these two environments, i.e.,  $\tau_R = \tau_b f_b + \tau_f f_f$ .  $\tau_b$  and  $\tau_f$  are the rotational correlation times for motion of the inverted micelles as a whole and the spin probe present in the fully hydrated micelles, respectively, and  $f_b$  and  $f_f$  are the fractions of bound and free water, respectively.

In 1990, alkyl substituted semiquinones were successfully used as EPR and ENDOR probes for reverse micelles, by Kurreck et. al.<sup>130</sup> CTAB/ $\text{CHCl}_3$ -n-heptane/water and CTAB/2-methylhexane-2-ol/cyclohexane/water were the systems chosen for this work. The radical anions of semiquinones gave different EPR spectra in alkaline aqueous solutions and reverse micelles. In reverse micelles the g-values,  $^{14}\text{N}$  hyperfine constants, and line widths showed remarkable changes when compared with alkaline solutions. More pronounced asymmetric line broadening was also observed. Attempts to record ENDOR spectra of aqueous solutions did not materialize; however, the reverse micellar analogues gave ENDOR spectra with ease. The ENDOR spectra obtained from reversed micellar solutions showed four pairs of lines due to ring t-butyl proton in 2-tert-butyl-1,4-benzoquinone, (TBBQ) and remarkable line broadening. In the case of 2 cyclohexyl-1,4-benzoquinone (CHBQ), the broadening and asymmetric linewidth effects were less obvious than for TBBQ. In the ENDOR spectra of  $(\text{CHBQ})^-$ , the line pair belonging to the second largest splitting was selectively broadened. The hyperfine couplings due to ring protons had

negative couplings and cyclohexyl protons gave positive couplings. Radical generation of the disubstituted semiquinone (DCHBQ)<sup>•-</sup> in reversed micelles was more difficult when compared to the monosubstituted ones. Proton hyperfine couplings of this radical in propan-2-ol and reverse micelles did vary. ENDOR spectra of 2-methyl-1,4-benzoquinone and 2,3-dimethyl-1,4-benzoquinone radicals in both alcohol and reverse micelles have been recorded and discussed.<sup>130</sup> The increase in the line width of the studied semiquinone radicals, in reverse micelles, indicated the possibility of immobilization and presence of a site for the radicals to be anchored. It was also seen that significant changes in g-values and hyperfine couplings were observed only in the case of unsymmetrically substituted semiquinones. Again, the likely anchoring site was surfactant-water interface in the reverse micelles.

The first ESEM study<sup>131</sup> on AOT reverse micelles was carried out in 1991 by Kevan and coworkers using doxyl group attached at different positions of the stearic acid as probes. In this study the continuous phase (isooctane-d<sub>37</sub>) and the dispersed phase (D<sub>2</sub>O) were selectively deuterated. Deuterium spin echo modulation depths were studied to reveal the interaction of the unpaired electron of nitroxide spin probes with deuterium located in the 'water' phase or in the 'oil' phase. Spin probes in AOT/isooctane/D<sub>2</sub>O system showed a decrease of the normalised deuterium modulation depths when the position of DOXYL group was changed from 5 to 16. This trend was expected only when n-DSA had an extended (all-trans) conformation. However, the spin probes showed an increase of the normalised deuterium modulation depth when present in AOT/isooctane-d<sub>37</sub>/water system, with the increase of the distance between doxyl and carboxyl group in the stearic acid. This trend was present for all water pool sizes, and the modulation depth strongly depended on the size of the water pools. This result confirmed the 'extended conformation' of the probe in the

2: AOT reverse micelles. When  $R=0$ , the normalised deuterium modulation depth for  
 e n-DSA (n denotes the position of doxyl group with respect to the carboxyl  
 group) in AOT/isooctane- $d_{37}$ /water increased from 0.25 for 5-DSA to 0.45 for  
 16-DSA. These values were indicative of whether the doxyl group was located in  
 the region which was strongly penetrated by isooctane- $d_{37}$  or not. The strong  
 decrease in the modulation was observed when R increases to 5 and 10, indicat-  
 ing that the probe moved towards a more polar environment. When the  
 'deuterium' was located in the water pool, symmetrical behaviour was observed.  
 At low R, the average area of hydrocarbon water interface would, of course, be  
 too small, so that the AOT polar head groups would pack densely. Consequently,  
 the bulky doxyl moiety will be forced out from the water-AOT polar head group  
 interface. This mechanism caused a decrease in modulation of the 5-DSA in  
 AOT/iso-octane  $d_{37}$ /water and increase in modulation AOT/isooctane/ $D_2O$  systems  
 compared 12-DSA and 16-DSA at low R. When R increased the area available per  
 AOT polar head group also increased, and the n-DSA probe could also move  
 towards the polar water pool. Thus Kevan's work demonstrated how the spin  
 probes could detect changes in the hydration and in the packing of the AOT  
 polar head group upto  $R = 10-15$ , and how further addition of water had little  
 effect on the deuterium modulation. From this study they could calculate that  
 the hydration number of AOT molecule at  $R > 20$  was about 20-22. This whole  
 study was done at low temperatures, which did not affect the micellar  
 structure.

The first EPR investigation of spin labelled enzymes incorporated in  
 reverse micelles was carried out in 1983 by Martinek et al.<sup>132</sup>  $\alpha$ -chymotrypsin  
 was spin labelled at the active site by 4-(2-iodoacetamide)-(2,2,6,6,-  
 tetramethylpiperidine-N-oxyl) and studied in AOT/octane/water-glycerol. In  
 this study, water in the reverse micelles was substituted by water-glycerol

mixture. The catalytic activity of the  $\alpha$ -chymotrypsin-catalyzed hydrolysis of N-benzoyl-L-tyrosine-p-nitro-anilide was monitored with varying R, and varying concentrations of the water miscible organic solvent. It was shown that the profile of the catalytic activity shifted towards the lower R values; also, the increase of catalytic activity was observed under optimal condition with increased concentration of the water miscible organic solvent. Shift of the catalytic activity profile to lower R values was shown to be due to the geometrical fit of the enzyme in the water pool under optimal conditions. The rotational frequency,  $\nu$ , of the  $\alpha$ -chymotrypsin spin labelled at the active site was also determined from EPR for AOT reverse micellar systems containing different concentrations of glycerol. Comparing the catalytic activity and rotational or conformational mobility of enzyme, it was concluded that the catalytic activity reached maximum values when the conformational mobility was minimal. The enzyme became more and more stabilized in the most active conformation with a concomitant enhancement of catalytic activity.

In a later study, Martinek et al.<sup>133</sup> used 2,3-butane-diol instead of glycerol. In this case the optimal catalytic activity of solubilised  $\alpha$ -chymotrypsin was 20 times higher than in aqueous solutions as compared with the maximal 7-fold increase observed<sup>132</sup> for glycerol-water systems. The observed influence of water-miscible organic solvents on the catalytic activity was explained in terms of high microviscosity of the inner cavity and increased rigidity of the surfactant shell of reversed micelles containing solubilized viscous solvents such as glycerol. Both of these factors decreased the conformational mobility of the entrapped enzyme molecule.

The ability of these reverse micelles to dampen the conformational fluctuations of the enzyme molecule led to another interesting phenomenon, namely, alteration of the observed substrate specificity of the enzyme. In

28

1989, Martinek et al.<sup>134</sup> investigated the  $\alpha$ -chymotrypsin-catalyzed hydrolysis of various substrates in AOT/octane/water-butanediol and CTAB/octane- $\text{CHCl}_3$ /water-DMSO reverse micelles under optimal conditions. The substrates used were N-benzoyl-L-tyrosine-p-nitroanilide, N-succinyl-L-phenylalanine-p-nitroanilide, N-benzyloxycarboxyl-L-tyrosine-p-nitro-phenolate, p-nitrophenyl caprylate and nitrophenyl trimethyl acetate. The catalytic constants ( $K_{\text{cat}}$ ) of  $\alpha$ -chymotrypsin-catalyzed hydrolysis of these substrates, calculated as a function of concentration of organic cosolvent inside reverse micelles, were inversely proportional to the conformational mobility of the spin labeled enzyme. The results showed that, with decreasing conformational mobility of the enzyme, the difference in  $K_{\text{cat}}$  between 'good' and 'bad' substrates strongly diminished, so that  $\alpha$ -chymotrypsin became almost equally highly effective towards any substrate introduced into the system. The enzyme acquired the ability to hydrolyze even p-nitroanilide, which is normally completely stable against chymotropic cleavage in aqueous solution. This peculiar behavior could be explained by the fact that in the 'frozen' state the active site of the enzyme molecule was forced into the most favorable configuration, which otherwise could be created only as a result of the binding of a 'good' substrate.

Very recently (1991), Marzola and coworkers<sup>135</sup> carried out a spin labeling study of Human Serum Albumin (HSA) in AOT/isooctane/water reverse micelles. In this work, 3-maleimidoproxyl (3 MAL) was spin labeled at the sulfhydryl group of the HSA. The EPR spectrum of labeled HSA contained contributions from both strongly immobilized component of the HSA spectrum due to the label bound to the sulfhydryl group and weakly immobilized component due to the freely rotating spin label. Their  $\tau_R$ 's were 0.21 ns and 11.1 ns, respectively. This weakly immobilized component was missing when the spin



labeled enzyme was incorporated in reverse micelles with low water content, but it was observable at high  $R$ . The hyperfine splitting and  $g_0$  values of the weakly immobilized component were the same as in buffer indicating that no significant change in the solvent polarity was experienced. The  $2A'_z$  values of the strongly immobilized component decreased with increase of  $R$ . Anisotropic model was assumed to simulate the EPR spectrum, and good fits to the experimental spectra were obtained by assuming a rapid reorientational motion around the nitroxide  $X$  axis, and a slower motion around the perpendicular plane. The magnetic parameters used to get the 'correct spectrum' was obtained by trial and error. Changes in  $A_{xx}$  and  $A_{yy}$  values of the order of 0.1 mT did not result in any improvement in the simulation. The  $\tau_{||}$  and  $\tau_{\perp}$  values decreased with increase of  $R$ . This was because at higher  $R$  a deep layer of water surrounded the protein and its motion was fast, while at low  $R$  the scarcity of water made the HSA rotation hindered. In aqueous solution the 3MAL molecule was localized in a restrictive crevice-like site in HSA, which prevented the label from rotating with respect to the structure of the protein as fast as it did in reverse micelles. Localisation of the label in a more open structure of the crevice could give rise to the observed anisotropic rotation. The HSA, when hosted in reverse micelles, underwent conformational changes.

Clark et.al.<sup>136</sup> reported the EPR studies of lysine labelled tryptophanase incorporated in the reverse micelles. The effect of  $R$  on the enzymes was examined by comparing the EPR spectra of lysine-labelled tryptophanase. Much broader spectra were obtained for reverse micelles when compared to aqueous solutions, and the calculated rotational correlation time of the attached label increased with  $R$ , signifying that the enzyme-bound spin label became more constrained as  $R$  decreased. Since the rotational correlation time of the entire protein in bulk water calculated from the Stokes-Einstein

equation was about 200 ns, motion of the spin label was still rapid relative to the tumbling rate of the enzyme. It was therefore concluded that broadening of the spectrum was apparently caused by a change in the local dynamics of tryptophanase rather than by a decrease in the enzyme's overall rotational rate. The tumbling rate of the enzyme could have decreased as well, however.

Lufimpadio and coworkers (1983)<sup>137</sup> used 5-DSA (5-doxylstearic acid) to probe the dynamics of the interface of CTAB/n-Hexanol/H<sub>2</sub>O reverse micelles. From the  $\tau_R$  values, they could show that the polar region of the interface was more rigid than the nonpolar part of the micelle. In addition, the mobility of the interface ( $\tau_R$ ) was related linearly to the [CTAB]/[n-Hexanol] ratio in the interface at constant [CTAB]/[water] ratio.

Caldararu<sup>138</sup> and coworkers (1991) have investigated the polyoxyethylene(4)nonylphenol(EO(4)NP)/cyclohexane/water reverse micelles by EPR spectroscopy using the following nitroxides as spin probes : 3-carbonyl-2,2,5,5,-tetramethylpyrroline-1-oxyl (1), 2,5-dihydro-2,2,5,5-tetramethyl-3-[[triethylammonio)methyl]pyrrole-1-oxylbromide (2), spin labeled surfactant (3) and 5-doxystearic acid (4).

The EPR spectra of spin probe (1) in reverse micelles was overlapped, leading to the inference that the spin probe might be present in two phases or locations. To confirm this, a water soluble Cu<sup>2+</sup> ion and a water-insoluble organic complex were added to the reverse micelles. Upon addition of Cu<sup>2+</sup> ions to the reverse micelles the EPR spectrum resembled that obtained for the spin probe dissolved in cyclohexane. Similarly, the water-insoluble Cu<sup>2+</sup> complex in the reverse micelles gave an EPR spectrum resembling that of the spin probe in water. The  $a_N$  values increased with R, and  $\tau_R$  values reached a maximum at R = 0.6 and followed a downward trend thereafter. The measured  $\tau_R$  values for R = 0.6 to R = 6.9 referred to intramicellar motion of the spin probe.

The cyclohexane insoluble spin probe (2) was expected to be in the water pools of the reverse micelles. This was confirmed by the 'quenching' of the EPR spectra by  $\text{CuCl}_2$ . The cyclohexane soluble  $\text{Cu}^{2+}$  complex also had its effects on the EPR spectra, reducing only the intensity without apparent broadening. Variations in  $a_N$  and  $\tau_R$  were similar to corresponding values of spin probe (1). Varying the temperature showed that  $\tau_R$  increased with decreasing water content. The increase in  $\tau_R$  was steepest at the lowest temperature. The  $a_N$  values did not vary over the investigated temperature range, indicating that micellar structure remained unchanged within this temperature, while the  $\tau_R$  variation reflected viscosity variations of the micellar core.

Addition of the cyclohexane soluble  $\text{Cu}^{2+}$  complex to the reverse micelles having spin-probe (2) facilitated an estimate of 'the closest approach' between the  $\text{Cu}^{2+}$  complex and the spin probe. Leigh's theory<sup>139</sup> has been used to find the Metal-Nitrosyl distance. As the water content increased, the metal ion and spin probes were separated further.

The spin labeled surfactant showed marked differences in properties when compared to the unlabelled surfactant. Attempts at forming the reverse micelles using cyclohexane and water in the spin labeled surfactants, however, failed. This indicated that the hydrophilic/hydrophobic balance of the EO(4)NP surfactants was modified due to substitution of its -OH group by the nitroxide moiety, and pointed out the role of OH groups in aggregation.

The EPR spectra obtained for 5-DSA dissolved in EO(4)NP reverse micelles transformed from 'isotropic' to a mixture of isotropic and anisotropic as the water content was increased. Broadening of the anisotropic spectra by  $\text{CuCl}_2$ , and the values of  $a_N$  and  $\tau_R$  showed that the nitroxide had to be associated with some EO(4)NP aggregates, since its motion was significantly restricted. Since the 5-DSA was soluble in cyclohexane also, the intrinsic

spectra obtained might be due to the fast exchange of the spin probe between cyclohexane and waterless EO(4)NP aggregates or between cyclohexane and micellar shell.<sup>138</sup> Order parameters were also calculated using the probe (4).

Based on these studies Caldararu<sup>138</sup> et al. concluded that there were significant changes in viscosity, exchange of probes, polarity, penetrability and ordering of surfactant chains as the water was increased.

Lossia and coworkers (1992)<sup>140</sup> report an EPR study on AOT reverse micelles to investigate the extent to which reverse micelles mimic locations of cations and dynamical process in perfluorinated ionomers containing pendent sulfonic acid groups (PFSA).  $\text{Cu}^{2+}$  and  $\text{VO}^{2+}$  are the cations used in this study. For  $R=2$ , the EPR spectra recorded at 120 K indicate ligation to the sulfonic groups of the surfactant. For  $R$  in the range of 5-20 the cation occupies two sites: near the sulfonic groups of the surfactant (site 1) and in water environment (site 2). The results suggest that the two types of sites are due to a micelle size distribution for a given value of  $R$  in this range. The cations experience a similar environment in AOT reverse micelles (water pool diameter of 90Å) and PFSA water pools of  $\approx 40\text{\AA}$ . The connectivity of the water pools in the ionomers and the existence of separated droplets in the reverse micelles are revealed by the correlation time measurements. In the case of reverse micelles, an octahedral symmetry of the cation is maintained at low water content, which is distorted in 'Nafion' dry membranes.

Overall survey shows that, at least from the viewpoint of EPR spectroscopy, the lecithin reverse micelles have been virtually untouched. This observation has prompted us to carry out EPR studies on lecithin reverse micelles by incorporating the simple 'tempo' spin label derivative, 'doxyl' spin label, and other paramagnetic probes.

Chapter 2 deals with our EPR studies of three different spin labels,

namely, (i) potassium iminoxide xanthogenate (PIX) (ii) spin labeled sodium hexyl sulfate (SL-SHS) and (iii) 5-doxyl stearic acid (5-DSA) on egg yolk lecithin reverse micelles.

Chapter 3 describes the effect of additives such as cholesterol, and the effect of temperature on the dynamics of TEMPOL (spin label) incorporated in the egg yolk lecithin reverse micelles.

Studies pertaining to the interaction of paramagnetic metal ion probes with the polar head groups of AOT, CTAB and egg lecithin reverse micelles are reported in Chapter 4.

As has been well-demonstrated in the literature, EPR lineshape studies often give a deep understanding of the motional processes taking place at the molecular level. This has induced us to do comprehensive EPR lineshape studies of nitroxide in the slow and fast motional regimes. The details are given in Chapter 5.

In Chapter 6, automation of our EPR spectrometer using a PC/AT interfacing unit has been demonstrated.

## REFERENCES

1. P. H. Elworthy and D. S. McIntosh, *J. Phys. Chem.* **68**, 3448 (1964).
2. H. -F. Eicke, *Top. Curr. Chem.* **87**, 85 (1980).
3. C. R. Singleterry, *J. Amer. Oil Chem. Soc.* **32**, 446 (1955).
4. M. Kotlarchyk, J. S. Huang and S. H. Chen, *J. Phys. Chem.* **89**, 4382 (1985).
5. C. J. O'Connor, E. J. Fendler and J. H. Fendler, *J. Am. Chem. Soc.* **96**, 370 (1974).
6. A. S. Kertes and H. Gutmann, in : **Surface and Colloid Science**, Vol-8, E. Matijevic (Ed.), Wiley, New York, (1976).
7. H. -F. Eicke in : **Interfacial Phenomena in Apolar Media**, H. -F. Eicke and G. D. Parfitt (Eds.), M. Dekker, New York, (1987).
8. P. L. Luisi and L. J. Magid, *CRC Crit. Rev. Biochem.* **20**, 409 (1986).
9. **Reverse Micelles : Biological and Technolgical Relevance of Amphiphilic Structures in Apolar Media**, P. L. Luisi and B. E. Straub (eds.), Plenum Press, New York (1984).
10. A. Kitahara, *Adv. Colloid Interface Sci.* **12**, 109 (1980).
11. K. Kon-no and K. Kitahara, *J. Colloid Interface Sci.* **37**, 469 (1971).
12. S. G. Frank and G. Zografi, *J. Colloid Interface Sci.* **29**, 27 (1969).
13. K. Martinek, A. V. Levashev, N. Klyachko, Y. L. Khmel'nitski and I. V. Berezin, *Eur. J. Biochem.* **155**, 453 (1986).
14. K. Martinek, I. V. Berezin, Y. L. Khmel'nitski and A. V. Levashev, *Collection Czech. Chem. Commun.*, **52**, 2589 (1987).
15. P. L. Luisi, M. Giomini, M. P. Pileni and B. H. Robinson, *Biochim. Biophys. Acta* **947**, 209 (1988) and references cited therein.
16. J. M. Woll, A. S. Dillon, R. S. Rahaman and T. A. Hatton, in : **Protein Purification : Micro to Macro**, R. Burgers (Ed.), Alan R. Liss Inc., New York, (1987).
17. T. A. Hatton in : **Surfactant Based Separation**, J. F. Scamehorn and J. H. Harwell (Eds.), M. Dekker, New York, (1989).
18. J. H. Fendler, *Acc. Chem. Res.* **9**, 153 (1976) and references cited therein.
19. P. R. Cullis and B. Dekruijff, *Biochim. Biophys. Acta* **559**, 399 (1979); *ibid* **602**, 474 (1980).

20. A. Verkleij, C. J. A. Van Echteld, W. J. Gerritsen, P. R. Cullis and B. Dekruiff, *Biochim. Biophys. Acta* **600**, 620 (1980).
21. **Micellization, Solubilization and Microemulsions**, K. L. Mittal (ed.), Plenum Press, New York (1977).
22. C. Tanford, **The Hydrophobic Effect: Formation of Micelles & Biological Membranes**, 2nd edn., John Wiley & Sons, New York (1980).
23. **Surfactants in Solution III**, K. L. Mittal and B. Lindman (eds.), Plenum Press, New York (1984).
24. **Physics of Amphiphiles : Micelles, Vesicles and Microemulsions**, V. deGiorgio and M. Cortesi (eds.), North-Holland, Amsterdam (1985).
25. **Microemulsions : Structure and Dynamics**, S. E. Friberg and P. Bothorel (eds.), CRC Press, Florida (1987).
26. **Structure and Reactivity in Reverse Micelles**, M. P. Pileni (ed.), Elsevier, Amsterdam (1989).
27. **Kinetics and catalysis in Microheterogeneous systems**, M. Grätzel and K. Kalyanasundaram (eds.), Marcel Dekker, Inc., New York (1991).
28. K. Vos, C. Laane and A. J. W. G. Visser, *Photochem. Photobiol.* **45**, 863 (1987).
29. P. Walde, A. M. Giuliani, C. A. Boicelli and P. L. Luisi, *Chem. Phys. Lipids* **53**, 265 (1990).
30. E. E. Bittar, **Membrane Structure and Function**, Wiley-Interscience, New York (1980).
31. M. K. Jain and R. C. Wagner, **Introduction to Biological Membranes**, Wiley-Interscience, New York (1980).
32. N. Robertson, **The Lively Membranes**, Cambridge University Press, Cambridge (1983).
33. R. B. Gennis, **Biomembranes : Molecular Structure and Function**, Springer-Verlag, New York (1989).
34. S. J. Singer and G. L. Nicholson, *Science* **175**, 720 (1972).
35. IUPAC-IUB, *Biochem. J.* **171**, 21 (1978).
36. R. Harrison and G. G. Lunt, **Biological Membranes : Their Structure and Function**, Blackie Editions, Glasgow (1975).
37. J. F. Mead, R. B. Alfin-Slater, D. R. Howton and G. Popjak, **Lipids : Chemistry, Biochemistry and Nutrition**, Plenum Press, New York (1986).
38. D. M. Small, in : **Handbook of Lipid Research**, D. J. Hanahan (ed.), Plenum Press, New York (1986).

39. (a) V. Luzzati and A. Tardieu, *Ann. Rev. Phys. Chem.* **25**, 79 (1974);  
(b) V. Luzzati, in *Biological Membranes*, D. Chapman (ed.), Vol. 1, Academic Press, New York (1968).
40. N. P. Franks and Y. K. Levine, in : *Membrane Spectroscopy*, E. Grell (ed.), Springer Verlag, Berlin (1981), Chap. 9 and references cited therein.
41. A. J. Verkleij and J. deGier, in : *Liposomes : From Physical Structure to Therapeutic Applications*, C.G. Knight (ed.), Elsevier - North Holland, Amsterdam (1981), Chap. 4 and references cited therein.
42. S. I. Chan, D. F. Bocian and N. O. Petersen, in:Ref. 50, Chaps. 1 and 2 and references cited therein.
43. G. H. Brown, J. W. Doane and V. D. Neff, *Crit. Rev. Solid state Sci.* **1**, 303 (1970).
44. M. Montal, in : Ref. 9.
45. P. R. Cullis and B. Dekruijff, *Biochim. Biophys. Acta* **513**, 31 (1978).
46. B. Dekruijff, P. R. Cullis and A. J. Verkleij, *Trends Biochem. Sci.* **5**, 79 (1980).
47. A. J. Verkleij, *Biochim, Biophys. Acta* **779**, 43 (1984).
48. D. P. Siegel, *Biophys. J.* **49**, 1155 (1986); *ibid* 1171 (1986).
49. P. R. Cullis and B. Dekruijff, *Biochim, Biophys. Acta* **559**, 399 (1979).
50. R. P. Rand and V.A. Parsegian, *Ann. Rev. Physiol.* **48**, 201 (1986).
51. A. J. Verkleij in : *Electron Microscopic Analysis of Subcellular Dynamics*, H. Plattner (ed.) CRC Press Inc., Boca Raton, USA (1989).
52. P. R. Cullis, B. de Kruijff, M. J. Hope, R. Nayar and S. L. Schmid, *Can. J. Biochem.* **58**, 1091 (1980).
53. P. R. Cullis, M. J. Hope and C. P. S. Tilcock, *Chem. Phys. Lipids* **40** 127 (1986).
54. (a) J. H. Fendler, in : Ref : 9, P. 305;  
(b) A. S. Kertes and H. Gutman, in : *Surface and Colloidal Science*, E. Matijevic (ed.), Vol. 8, Wiley, New York (1976);  
(c) A. S. Kertes, in : Ref : 21, P. 445.
55. (a) J. N. Israelachvili, in : Ref : 25;  
(b) J. N. Israelachvili and H. Wennerstrom, *J. Phys. Chem.* **96**, 520 (1992).
56. A. C. Balazs, M. Gempe, and J. E. Brady, *J. Chem. Phys.* **92**, 2036 (1990).



57. D. F. Evans, *Langmuir* **4**, 3 (1988).
58. B. L. Silver, *The Physical Chemistry of Membranes*, Allen & Unwin (Boston) and The solomon Press, New York (1985).
59. H. L. Rosano and G. B. Lyons, *J. Phys. Chem* **89**, 363 (1985).
60. Y. F. Lo, B. M. Escot, E. J. Fendler, E. T. Adams, R. D. Larsen and P. W. Smith, *J. Phys. Chem* **79**, 2609 (1975).
61. B. Lindman and H. Wennerstrom, *Top. Curr. Chem* **87**, 1 (1980).
62. C. Tanford, in : Ref: 21; K. S. Birdi, in : Ref. 21; E. Rucknestein and R. Nagarajan, in : Ref: 21.
63. C. Chachaty, *Prog. NMR Spectrosc.* **19**, 183 (1987) and references cited therein.
64. M. Giomini, A. M. Giuliani, E. Trotta and C. A. Boicelli, *Chem. Phys. Lett.* **158**, 334 (1989).
65. B. Lindman, in : Ref : 24 ; C. Tanford, in : Ref : 21.
66. N. Muller, *J. Phys. Chem.* **79**, 287 (1975).
67. R. Haque, I. J. Tinsley and D. Schmedding, *J. Biol. Chem.* **247**, 157 (1972).
68. A. Faure, A. M. Tistchenko, T. Zemb and C. Chachaty, *J. Phys. Chem.* **89**, 3373 (1985).
69. S. E. Friberg and M. Podzimek, *Colloid Polym. Sci.* **262**, 252 (1984).
70. Z. J. Yu, N. F. Zhou and R. D. Neuman, *Langmuir*, **8**, 1885 (1992).
71. F. Nome, S. A. Chang and J. H. Fendler, *J. Colloid Interface Sci.* **56**, 146 (1976).
72. M. Wong, J. K. Thomas and T. Nowak, *J. Am. Chem. Soc.* **99**, 4730 (1977).
73. O. A. El Seound, in : Ref : 9.
74. P. Douzou, *Adv. Enzymology*, **51**, 1 (1980).
75. R. A. Day, B. H. Robinson, J. H. R. Clarke and J. V. Doherty, *J. Chem. Soc. Faraday Trans. I.* **75**, 132 (1979).
76. V. V. Kumar, C. Kumar and P. Raghunathan, *J. Colloid Interface Sci.* **99**, 315 (1984).
77. K. Tsujii, J. Sunamoto and J. H. Fendler, *Bull. Chem. Soc. Jpn.* **56**, 2886 (1983).
78. V. V. Kumar and P. Raghunathan, *Chem. Phys. Lipids* **41**, 159 (1986).
79. H. F. Eicke and P. E. Zinsli, *J. Colloid Interface Sci.* **65**, 131 (1978).

80. E. Keh and B. Valeur, *J. Colloid Interface Sci.* **79**, 465 (1981); C. Bohne, E. B. Abuin and J. C. Scaiano, *Langmuir* **8**, 469 (1992).
81. V. V. Kumar and P. Raghunathan, *Lipids* **21**, 764 (1986).
82. H. Fujii, T. Kawai, H. Nishikawa and G. Ebert, *Colloid & Polymer Sci.* **260**, 697 (1982).
83. K. P. Henrikson, *Biochim. Biophys. Acta* **203**, 228 (1970).
84. Y-H. Shaw, L-S. Kan and N. C. Li, *J. Magn. Reson.* **12**, 209 (1973).
85. V. V. Kumar, P. T. Manoharan and P. Raghunathan, *J. Biosci.* **4**, 449 (1982).
86. (a) R. C. Cooke and R. Wien, *Biophys. J.* **11**, 1002 (1971).  
(b) L. A. Abetsedarskaya, F. G. Miftakhutdinova, V. D. Fedotov and N. A. Mal'tsev, *Mol. Biol.* **1**, 451 (1967).
87. P. Grigolini and M. Maestro, *Chem. Phys. Lett.* **127**, 248 (1986).
88. (a) J. R. Hansen and W. Yellin, in : **Water Structure at the Water-Polymer Interface**, H.H.G. Jellinek (ed.), Plenum Press, New York (1972), p. 19.  
(b) S. H. Koenig and W. E. Schillinger, *J. Biol. Chem.* **244**, 3283 (1969).  
(c) A. de Marco, E. Menegatti, P. L. Luisi, *J. Biochem. Biophys. Methods* **12**, 325 (1986).  
(d) H. -F. Eicke, in : **Microemulsions**, I. D. Robb (ed.), Plenum Press, New York (1982).
89. C. A. Boicelli, M. Giomini, A. M. Giuliani, *Appl. Spectrosc.* **38**, 537 (1984).
90. T. K. Jain, M. Varshney and A. Maitra, *J. Phys. Chem.* **93**, 7409 (1989).
91. A. Goto, H. Yoshioka, H. Kishimoto and T. Fujita, *Langmuir* **8**, 441 (1992).
92. Z. Shervani, A. Maitra, T. K. Jain and Dinesh, *Colloids and Surfaces*, **60**, 161 (1991); Z. Shervani, T. K. Jain and A. Maitra, *Colloid & Polymer Sci.* **269**, 720 (1991).
93. A. M. Howe, C. Toprakcioglu, J. C. Dore and B. H. Robinson, *J. Chem. Soc. Faraday Trans. I* **82**, 2411 (1986).
94. P. D. I. Fletcher, B. H. Robinson and J. Tabony, *J. Chem. Soc. Faraday Trans. I* **82**, 2311 (1986).
95. S. H. Chen, *Ann. Rev. Phys. Chem.* **37**, 351 (1986).
96. M. P. Pileni, T. Zemb and C. Petit, *Chem. Phys. Lett.* **118**, 414 (1985); P. D. I. Fletcher, A. M. Howe, N. M. Perrins, B. H. Robinson, C. Toprakcioglu and J. C. Dore, in : *Ref : 9*, p. 1745.
97. *Ref : 32*, p. 166.

98. P. Schurtenberger, L. J. Magid, S. M. King and P. Linder, *J. Phys. Chem.* **95**, 4173 (1991) and references cited therein.
99. P. Schurtenberger, L. J. Magid, J. Penfold and R. Heenan, *Langmuir* **6**, 1800 (1990).
100. J. Peyrelasse and C. Boned, *J. Phys. Chem.* **89**, 370 (1985).
101. A. Boussaha and H-J. Ache, *J. Phys. Chem.* **84**, 3249 (1980).
102. M. Zulauf and H. -F. Eicke, *J. Phys. Chem.* **83**, 480 (1979); R. A. Day, B. H. Robinson, J. H. R. Clarke and J. V. Doherty, *J. Chem. Soc. Faraday Trans. I.* **75**, 132 (1979).
103. P. Bode and J. W. J. Van Dorp, *Appl. Radiat. Isot.* **42**, 599 (1991).
104. V. Govindaraju, Ph.D. Thesis, Indian Institute of Technology, Kanpur, India, 1993.
105. H. Tanaka and J. H. Freed, *J. Phys. Chem.*, **89**, 350 (1985).
106. E. A. G. Aniansson, S. N. Wall, M. Almgren, H. Hoffmann, I. Kielmann, W. Ulbricht, R. Zana, J. Lang and C. Tondre, *J. Phys. Chem.*, **80**, 905 (1976).
107. N. M. Atherton, *Electron Spin Resonance*, Ellis Horwood, Chichester, England, 1973.
108. J. N. Israelachvili, S. Marčelja and R. G. Horn, *Quart. Rev. Biophys.*, **13**, 121 (1980).
109. A. Carrington and A. D. MacLachlan, *Introduction to Magnetic Resonance*, Harper and Row, New York, 1969.
110. P. Baglioni, M. F. Ottaviani, G. Martini and E. Ferroni in : **Surfactants in Solutions**, Vol-1, K.L. Mittal and B. Lindmann (Eds), Plenum, 1984.
111. O. H. Griffith and A. S. Waggoner, *Acc. Chem. Res.*, **2**, 17 (1969).
112. K. Vos, C. Laane and A. J. W. G. Visser, *Photochemistry and Photobiology* **45**, 863, (1987).
113. F. M. Menger, G. Saito, G. V. Sanzero and J. R. Dodd, *J. Am. Chem. Soc.* **97**, 909, (1975).
114. Y. Y. Lim and J. H. Fendler, *J. Am. Chem. Soc.* **100**, 7490, (1978).
115. C. Kumar and D. Balasubramanian, *J. Phys. Chem.* **84**, 1895 (1980).
116. H. Yoshioka, *J. Colloid Interface Sci.* **63**, 378 (1978).
117. H. Yoshioka, *J. Colloid Interface Sci.* **95**, 81 (1983).
118. H. Yoshioka and S. Kazama, *J. Colloid Interface Sci.* **95**, 240 (1983).

119. E. Gandin, Y. Lion and A. Van De Vorst, J. Phys. Chem. 88, 280 (1984).
120. P. Bruggeller, J. Phys. Chem. 90, 1830 (1986).
121. A. Barelli and H. -F. Eicke, Langmuir 2, 780 (1986).
122. a) H. Hoffmann, Prog. Colloid Polymer Sci. 65, 140 (1978).  
b) P. E. Zinsli, J. Phys. Chem. 83, 3223 (1979).
123. E. G. Janzen, Y. Kotake, G. A. Coulter and W. M. Oehler, Chem. Phys. Lett. 126, 205 (1986).
124. a) N. Bretz, I. Mastalsky, M. Elsmer and H. Kurreck, Angew. Chem. Int. Ed. Engl. 26, 345 (1987).  
b) H. Kurreck, N.H. Bretz, N. Helle, N. Henzel and E. Weilbacher, J. Chem. Soc. Faraday Transaction I, 84, 3293 (1988).
125. Y. Kotake and E. G. Janzen, J. Phys. Chem. 92, 6357 (1988).
126. M. Okazaki and K. Toriyama, J. Magn. Reson. 79, 158 (1988).
127. G. Haering, P. L. Luisi and H. Hauser, J. Phys. Chem. 92, 3574 (1988).
128. M. Okazaki and K. Toriyama, J. Phys. Chem. 93, 5027 (1989).
129. H. Hauser, G. Haering, A. Pande and P. L. Luisi. J. Phys. Chem., 93, 7869 (1989).
130. D. Niehammer, B. Kirste and H. Kurreck., J. Chem. Soc. Faraday Trans. 86, 3191 (1990).
131. P. Baglioni, H. Nakamure and L. Kevan. J. Phys. Chem., 95, 3856 (1991).
132. O. V. Belonogova, G. I. Likhtenstein, A. V. Levashev, Y. L. Khmeniltshu, N. L. Klyachko and K. Martinek, Biokhimiya 48, 379 (1983)
133. N. L. Klayachko, N. G. Bogdarova, V. K. Koltover, K. Martinek and A. V. Levashev, Biokhimiya 54, 1224 (1989).
134. A. V. Levashev, N. L. Klayachko, N. G. Bogdarova and K. Martinek, Dokl. Akad. Nauk. SSSR 306, 898 (1989).
135. P. Marzola, C. Pinzino and C. A. Veracini, Langmuir 7, 238 (1990).
136. D. S. Clark, L. Creagh, P. Skerker, M. Guinn, J. Prausnitz and H. Blanch in : **Biocatalysis and Biomimetics**, J. D. Burrington and D. S. Clark (Eds.), ACS Symposium Series, 392, Amer. Chem. Soc., Washington D.C., 1989, p 104.
137. N. Lufimpadio, J. B. Nagy and E. G. Derouane in : **Surfactants and Solutions, III**, K. L. Mittal and B. Lindmann (Eds), Plenum Press, New York, 1984, p 1483.
138. H. Caldaru, A. Caragheorgheopol, M. Domonie, D. Donescu and I. Dragutan, J. Phys. Chem. 96, 7109 (1992).

139. J. S. Leigh, (Jr.) J. Chem. Phys. **52**, 2608 (1970).
140. S. A. Lossia, S. G. Flore, S. Nimmala, H. Li and S. Schlick, J. Phys. Chem. **96**, 6071 (1992).

## CHAPTER 2

## EPR OF NITROXIDE SPIN LABELS IN LECITHIN REVERSE MICELLES

## 2.1 Introduction

Interesting questions often arise bearing on the structural organization of surfactant layer at the interface between the internal water pool and the external organic phase of reverse micelles, and the dynamical properties of molecules present in different micellar compartments including the inter-compartmental exchange of these molecules. Various spectroscopic and physical techniques have been effectively used to obtain proper answers for the questions raised above. This subject has been reviewed at length in section 1.7 of chapter 1 as well as in other published monographs.<sup>1-3</sup>

EPR spin labeling is a technique which typically possesses the essential features<sup>4</sup> for the physicochemical characterization of the compartmental structure of reverse micelles. An exhaustive survey of the literature available to date in this area has been made in section 1.8 of the previous chapter. Our survey reveals that only reverse micelles of synthetic surfactants such as cetyl trimethyl ammonium bromide (CTAB), Aerosol OT(AOT), dodecyl ammonium propionate (DAP), and Triton have so far been investigated using EPR spin labeling.

Investigations regarding the structure and reactivity of egg yolk lecithin (EYL) reverse micelles have been the center of attraction in recent years.<sup>5</sup> Although various other techniques such as NMR, UV-visible, IR, etc., have been widely used to characterize EYL reverse micelles,<sup>6-8</sup> EPR spin labeling has not been adequately utilized to our knowledge. This observation has prompted us to take up EPR studies of labeled lecithin reverse micelles.

In this chapter, we report our EPR studies of reverse micelles using some nitroxide spin labels. The reverse micellar system chosen is lecithin/cyclohexane/H<sub>2</sub>O, and the spin labels used are (1) potassium iminoxide xanthogenate (PIX), (2) spin-labeled sodium hexyl sulfate (SL-SHS), and (3) 5-doxyl stearic acid (5-DSA).

## 2.2 Theory of EPR Spectroscopy of Nitroxide Spin Labels

The total spin Hamiltonian that describes the behavior of a collection of nitroxide spin labels is<sup>9</sup>

$$\mathcal{H} = \mathcal{H}_{\text{zeeman}} + \mathcal{H}_{\text{hyperfine}} + \mathcal{H}_J + \mathcal{H}_D \quad (2.1)$$

The  $\mathcal{H}_J$  and  $\mathcal{H}_D$  are the electron-electron exchange Hamiltonian and the electron-electron dipole Hamiltonian. These two terms may be neglected when the local concentrations of the spin label are minimal and only mono nitroxide spin labels are used. Further,  $\mathcal{H}_{\text{zeeman}}$  will have both electron and nuclear terms, the latter often being neglected. The Eq. 2.1 is then expressed as

$$\mathcal{H} = \beta \mathbf{S} \cdot \tilde{\mathbf{g}} \cdot \mathbf{B} + \mathbf{S} \cdot \tilde{\mathbf{A}} \cdot \mathbf{I} \quad (2.2)$$

where  $\beta, \mathbf{B}, \tilde{\mathbf{g}}, \tilde{\mathbf{A}}, \mathbf{S}$  and  $\mathbf{I}$  are the Bohr magneton, the laboratory magnetic field strength, the  $\mathbf{g}$  matrix, the hyperfine matrix, the electron spin operator, and the nuclear spin operator, respectively. The first term on the right side of Eq. 2.2 is the electron Zeeman term and represents the interaction of the electron spin with the external magnetic field. The second term in this equation represents the interaction between the unpaired electron and the nitrogen nucleus of the nitroxide N-O group. This term is much weaker than the electron Zeeman interaction.

CENTRAL LIBRARY  
I I T KANPUR

Acc. No. A. 117872

Generally, EPR spectra of nitroxides are obtained (1) in single crystals, (2) in randomly oriented solids, and (3) in the liquid phase. In each of these cases the mono nitroxide spin label molecule is diluted in a diamagnetic host (the solvent, or a suitable crystal lattice) to avoid interactions between nearby spins, which would otherwise produce dipole broadening. In the following subsections we outline the methods of analysis of the resulting EPR spectra.<sup>10</sup>

### 2.2.1 Nitroxide Spin Label in Oriented Crystals

Let us consider an organic single crystal doped with a small amount of di-*t*-butyl nitroxide (1). The crystal lattice facilitates the orientation



of nitroxide free radicals and prevents nitroxide-nitroxide interactions. The host crystal orients the nitroxide molecules so that their molecular axes (*x* axis parallel to the N-O bond, *z* axis parallel to the nitrogen *p* orbital and *y* axis perpendicular to both the *x* and the *z* axes) are aligned in certain directions relative to the crystal axis. The coordinate system (*x*,*y*,*z*) of the nitroxide molecules is explained in Fig. 2.1 (a). If the crystal is rotated in such a way that the magnetic field aligns with *x*, *y* and *z* axes of the nitroxide, then the resultant spectra will look like those shown in Fig. 2.1 (b)-(d). The three spectra of Fig. 2.1 differ, of course, but the appearance of each of them can be characterized by the linewidth and two important parameters, the *g* value and the hyperfine coupling, *A*. These spectra further show that the *A* and *g* parameters are anisotropic in the sense that they vary with the orientation of the crystal in the magnetic field.<sup>11a</sup>



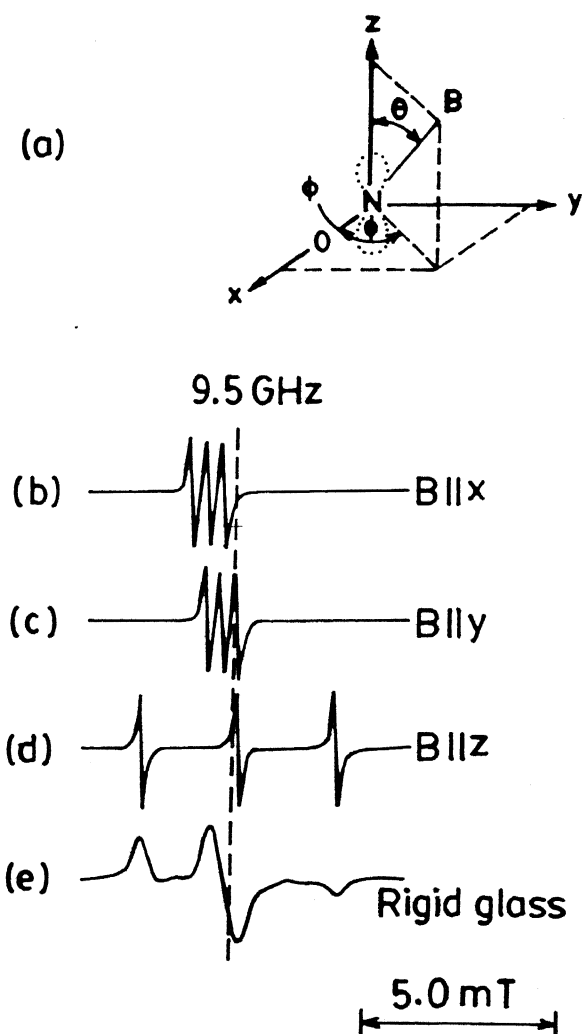


Fig. 2.1 (a) Nitroxide coordinate system,

(b)-(d) X-band EPR spectra with the magnetic field along each axis of a rigidly oriented nitroxide,

(e) EPR spectral response of a collection of randomly oriented nitroxides in the absence of motion (from Ref. 4).

The spin Hamiltonian<sup>11b</sup> becomes, in the laboratory coordinate system (XYZ),

$$\mathcal{H} = G_{ZZ} \beta B S_z + A_{ZZ} S_z I_z + A_{XZ} S_z I_x + A_{YZ} S_z I_y \quad (2.3)$$

where Z is defined to be the direction of the laboratory magnetic field. In the X,Y,Z system, g and A become the nondiagonal matrices g' and A' calculated from the similarity transformations

$$g' = L \cdot g \cdot L^T \quad \text{and} \quad A' = L \cdot A \cdot L^T,$$

where the prime indicates quantities in the laboratory coordinate system, T denotes transpose and L is the transformation matrix which rotates the nitroxide x, y, z axes into the laboratory X, Y, Z axes.

The  $g_{ZZ}$ ,  $A_{ZZ}$ ,  $A_{YZ}$ ,  $A_{XZ}$  terms are related to the nitroxide principal values  $g_{xx}$ ,  $g_{yy}$ ,  $g_{zz}$  and  $A_{xx}$ ,  $A_{yy}$ ,  $A_{zz}$  by the following equations.

$$g_{ZZ} = g_{xx} l_{Zx}^2 + g_{yy} l_{Zy}^2 + g_{zz} l_{Zz}^2 \quad (2.4)$$

$$A_{ZZ} = A_{xx} l_{Zx}^2 + A_{yy} l_{Zy}^2 + A_{zz} l_{Zz}^2 \quad (2.5)$$

$$A_{XZ} = A_{xx} l_{Zx} l_{Xx} + A_{yy} l_{Zy} l_{Yx} + A_{zz} l_{Zz} l_{Xz} \quad (2.6)$$

$$A_{YZ} = A_{xx} l_{Yx} l_{Zx} + A_{yy} l_{Yy} l_{Zy} + A_{zz} l_{Zz} l_{Yz} \quad (2.7)$$

where  $l$ 's are the direction cosines between the nitroxide x, y, z axes and the laboratory X, Y, Z axes. For example  $l_{Zx}$  is the cosine of the angle between N-O bond and the laboratory Z axis.

In Eq. 2.3, the less important terms (i.e.,  $S_x$ ,  $S_y$ ) leading to small off-diagonal matrix elements, have been omitted. With this simplification, the

6x6 secular determinant for nuclear spin  $I = 1$  reduces to two 3x3 determinants, and each of these factors to give one eigenvalue directly and the other two as roots of a quadratic equation. The resulting eigenvalues of Eq. 2.3 are

$$E_{(\pm\frac{1}{2},1)} = \pm \frac{1}{2} g_{zz} \beta B_0 \pm \frac{1}{2} [A_{zz}^2 + A_{xz}^2 + A_{yz}^2] \quad (2.8)$$

$$E_{(\pm\frac{1}{2},0)} = \pm \frac{1}{2} g_{zz} \beta B_0 \quad (2.9)$$

The allowed transitions are  $\Delta M_S = \pm 1$ ,  $\Delta M_I = 0$ , so that for all orientations of the spin label in the magnetic field the  $^{14}\text{N}$  hyperfine spectrum of a nitroxide consists of  $2I+1 = 3$  lines of equal intensity, the center line position characterized by  $g$  and the distance between adjacent lines given by the splitting constant  $A$ , where

$$g = g_{zz} \quad (2.10)$$

$$A = \left( A_{zz}^2 + A_{xz}^2 + A_{yz}^2 \right)^{1/2} \quad (2.11)$$

Substituting the quantities of Eqs. 2.4-2.7 reduces Eqs. 2.10 and 2.11 to the more familiar forms

$$g = g_{xx} I_{Zx}^2 + g_{yy} I_{Zy}^2 + g_{zz} I_{Zz}^2 \quad (2.12)$$

$$A = A_{xx} I_{Zx}^2 + A_{yy} I_{Zy}^2 + A_{zz} I_{Zz}^2 \quad (2.13)$$

Further, the principal components of hyperfine tensor are related to the isotropic coupling constant 'a' by the following relation

$$a = \frac{1}{3} [A_{xx} + A_{yy} + A_{zz}]. \quad (2.14)$$

### 2.2.2 Nitroxide Spin Label in Non-oriented Systems<sup>10</sup>

In polycrystalline or vitreous samples, the principal axes of the paramagnetic molecules assume all possible orientations relative to the magnetic field direction. Under these conditions, the EPR spectrum is expected to be the superposition of spectra corresponding to all possible orientations, and to become spread over the entire field range determined by the  $g$ -factor and hyperfine anisotropies. The distribution of the absorption intensity, however, is not uniform in this range. This fact can be understood if we consider a system with an axially symmetric  $g$  factor, the symmetry axis being the  $z$  axis. As a consequence of the random orientation, there will be many more molecules with the axis parallel to the field. Therefore there will be more paramagnets absorbing at the resonance field determined by  $g_{\perp}$  than those absorbing in the field regions determined by  $g_{\parallel}$ . At these two field values, which correspond to the extrema of the range in which transitions can occur, turning points with different intensity result in the absorption spectrum and therefore maxima or minima appear in the first derivative presentation.<sup>12</sup>

If the  $g$ -factor anisotropy is small and if the hyperfine component  $A_{zz}$  is larger than the other two components, the outermost lines of the derivative spectrum have the appearance of absorption lines, centered at field values  $(h\nu \pm A_{zz}I)/(g_{zz}\beta)$ . A spectrum of this sort, in a rigid glass, is shown in Fig. 2.1(e).

### 2.2.3 Nitroxide Spin Labels in Solution

The angular dependence of the spin Hamiltonian for a nitroxide radical in the nitroxide coordinate system can also be written as:<sup>13</sup>

$$\mathcal{H} = g\beta B_0 S_z + a I_z S_z + \frac{1}{3} (3\cos^2\theta - 1) [\Delta g \beta B_0 S_z + \Delta A I_z S_z] \quad (2.15)$$

where  $\Delta g = g_{zz} - \frac{1}{2} (g_{xx} + g_{yy})$ ,  $\Delta A = A_{zz} - \frac{1}{2} (A_{xx} + A_{yy})$  and  $\theta$  is the angle between the magnetic field direction and the nitroxide z-axis. Pseudo secular terms are neglected in Eq. 2.15 and the hyperfine and g-tensors have been separated into isotropic (g and a) and anisotropic ( $\Delta g$  and  $\Delta A$ ) parts.

If the spin labels are dissolved in a low-viscosity solvent then the fast molecular reorientations due to thermal motion average out the anisotropic terms of the spin Hamiltonian (Eq. 2.15). More appropriately, the term containing  $(3\cos^2\theta-1)$  will vanish in Eq. 2.15. Under these conditions the spin system is considered as an isotropic system. Then, the resulting Hamiltonian for this isotropic system is expressed as

$$\mathcal{H} = g\beta B_0 S_z + a S_z I_z \quad (2.16)$$

Since  $S = \frac{1}{2}$  and  $I = 1$  for the nitroxide radicals, there are six spin states represented by  $|M_S, m_I\rangle$ ,

$$\begin{array}{ll} | +1/2, +1 \rangle & | -1/2, +1 \rangle \\ | +1/2, 0 \rangle & | -1/2, 0 \rangle \\ | +1/2, -1 \rangle & | -1/2, -1 \rangle . \end{array}$$

The total Hamiltonian matrix could be constructed using Pauli spin matrices for  $S_z$  and  $I_z$  and subsequent manipulations will give the corresponding energies.<sup>14</sup> They are

$$\begin{aligned} E_{|+1/2, +1\rangle} &= \frac{1}{2} g\beta B_0 + \frac{1}{2} a \\ E_{|+1/2, 0\rangle} &= \frac{1}{2} g\beta B_0 \\ E_{|+1/2, -1\rangle} &= \frac{1}{2} g\beta B_0 - \frac{1}{2} a \end{aligned}$$

$$E_{|-1/2, -1\rangle} = -\frac{1}{2} g\beta B_0 + \frac{1}{2} a$$

$$E_{|-1/2, 0\rangle} = -\frac{1}{2} g\beta B_0$$

$$E_{|-1/2, +1\rangle} = -\frac{1}{2} g\beta B_0 - \frac{1}{2} a$$

Thus a total of nine EPR transitions is possible among these energy levels. However, according to the 'high-field' selection rules  $\Delta M_S = \pm 1$  and  $\Delta m_I = 0$ , there are only *three* allowed transitions. These are depicted in Fig. 2.2(a). Since it is normal practice in EPR to keep microwave frequency constant and sweep the magnetic field, transitions will occur at the resonant fields

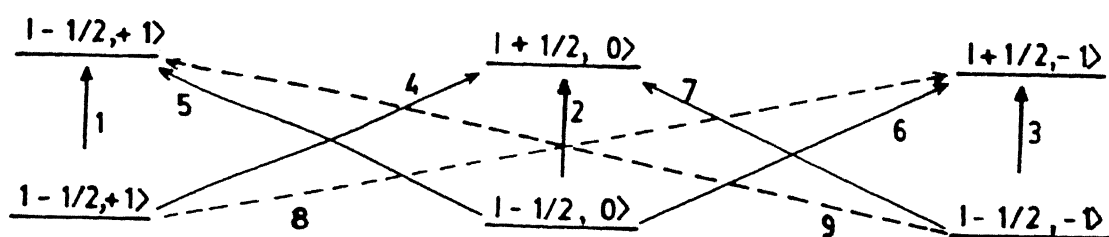
$$B_{m_I=+1} = \frac{h\nu_0}{g\beta} - a_0 \quad \text{where } a_0 = \left(\frac{a}{g\beta}\right)$$

$$B_{m_I=0} = \frac{h\nu_0}{g\beta} \quad \text{and} \quad B_{m_I=-1} = \frac{h\nu_0}{g\beta} + a_0$$

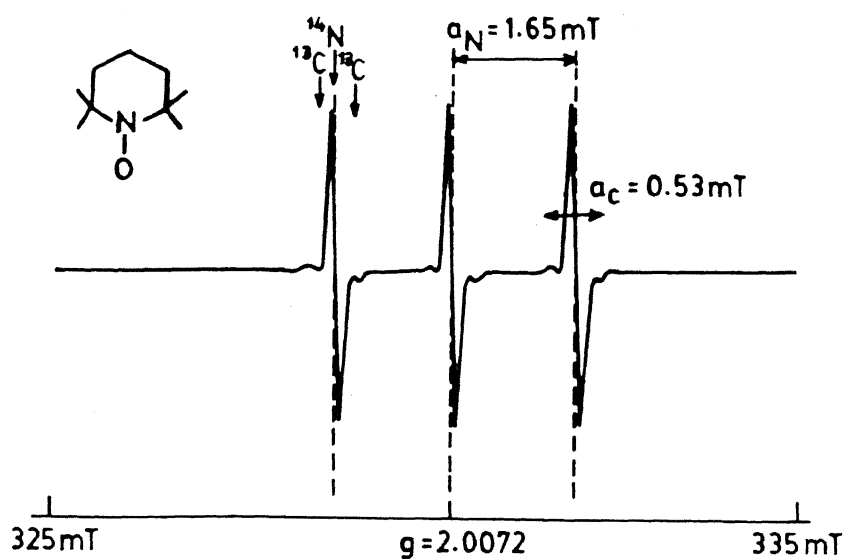
Fig. 2.2(b) represents the typical EPR spectrum obtained for the aqueous solution of TEMPO spin label.

#### 2.2.4 Effect of Motion on the EPR Spectra of Nitroxide Solutions

As we already mentioned, the anisotropic effects are very nearly averaged to zero if the radicals are tumbling rapidly in water or other non-viscous solvents (Fig. 2.2b). If, however, the viscosity of the solution is increased or the size of the spin labeled molecule becomes large, then the rotational motion of the nitroxide decreases and the spectra become increasingly asymmetric, as shown in Fig. 2.3. The bottom spectrum of Fig. 2.3 is the limiting case approached as the viscosity becomes very large. Although not obvious at first glance, the spectrum shown in Fig. 2.3(d) is simply the sum of



(a)



(b)

Fig. 2.2 (a) Energy levels and transitions for a nitroxide in high magnetic fields. Here  $S = 1/2$  and  $I = 1$  and the notation is  $|M_S, m_I\rangle$  (from Ref. 4).

(b) X-band EPR spectrum of the TEMPO nitroxide spin label in aqueous solution. The three main lines arise from nitrogen hyperfine structure, and small satellite lines from the  $^{13}\text{C}$  hyperfine structure (from Ref. 4).

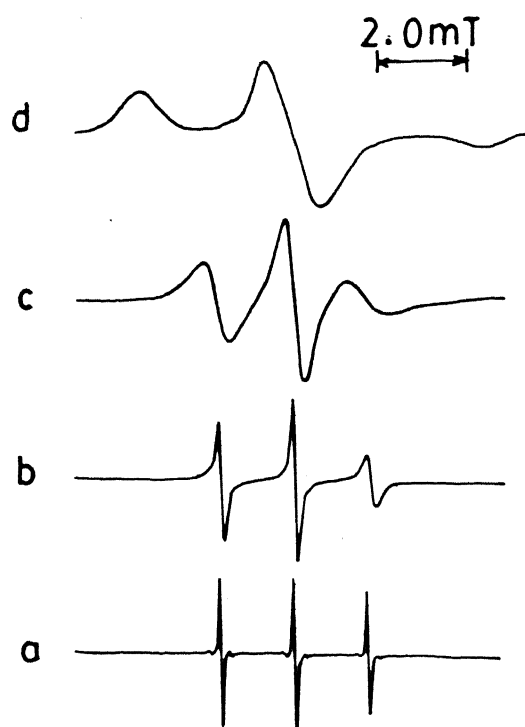


Fig. 2.3 X-band EPR spectra of nitroxide (1) dissolved in ethylene glycol at (a) 298 K (b) 248 K (c) 193 K (d) 123 K (from Ref. 11a).



the three extreme single crystal spectra of Fig. 2.1 and the spectra of all intermediate orientations in the magnetic field. It follows directly that the splitting between the outermost lines of Fig. 2.3(d) is equal to the total splitting ( $2a_{zz}$ ) of Fig. 2.1d. Fig. 2.3(d) is frequently referred to as the powder spectrum, the rigid glass spectrum or the polycrystalline spectrum.

Between the two limits of very rapid motion and a rigid glass, the spectra are quite complex. This complexity provides much of the information that can be obtained about molecular motion using spin-labeling techniques. The complexity of the problem is somewhat greater as one approaches either of the two extremes of very fast or very slow molecular tumbling. If the rate of tumbling is extremely rapid, then spin rotation interactions must also be considered. On the other hand, if the rotation is very slow, the time dependent perturbations become too large for normal perturbation calculations to be valid.

#### 2.2.5 Determination of $\tau$ from the Lineshape

Vital information about the motion of the spin label could be derived by relating the EPR lineshapes to a parameter,  $\tau$ , the rotational correlation time. Generally, as far as anisotropic interactions modulated by Brownian motion are concerned, the correlation time is a measure of the length of time over which the molecules persist in a given orientation.<sup>4</sup> In other cases, in which the modulation of magnetic parameters of the system results from solvent interactions or conformational changes, the correlation time will be related to the mean time of existence of any particular molecular configuration. Thus  $\tau$  is inversely related to the tumbling rate of the molecule. In EPR terminology,  $\tau$  values less than  $6.8 \times 10^{-9}$  s are considered to represent 'fast' motion, while larger values represent 'slow' motion.

For nitroxide radicals without  $\alpha$ -hydrogen atoms, where the spectral lines are due to hyperfine interaction with a single nitrogen nucleus, the dependence of the linewidth ( $1/T_2$ ) on the nuclear spin quantum number  $m_I$  can be described by the equation<sup>15</sup>

$$\frac{\sqrt{3}}{2} \left( \frac{g_o \beta}{\hbar} \right) \Delta B_{m_I} = \frac{1}{T_2} (m_I) = A + B m_I + C m_I^2, \quad (2.17)$$

where  $\Delta B_{m_I}$  is the peak-to-peak linewidth and  $T_2$  is the spin-spin (transverse) relaxation time. The parameters A, B and C are width parameters, and depend on the magnitude of the magnetic anisotropies as well as on the rate of molecular reorientation in the liquid.

Applying Eq. 2.17 to the three possible values of  $m_I$ , and considering that for a Lorentzian spectral lineshape the peak-to-peak intensity or height ( $h_{m_I}$ ) of the first derivative varies with the inverse square of the peak-to-peak width ( $\Delta B_{m_I}$ ) i.e.

$$\left( \frac{\Delta B_{\pm 1}}{\Delta B_o} \right)^2 = \frac{h_o}{h_{\pm 1}}, \quad (2.18)$$

the following expressions for the width parameters are deduced,

$$A = \frac{\sqrt{3}}{2} \left( \frac{g_o \beta}{\hbar} \right) \Delta B_o \quad (2.19)$$

$$B = \frac{\sqrt{3}}{2} \left( \frac{g_o \beta}{\hbar} \right) \left( \frac{\Delta B_o}{2} \right) \left[ \left( \frac{h_o}{h_{+1}} \right)^{1/2} - \left( \frac{h_o}{h_{-1}} \right)^{1/2} \right] \quad (2.20)$$

$$C = \frac{\sqrt{3}}{2} \left( \frac{g_o \beta}{\hbar} \right) \left( \frac{\Delta B_o}{2} \right) \left[ \left( \frac{h_o}{h_{+1}} \right)^{1/2} + \left( \frac{h_o}{h_{-1}} \right)^{1/2} - 2 \right] \quad (2.21)$$

where A, B and C are expressed in  $\text{rad s}^{-1}$ .

In terms of the g and hyperfine tensor anisotropies, the following expressions for B and C parameters are obtained,<sup>15</sup>

$$B = \frac{4}{15} b (\Delta\gamma) B_o \tau_B \quad (2.22)$$

$$C = \frac{1}{8} b^2 \tau_c \quad (2.23)$$

where

$$b = \frac{4}{3} \pi (A_{\parallel} - A_{\perp}) \quad (\text{or}) \quad \frac{4}{3} \pi (A_{zz} - \frac{1}{2} (A_{xx} + A_{yy})) \quad (2.24)$$

all the 'A' values being expressed in MHz units, and

$$\Delta\gamma = \beta\hbar^{-1} [g_{zz} - \frac{1}{2} (g_{xx} + g_{yy})] \quad (2.25)$$

From Eqs. 2.20-2.23,  $\tau$  can be expressed as follows

$$\tau_B = \left( \frac{15}{4b\Delta\gamma B_o} \right) \left( \frac{\sqrt{3}}{2} \frac{g_o \beta}{\hbar} \right) \frac{\Delta B_o}{2} \left[ \left( \frac{h_o}{h_{+1}} \right)^{1/2} - \left( \frac{h_o}{h_{-1}} \right)^{1/2} \right] \quad (2.26)$$

and

$$\tau_c = \left( \frac{8}{b^2} \right) \left( \frac{\sqrt{3}}{2} \frac{g_o \beta}{\hbar} \right) \frac{\Delta B_o}{2} \left[ \left( \frac{h_o}{h_{+1}} \right)^{1/2} + \left( \frac{h_o}{h_{-1}} \right)^{1/2} \right]^{-2} \quad (2.27)$$

The hyperfine coupling constant and g-factors of most doxyl nitroxides doped single diamagnetic crystals are very nearly the same. This has led to the practice of using anisotropic data of one particular nitroxide to calculate  $\tau$  values for various nitroxides in different environments.

Using the hyperfine coupling constant and g-factor values reported by Griffith et al.<sup>16</sup> for di-tert-butyl nitroxide (1), and for field value of about 340 mT, the Eqs. 2.26 and 2.27 will become

$$\tau_B = -6.53 \times 10^{-10} \left[ \left( \frac{h_o}{h_{+1}} \right)^{1/2} - \left( \frac{h_o}{h_{-1}} \right)^{1/2} \right] \Delta B_o \quad (2.28)$$

and

$$\tau_c = +6.53 \times 10^{-10} \left[ \left( \frac{h_o}{h_{+1}} \right)^{1/2} + \left( \frac{h_o}{h_{-1}} \right)^{1/2} - 2 \right] \Delta B_o \quad (2.29)$$

respectively. By measuring  $\Delta B_o$ ,  $h_o$ ,  $h_{-1}$ , and  $h_{+1}$  from the EPR spectrum of nitroxide spin label solution, it is possible to calculate  $\tau$  from Eqs. 2.26 and 2.27.

Another method,<sup>17</sup> also used in the literature to calculate  $\tau$  from the EPR lineshapes, has been adapted and used by us in this work. This is also based on Kivelson's expression.<sup>15</sup> In this method, Eq. 2.11 can be slightly modified as follows,

$$\Delta B_{m_I} = A' + B' m_I + C' m_I^2 \quad (2.30)$$

where  $A'$ ,  $B'$  and  $C'$  are expressed in Gauss, and also

$$A' = \Delta B_o \quad (2.31)$$

$$B' = \left( \frac{\Delta B_o}{2} \right) \left[ \left( \frac{h_o}{h_{+1}} \right)^{1/2} - \left( \frac{h_o}{h_{-1}} \right)^{1/2} \right] \quad (2.32)$$

$$C' = \left( \frac{\Delta B_o}{2} \right) \left[ \left( \frac{h_o}{h_{+1}} \right)^{1/2} + \left( \frac{h_o}{h_{-1}} \right)^{1/2} - 2 \right] \quad (2.33)$$

In terms of  $g$ - and  $A$ -anisotropies the above Eqs. 2.32 and 2.33 can be expressed as<sup>17</sup>

$$B' = 0.103 \omega_o [\Delta g \Delta a + 3(\delta g)(\delta a)] \tau_B \left[ 1 + \frac{3}{4} (1 + \omega_o^2 \tau_B^2)^{-1} \right], \quad (2.34)$$

and

$$C' = 1.81 \times 10^6 [(\Delta a)^2 - 3(\delta a)^2] \tau_c, \left[ 1 - \frac{3}{8} \left( 1 + \omega_N^2 \tau_c^2 \right)^{-1} - \frac{1}{8} \left( 1 + \omega_e^2 \tau_c^2 \right)^{-1} \right] \quad (2.35)$$

$$\begin{aligned} \text{where} \quad \Delta a &= a_{zz} - \frac{1}{2} (a_{xx} + a_{yy}) \quad , \quad \delta a = \frac{1}{2} (a_{xx} - a_{yy}) \\ \Delta g &= g_{zz} - \frac{1}{2} (g_{xx} + g_{yy}) \quad , \quad \delta g = \frac{1}{2} (g_{xx} - g_{yy}) \end{aligned}$$

with the 'a' terms in Gauss, and  $\omega_N = 8.8 \times 10^6 a_N$ , where  $a_N$  is the isotropic hyperfine splitting (in Gauss),  $\omega_e$  is the EPR spectrometer frequency in angular units ( $\omega_e = 2\pi\nu_o$ )

Now the eqs. 2.34 and 2.35 can be recast as

$$4B_1 \omega_e^3 \tau_B^3 - 4B_1' \omega_e^2 \tau_B^2 + 7B_1 \omega_e \tau_B - 4B_1' = 0 \quad (2.36)$$

and

$$\begin{aligned} 8C_1 \omega_N^2 \omega_e^2 \tau_c^5 - 8C_1' \omega_N^2 \omega_e^2 \tau_c^2 + (5\omega_e^4 + 7\omega_N^2) C_1 \tau_c^3 \\ - 8C_1' (\omega_N^2 + \omega_e^2) \tau_c^2 + 4C_1 \tau_c - 8C_1' = 0 \end{aligned} \quad (2.37)$$

$$\begin{aligned} \text{where} \quad B_1 &= 0.0103 [\Delta g \Delta a + 3\delta g \delta a] \\ C_1 &= 1.81 \times 10^6 [(\Delta a)^2 + 3(\delta a)^2] \end{aligned}$$

Therefore, by solving either the cubic equation (Eq. 2.36) or the fifth degree polynomial (Eq. 2.37)  $\tau$  can be calculated.

## 2.3 Experimental Details

### 2.3.1 Materials

#### Egg Yolk Lecithin (EYL)

The extraction of chromatographically homogeneous EYL was carried out using the method of Singleton et al.<sup>18</sup> The extracted lecithin was stored at

-20°C in a 9:1 V/V mixture of chloroform and methanol. A single spot on a thin layer chromatogram confirmed the purity of the extracted lipid. Silica gel coated plates were used in the TLC. The developing solvent used in TLC was chloroform-methanol-water (65:25:4, V/V).

Prior to using the lipid, the solvent was evaporated under vacuum and the residual solid lipid was left in vacuum overnight for complete drying. The dried solid lipid was dissolved in dry cyclohexane for forming reverse micelles and for further characterization. The molecular weight of EYL reported in most studies is in the range of 750-770. We have assumed a value of 760 for our studies.<sup>6-8</sup>

## Cyclohexane

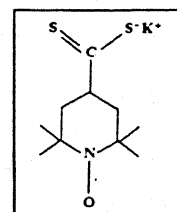
AR grade solvent was further purified by distilling once and refluxing it in the presence of sodium wire for about three to four hours and then redistilling (b.p. 81°C). The dry solvent was stored over sodium.

## Water

The water used to form reverse micelles in all our experiments was deionized and double distilled.

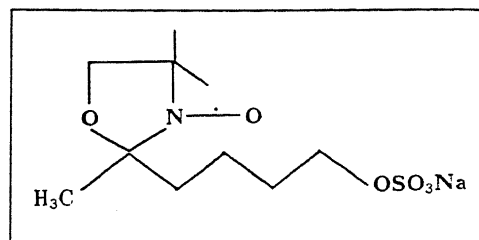
Potassium Iminoxide Xanthogenate (PIX) or Potassium (2,2,6,6 - tetramethyl-1-oxypiperidin-4-yl) xanthate :

This spin label was prepared by the following procedure, reported elsewhere.<sup>19</sup> To 200 mg of 4-hydroxy-2,2,6,6-tetramethyl-1-oxypiperidinyll (TEMPOL) dissolved in water was added 65 mg of KOH in a few drops of water. Carbon disulfide was added slowly while cooling. The reaction mixture was stirred for two to three hours. The precipitate was then filtered, washed with ether, and dried under vacuum. The pale-yellow precipitate was recrystallized from acetone/ether. The Tempol used in this reaction was procured from Sigma Chemical Co. USA.



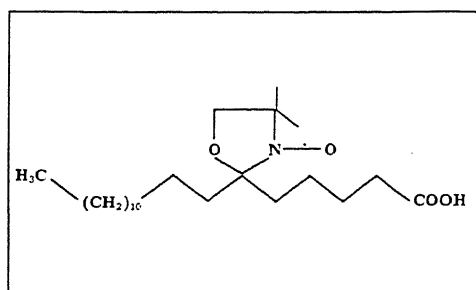
### Spin-labeled Sodium Hexyl Sulfate (SL-SHS).

This spin label was received as a gift from Prof. H. -F. Eicke, of Basel University, Switzerland. The details of the synthesis are given elsewhere.<sup>20</sup>



### 5-Doxyl Stearic Acid (5-DSA)

This is a commercially available spin label purchased from Sigma Chemical Co. USA. and was used without further purification.



#### 2.3.2 Sample Preparations

*Spin Label stock Solution* : Approximately  $10^{-3}$  M stock solutions of all the spin labels were prepared by dissolving appropriate amount of solid spin label in double distilled, deionized water. The solutions were degassed by passing dry nitrogen through the solution before the preparation of reverse micellar solution.

*Surfactant Stock Solutions* : A standard EYL solution weighing 2.5 g EYL in 50 ml [0.067M] of cyclohexane was prepared and used throughout this work.

*Reverse Micellar Solution* : Into an appropriate volume of surfactant stock solution, the desired amount of spin label stock solution and double distilled water (if necessary), were injected using micropipette (Sigma

Chemical Co., USA). Thorough shaking of this mixture ensured a clear homogeneous solution. Samples were prepared according to the desired 'R' value, which is given by  $R = [H_2O]/[surfactant]$ .

### 2.3.3 EPR Spectrometry

All our EPR measurements were made with a Varian E-109 spectrometer operating at X-band (~9.5 GHz) and 100 KHz magnetic field modulation. 'g' values were calibrated using DPPH as standard ( $g = 2.0036 \pm 0.00027$ ). To avoid microwave dielectric loss in the aqueous media, all the recordings were done using EPR quartz cell. Since nitroxide EPR spectral lineshapes could be affected by improper spectrometer settings such as receiver gain, field modulation amplitude, microwave power, scan time and time constant, we have used in all our experiments the suggested standard settings.<sup>21</sup> We have also found out experimentally that the following settings gave satisfactory lineshapes for nitroxide EPR spectra without any appreciable distortion : receiver gain  $\sim 10 \times 10^3$ , modulation amplitude  $\sim 1.0 \times 1.0$  G, microwave power  $\leq 5$  mW, scan time  $\sim 8.0$  min, and time constant  $\sim 0.032$  s.

## 2.4 Results and Discussion

Before studying the EPR of spin labels in reverse micellar environment, it is essential, needless to say, to have some knowledge about the solubility and subsequent EPR characteristics of those spin labels in different constituent solvents which were used to form reverse micelles. In this work cyclohexane and water are the solvents chosen to form lecithin reverse micelles. All the spin labels that we have chosen are readily soluble in water, but only PIX is soluble in cyclohexane also.

Dilute solutions of PIX in water and cyclohexane, SL-SHS in water



and 5-DSA in  $\text{CHCl}_3/\text{MeOH}$  (2:1 v/v) were prepared and subsequent EPR recordings were carried out at room temperature. The recorded spectra are shown in Fig. 2.4. All the samples exhibit three line isotropic spectra which show that those spin labels are undergoing 'fast' or 'rapid' tumbling motion. The intensities of the three hyperfine components in each spectrum are more or less equal. The isotropic  $^{14}\text{N}$  hyperfine splitting values and  $g_0$  values measured directly from those spectra are given in Table 2.1.

**Table 2.1** Spectroscopic splitting factor (g-factor) and hyperfine coupling constant ( $a$ ) for different spin labels in different solvents at room temperature.

Spin Label	Solvent	g-factor $\pm 0.0001$	$a_N \pm 0.002$ (mT)
PIX	cyclohexane	2.0061	1.516
PIX	Water	2.0056	1.690
SL-SHS	Water	2.0052	1.571

#### 2.4.1 EPR Studies of PIX in Lecithin Reverse Micelles

The system chosen for this work is EYL/cyclohexane/ $\text{H}_2\text{O}$ . Two types of reverse micellar samples were prepared by dissolving the PIX in (1) water (2) cyclohexane. Hereafter the former will be referred as EYL/cyclohexane/ $\text{H}_2\text{O}$ (PIX) and the latter as EYL/cyclohexane(PIX)/ $\text{H}_2\text{O}$ . EYL/cyclohexane/ $\text{H}_2\text{O}$ (PIX) sample for  $R = 1$  was prepared by injecting  $2.5 \mu\text{l}$  of aqueous PIX solution into a 2 ml of 5% EYL/cyclohexane solution followed by vigorous shaking to ensure homogeneity. Unit increment in 'R' was achieved by adding  $2-5 \mu\text{l}$  of double distilled water. To prepare EYL/cyclohexane(PIX)/ $\text{H}_2\text{O}$  samples, a dilute solution of PIX in cyclohexane was used to prepare surfactant stock solution.

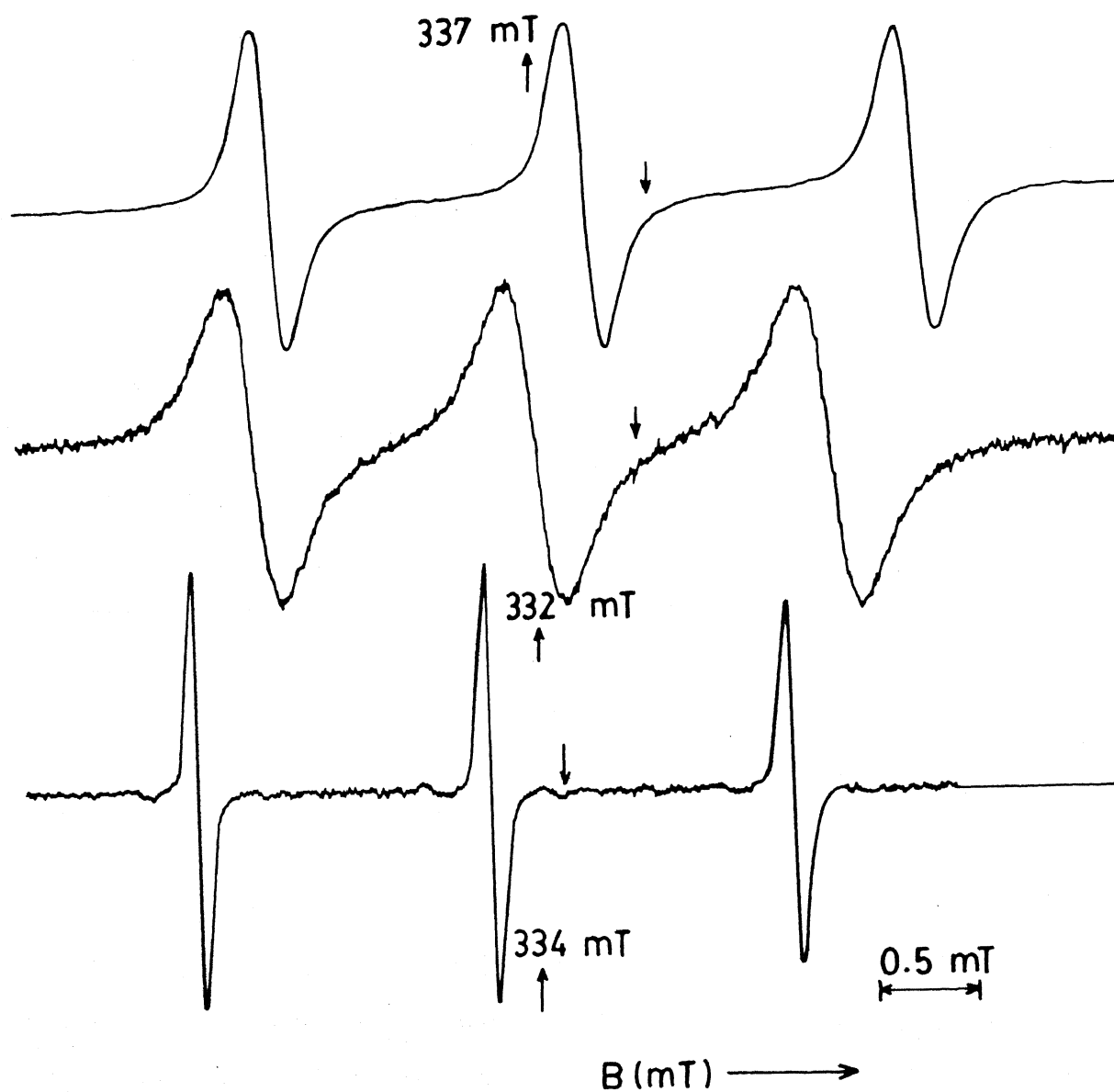


Fig. 2.4

Room Temperature EPR spectra of PIX and SL-SHS in pure solvents (water and cyclohexane). Top : PIX in water  
Middle : PIX in cyclohexane Bottom : SL-SHS in water

2 ml of this solution was then pipetted out, for  $R = 1$ , followed by the addition of 2.5  $\mu$ l of double distilled water. A portion of these samples can be transferred into a quartz EPR cell and subjected to EPR studies. The spectral responses were recorded and analyzed.

#### 2.4.1.1 EYL/Cyclohexane/ $H_2O$ (PIX)

Fig. 2.5 shows the X-band EPR spectra recorded for EYL/cyclohexane/ $H_2O$ (PIX) samples at room temperature as a function of water content ( $R$ ). Comparing Fig. 2.4 and 2.5, we notice that there are marked changes in the EPR spectral lineshapes of PIX in aqueous and reverse micellar environments. The changes observed in the lineshapes of PIX are (i) amplitude of the high field line is reduced (ii) splitting between the outermost lines is also decreased. The reduction in the amplitude of the high field line clearly indicates that the motion of the spin label is slowed down in the reverse micellar environment. This could be rationalized by recalling Eqs. 2.17, 2.22 and 2.23. For normal nitroxides,  $B$  will have negative values, and also  $C \approx -B$ . Whenever there is an increase in ' $\tau$ ' (i.e. slow motion) that will be reflected in the high field lines amplitude and in turn linewidth.

Now considering only Fig. 2.5, the isotropic  $^{14}N$  hyperfine splitting constant ( $a_N$ ) values show a weak dependence of water content. The  $a_N$  values increase over a a range as ' $R$ ' is increased. This trend is clearly shown in Fig. 2.6. When the water content is increased from  $R = 2$  to  $R = 10$  the  $a_N$  also vary, though by small amounts, and then level off after  $R = 10$ . The overall increase in  $a_N$  as we go from  $R = 2$  to  $R = 15$  is  $\sim 0.02$  mT.

#### Linewidth Analysis and Correlation Time Measurement

Peak-to-peak amplitudes (heights) of all the three hyperfine components and the peak-to-peak width of the central field line of the  $^{14}N$  EPR

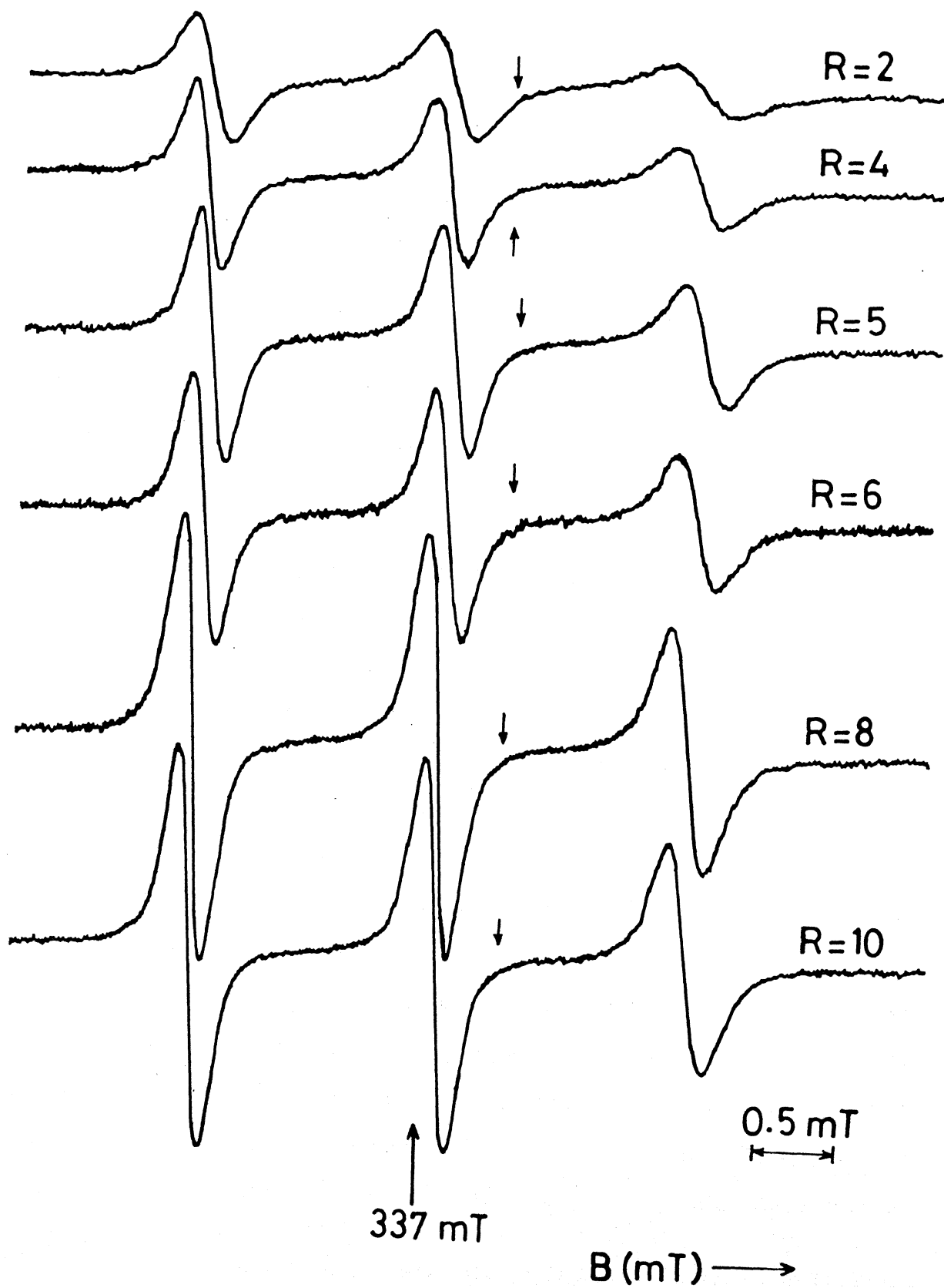


Fig. 2.5 X-band EPR spectra of EYL/Cyclohexane/ $\text{H}_2\text{O}(\text{PIX})$  reverse micelles as a function of water content ' $R$ '.

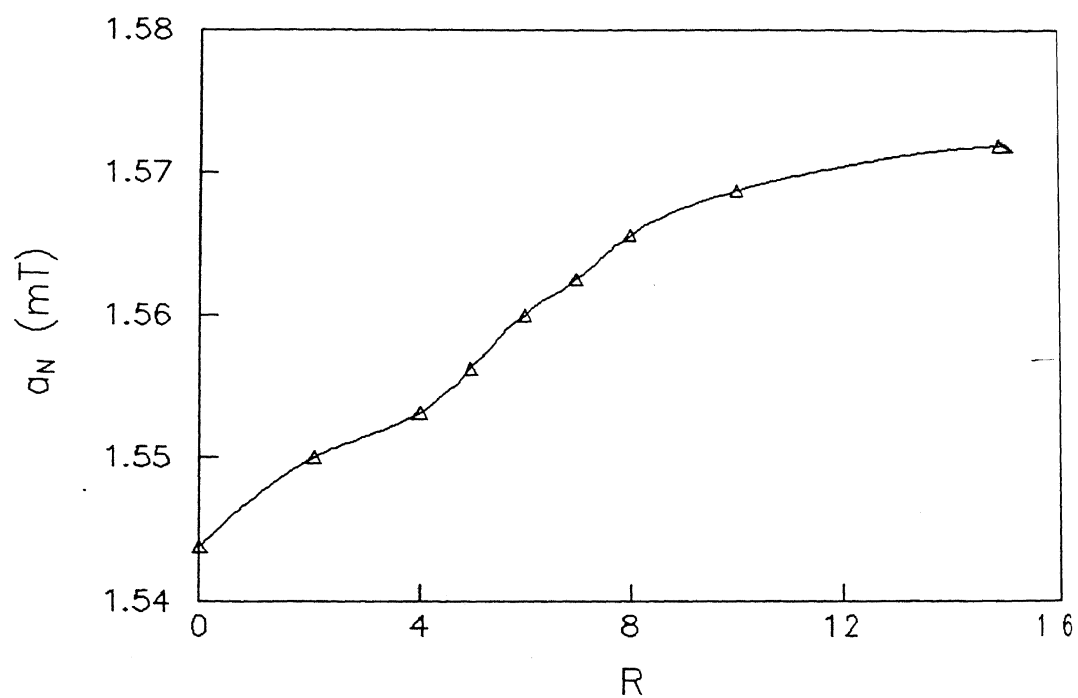


Fig. 2.6 Isotropic  $^{14}\text{N}$  hyperfine splitting constant  $a_N$  (mT) of EYL/cyclohexane/ $\text{H}_2\text{O}$ (PIX) reverse micelles as a function of  $R$

spectra recorded for different 'R' can be directly measured from the experimental spectra. These values are listed in Table 2.2.

Table 2.2 Experimental parameters measured from EPR spectra of EYL/Cyclohexane/H<sub>2</sub>O(PIX)

'R'	$\Delta B_o$ (mT)	Amplitude of Hyperfine components		
		$h_{+1}$	$h_o$	$h_{-1}$
2	0.250	2.40	2.05	0.85
4	0.225	4.70	4.00	1.95
5	0.200	6.15	5.55	2.90
6	0.200	6.60	6.10	3.20
8	0.175	10.85	10.40	5.90
10	0.188	9.80	9.60	5.53
15	0.163	8.85	9.10	5.20

Since normal nitroxide EPR lineshapes are assumed to be Lorentzian in nature, from the experimental data shown in Table 2.1 it is possible to calculate peak-to-peak linewidth of high and low field lines using Eq. 2.18.

Another notable feature in the EPR spectra shown in Fig. 2.5 is that the low field lines are sharper (greater amplitude) than the central lines. Such lineshapes are expected only when the nitroxide spin label undergoes anisotropic motion about the x-principal axis or N-O axis.<sup>22</sup> Analogous lineshapes have been previously observed for spin labels undergoing anisotropic rotational motion in aqueous regions of *lecithin* multilayers.<sup>23</sup> The parameter ( $h_{+1}/h_o$ ), which could be treated as a measure of anisotropic rotational motion and also expressed as an anisotropy parameter, has been used to find out the extent of this peculiar motion.<sup>23</sup> The  $h_{+1}/h_o$  values, calculated from Table 2.2, for the PIX spin label in EYL/cyclohexane/H<sub>2</sub>O(PIX) reverse

micelles vary with the water content. This varying trend is shown in Fig. 2.7. The anisotropic motion parameter does not vary much in the range  $R = 2$  to  $4$ , after which it shows a sharp decrease for  $R = 5$ . From there on end the decrease in  $h_{+1}/h_0$  is moderate and reaches a value close to  $1$  when  $R = 10$ . This parameter will be  $\leq 1.00$  for isotropic motion at X-band frequency.

Another parameter, calculated from the amplitudes of mid-field and high-field lines (i.e.,  $h_0/h_{-1}$ ), can be related to the rotational motion of the nitroxide radicals provided that a possible exchange of spin labels between different compartments is ignored.  $h_0/h_{-1}$  for the system under study was calculated for various 'R' and plotted. Fig. 2.8 shows the variation of this parameter as the water content increases. Upto  $R = 5$ , this parameter decreases almost linearly. A slight deviation from linearity is observed when  $R = 6$ , whereafter the trend decreases further and eventually levels off.

Further, using the width of the mid-field line and the amplitudes of all the three hyperfine components we could calculate the rotational correlation time  $\tau$  from Eqs. 2.32 to 2.37. As the  $g$ - and  $A$ -tensor values of PIX are not known, we have used those of TEMPOL since its molecular structure and geometry are similar. The cubic equation (Eq. 2.36) and polynomial equation (Eq. 2.37) have been solved to obtain  $\tau$  values. A Fortran code has been used for this purpose. The  $\tau$ 's thus obtained are seen to have a marked dependence on water content. Fig. 2.9 shows the dependence of  $\tau$  of PIX on water content.

#### 2.4.1.2 EYL/Cyclohexane(PIX)/H<sub>2</sub>O

EPR spectra recorded for these samples at room temperature as a function of 'R' are depicted in Fig. 2.10. Comparison of Fig. 2.4 and Fig. 2.10 reveals that spectral lineshapes of PIX in cyclohexane have been modified by reverse micellar environment. As in the case of EYL/cyclohexane/H<sub>2</sub>O(PIX), here

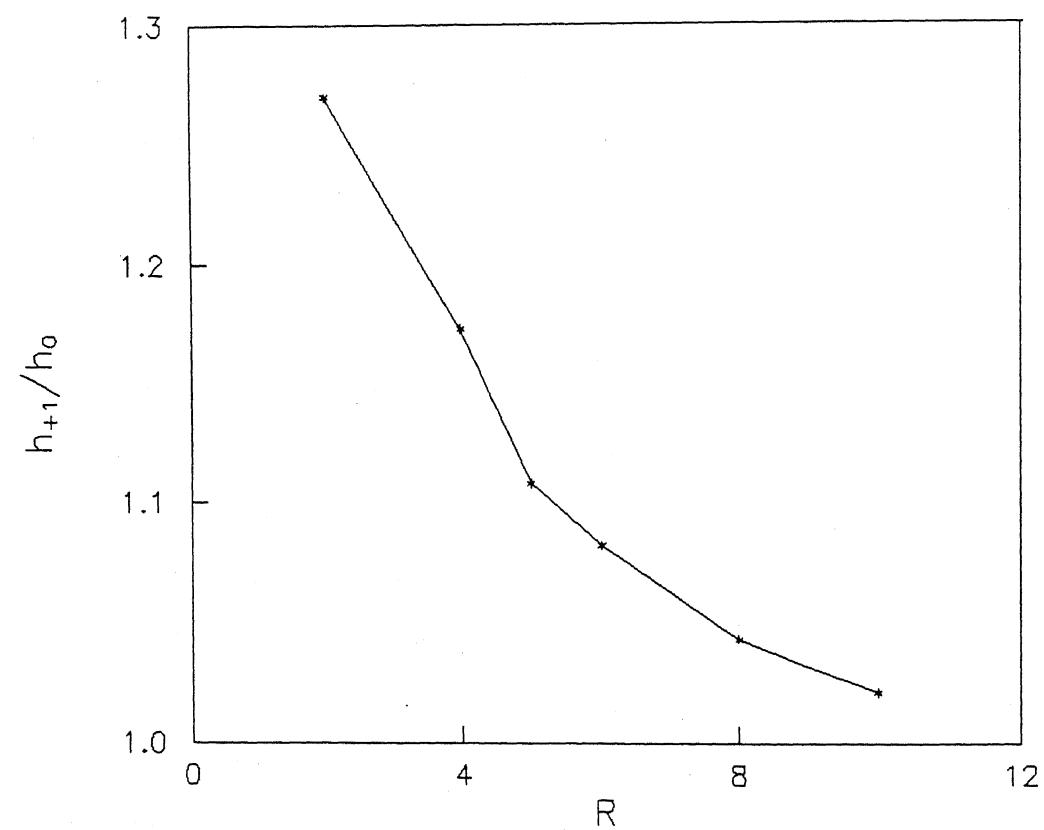


Fig. 2.7 Ratio of the relative amplitudes of low-field  $^{14}\text{N}$  hyperfine line to the central-field line,  $h_{+1}/h_0$  vs 'R' for EYL/cyclohexane/ $\text{H}_2\text{O(PIX)}$  reverse micelles.

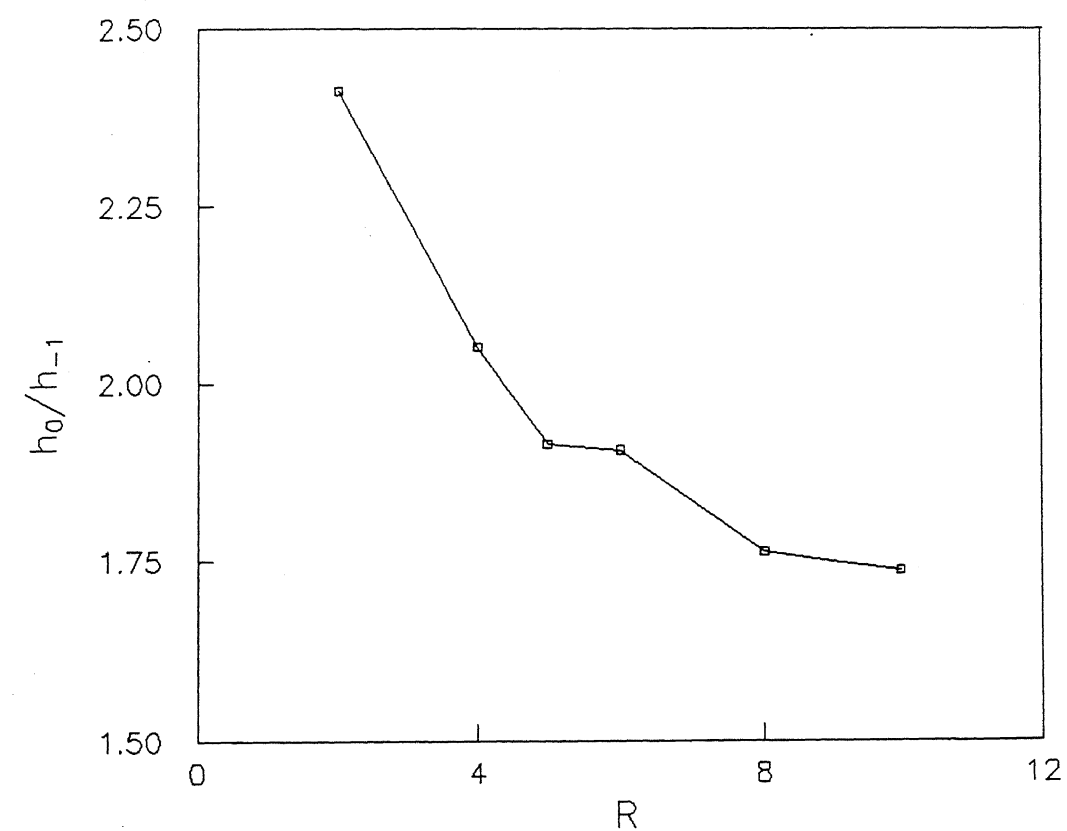


Fig. 2.8 Ratio of relative amplitudes of central-field line to high-field line against 'R' for EYL/cyclohexane/ $\text{H}_2\text{O(PIX)}$  system.



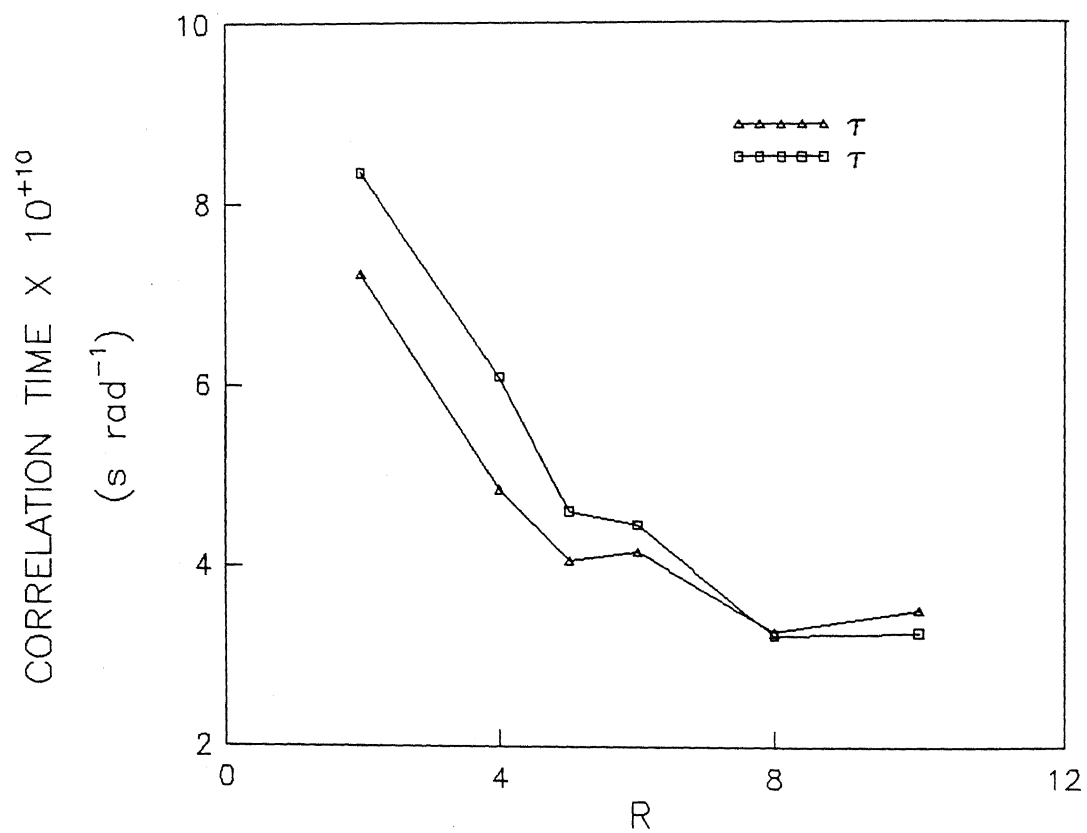


Fig. 2.9 Variation of rotational correlation times,  $\tau_B$  (from Eq. 2.36) and  $\tau_C$  (from Eq. 2.37), as functions of 'R' for EYL/cyclohexane/H<sub>2</sub>O(PIX) system.

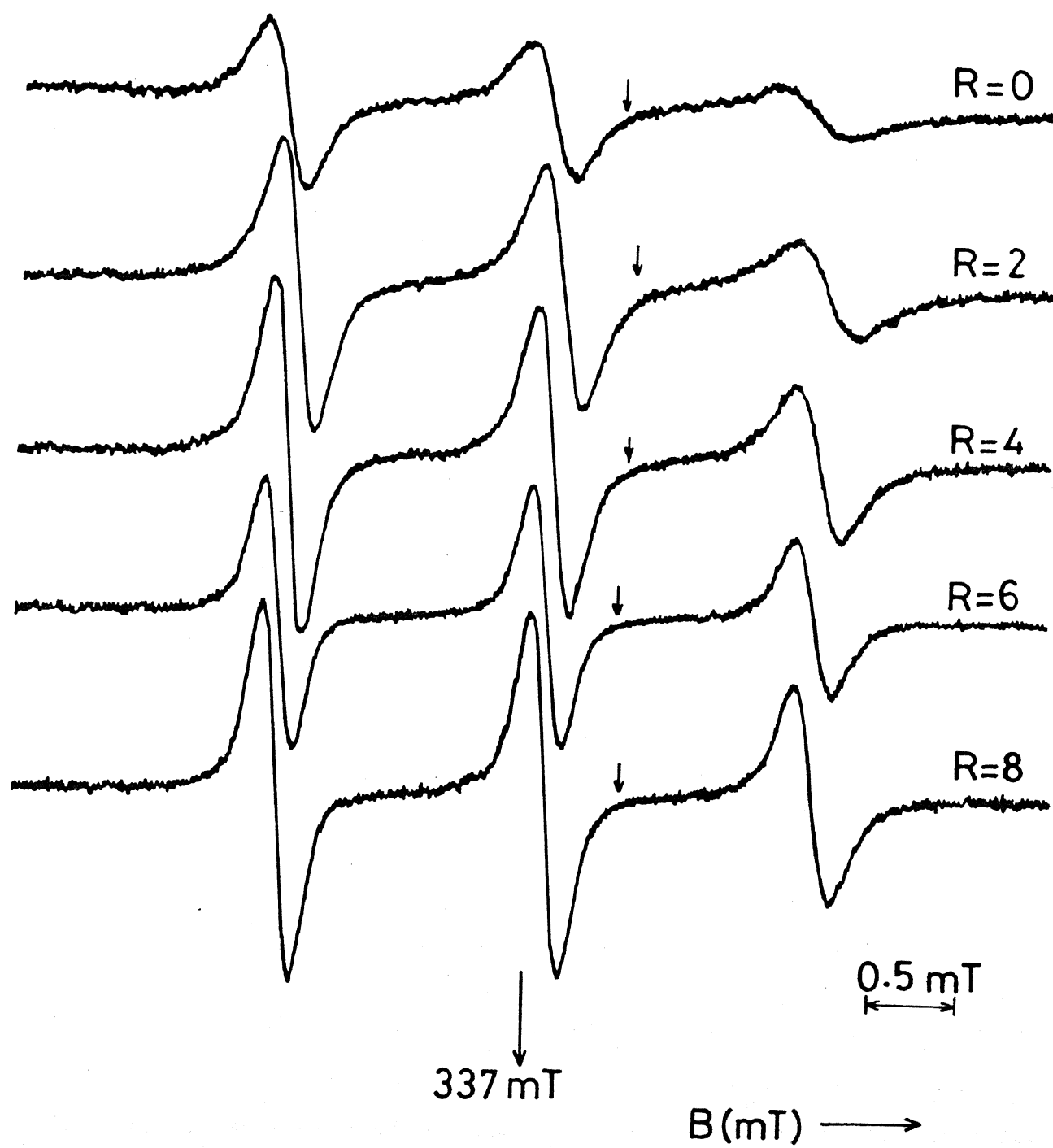


Fig. 2.10 EPR spectra of EYL/cyclohexane(PIX)/H<sub>2</sub>O as a function of 'R'.

also changes in amplitude of high-field line and in the separation of outermost lines have taken place.

### Linewidth Analysis and Correlation Time Measurement

In this system also the linewidths of hyperfine components have been analyzed in terms of amplitude ratios of mid-field to high-and low field lines. The values of amplitudes and widths of hyperfine components were directly measured from the EPR spectra and presented in Table 2.3. PIX spin label undergoes anisotropic motion which is evident by the anisotropic parameter values.

Table 2.3 Experimental parameters derived from  
EYL/Cyclohexane(PIX)/H<sub>2</sub>O

'R'	$\Delta B_o$ (mT)	Amplitude of Hyperfine components		
		$h_{+1}$	$h_o$	$h_{-1}$
0	0.2500	4.0	3.175	1.15
2	0.2380	6.7	5.700	2.35
4	0.2060	8.2	7.150	3.50
6	0.2060	4.5	4.250	2.30
8	0.1880	8.15	8.400	5.00

These values of  $h_{+1}/h_o$ ,  $h_o/h_{-1}$  and  $\tau$  have been calculated from the data presented in Table 2.3. The variation of these parameters as functions of water content follows the same trend that has been observed for EYL/cyclohexane(PIX)/H<sub>2</sub>O. Calculated values of  $h_{+1}/h_o$ ,  $h_o/h_{-1}$  and  $\tau$  have been reported in Table 2.4. As already mentioned a Fortran code was used to solve the polynomial (Eq. 2.37) in order to get  $\tau$  values.

**Table 2.4**      **Anisotropic parameters and correlation time of**  
**PIX in EYL/Cyclohexane(PIX)/H<sub>2</sub>O reverse micelles.**

R	$h_{+1}/h_o$	$h_o/h_{-1}$	$\tau_B \times 10^{+10}$ (s rad) <sup>-1</sup>	$\tau_c \times 10^{+10}$ (s rad) <sup>-1</sup>
0.0	1.259	2.761	10.24	8.36
2.0	1.175	2.426	8.03	6.92
4.0	1.147	2.043	5.42	4.55
6.0	1.059	1.848	4.24	4.15
8.0	1.030	1.680	2.80	3.56

Based on the above results, we may rationalize our EPR investigation on EYL/cyclohexane/H<sub>2</sub>O reverse micelles as follows. The solubility of PIX in both water and cyclohexane leads us to three possible sites available where the spin probe can be accommodated. They are (1) water pool (2) organic phase and (3) interfacial region. If the PIX stays only in non-polar phase of the lecithin reverse micelle, the general spectral response should not be much different from the one we have obtained for PIX in pure organic solvent (Fig. 2.4b), i.e., a nearly isotropic spectrum should result. The spectral profiles shown in Fig. 2.5 and 2.10 belie this expectation. Anisotropy in the line-shapes tell us that PIX can be accommodated either in the interfacial region or in the aqueous water pool only. Isotropic <sup>14</sup>N hyperfine coupling constant of PIX in bulk water (1.69 mT) clearly indicates that the spin probe cannot be present in the interior of the water pool. Based on the arguments given so far, the likely binding site of PIX is the interfacial region.

From the  $h_{+1}/h_o$  values reported in Table 2.4, it is evident that,

there is a pronounced anisotropic motion about the x principal axis of the spin label when no water is present in reverse micelles ( $R = 0$  case). In this situation, the piperidine ring of the spin label is likely to orient between the two surfactant molecules. This position would be expected to result in enhanced motion about the X principal axis of the nitroxide. In response to addition of water ( $R > 0$  cases), the anisotropic parameter also decreases, which shows that the anisotropic motion about a preferential axis decreases. This may be due to the penetration of water molecules into the interfacial region of reverse micelles which is facilitated by the large size of the water pool. At the same time, the interaction of the polar region of spin label ( $\text{-C} \begin{smallmatrix} \text{S} \\ \text{S} \end{smallmatrix}$  -part) and head group of lecithin does not allow the spin label to go far into interior of the water pools.

The marginal increase in the  $a_N$  values as the water content increases, endorses the above argument regarding possible binding site of the spin label (PIX). The binding of PIX in the interfacial region restricts its own motional freedom, which very well explains the  $(h_0/h_{-1})$  variation as a function 'R'. When 'R' = 0, the spin label experiences a restricted environment which is reflected in  $\tau$ . Progressive addition of water to reverse micelles slowly facilitates the speeding-up of the motion of the spin label. This is possible because of the penetration of water molecules inside the interfacial region. The decreasing trend in  $\tau$  as 'R' increases, conveys the same meaning.

We shall now examine the possibility of applying a 'two-state model',<sup>24</sup> to our system. The spin label (PIX) in EYL/cyclohexane/H<sub>2</sub>O may be in a bound state when the reverse micelle is free of water. As the size of the water pool increases, however, the spin label may come to a loose, but not totally free, state. Thus it may experience two different environments. For

such a model, the observed correlation time  $\tau$  may be given by

$$\tau_c = \tau_b f_b + \tau_f f_f ,$$

where  $\tau_b$  and  $\tau_f$  are the correlation times of spin label in 'bound' and 'free' state and  $f_b$  and  $f_f$  are the fractions of bound and free label, respectively. Correlation time measured when the reverse micellar system is free of water, is considered as  $\tau_b$  and  $\tau_f$  is the correlation time of PIX in  $R = 15$  case, and using the relation  $f_b + f_f = 1$ , it is possible to find out  $f_b$  and  $f_f$ . The  $f_b$  thus determined is plotted against 'R' as shown in Fig. 2.11.

#### 2.4.2 EPR Studies of SL-SHS in the Water Pools of EYL/Cyclohexane/H<sub>2</sub>O Reverse Micelles

SL-SHS, doxyl spin-labeled sodium hexyl sulfate, is a surface active spin label having both polar and non-polar groups which confer a measure of amphiphilic character on the label. This is soluble *only* in water. As was already mentioned, dilute aqueous solution of SL-SHS gives isotropic EPR spectrum with equally spaced and equally intensified hyperfine components. The parameters derived directly from the spectrum are reported in Table 2.1.

X-band EPR spectra obtained for SL-SHS incorporated in EYL/cyclohexane/H<sub>2</sub>O reverse micelles at room temperature are shown in Figs. 2.12 and 2.13 as a function 'R'. Though these spectra are generally isotropic in nature, their individual hyperfine component widths and amplitudes are significantly different from those of the corresponding aqueous solutions. Unlike PIX, SL-SHS exhibits typical lineshapes in which the low-field lines are broader (shorter amplitude) than the mid-field lines. This observation clearly indicates that SL-SHS does not undergo any preferential anisotropic motion

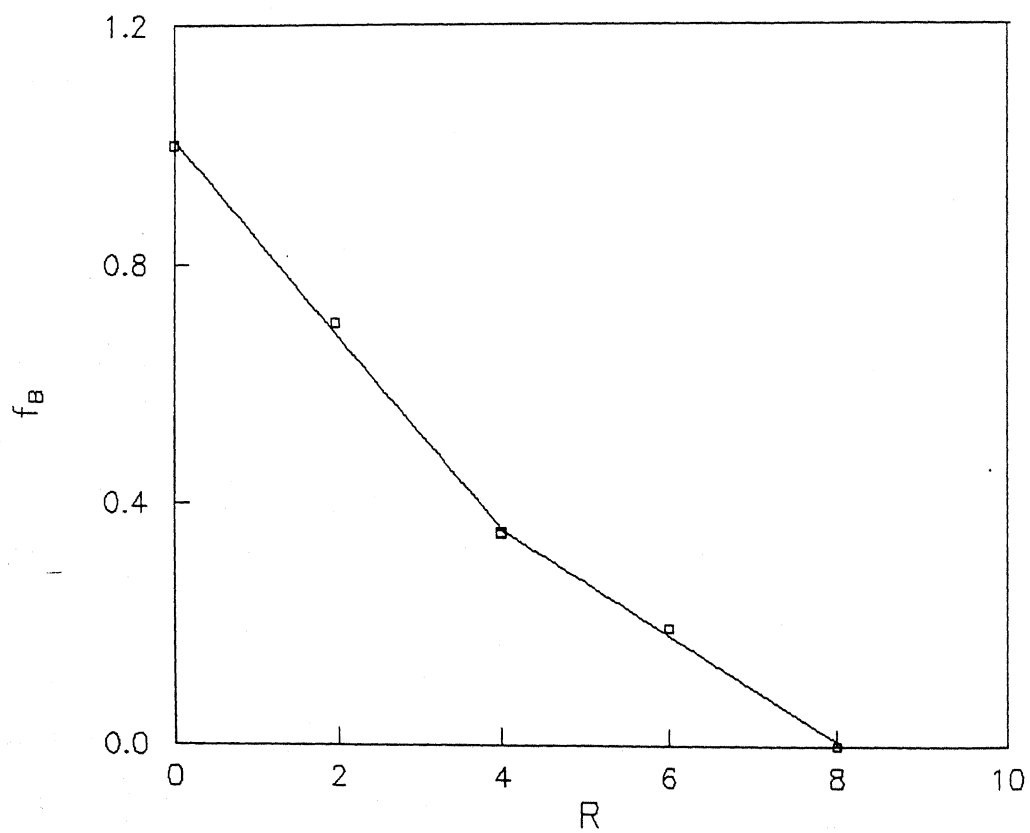


Fig. 2.11 Variation of the fraction of bound water in EYL/cyclohexane/H<sub>2</sub>O reverse micelles as a function of 'R'.

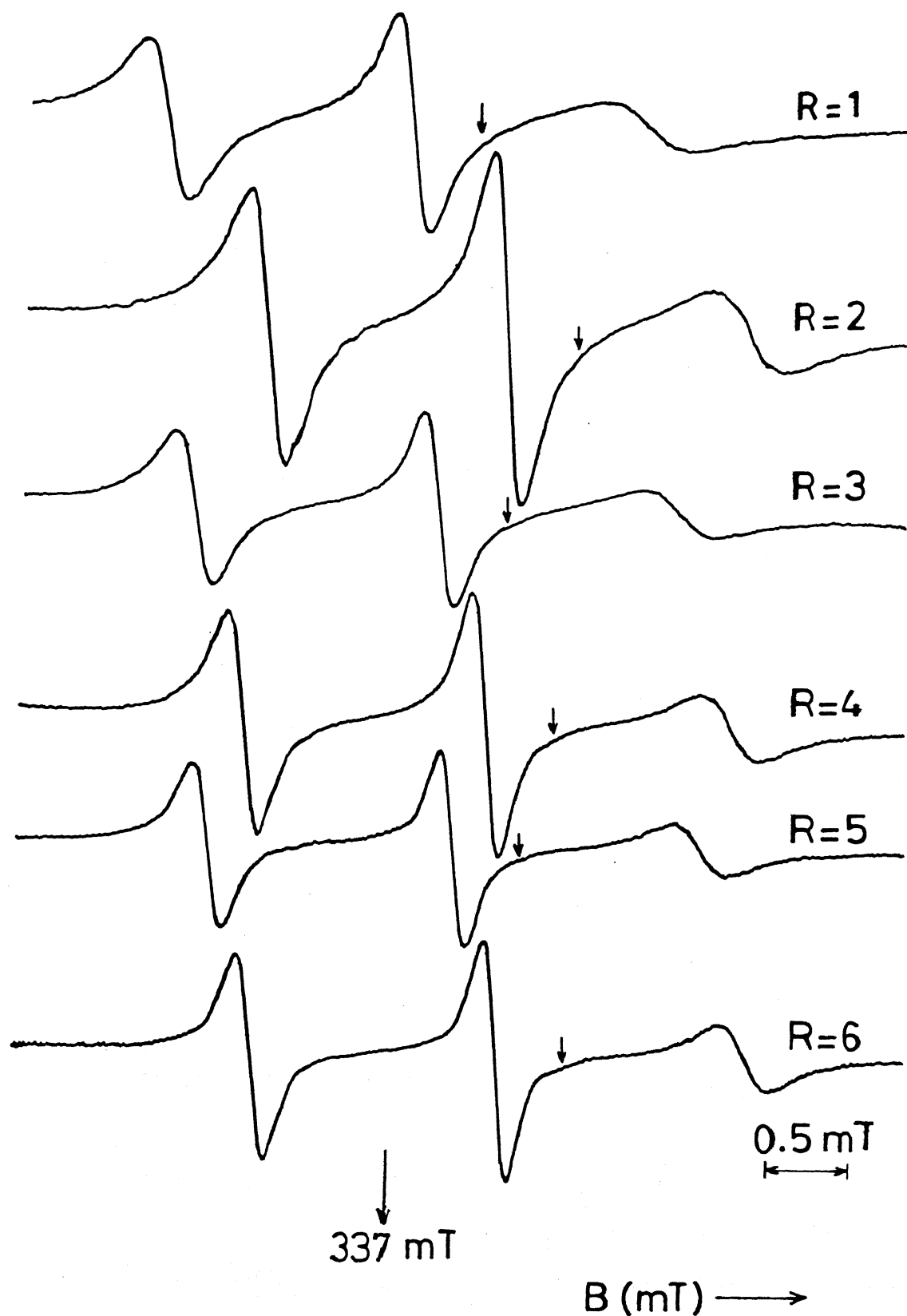


Fig. 2.12 EPR spectra of SL-SHS, in EYL/cyclohexane/H<sub>2</sub>O reverse micelles (R = 1-6 cases) (small arrows denote g value marker positions and bigger arrow indicates central field position)



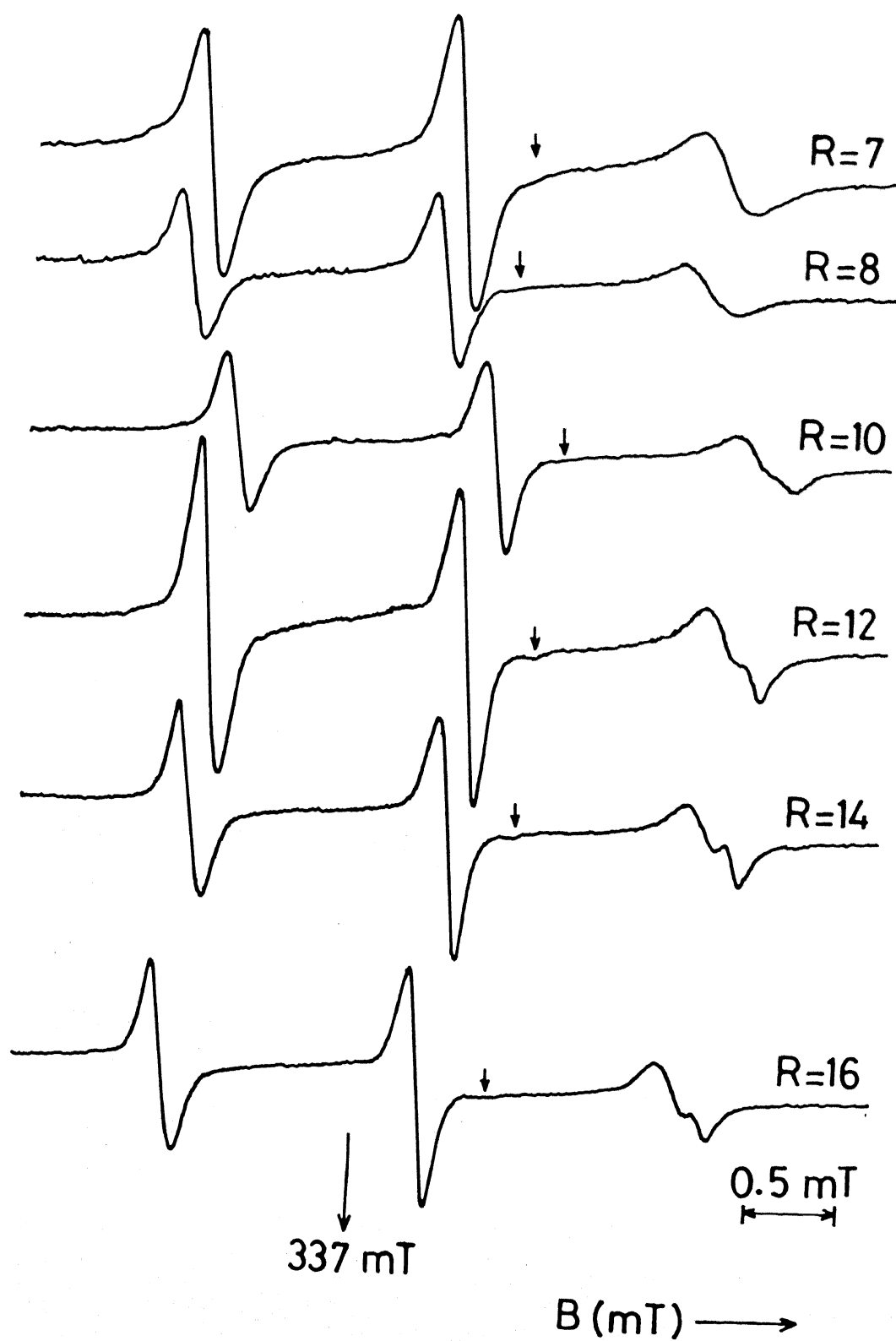


Fig. 2.13 EPR spectra of SL-SHS, in EYL/cyclohexane/H<sub>2</sub>O reverse micelles (R=7 to 16 cases) (small arrows denote g value marker positions and bigger arrow indicates central field position)

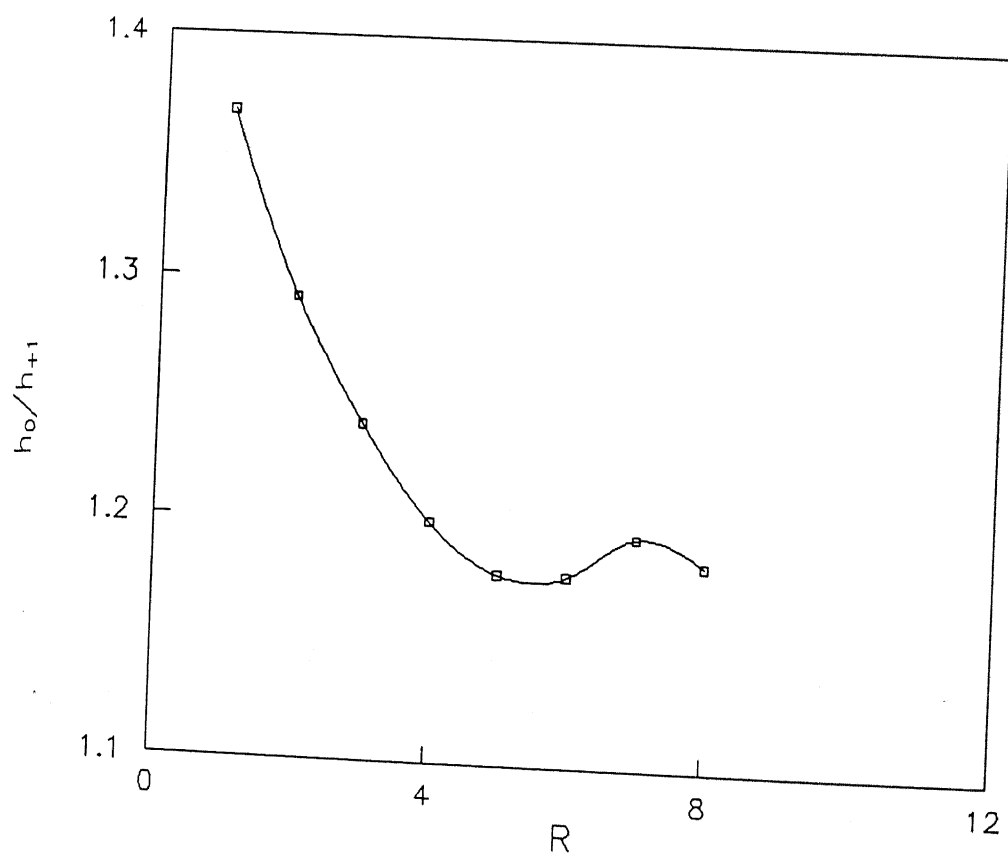


Fig. 2.14 Variation of the ratio of amplitudes of central-field line to low-field EPR lines of EYL/cyclohexane/H<sub>2</sub>O (SL-SHS) system for different 'R' values.

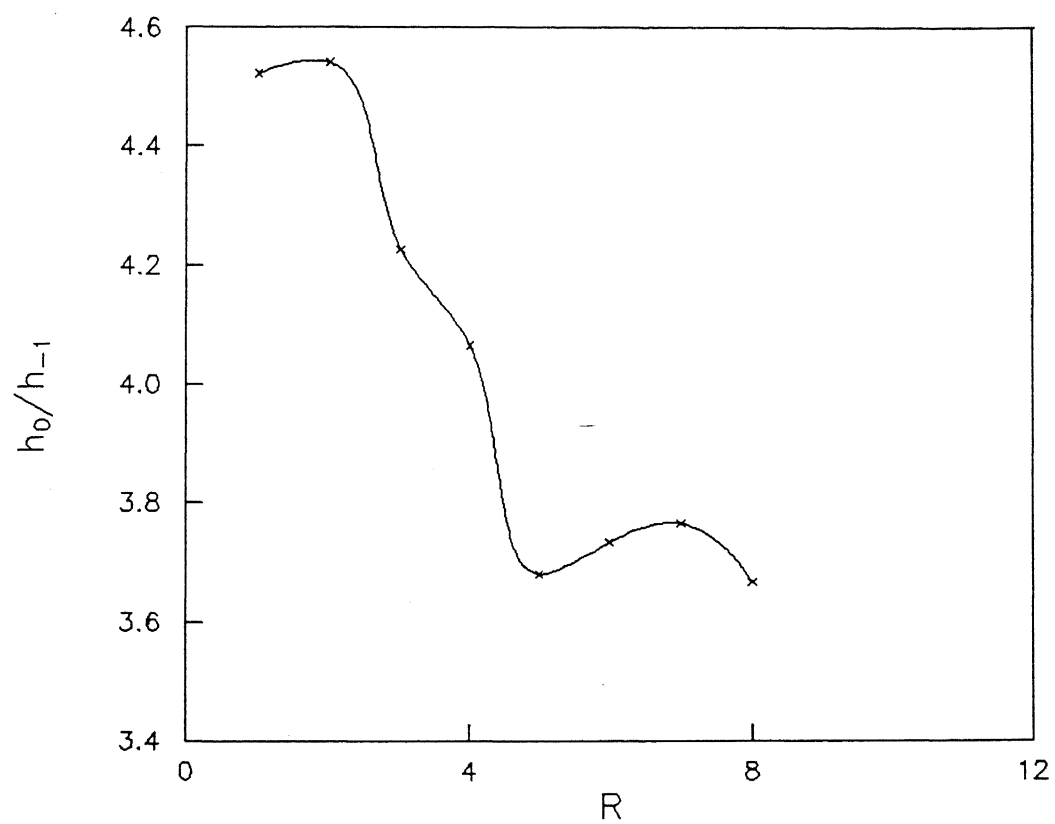


Fig. 2.15 Variation of the ratio of amplitudes of central-field line to high-field EPR lines as a function of 'R'.

amplitude ratios. In the studied range, i.e.,  $R = 1$  to  $8$ , the observed trend is just the opposite of what was observed for SL-SHS in AOT/isooctane/ $H_2O$  microemulsions.<sup>20</sup> In an attempt to find out the polarity of the medium in which the SL-SHS resides, the  $^{14}N$  hyperfine splitting constants,  $a_N$ , have been measured from the experimental spectra. The dependence of  $a_N$  on the water content of EYL reverse micelles is depicted in Fig. 2.16, and it is seen that the  $a_N$  values change linearly with the water content. Mobility of the SL-SHS in presence of reverse micellar water pool was determined by calculating rotational correlation times,  $\tau$ 's. Fig. 2.17 shows the variation of  $\tau$ 's as a function of 'R'.  $\tau$  decreases as 'R' increases and this increment was significant when going from  $R = 4$  to  $5$ . Minimum  $\tau$  value is observed for  $R = 6$ .

Another interesting aspect has been noticed in the lineshapes of SL-SHS in this study, namely, the high field line splits into two partially overlapped lines at values beyond  $R = 8$ . This behavior persists until  $R$  becomes  $16$ . EPR lineshapes of this kind have been encountered in temperature dependent EPR studies of spin labels in AOT reverse micelles.<sup>20,25</sup> Such a splitting of the high field line clearly indicates that SL-SHS experiences two distinct environments in the reverse micellar solutions of high water content.

Interpretation of the results presented so far may now be carried out. Since SL-SHS is insoluble in cyclohexane even in the presence of EYL, only the water pool of the reverse micelles can accommodate these surface active spin label molecules. Thus, by deciding the location of the spin label, a rationalization of  $h_o/h_{+1}$  and  $h_o/h_{-1}$  variations can be attempted with the aid of  $^1H$  NMR relaxation studies carried out on the water pools of EYL based reverse micelles in our laboratory.<sup>7,26</sup> Spin-spin relaxation time,  $T_2$ , of water protons in EYL reverse micelles [EYL/Dicyclohexyl carbodiimide/cyclohexane/ $H_2O$ ] increases with water content until  $R = 5$ , with a sharp increase in

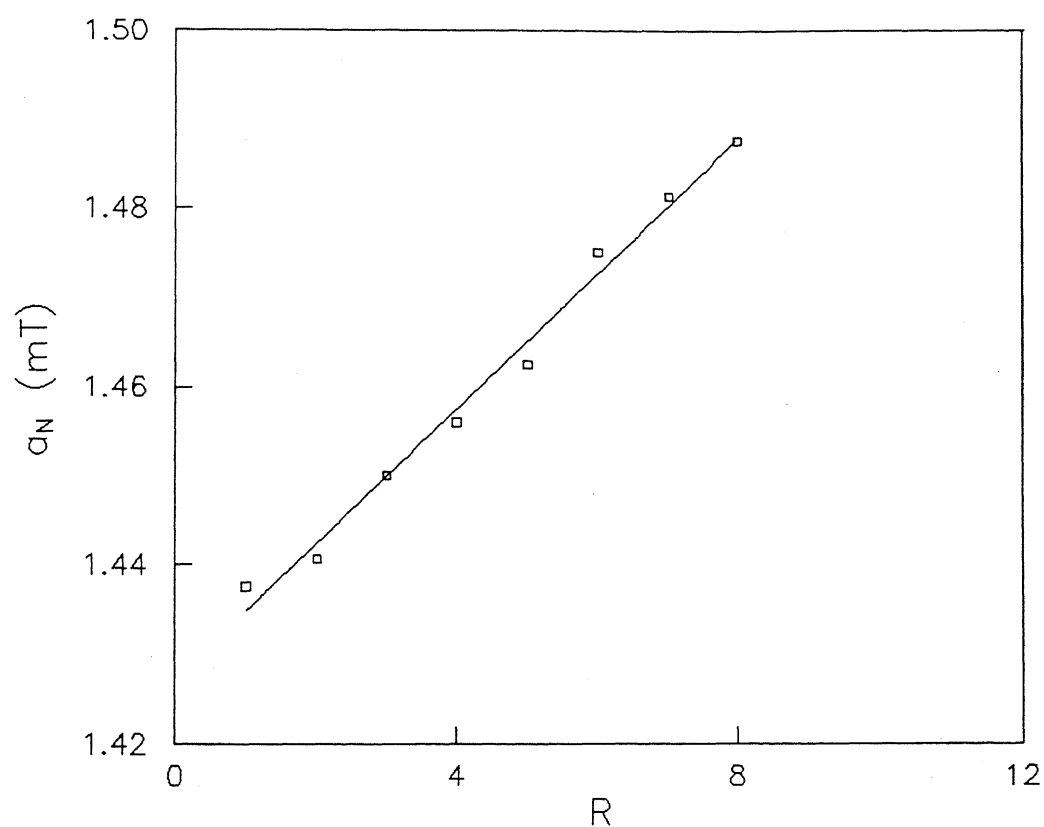


Fig. 2.16 Isotropic  $^{14}\text{N}$  hyperfine coupling constant  $a_N$  (mT) of SL-SHS in EYL/cyclohexane/ $\text{H}_2\text{O}$ , as a function of 'R'.

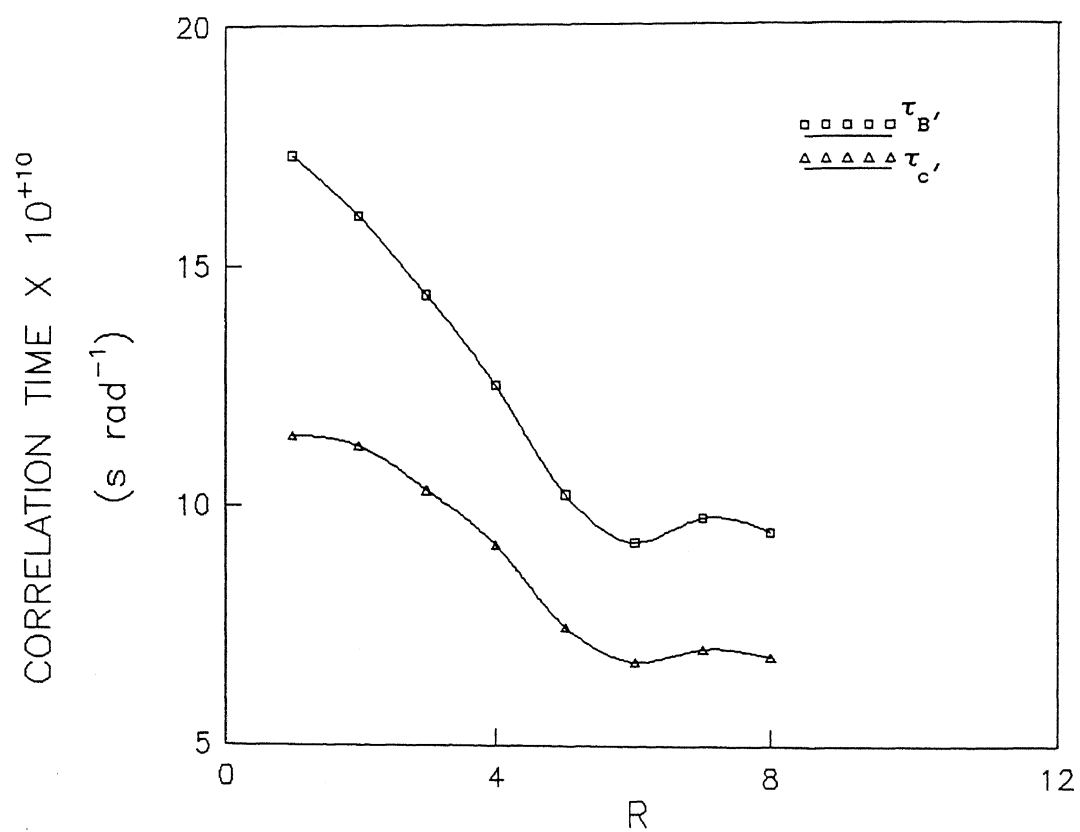


Fig. 2.17 R-values dependence of  $\tau_{B'}$ , (from Eq. 2.36) and  $\tau_{C'}$ , (from Eq. 2.37) of SL-SHS in EYL/cyclohexane/H<sub>2</sub>O system.

the region  $R = 4$  to  $5$  and then starts decreasing.<sup>26</sup> This observation has suggested a model where the water present in the pools behaves differently beyond  $R = 5$  and also some of the molecular organizational rearrangements necessary for the phase transition take place in this region.<sup>7</sup> Amplitude ratio variations observed in SL-SHS of EYL/cyclohexane/ $H_2O$  reverse micelles are also well accommodated assuming such a model.

Isotropic  $^{14}N$  hyperfine splitting values ( $a_N$ ) of SL-SHS in EYL/cyclohexane/ $H_2O$  reverse micelles indicate, as shown in Fig. 2.16, that the polarity of water in EYL and AOT reverse micelles<sup>20</sup> is almost the same in the low water content regions (i.e.,  $R \leq 8$ ).  $a_N$  values beyond  $R = 8$  could not be determined because of the aforementioned splitting of the high field line.

A further indication of mobility of the spin label is, of course, the rotational correlation time,  $\tau$ , and this has been determined directly from the parameters shown in Table 2.5. The decrease in  $\tau$  when the water content is increased is due to the rotational freedom SL-SHS experiences in the water pool as the size of the pool becomes larger. There is a sharp increase in the mobility of the spin label in between  $R = 4$  and  $R = 5$ . This behavior is well accounted by the fact that phase transition from viscous phase to gel phase takes place exactly in this region.<sup>27</sup> It is presumed that this phase transition will have its effects on the water pool and, in turn, on the spin label mobility. The 'bound' water / 'free' water concept also supports the trend observed in  $\tau$  variation.

As regards the splitting of the high field line of SL-SHS in reverse micelles with high water content, an explanation can be offered by proposing a 'cage model' of the reverse micellar water pools. Biradical spin labels present in these 'cages' have been studied already.<sup>28</sup> According to this model, the EPR spectra of long chain biradicals represent the superposition of

spectra from the non-reacting radical moieties in the elongated or stretched-out conformation and those from the cage where the radical moieties are closer together and can interact with each other. Though our case involves only monoradicals, it may be postulated that the mono-radical also assumes two conformations inside the cage (water pool) considering the 6 carbon chain of the SL-SHS. This influences the high field line splitting. More proof, however, will have to be sought by performing temperature dependent EPR studies on EYL reverse micelles with biradical spin labels.

#### 2.4.3 EPR studies of 5-Doxyl Stearic Acid in EYL/Cyclohexane/H<sub>2</sub>O Reverse Micelles

In our attempt to study the spin labels in different environments provided by the different compartments of EYL reverse micelles, we have noticed that (1) the PIX spin label initially resides in the interfacial region and then slowly penetrate into water pools as the size of the pool becomes larger, (2) water soluble SL-SHS resides only in different regions within the water pool. Search for a spin label which could reside exclusively at the interfacial region resulted in the identification of 5-DSA. This spin label has a doxyl group attached at fifth position of the stearic acid (fatty acid) chain, and has been used as spin probe in studies of biological membranes<sup>29</sup> and phospholipid vesicles.<sup>30</sup>

Figs 2.18 and 2.19 show the X-band EPR spectra recorded for 5-DSA labeled EYL reverse micelles at room temperature. All these spectra, by and large, exhibit distinct parallel and perpendicular features. The maximum and minimum hyperfine splitting,  $A_{\max}$  and  $A_{\min}$ , respectively, could be read from the sufficiently resolved EPR spectra. Since  $A_{\max}$  is considered as a very good measure of  $2A_{\parallel}$  and  $A_{\min} \approx 2A_{\perp}$  to a fair approximation,<sup>11b</sup> these values



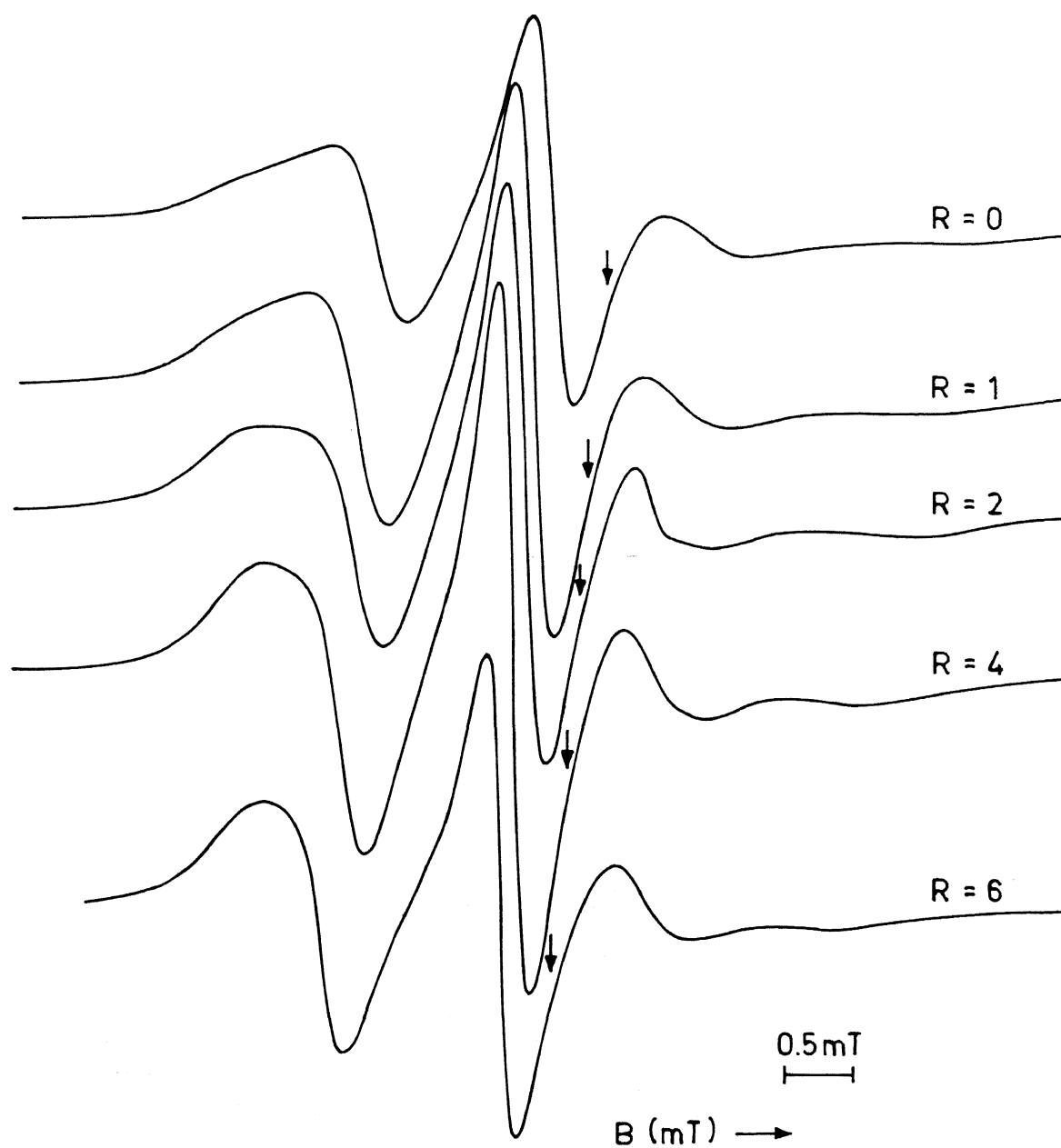


Fig. 2.18 EPR spectra of 5-DSA in EYL/cyclohexane/H<sub>2</sub>O reverse micelles for values of R between 0 and 6.

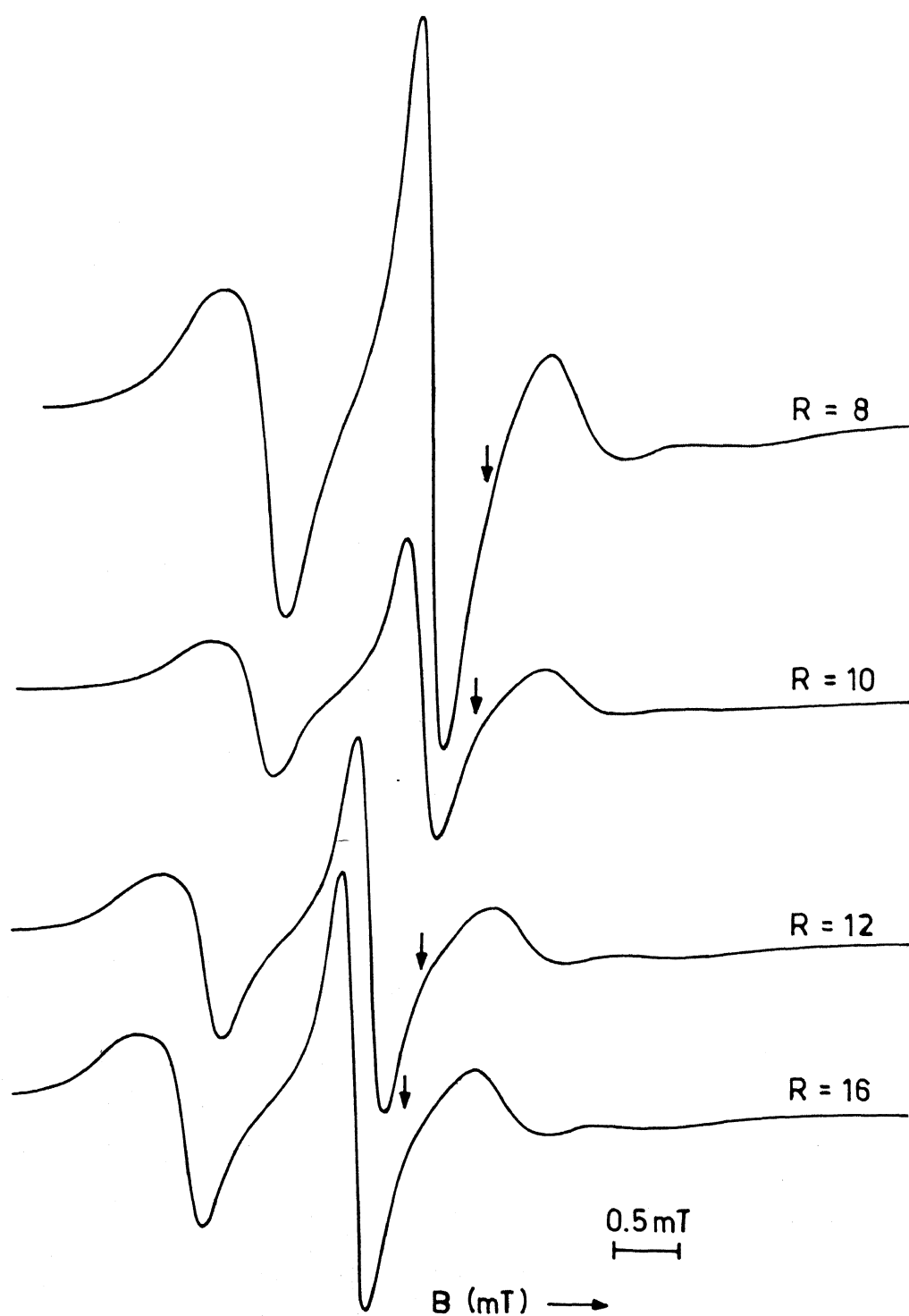


Fig. 2.19 EPR spectra of 5-DSA in EYL/cyclohexane/ $\text{H}_2\text{O}$  reverse micelles for values of  $R$  between 8 and 16.

( $A_{\parallel}$  and  $A_{\perp}$ ) can be derived directly from the spectra and have been presented in Table 2.6.

**Table 2.6 Spectral parameters of 5-DSA in EYL reverse micelles**

R	$A_{\parallel}$ (mT)	$A_{\perp}$ (mT)	R	$A_{\parallel}$ (mT)	$A_{\perp}$ (mT)
0	--	0.990	7	2.075	1.056
1	2.675	0.975	8	2.069	1.066
2	2.425	0.963	10	2.025	1.075
3	2.388	0.950	12	2.025	1.081
4	2.250	0.981	14	2.013	1.088
5	2.238	1.0006	16	2.025	1.091
6	2.163	1.0044			

Determination of the spectral parameters of Table 2.6 facilitates the calculation of order parameter,  $S$ , of the spin label in reverse micelles. The order parameter is a measure of the distribution of molecular orientations relative to some reference axis (the director). In membrane studies this director axis is chosen to be normal to the membrane surface. In reverse micelles it is considered as a parameter which reflects the amplitude of molecular and segmental motions taking place with high frequencies  $\nu \geq (A_{zz} - A_{xx}) \geq 10^8 \text{ s}^{-1}$ . 'S' can be calculated using the following expression :

$$S = \frac{A_{\parallel} - A_{\perp}}{A_{zz} - 0.5 (A_{xx} + A_{yy})} \cdot \frac{a_o}{a_N} \quad (2.38)$$

where  $A_{xx} = 0.63$  mT,  $A_{yy} = 0.58$  mT, and  $A_{zz} = 3.36$  mT are principal values of the hyperfine splitting tensor of 5-DSA. The isotropic hyperfine splittings  $a_o$  and  $a_N$  are defined as

$$a_o = \frac{1}{3} (A_{xx} + A_{yy} + A_{zz}) \quad \text{and} \quad a_N = \frac{1}{3} (A_{\parallel} + 2A_{\perp}).$$

Order parameters calculated using the above values in Eq. 2.38 are plotted versus 'R' in Fig. 2.20. The order parameter is seen to decrease up to  $R = 8$  and then level off beyond  $R = 8$ . The structures of EYL and 5-DSA give us a plausible idea about the arrangement of these molecules in the reverse micelles. Since 5-DSA has a long hydrocarbon chain, and since it does not dissolve in water, one may envisage that the spin label becomes intercalated between two EYL molecules so that  $\text{COO}^-$  group of the spin label can interact with  $\text{N}^+(\text{CH}_3)_3$  group of EYL. Further, since doxyl group is attached at the fifth position of the stearic acid chain, it would be located near the phosphate group of EYL. It is reasonable to expect that any motional changes occurring in this region would be reflected in the spin probe motion and, in turn, in its order parameter. The gradual decrease in the order parameter as 'R' increases clearly manifests the increased motion of the phosphate segment. Reported  $^{31}\text{P}$  NMR  $T_2$  relaxation studies<sup>31</sup> strongly supports this view.

No attempt has been made to calculate ' $\tau$ ' for 5-DSA in this system. Comprehensive lineshape studies will definitely give more accurate  $\tau$  values and other spectral parameters such as  $A_{\parallel}$ ,  $A_{\perp}$ , etc. These parameters will assist us in calculating the order parameter accurately.

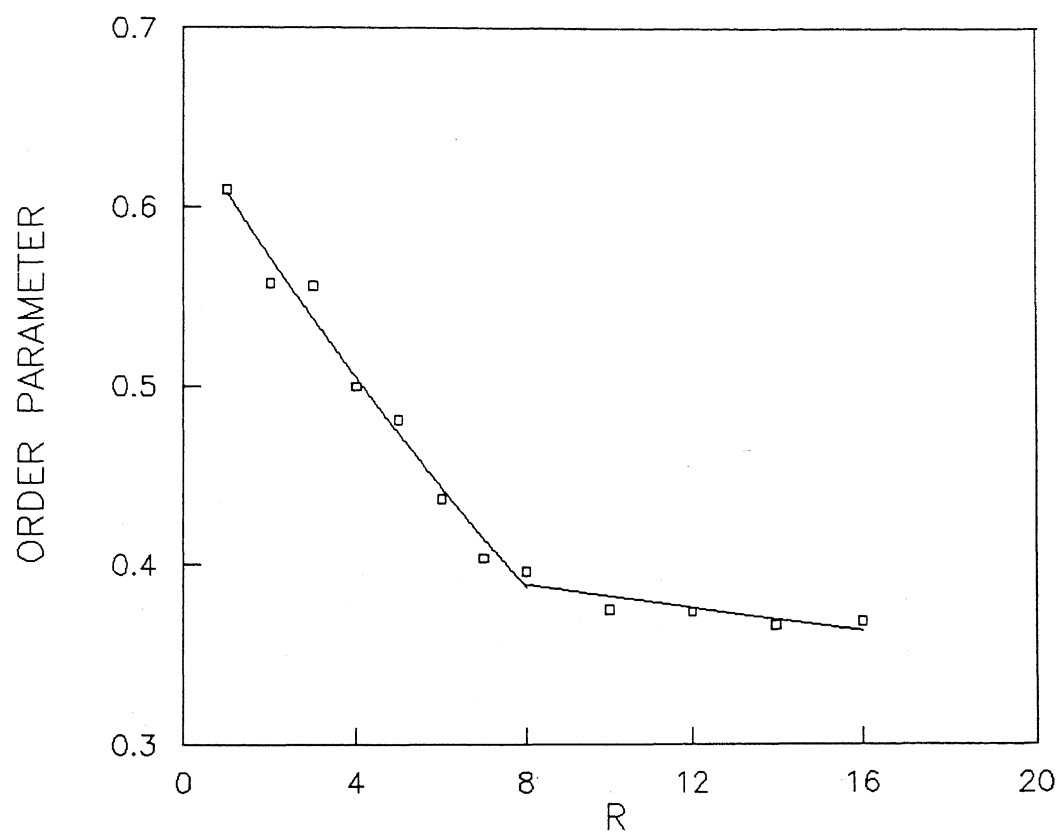


Fig. 2.20 Order parameter variation of 5-DSA in EYL/cyclohexane/H<sub>2</sub>O reverse micelles as a function of 'R'.

## 2.5 Conclusions

The overall conclusions of our EPR studies on the three spin labels, namely, PIX, SL-SHS and 5-DSA, shall be summarized as follows.

- (1) EPR investigations of EYL/cyclohexane/H<sub>2</sub>O reverse micelles using PIX as a probe have enabled us to find out the binding site of the label in the reverse micelles. Also, it has been demonstrated that the reverse micellar structure and size of the water pool are responsible for the anisotropic motion of the label (PIX) in lecithin reverse micelles.
- (2) The overall motion of the label, as determined from  $\tau$  value estimates, is shown to be a function of 'R'. A two-state model has been successfully applied to lecithin reverse micelles, and the fraction of bound water has been determined as a function of 'R'.
- (3) The polarity of the water pool of EYL/cyclohexane/H<sub>2</sub>O reverse micelles, as indicated by the  $a_N$  (<sup>14</sup>N) values of SL-SHS, increases gradually with 'R'. A 'cage model' has been proposed to explain the splitting of the high-field line of SL-SHS in lecithin reverse micelles.
- (4) The order parameter of 5-DSA in EYL/cyclohexane/H<sub>2</sub>O reverse micelles shows a strong dependence on 'R'. This parameter, which has been rationalized to be a measure of motion of the phosphate segment of EYL molecules, decreases steeply until R = 8 and then flattens out. This finding is in accordance with <sup>31</sup>P NMR studies carried out earlier in our laboratory.<sup>31</sup>

## REFERENCES

1. **Structure and Reactivity in Reverse Micelles**, M. P. Pileni (ed.), Elsevier, Amsterdam (1989).
2. **Reverse Micelles : Biological and Technological Relevance of Amphiphilic Structures in Apolar Media**, P. L. Luisi and B. E. Straub (eds.), Plenum, New York (1984).
3. **Microemulsions : Structure and Dynamics**, S. E. Friberg and P. Bothorel (eds.), CRC, Florida (1987).
4. **Spin Labeling : Theory and Applications**, L. J. Berliner (ed.), Academic, New York (1976).
5. P. Walde, A. M. Giuliani, C. A. Biocelli and P. L. Luisi, *Chem. Phys. Lipids* **53**, 265 (1990).
6. V. V. Kumar, C. Kumar, and P. Raghunathan, *J. Colloid Interface Sci.* **99**, 315 (1984).
7. V. V. Kumar and P. Raghunathan *Chem. Phys. Lipids* **41**, 159 (1986).
8. V. V. Kumar and P. Raghunathan, *Lipids* **21**, 764 (1986).
9. A. Carrington and A. D. MacLachlan, **Introduction to Magnetic Resonance**, Harper and Row, New York, (1967).
10. P. L. Nordio in : Ref. 4, Chapter 2, p 5.
- 11 (a) O. H. Griffith and A. S. Waggoner, *Acc. Chem. Res.* **2**, 17 (1969).  
 (b) O. H. Griffith and P. C. Jost, in : Ref. 4, Chapter 12, p 453.
12. J. E. Wertz and J. R. Bolton, **Electron Spin Resonance : Elementary Theory and Practical Applications**, McGraw-Hill, New York (1972).
13. **Advanced EPR : Applications in Biology and Biochemistry**, A. J. Hoff (ed.), Elsevier, Amsterdam (1989), Chapter 20, p 707.
14. C. P. Poole and H. A. Farach, **Theory of Magnetic Resonance** Wiley-Interscience, New York, (1972).
15. D. Kivelson *J. Chem. Phys.* **33**, 1094 (1960).
16. O. H. Griffith, D. W. Cornell and H. M. McConnell, *J. Chem. Phys.* **43**, 2909 (1965).
17. S. Schreier, C. P. Polnaszek and I. C. P. Smith, *Biochim. Biophys. Acta* **515**, 375 (1978).
18. W. S. Singleton, M. S. Gray, M. L. Brown and J. L. White, *J. Am. Oil. Chem. Soc.* **42**, 53 (1965).

19. L. N. Krichenko and A. A. Medzhidov, Bull. Acad. Sci. USSR (Chemical Sciences) 2685 (1969).
20. A. Barelli and H. -F. Eicke, Langmuir 2, 780 (1986).
21. P. C. Jost and O. H. Griffith, in : Ref. 4, Chapter 7,
22. P. L. Nordio Chem. Phys. Lett. 6, 250 (1970).
23. A. D. Keith, W. Snipes and D. Chapman, Biochemistry 16, 634 (1977).
24. H. Hauser, G. Haering, A. Pande and P. L. Luisi, J. Phys. Chem. 93, 7869 (1989).
25. H. Yoshioka and S. Kazama, J. Colloid Interface Sci. 95, 240 (1983).
26. V. Govindaraju, Ph.D. Dissertation, I.I.T. Kanpur, India (1993).
27. Z. Shervani, A. Maitra, T. K. Jain and Dinesh, Colloids Surfaces, 60, 161 (1991).
28. V. N. Parmon, A. I. Kokorin, Z. M. Zhidomirov and K. I. Zamaraev, Mol. Phys. 30, 695 (1975).
29. D. Marsh, in : **Membrane Spectroscopy**, E. Grell (ed.), Springer-Verlag, New York, 1981.
30. J. Hiff and L. Kevan, J. Phys. Chem. 93, 1572 (1989).
31. V. V. Kumar, P. T. Manoharan and P. Raghunathan, J Biosci. 4, 449 (1982).



## CHAPTER 3

DYNAMICS OF SPIN LABELS INCORPORATED EYL/CYCLOHEXANE/H<sub>2</sub>O REVERSE MICELLES :  
EFFECTS OF TEMPERATURE AND CHOLESTEROL ADDITION

## 3.1 Introduction

It has been established<sup>1</sup> that cholesterol plays an important structural role in the lipid core of biological membranes. To understand the function of cholesterol in biological membranes, several techniques have been applied on artificial 'model' systems such as monolayers,<sup>2</sup> bilayers<sup>3</sup> and liposomes.<sup>4a-b</sup> Differential scanning calorimetry, X-ray diffraction, NMR, EPR and fluorescence polarization have been variously employed for the study of lipid-cholesterol interactions, and these studies have shown that cholesterol can exhibit a condensing effect on lipids in the liquid crystalline state and a liquefying effect on lipids in the crystalline state leading to an intermediate gel state. The spin label method has been used by many workers<sup>5</sup> to study lipid-cholesterol interactions.

Addition of cholesterol to reverse micellar solutions has been reported to induce significant changes not only in the structural organization of these membrane mimicking systems but also on the physicochemical properties such as water-solubilizing ability, thermodynamical stability etc. Cholesterol mainly acts as a co-surfactant in the reverse micelles. In recent years, attention has been focused on the effect of cholesterol on the lecithin reverse micelles.<sup>6,7</sup> <sup>31</sup>P NMR linewidth study has revealed some motional details of phosphate group of lecithin in EYL/cholesterol/cyclohexane/H<sub>2</sub>O system.<sup>7</sup>

These observations indicate that 'cholesterol added' biologically relevant systems behave differently in many respects when compared with the systems free of cholesterol. It would be logical to expect, then, that the motional properties of nitroxide spin labels in such systems will also be affected. In this chapter, we have investigated such effects. In addition temperature effects on the dynamical properties of nitroxide spin labels incorporated in the water pools of EYL reverse micelles have also been studied.

### 3.2 Experimental Details

Extraction of lecithin from egg yolk and the further purification has been documented in section 2.3 of chapter 2. The co-surfactant, cholesterol, has been procured from S.D. fine chemicals, India and used without further purification. AR grade cyclohexane was distilled, refluxed in the presence of sodium wire for about 3-4 hours, and the redistilled (b.p. 81° C). Deionized water was double distilled prior to use.

The spin label, TEMPOL (2,2,5,5 tetramethyl-4-hydroxy-1-oxyl piperidine) procured from Sigma Chemical Co. USA, which was used without further purification. The spin label, SL-SHS (spin labeled sodium hexyl sulfate) was a gift sample received from Prof. H. -F. Eicke, Basel university, Switzerland.

Surfactant-cosurfactant solution was prepared by dissolving equimolar EYL and cholesterol (1:1 mole ratio) in cyclohexane. By injecting an appropriate amount of spin label solution (water) to a calculated amount of surfactant-cosurfactant stock solution, reverse micellar solutions of different 'R' values have been prepared. Details of reverse micelle preparations are given in chapter 2.

### 3.3 Results and Discussion:

#### 3.3.1 Effect of Cholesterol on the Dynamics of 'TEMPOL' Incorporated in EYL/Cyclohexane/H<sub>2</sub>O Reverse Micelles.

The spin label (TEMPOL) used in this study has the ability to become dissolved in both water and cyclohexane. The EPR spectrum of a dilute solution of TEMPOL in pure solvents (both cyclohexane and water) resembles those we have already shown in Fig. 2.4. This is because of the free tumbling of the spin label in low viscosity solvents. These spectra are isotropic, with well resolved <sup>14</sup>N hyperfine lines having narrow width.

To observe the effect of cholesterol on the dynamics of the spin label, we have first prepared a series of blank samples of EYL reverse micelles (hereafter referred to as 'cholesterol free' system) of various 'R' values, and have recorded EPR spectra for the purpose of comparison. These EPR lineshapes indicate that the motion of the spin label is in the 'fast motion' limit. Moreover, the amplitude of the high field line is reduced (i.e., width is increased) in the reverse micelles. These trends are similar to those observed for PIX (potassium iminoxide xanthogenate) in EYL reverse micelles (Refer section 2.4.1 of chapter 2).

Various samples of reverse micelles of different 'R', containing cholesterol (hereafter referred as 'cholesterol added' systems) were then prepared as per details given in section 3.2, and subjected to EPR investigations. No drastic change in the lineshapes was observed when compared with 'cholesterol free' systems, in general. However, the presence of cholesterol does induce significant changes in ratios of widths of different <sup>14</sup>N hyperfine lines, and these shall be further considered below. Measurement of hyperfine splitting constant ( $a_N$ ) and  $g_0$  values from the EPR spectra revealed that the addition of equimolar cholesterol-to-lipid (lecithin) did not have remarkable effects on these parameters.

### Linewidth Analysis and Correlation Time Measurement

Amplitudes of individual hyperfine lines are measured directly from the EPR spectra, and these values along with widths of mid-field lines were directly used in Eq. 2.18 to calculate the width of high, low and mid-field lines. Inspection of the widths of TEMPOL incorporated in 'cholesterol free' system shows that the spin label undergoes preferential anisotropic motion about a particular axis. For a better insight, the well-known 'anisotropic motion parameter' ( $h_{+1}/h_0$ ) was determined from the experimental spectra and plotted against 'R' in Fig. 3.1. From this figure it is clear that the anisotropic motion parameter decreases as the size of the water pool (proportional to 'R') increases. TEMPOL in 'cholesterol added' systems also exhibits anisotropic motion. Variation of the anisotropy parameter with 'R' parallels that observed for 'cholesterol free' system. However, there is a significant difference in the magnitudes of the anisotropic motion parameter measured at a particular 'R'. This difference is maintained over almost all 'R' values. A comparison of 'cholesterol free' and 'cholesterol added' systems is shown in Fig. 3.1.

The overall motional parameter ( $h_0/h_{-1}$ ) of TEMPOL in both 'cholesterol free' and 'cholesterol added' systems has been calculated for various 'R', and is shown in Fig. 3.2. In 'cholesterol free' reverse micelles, motional parameter of TEMPOL shows a decreasing trend with increasing 'R'. Addition of cholesterol (1) increases  $h_0/h_{-1}$  values when 'R' is small ( $R < 4$ ) (2) has minimal effect when  $R \approx 4$  and (3) decreases  $h_0/h_{-1}$  when  $R > 4$ .

The rotational correlation time ( $\tau$ ) of TEMPOL in these systems was determined as a function of 'R' using the methods already described in chapter 2. The dependence of  $\tau$  on 'R' for 'cholesterol added' and 'cholesterol free' systems has been depicted in Fig. 3.3. The varying trend of ' $\tau$ ' with 'R' and

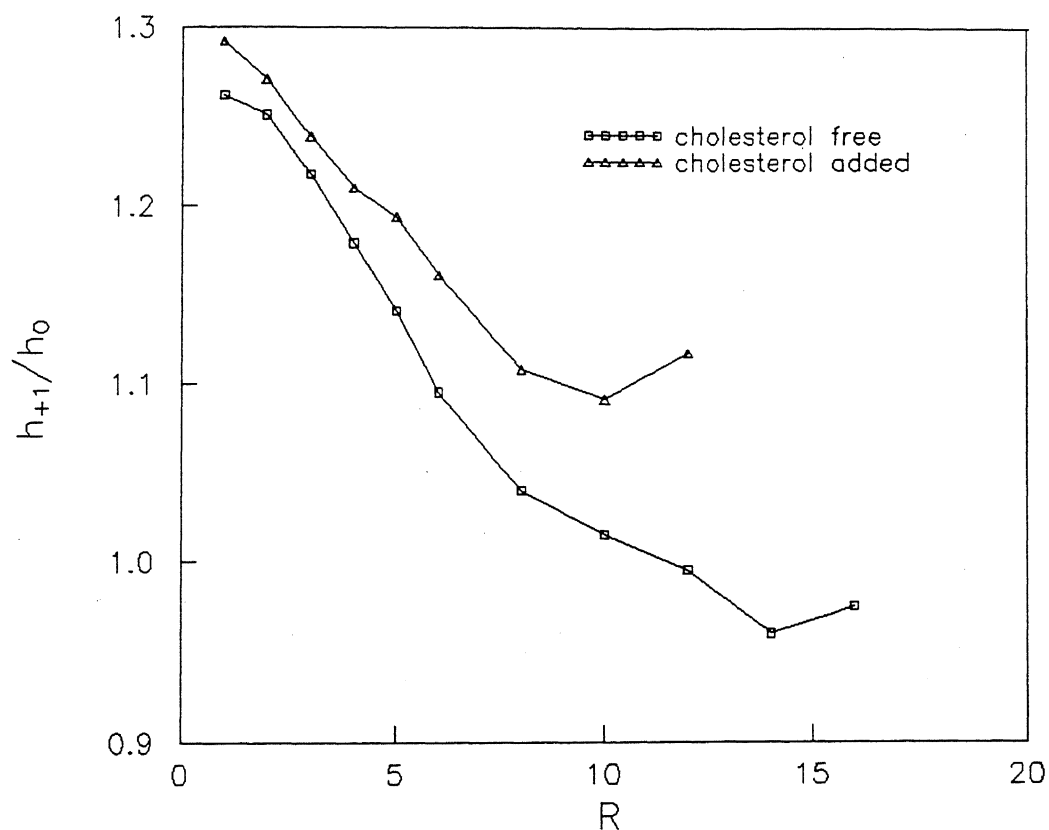


Fig. 3.1 Ratio of the relative amplitudes of low-field  $^{14}\text{N}$  hyperfine line to the central-field line,  $h_{+1}/h_0$  vs 'R' for (i) EYL/cholesterol/cyclohexane/ $\text{H}_2\text{O}$ (TEMPOL) (ii) EYL/cyclohexane/ $\text{H}_2\text{O}$ (TEMPOL) reverse micelles.

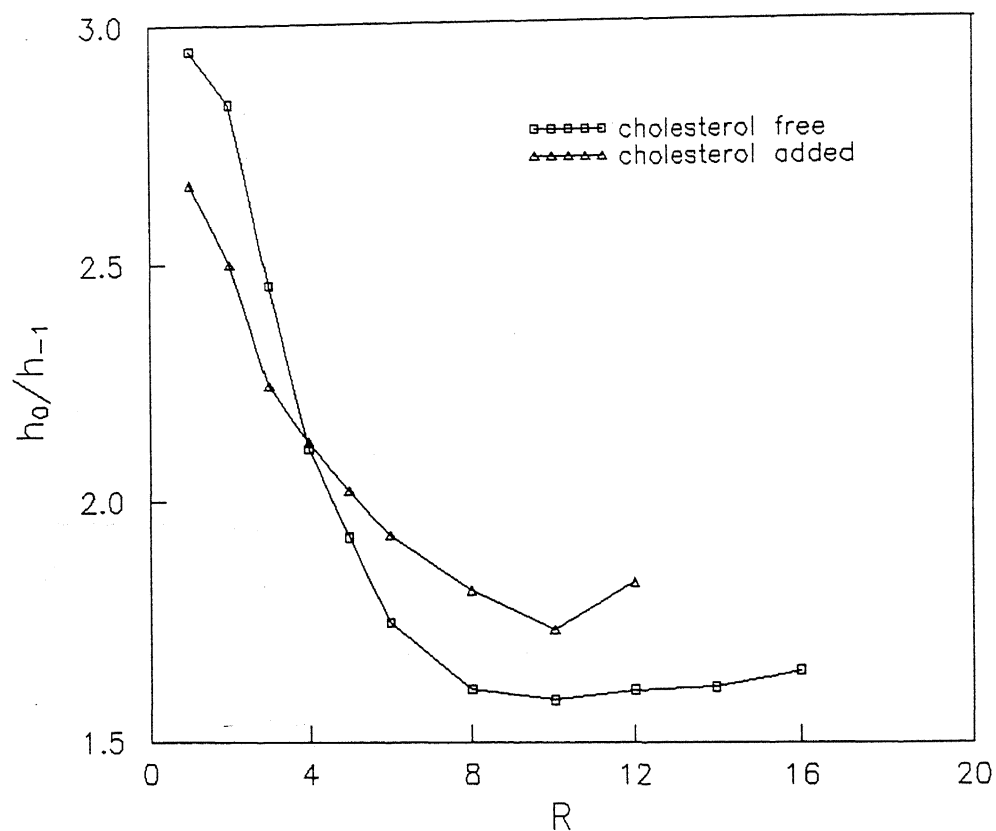


Fig. 3.2 Ratio of the relative amplitudes of central-field  $^{14}\text{N}$  hyperfine line to the high-field line,  $h_0/h_{-1}$  vs  $R'$  for (i) EYL/cholesterol/cyclohexane/ $\text{H}_2\text{O}$ (TEMPOL) (ii) EYL/cyclohexane/ $\text{H}_2\text{O}$ (TEMPOL) reverse micelles.

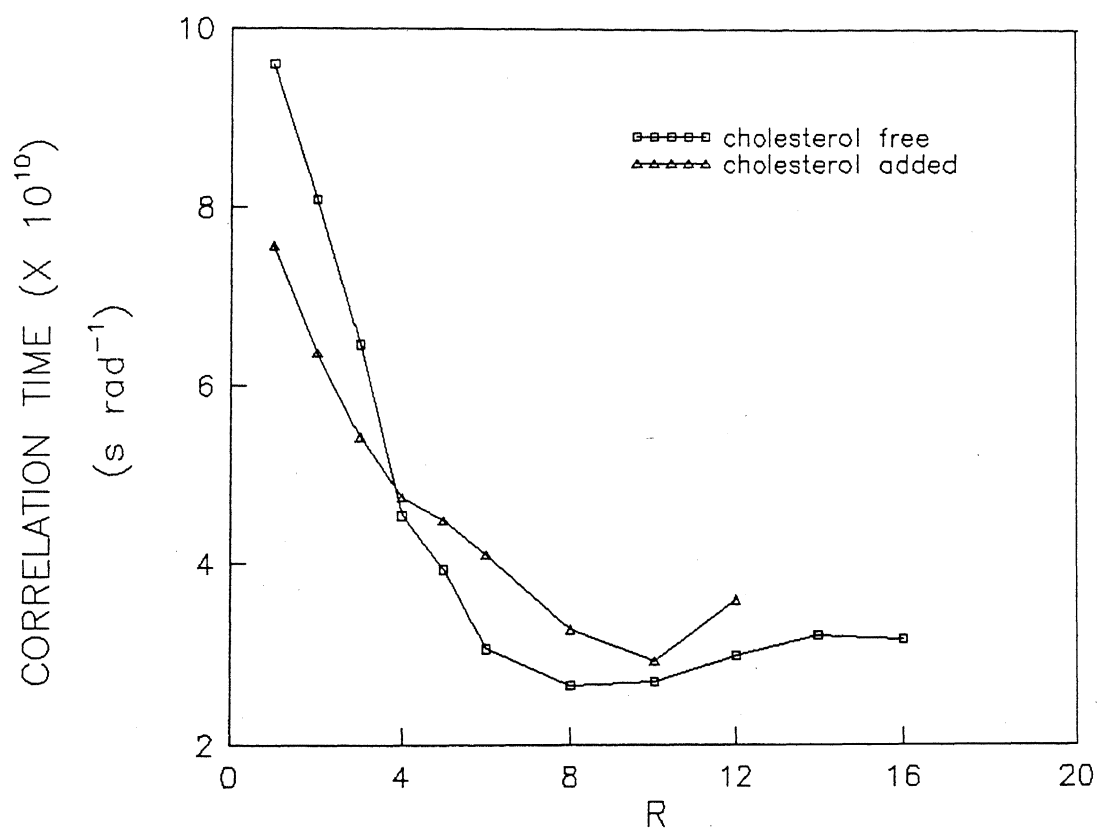


Fig. 3.3 Variation of rotational correlation times of TEMPOL as a function of 'R' in (i) cholesterol added system (ii) cholesterol free system.

the difference in the magnitudes of  $\tau$  for the abovementioned systems at a particular 'R' are similar to that noticed for  $h_0/h_{-1}$ .

From a comparison of  $h_{+1}/h_0$  values (shown in Fig. 3.1) of TEMPOL in 'cholesterol added' and 'cholesterol free' systems, it is evident that this spin label present in 'cholesterol added' system experiences enhanced motion about its principal x-axis. This enhanced anisotropic motion persists throughout the range of 'R' values we have studied. This kind of peculiar motion is expected in the simple spin labels having piperidine ring only when the ring of the label orients between two surfactant molecules. Since cholesterol is a 'bulky' steroid molecule with a tendency to intercalate between surfactant (phospholipid) molecules, the spin label's anisotropic motion is enhanced compared to 'cholesterol free' system.

The trend in the variation of overall motional parameter,  $h_0/h_{-1}$  shown in Fig. 3.2, could be rationalized in terms of formation of gels which is normally observed in EYL/cyclohexane/H<sub>2</sub>O reverse micelles. In the case of 'cholesterol free' reverse micelles, 'gel formation' starts at lower 'R' values ( $\approx 4$ ). This is evident by the appearance of 'highly viscous' (semi solid) reverse micellar solutions when  $R > 6$ . It is interesting to note that the cholesterol addition prevents this 'gel formation' (i.e., reverse micellar solutions having cholesterol do not become viscous even at higher 'R'). Such a phenomenon has also been reported by other workers.<sup>6</sup> From our EPR studies it is clear that cholesterol addition has significant effects on the interfacial region of the reverse micelles during the pre-gelation regime (i.e.,  $R \leq 4$ ). Because of this, the  $h_0/h_{-1}$  values are larger compared with 'cholesterol free' system at a particular 'R'. After  $R = 4$  the presence of cholesterol prevents gel-formation and thereby further decreases  $h_0/h_{-1}$ .

The dependence of ' $\tau$ ' values on 'R', shown in Fig. 3.3, offers



further support to our arguments given so far for the behavior of the overall motional parameter. In the 'cholesterol added' system, TEMPOL reorients slowly for values of  $R < 4$ , and undergoes 'fast motion' beyond  $R = 4$ .

### 3.3.2 Effect of Cholesterol on the Dynamics of SL-SHS Incorporated in EYL/Cyclohexane/H<sub>2</sub>O Reverse Micelles.

Peculiar EPR lineshapes observed for SL-SHS in the 'cholesterol free' reverse micellar system ( Refer section 2.4.2 of chapter 2 ) have led us to carry out a similar EPR study on 'cholesterol added' system also. X-band EPR spectra obtained for SL-SHS in EYL/cholesterol/cyclohexane/H<sub>2</sub>O reverse micelles at room temperature are shown in Fig. 3.4 for some selected 'R' values. Similar to those obtained for TEMPOL in 'cholesterol free' system the spectra here are again generally isotropic, with well-resolved hyperfine lines. Amplitudes of low-field and mid-field hyperfine lines indicate that SL-SHS does not undergo any preferential anisotropic motion about a particular axis even in the presence of added cholesterol.

Further careful examination of EPR lineshapes of SL-SHS in the 'cholesterol added' system indicates that significant changes do take place in the high-field line. Unlike SL-SHS in 'cholesterol free' system, where splitting in the high field line occurs only beyond  $R = 8$ , in 'cholesterol added' system the splitting in the high field line starts even at  $R = 4$ . Furthermore, nitroxide hyperfine lines appear highly asymmetric when  $R \geq 5$ .

The isotropic <sup>14</sup>N hyperfine splitting constants ( $a_N$ ) were also measured directly from the EPR spectra of spin labeled 'cholesterol added' system. These  $a_N$  values increase with increasing R value. At any particular 'R', there is a significant difference between the  $a_N$  values observed for 'cholesterol free' and 'cholesterol added' systems.

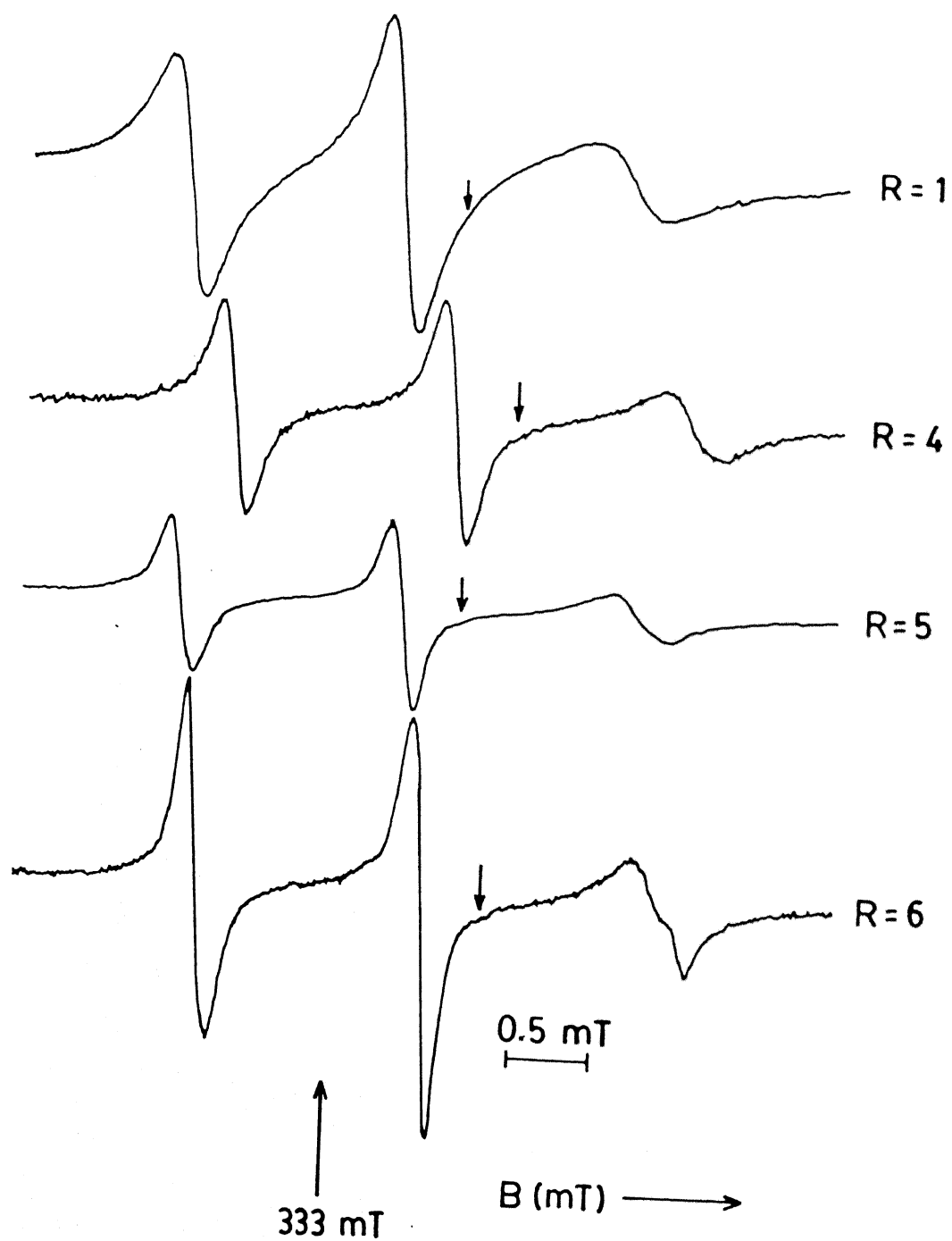


Fig. 3.4 EPR spectra of SL-SHS in EYL/cholesterol/cyclohexane/H<sub>2</sub>O reverse micelles as a function of 'R'.

Ratios of hyperfine-line amplitudes ( $h_0/h_{+1}$  and  $h_0/h_{-1}$ ) of SL-SHS in 'cholesterol added' system have been determined for the range of 'R' values 1-4. Since line distortion starts beyond  $R = 4$ , no attempt has been made to calculate the corresponding  $h_0/h_{+1}$  and  $h_0/h_{-1}$  values.

The variation of  $a_N$  with 'R' clearly indicates that the environment of SL-SHS is becoming more polar as 'R' increases. This increase in  $a_N$  values is steeper in 'cholesterol added' system when compared to 'cholesterol free' system. Recalling the behavior of cholesterol, namely, that it absorbs some amount of water (especially 'bound' water), it is rationalized that the spin label is forced into the interior of the water pool (which behaves like 'normal' water), in order to stay in solution, and thus experiences increased polarity.

The amplitude ratios also confirm this finding in 'cholesterol added' system. Since SL-SHS happens to stay in 'bulk' water, its mobility would, of course, be rapid enough to reduce  $h_0/h_{-1}$  values when cholesterol is added.

Another important observation made for SL-SHS is the splitting of the high-field hyperfine line. Of particular interest is the surprising correlation between the  $a_N$  values and the high field line distortion. We have observed that the splitting of high field line occurs as the  $a_N$  value of SL-SHS incorporated in both 'cholesterol free' and 'cholesterol added' systems tends to become 1.475 mT. This value is attained for SL-SHS 'cholesterol added' system when  $R = 4$ , the line splitting also occurring at exactly the same R value. However, in the 'cholesterol free' system, the  $a_N$  of 1.48 mT is attained only when  $R = 8$  ( Refer Fig. 2.16), after which the hyperfine line distortion also sets in.

A plausible interpretation of the results would be as follows. Addition of cholesterol modifies the water environment significantly which is

the main cause for abnormal behavior of SL-SHS in 'cholesterol added' system. In the literature, similar 'cholesterol addition effects' have been encountered in phospholipid multilayers<sup>8</sup> and vesicles.<sup>9</sup> It has been established in these systems that addition of cholesterol generally increases the spacing between adjacent phospholipid molecules due to intercalation of cholesterol.

### 3.3.3 Effect of Temperature on the EPR Spectral Profiles of TEMPOL in EYL/Cyclohexane/H<sub>2</sub>O Reverse Micelles.

Generally, EPR spectral parameters and lineshapes are sensitive to temperature variations. To get answers for such queries as "how sensitive are these parameters of a spin label in reverse micelles" and "how are various dynamical modes promoted by temperature", we have examined the temperature dependence of EPR lineshapes in EYL reverse micelles using TEMPOL as the spin probe. The system chosen is EYL/cyclohexane/H<sub>2</sub>O (TEMPOL) reverse micellar solution of  $R = 4$ . Fig. 3.5 represents some of the typical EPR spectra recorded for TEMPOL in EYL/cyclohexane/H<sub>2</sub>O reverse micelles over a temperature range of 265 K to 193 K.

In the temperature range specified two sets of spectral profiles have been observed. From 265 K to 245 K, spectra recorded are isotropic in nature. When the temperature of the system is brought down to 230 K, spectral responses are mixture of anisotropic and isotropic components, with parallel and perpendicular features starting to appear. Further cooling results in an EPR spectrum typical of an immobilized nitroxide, which slowly transforms into a 'rigid glass' spectrum when the temperature comes down to  $\approx 200$  K.

In the first set of profiles (i.e., those obtained in the range 265 K to 245 K) the anisotropic parameter ( $h_{+1}/h_0$ ) is  $\geq 1$ . This clearly indicates that anisotropic motion of the spin label along x-axis persists until the

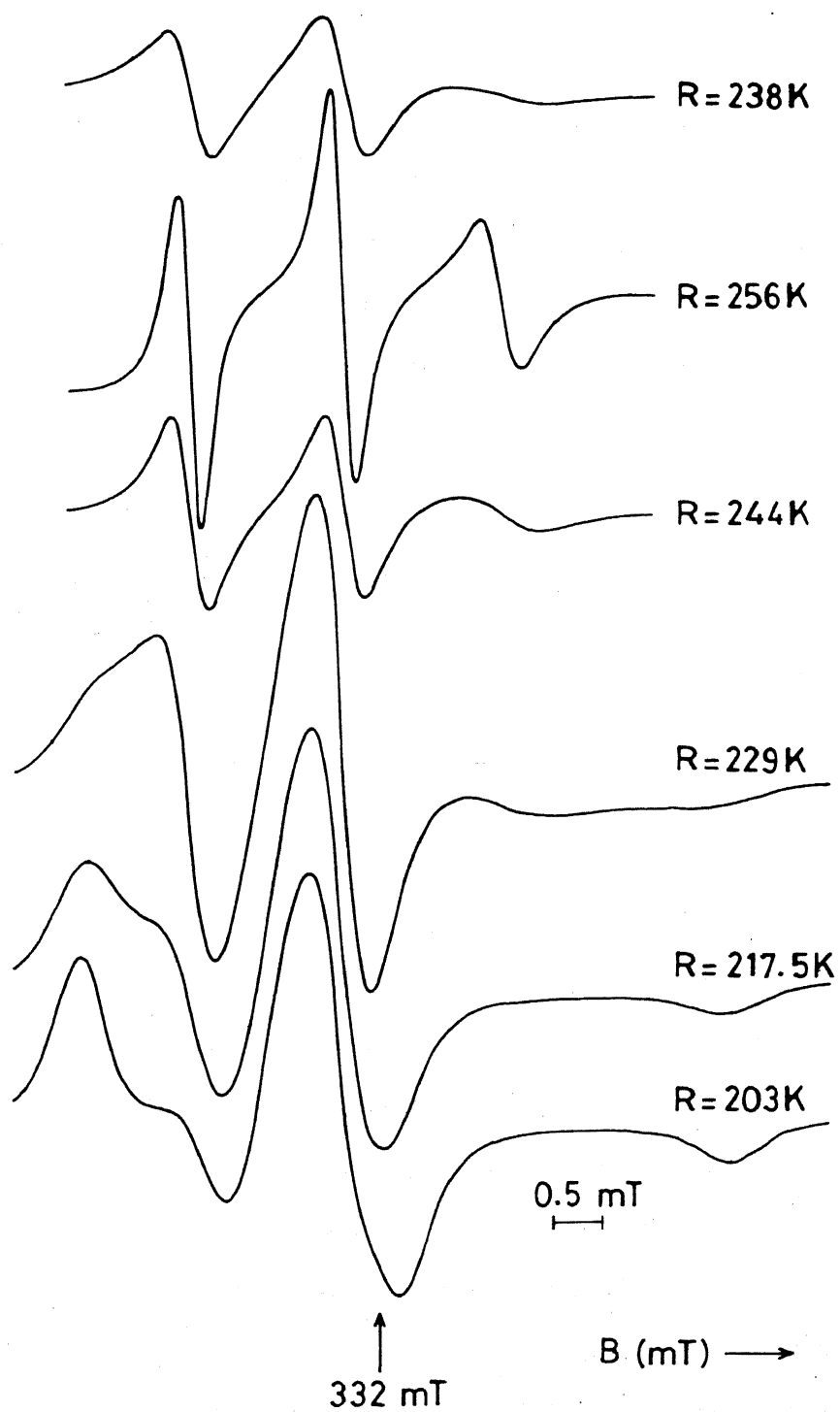


Fig. 3.5 Temperature dependent EPR spectra of TEMPOL in EYL/cyclohexane/H<sub>2</sub>O reverse micelles as a function of 'R'.

temperature becomes 245 K. This motion slows down further when the temperature is lowered further. In the temperature range 265 to 245 K, the spin label undergoes 'fast' motion, as heralded by the isotropic nature of the spectra. Beyond this range the motion of the spin label slows down, which the consequent resolution of parallel and perpendicular components in the spectral profiles.

The appearance of isotropic spectra could be attributed to the fact that the water of the reverse micellar 'water pool' could not be frozen down to  $\approx 245$  K. Because of this, the spin label incorporated in the water pools finds more freedom to rotate. Our findings are supported by the established fact that reverse micelles retain their structure even at 77 K, and that water cannot be frozen until  $\approx -40^\circ$  C. Appearance of anisotropic components in the spectral profiles beyond 245 K is the clear indication of water gets frozen below 245 K only.

### 3.4 Conclusions:

- (1) Cholesterol addition causes significant effects on the interfacial region of the EYL/cyclohexane/H<sub>2</sub>O reverse micelles. Anisotropic motion about x-axis of the spin label (TEMPOL) becomes enhanced by the addition of cholesterol. The fact that cholesterol addition prevents the gelation of the reverse micellar medium does not affect the above anisotropic motion.
- (2) The overall motion of TEMPOL, as revealed by its  $\tau$  and  $h_0/h_{-1}$  values, is decreased in the presence of cholesterol in the 'pre-gelation' regime (  $R < 4$  ). Beyond  $R = 4$ , prevention of gel formation by cholesterol increases the spin label's motion in lecithin reverse micelles.

- (3) SL-SHS in 'cholesterol added' system finds itself in a more polar environment compared with 'cholesterol free' system. This eventually also results in splitting of the high field  $^{14}\text{N}$  hyperfine line.
- (4) Our variable temperature EPR study confirms that the reverse micellar water does not freeze even down 245 K.

## REFERENCES

- R. A. Demel and B. Dekruyff, *Biochim. Biophys. Acta* **457**, 109 (1976).
- Y. London, R. A. Demel, W. S. M. Gewtze van Kessel, P. Zahler and L. L. M. Van Deenen, *Biochim. Biophys. Acta* **332**, 69 (1974).
- T. J. McIntosh, *Biochim. Biophys. Acta* **513**, 43 (1978).
- (a) D. Chapman in : **Biological Membranes**, D. Chapman and D. F. H. Wallach (eds.), Vol. 2, p. 91, (1973).
- (b) M. C. Phillips, *Prog. Surf. Membrane Sci.*, **5**, 139 (1972).
- P. C. Jost, A. S. Waggoner and O. H. Griffith, in : **Structure and Function of Biological Membranes**, L. I. Rothfield (ed.), Academic, New York. (1971).
- Z. Shervani, A. Maitra, T. K. Jain and Dinesh, *Colloids Surfaces* **60**, 161 (1991).
- Z. Shervani, T. K. Jain and A. Maitra, *Colloid Polym. Sci.* **269**, 720 (1991).
- A. D. Keith, W. Snipes and D. Chapman, *Biochemistry* **16**, 634 (1977).
- I. Hiromitsu and L. Kevan, *J. Am. Chem. Soc.* **109**, 4501 (1987).



## CHAPTER 4

EPR STUDIES OF THE  $\text{VO}^{2+}$  PROBE IN REVERSE MICELLES CONTAINING  
CATIONIC, ANIONIC, AND ZWITTERIONIC SURFACTANTS

## 4.1 Introduction

Metal ions in many proteins successfully lead us to find out how various biologically relevant processes take place. In particular, metal ions serve as useful spectrochemical probes of molecular structure, electron transfer, and enzyme kinetics. To probe such types of information spectroscopically, various techniques such as nuclear magnetic resonance (NMR), Mössbauer, optical absorption, or electron paramagnetic resonance (EPR) spectroscopy are widely used. Depending on the choice of the technique and the property to be studied, the native metal ion in these proteins will be substituted.

Due to the relatively uncomplicated magnetic interactions, the Vanadyl ion or oxycation,  $\text{VO}^{2+}$ , has become a much-favored spin probe for carrying out EPR studies on systems of importance in biochemical and biomedical fields. This probe has been successfully employed to gain structural information on metal ion binding sites in proteins<sup>1a-c</sup> and their role in protein function. In addition to protein studies, vanadyl ion spin probe investigations have been undertaken to study a variety of interesting problems such as the dynamics in nucleic acids,<sup>2</sup> the counterion mobility in micellar solutions,<sup>3,4</sup> the nature of motion at the anionic vesicle surface of phospholipid bilayers,<sup>5</sup> the long-range ordering occurring in nematic liquid crystals,<sup>6a-c</sup> the metal ion binding sites of humic and fulvic acids<sup>7a-b</sup> and the structural arrangement of anisotropic mesophase spherules formed from carbonization of Gachsaran residue in fossil fuels.<sup>8</sup>

Though vanadyl EPR spectroscopy has been used in micelles,<sup>3</sup> vesicles,<sup>5</sup> and micellar liquid crystal systems<sup>4</sup> to probe the state of aggregation and motion, it has been only sparingly exploited in reverse micellar media as such. To the best of our knowledge, only three qualitative reports have been documented regarding EPR studies on reverse micelles containing a transition metal ion.<sup>9-11</sup> Transition metal ions have been used with a view to explore the coordination site in reverse micelles<sup>9</sup> and thereby to develop some efficient catalysts; other studies relate to the dynamical properties of these metal ions.<sup>11a-b</sup>

For obtaining satisfactory answers to such important queries as (1) how is the dynamics of  $\text{VO}^{2+}$  ion affected in the presence of reverse micelles containing cationic, anionic, and zwitterionic surfactants and (2) whether the electrostatic interaction between the surfactants head group and the guest molecules are likely to be affected by the size of the water pool, etc., we have carried out a series of detailed quantitative EPR studies of  $\text{VO}^{2+}$  in reverse micelles containing cationic (CTAB), anionic (AOT), and zwitterionic (lecithin) surfactants. Our EPR investigations and the results are being presented in this chapter.

This chapter comprises a brief resume of the general characteristics of EPR of vanadyl spin probe, a discussion of the experimental details, the results accumulated for vanadyl EPR in 'ionic' reverse micelles, and our conclusion based on the experiments.

#### 4.2 EPR Spectroscopy of Vanadyl Ion

Among the first row transition ions, vanadyl (IV) is the most stable oxyanion. This ion has an unpaired electron in its outermost 3d orbital. The  $3d^1$  ground state of vanadyl complexes is orbitally nondegenerate with no

electronic states nearby in energy. Further, among all the paramagnetic metal ion complexes, only those of  $\text{VO}^{2+}$  consistently give relatively sharp EPR spectra under both low temperature and room temperature conditions. This characteristic feature often facilitates experimental studies over a wide timescale range.

Room temperature EPR spectra of vanadyl complexes in aqueous solutions exhibit eight highly resolved hyperfine lines due to the coupling of the 3d unpaired electron with a single  $^{51}\text{V}$  nucleus ( $I = 7/2$ ). The  $^{51}\text{V}$  nucleus has a large magnetic moment and is nearly 100% abundant. A typical spectrum is shown in Fig. 4.1. Fairly straightforward procedures are routinely used to analyze the linewidths and lineshapes of such EPR spectra.

General EPR spectra of vanadyl ions are described by a spin Hamiltonian which includes the electron Zeeman interaction and the electron- $^{51}\text{V}$  nuclear hyperfine interaction, namely,

$$\mathcal{H} = \beta B(g_{xx} S_x + g_{yy} S_y + g_{zz} S_z) + hc (A_{xx} S_x I_x + A_{yy} S_y I_y + A_{zz} S_z I_z) \quad (4.1)$$

where xyz is the axis system which diagonalizes both the  $g$  and nuclear hyperfine  $A$  tensors.  $A$  is expressed in  $\text{cm}^{-1}$ .  $\beta, h, c$  and  $B$  are the Bohr magneton, Planck's constant, the speed of light, and the applied magnetic field in gauss, respectively.

X-band EPR spectra can often be described by axially symmetric tensors, in which case  $g_{\parallel} = g_{zz}$ ,  $g_{\perp} = g_{xx} = g_{yy}$ ,  $A_{\parallel} = A_{zz}$ , and  $A_{\perp} = A_{xx} = A_{yy}$ . Because of the essentially nonbonding  $d_{xy}$  ground state, ligand nuclear superhyperfine couplings in vanadyl complexes are not usually observed. In some instances, however, superhyperfine couplings have been resolved.<sup>20</sup> A typical 'axial' EPR spectrum of frozen solution is shown in Fig. 4.2. Details

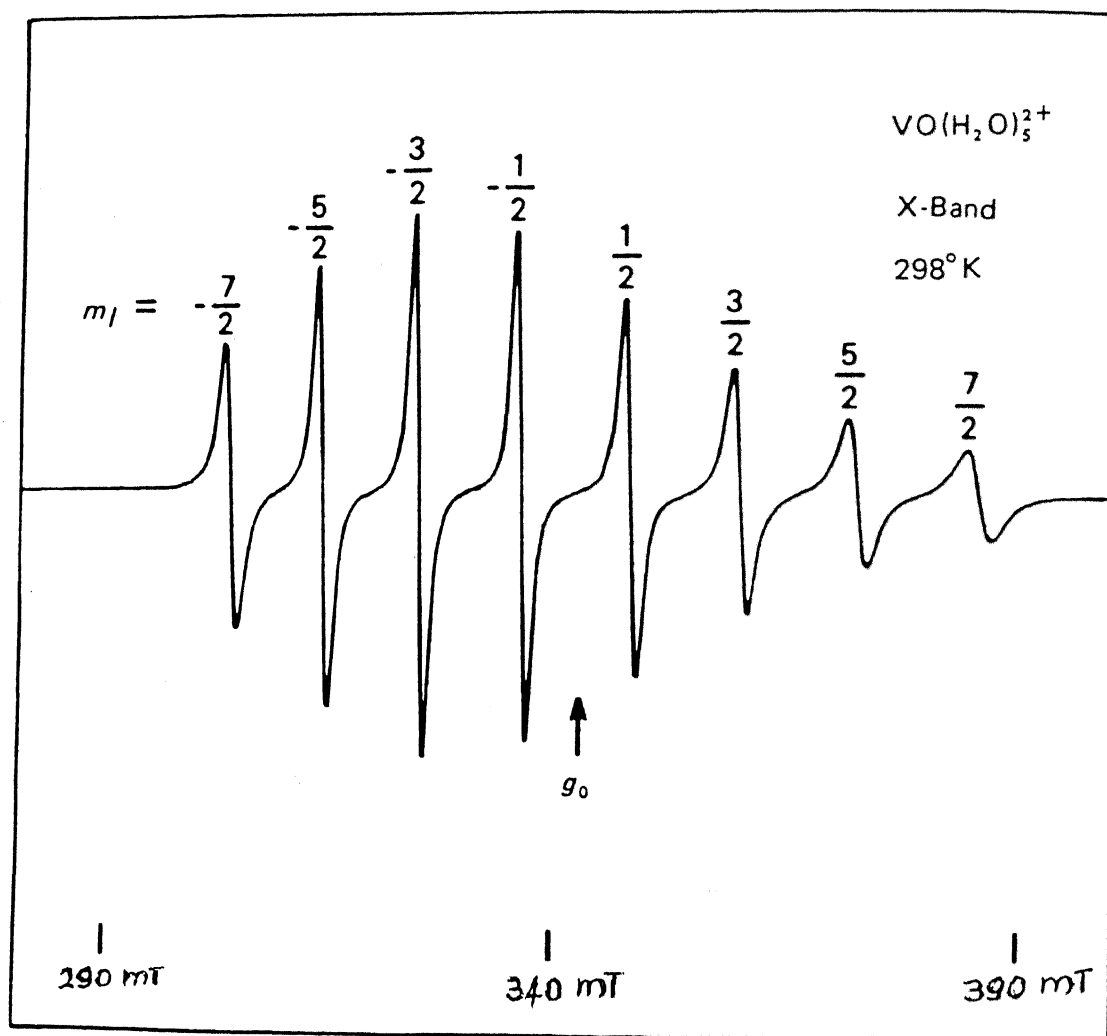


Fig. 4.1 Isotropic X-band EPR spectrum of the pentaquo vanadyl(IV) ion in room temperature aqueous solution (from ref. 13).

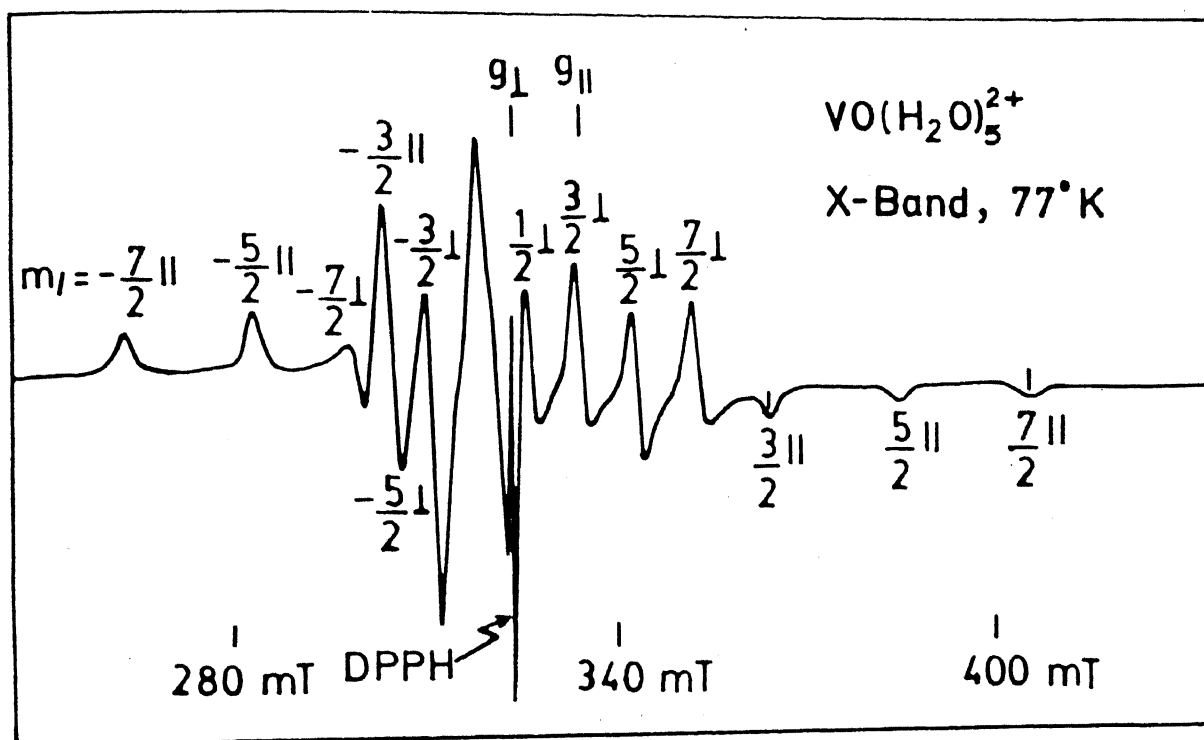


Fig. 4.2 Rigid-limit X-band EPR spectrum of the pentaquo vanadyl(IV) ion in frozen (77 K) aqueous solution (from ref. 13).

of the EPR lineshape analysis of these frozen solutions can be found elsewhere.<sup>12,13</sup>

#### 4.2.1 Effect of Motion on the EPR Spectral Profiles of $\text{VO}^{2+}$

If the  $\text{VO}^{2+}$  ion is in an isotropic, low-viscosity solvent, such as water, it will undergo rapid rotational motion ('fast' motion) at room temperature and the resulting X-band EPR spectrum will resemble the one shown in Fig. 4.1. An interesting feature of this spectrum, first noted by Pake and Sands,<sup>14</sup> is the variation of the linewidths of the individual hyperfine lines with the nuclear quantum number  $m_I$ . This dependence is principally due to the incomplete rotational averaging of the  $g$  and  $A$  tensors. The lines in the wings of the spectrum are broadest since they are the most anisotropic [i.e.,  $B_{m_I}(0^\circ) - B_{m_I}(90^\circ)$  is large] and less completely averaged by rotational diffusion. The linewidths measured at X-band can be fitted to a cubic equation in  $m_I$ , viz,

$$\Delta B_{m_I} = \alpha' + \alpha'' + \beta m_I + \gamma m_I^2 + \delta m_I^3 \quad (4.2)$$

where  $\alpha'$ ,  $\alpha''$ ,  $\beta$ ,  $\gamma$  and  $\delta$  are constants.

The theory of Wilson and Kivelson<sup>15</sup> relates  $\alpha'$ ,  $\beta$ ,  $\gamma$  and  $\delta$  to the components of the  $g$  and  $A$  tensors and the molecular reorientation (rotational correlation) time  $\tau$ .  $\alpha''$  is the residual linewidth, and is attributed to all other line broadening mechanisms such as spin-rotation interaction and unresolved superhyperfine splittings.  $\beta$  and  $\gamma$  are usually estimated from a least-squares fit of Eq. 4.2 to the experimental linewidths.

When highly viscous  $\text{VO}^{2+}$  solutions are considered, or when the  $\text{VO}^{2+}$  ion in low-viscous solution was cooled to subzero temperature, a complex EPR spectrum as shown in Fig. 4.3 will be observed. This is because of the vanadyl

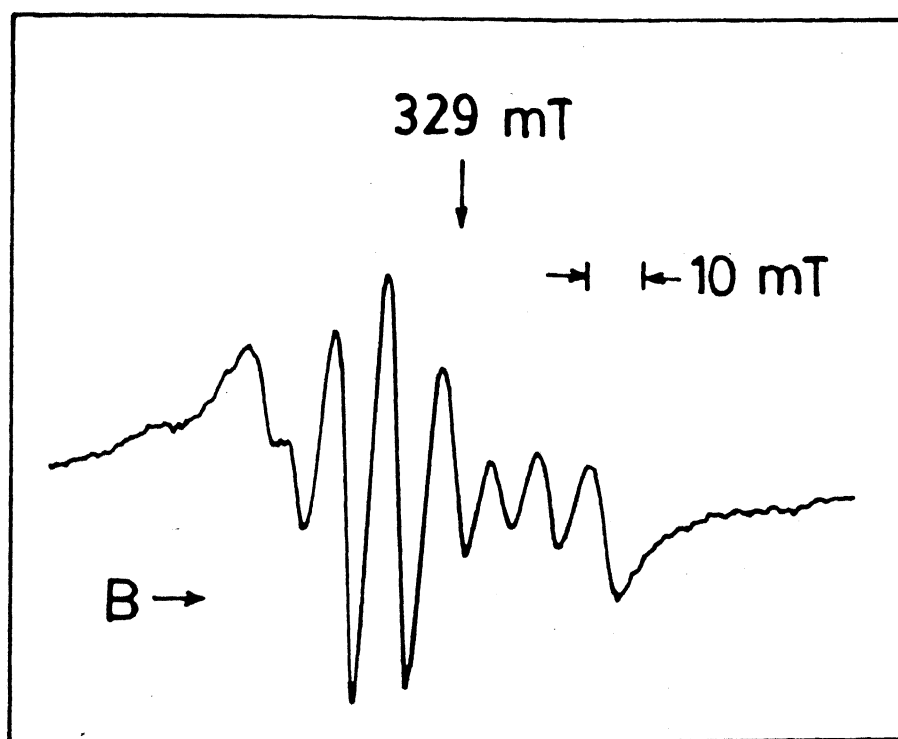


Fig. 4.3 X-band EPR spectrum of  $\text{VO}(\text{acac})_2$  in toluene at 193 K intermediate motional region (from ref. 16).

ions undergoing incipient slow tumbling motion ('intermediate' motion) under the abovementioned circumstances. We notice that, in this case, EPR lines are asymmetric and unequally spaced (because of overlapping).

When the solution of  $\text{VO}^{2+}$  is completely frozen, the resultant spectrum will look like the one shown in Fig. 4.2. Under this circumstance the spectrum approaches the rigid limit and exhibits clearly resolved parallel and perpendicular features. This, of course, is the case of the  $\text{VO}^{2+}$  ion motion having totally slowed down ('slow' motion).

These three different kinds of motion of vanadyl ion, sensitive to the environment, are well characterized by the rotational correlation time,  $\tau$ . In the 'fast' motion region,  $\tau$  will be of the order of  $10^{-10}$ – $10^{-11}$  s  $\text{rad}^{-1}$ . In the incipient slow-motional region or 'intermediate' motional region,  $\tau \geq 10^{-10}$  s  $\text{rad}^{-1}$  and in the 'slow' motional region,  $\tau > 10^{-9}$  s  $\text{rad}^{-1}$ . The methods used to measure these  $\tau$  values are further discussed in section 4.4. The  $\text{VO}^{+2}$  EPR lineshape is insensitive<sup>16</sup> to correlation times longer than about  $7 \times 10^{-8}$  s  $\text{rad}^{-1}$ , which is an order of magnitude smaller than a similar  $\tau$  parameter for nitroxide spin labels.

### 4.3 Experimental Details

#### 4.3.1 Materials

##### 1) Cetyl Trimethyl Ammonium Bromide (CTAB)

CTAB was procured from Sigma Chemical Co. U.S.A. The powdered surfactant was purified as follows : CTAB was treated with cooled diethyl ether ( $< 10^\circ \text{C}$ ), shaken thoroughly in a flask and filtered off. The ether-treated CTAB was then dissolved in a minimum amount of purified ethanol. To the clear CTAB solution, an excess of cold acetone was added, and the solution kept in a refrigerator. Fine needle shaped crystals obtained after 24 hr. were filtered



off and dried under high vacuum. Thoroughly dried CTAB was preserved for further EPR studies. All the solvents used in this purification process were of a commercial grade, and these were purified before use by distillation and dried by usual means.

## 2) Diethylhexyl Sodium Sulfosuccinate, Aerosol OT (AOT)

AOT was purchased from Sigma Chemical Co., USA, in bulk amount and was purified as follows:<sup>17</sup> 100 g of AOT was dissolved in 1000 ml of methanol and 30 g of activated charcoal was added. The mixture was allowed to stand for 24 hr. with stirring, at room temperature. This mixture was then filtered using a G-4 sintered glass filter, and the filtrate evaporated in a rotary evaporator to remove the methanol. The residue was dissolved in 750 ml of petroleum ether (40<sup>0</sup>-60<sup>0</sup> C fraction), and 200 ml of water was added to the above petroleum ether solution. This mixture was shaken well in a separatory flask and the petroleum ether phase was retained. A gel like substance was obtained when the petroleum ether was evaporated. This sticky substance was re-dissolved in 500 ml of methanol and washed three times with 300 ml, 100 ml, and 100 ml portions of petroleum ether. The methanol phase was separated and evaporated to dryness under reduced pressure.

The residual AOT was dried under high vacuum, dissolved in dry diethyl ether and re-dried under reduced pressure. Finally, the AOT was dried for 24 hr. under high vacuum and stored as 5 g portions in sealed bottles under nitrogen at -20° C.

## 3) Egg Yolk Lecithin

The extraction and purification methods are the same as those given in Chapter II.

#### 4) n-Octane

AR grade n-octane was obtained from Sigma Chemical Co., U.S.A. This was distilled once and allowed to stand over sodium. Again, spectral purity was ensured by recording  $^1\text{H}$  NMR spectrum.

#### 5) Chloroform, $\text{CHCl}_3$

Commercial grade  $\text{CHCl}_3$  was purchased from S.D. Fine Chemicals, India. This was shaken five or six times with half its volume of water in a separatory flask, then dried over anhydrous calcium chloride for at least 24 hr. and distilled. The  $60-61^\circ\text{C}$  fraction was collected and stored in an amber colored bottle. The spectral purity was monitored using  $^1\text{H}$  NMR.

#### 6) Iso-octane

The commercial grade solvent was double-distilled and stored under fresh sodium wire.

#### 7) Water

The water used in all our experiments was deionized and double distilled.

#### 8) $\text{VOSO}_4 \cdot 2\text{H}_2\text{O}$

The AR grade sample was dried in a hot-air oven for 2 hr. at  $110^\circ\text{C}$ , and then desiccated before use.

### 4.3.2 Sample Preparations

1) *Vanadyl Stock Solution* : A 1 M stock solution of the vanadyl probe was prepared by dissolving appropriate amount of solid vanadyl sulfate in 0.001 N HCl. Since pH dependence studies<sup>13</sup> of aqueous  $\text{VO}^{2+}$  solution showed that the relative intensity of EPR spectrum started to decrease as the pH was

increased above 3.5, the pH of the vanadyl stock solution was kept below 3.5. To avoid oxidation of the vanadyl ion, the solution was deoxygenated by bubbling moist, prepurified  $N_2$  gas during, and at least 1 hr. before, the preparation of reverse micellar solution. The vanadyl sulfate solution was standardized spectrophotometrically at 750 nm with a molar extinction coefficient of 18.0 ( $\pm 0.2$ ).

2) *Surfactant Stock Solution* : A standard CTAB solution weighing 2.5 g CTAB in 50 ml [0.13M] of 2:1 v/v  $CHCl_3$ -n-octane mixture was prepared and used throughout this work. AOT stock solution weighing 1.661 g AOT in 25 ml of iso-octane and 5% lecithin solution in cyclohexane were also prepared. All these surfactant solutions were deoxygenated using  $N_2$  gas without any appreciable evaporation of solvent.

3) *Reverse micellar solution* : Into an appropriate volume of surfactant solution, the desired amount of vanadyl stock solution and doubly distilled water (if necessary) were injected using micropipette (Sigma Chemical Co., USA). Thorough shaking of this mixture ensured a clear homogeneous solution. Samples were prepared according to the desired 'R' value, which is given by  $R = [H_2O]/[SURFACTANT]$ .

The compositions of the reverse micelles for different R values are given in Tables 4.1 to 4.3.

#### 4.3.3 EPR Spectrometry

All our EPR measurements were made with a Varian E-109 spectrometer operating at X-band ( $\sim 9.5$  GHz) and 100 KHz magnetic field modulation. 'g' values were calibrated using DPPH as standard ( $g = 2.0036 \pm 0.0002$ ). To avoid microwave dielectric loss in the aqueous media, all the recordings were done

Table 4.1 : Composition of CTAB/ $\text{CHCl}_3$ -n-octane/water reverse micellesConcentration of (1) CTAB solution = 0.1372 M; (2)  $\text{VO}^{2+}$  solution  $\approx 1.0\text{M}$ 

R	Volume of CTAB. solution (ml)	Volume of $\text{VO}^{2+}$ solution ( $\mu\text{l}$ )	Volume of water ( $\mu\text{l}$ )	R	Volume of CTAB solution (ml)	Volume of $\text{VO}^{2+}$ solution ( $\mu\text{l}$ )	Volume of water ( $\mu\text{l}$ )
0.50	2	2.50	0	2.00	2	2.50	7.50
0.75	2	2.50	1.25	3.00	2	2.50	12.50
1.00	2	2.50	2.50	4.00	2	2.50	17.50
1.25	2	2.50	3.75	5.00	2	2.50	22.50
1.50	2	2.50	5.00	10.00	2	2.50	47.50
1.75	2	2.50	6.25				

Table 4.2 : Composition of AOT/iso-octane/water reverse micelles

Concentration of (1) AOT solution : 0.13 M; (2)  $\text{VO}^{2+}$  solution  $\approx 0.67\text{M}$ 

R	Volume of AOT solution (ml)	Volume of $\text{VO}^{2+}$ solution ( $\mu\text{l}$ )	Volume of water ( $\mu\text{l}$ )	R	Volume of AOT solution (ml)	Volume of $\text{VO}^{2+}$ solution ( $\mu\text{l}$ )	Volume of water ( $\mu\text{l}$ )
1.0	1.0	2.5	0.0	9.0	1.0	2.5	20.0
2.0	1.0	2.5	2.5	10.0	1.0	2.5	22.5
3.0	1.0	2.5	5.0	15.0	1.0	2.5	35.0
4.0	1.0	2.5	7.5	20.0	1.0	2.5	47.5
5.0	1.0	2.5	10.0	25.0	1.0	2.5	60.0
6.0	1.0	2.5	12.5	30.0	1.0	2.5	72.5
7.0	1.0	2.5	15.0	50.0	1.0	2.5	122.5
8.0	1.0	2.5	17.5				

**Table 4.3 : Composition of lecithin/cyclohexane/water reverse micelles**Concentration of (1) lecithin solution = 0.0523 M; (2)  $\text{VO}^{2+}$  solution  $\approx 1.0 \text{ M}$ 

R	Volume of lecithin solution (ml)	Volume of $\text{VO}^{2+}$ solution ( $\mu\text{l}$ )	Volume of water ( $\mu\text{l}$ )	R	Volume of lecithin solution (ml)	Volume of $\text{VO}^{2+}$ solution ( $\mu\text{l}$ )	Volume of water ( $\mu\text{l}$ )
2	2.0	1.88	1.88	7	2.0	1.88	11.28
3	2.0	1.88	3.76	8	2.0	1.88	13.16
4	2.0	1.88	5.64	9	2.0	1.88	15.04
5	2.0	1.88	7.52	10	2.0	1.88	18.80
6	2.0	1.88	9.40	12	2.0	1.88	20.68

using EPR quartz cell, except at low temperature. Microwave power, modulation amplitude and receiver gain were typically at 5 mW, 4.0 G, and  $10 \times 10^3$  respectively.

Rigid limit parameters, i.e.,  $A_{\parallel}$ ,  $A_{\perp}$ , and  $g_{\parallel}$ ,  $g_{\perp}$  were determined from frozen samples whose spectra were recorded at  $\sim 77 \text{ K}$ . These parallel and perpendicular resonance fields were determined with reasonable accuracy. To get an accurate measure of the field positions of parallel resonances, which were sometimes very weak, 'receiver gain' was increased to  $2 \times 10^4$  and power was kept at 20 mW. The effective concentration of  $\text{VO}^{2+}$  ion in reverse micelles was kept less than  $10^{-3} \text{ M}$  for all 'R' values. At this concentration and at room temperature, any exchange narrowing was ruled out.

#### 4.4 Results and Discussion

##### 4.4.1 EPR studies of $\text{VOSO}_4$ in reverse micelles containing cationic surfactants

The system chosen for this work is CTAB/ $\text{CHCl}_3$ -n-octane/ water. Samples were prepared according to the compositions given in Table 4.1. The 'R' was varied in steps of 0.25 in the range 0.5 to 2.0. Beyond this range,

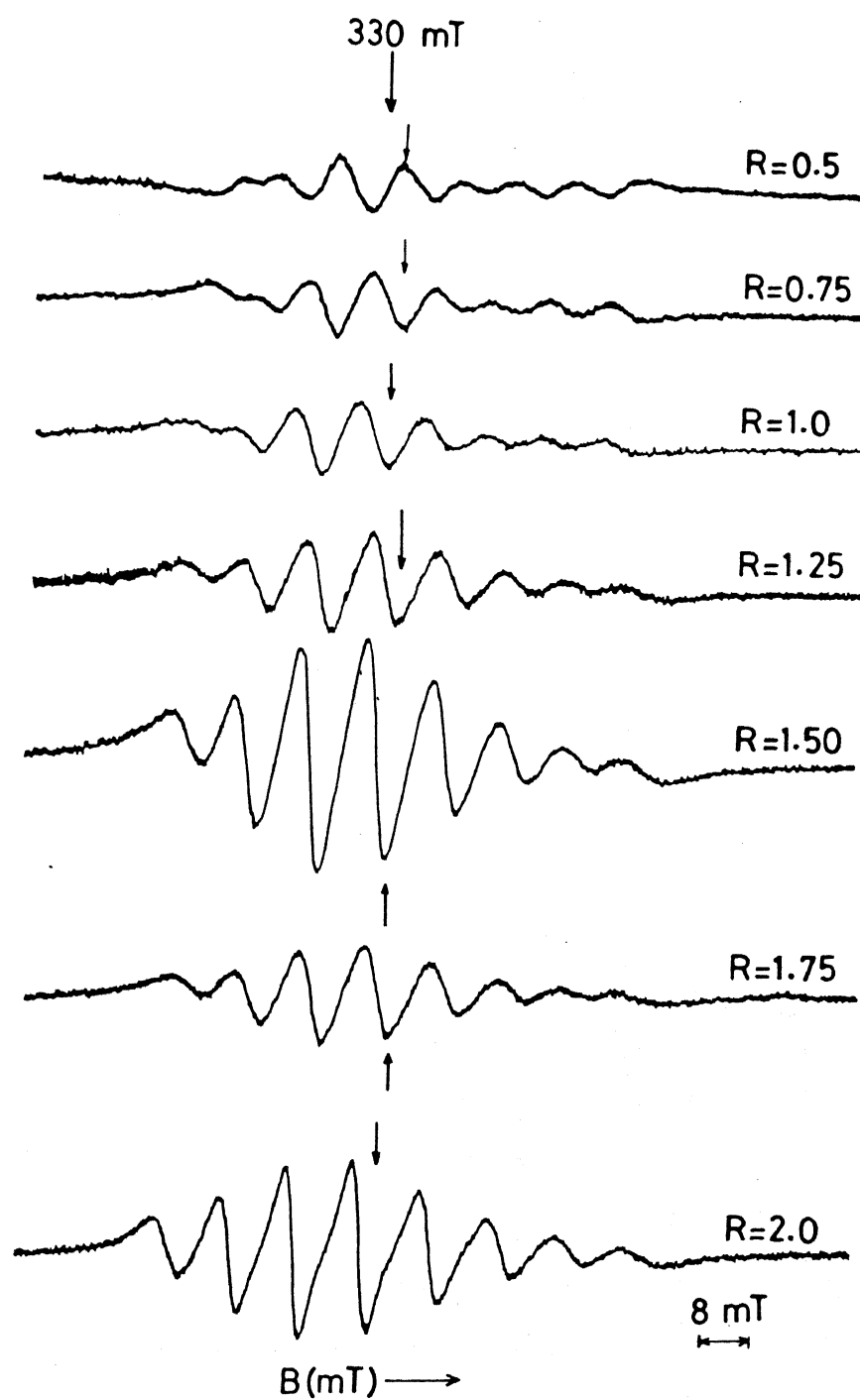
unit increment was maintained.

The X-band EPR spectra recorded at room temperature for these samples are shown in Figs. 4.4 and 4.5. The EPR spectral lineshapes of vanadyl ion undergo significant changes as the water content of the reverse micelles is varied.

The spectral responses presented in Figs. 4.4 and 4.5 may be, at this moment, qualitatively compared with those observed for numerous analogous systems reported in vanadyl EPR literature. However, our inspection revealed that our results were reminiscent of one particular system, namely, Nafion membrane with  $\text{VO}^{2+}$  incorporated in it.<sup>18</sup>

Under progressive addition of water, ionic mobility of  $\text{VO}^{2+}$  has been investigated using EPR.<sup>18</sup> Changes occurring in  $\text{VO}^{2+}$  EPR lineshapes by varying the water content in both CTAB reverse micelles (Figs. 4.4 and 4.5) and Nafion membranes (Ref. 18, Fig.3) follow a similar trend. In this context we recall that a very interesting model of 'spherical cluster-network' has been proposed for Nafion membranes using the  $\text{VO}^{2+}$  EPR study.<sup>18</sup> According to this model, the Nafion membranes form an approximately spherical, inverted micellar structure in which the absorbed water is contained inside the spherical domains and ion-exchange sites dip into the water phase at the interface; the domains are thought to be connected by channels with a diameter  $\approx 1$  nm.

Reverting to our spectra, Figs. 4.4 and 4.5, when  $R \leq 2$ , the  $m_I$  lines (especially those observed at low field) are seen to overlap each other. As 'R' is increased gradually, the overlapping becomes negligible and  $m_I$  lines are very well resolved when 'R' reaches 3. Routine linewidth calculation procedures<sup>19</sup> which could be utilized extensively for non overlapping spectral profiles such as those shown in Fig. 4.5, cannot be used for the abovementioned 'overlapped' shapes (Fig. 4.4) observed for very low R values. For these



EPR spectra of  $\text{VO}^{2+}$  ion in  $\text{CTAB}/\text{CHCl}_3$ -Octane/ $\text{H}_2\text{O}$  reverse micelles for  $R = 0.5$  to  $2.0$ .

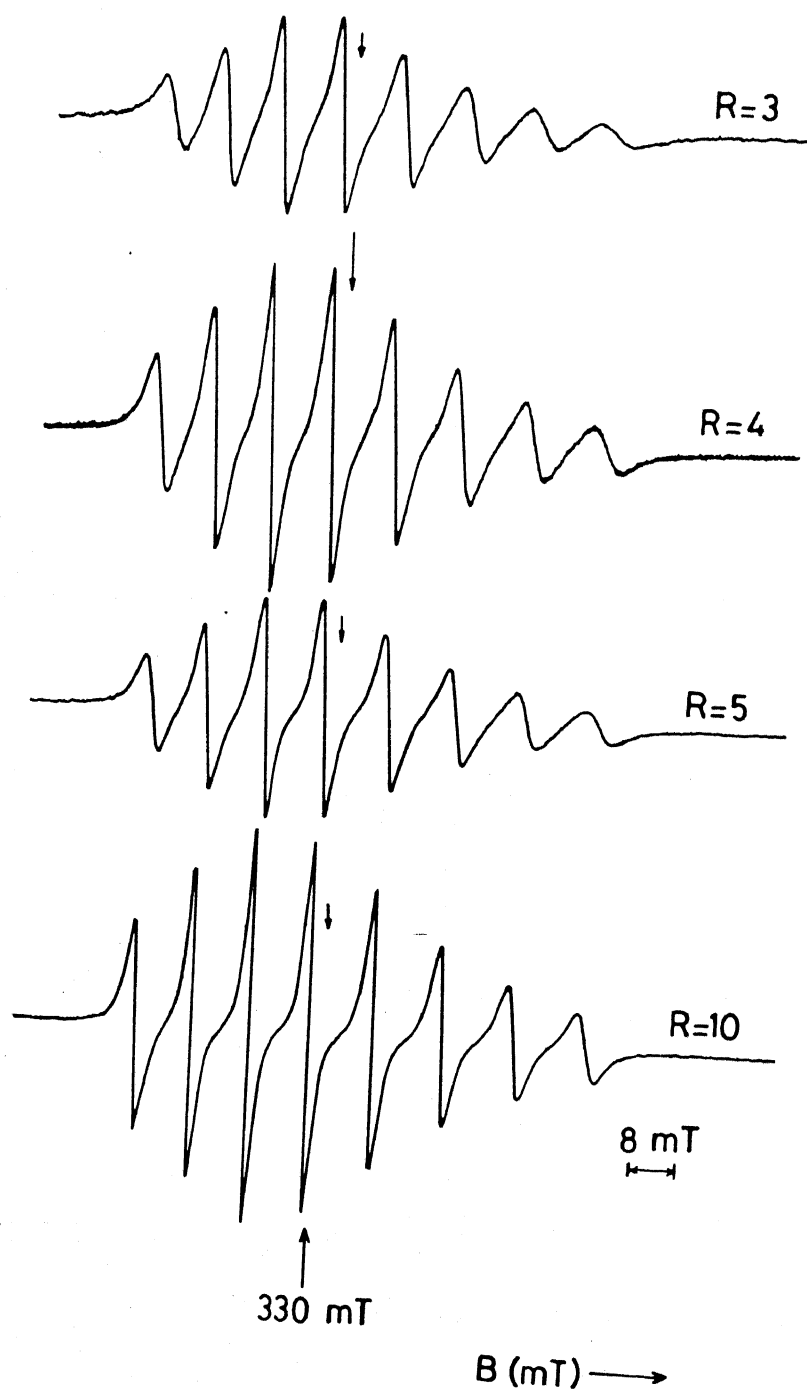


Fig. 4.5

EPR spectra of  $\text{VO}^{2+}$  ion in  $\text{CTAB}/\text{CHCl}_3$ -Octane/ $\text{H}_2\text{O}$  reverse micelles for  $R = 3.0$  to  $10.0$ .



latter cases, a special 'in-depth' calculation routine, developed by us in a recent work,<sup>12</sup> becomes necessary.

Before carrying out a detailed linewidth analysis of the modulated spectral responses which we have described above, it is essential, first of all, to find out the anisotropic EPR parameters. To do this, we have performed low temperature EPR experiments which involved frozen solution of CTAB reverse micelles. As shown in Fig. 4.2 all 'frozen limit' spectra will have sixteen lines due to the parallel and perpendicular features. The corresponding sixteen resonance field positions describing the features of the spectra of frozen samples may be given by:<sup>21</sup>

$$B_{m_I}(0^\circ) = \left\{ \bar{\nu}_o + A_{\parallel} m_I + \frac{A_{\perp}^2}{2\bar{\nu}_o} [I(I+1) - m_I^2] \right\} / g_{\parallel} \mu_B, \quad (4.3a)$$

$$B_{m_I}(90^\circ) = \left\{ \bar{\nu}_o + A_{\perp} m_I + \left( \frac{A_{\parallel}^2 + A_{\perp}^2}{4\bar{\nu}_o} \right) [I(I+1) - m_I^2] \right\} / g_{\perp} \mu_B. \quad (4.3b)$$

For two parallel (or perpendicular) lines which are symmetrically disposed about the 'center' of the multiplet, Eq. 4.3a can be used directly to obtain the EPR parameters from the experimental line positions. However, in the perpendicular region of the spectrum (Fig. 4.2) it is often difficult to accurately select symmetrically disposed pairs of lines because of the large *second-order* effects on the splittings and because of overlap with parallel lines. However, the high-field perpendicular lines  $m_I = 7/2, 5/2, 3/2, 1/2$  are all resolved and well suited for determining  $A_{\perp}$  and  $g_{\perp}$ . In order to do this, Eqs. 4.3a-b can be rearranged for any two pairs of lines  $m_{1,\parallel}$  and  $m_{2,\parallel}$ ,  $m_{1,\perp}$  and  $m_{2,\perp}$ , where  $m_{2,i} > m_{1,i}$  ( $i = \parallel$  or  $\perp$ ), to give the following expressions for  $A_{\parallel}$ ,  $A_{\perp}$ ,  $g_{\parallel}$  and  $g_{\perp}$ :

$$A_{\parallel} = \left[ g_{\parallel} \mu_B (B_{m_{2,\parallel}} - B_{m_{1,\parallel}}) + \frac{A_{\perp}^2}{2\bar{\nu}_0} (m_{1,\parallel}^2 - m_{2,\parallel}^2) \right] / (m_{2,\parallel} - m_{1,\parallel}) \quad (4.4)$$

$$g_{\parallel} = \left\{ 2\bar{\nu}_0 + A_{\parallel} (m_{2,\parallel} + m_{1,\parallel}) - \frac{A_{\perp}^2}{\bar{\nu}_0} \left[ I(I+1) - \frac{(m_{2,\parallel}^2 + m_{1,\parallel}^2)}{2} \right] \right\} / \mu_B (B_{m_{2,\parallel}} + B_{m_{1,\parallel}}) \quad (4.5)$$

$$A_{\perp} = \left[ g_{\perp} \mu_B (B_{m_{2,\perp}} - B_{m_{1,\perp}}) + \left( \frac{A_{\parallel}^2 + A_{\perp}^2}{4\bar{\nu}_0} \right) (m_{1,\perp}^2 - m_{2,\perp}^2) \right] / (m_{2,\perp} - m_{1,\perp}) \quad (4.6)$$

$$g_{\perp} = \left\{ 2\bar{\nu}_0 + A_{\perp} (m_{2,\perp} + m_{1,\perp}) - \left( \frac{A_{\parallel}^2 + A_{\perp}^2}{2\bar{\nu}_0} \right) \left[ I(I+1) - \frac{(m_{2,\perp}^2 + m_{1,\perp}^2)}{2} \right] \right\} / (B_{m_{2,\perp}} + B_{m_{1,\perp}}) \mu_B \quad (4.7)$$

where  $\bar{\nu}_0$  is the spectrometer frequency in  $\text{cm}^{-1}$ , and  $B_{m_{1,i}}$  and  $B_{m_{2,i}}$  ( $i = \parallel, \perp$ ) are the principal resonance fields of any two parallel or perpendicular lines.

Because of the interdependence of the parameters in Eqs. 4.4 - 4.7, an iterative procedure can be adopted. Initial values for this iterative procedure can be calculated from the *first-order* equations where  $a_{\parallel}$  and  $a_{\perp}$  are the hyperfine splittings in gauss, namely,

$$a_{\parallel} = (B_{m_{2,\parallel}} - B_{m_{1,\parallel}}) / (m_{2,\parallel} - m_{1,\parallel}) \quad (4.8)$$

$$g_{\parallel} = \bar{\nu}_0 / \mu_B (B_{m_{1,\perp}} - m_{1,\parallel} a_{\parallel}) \quad (4.9)$$

$$A_{\parallel} = a_{\parallel} g_{\parallel} \mu_B \quad (4.10)$$

$$a_{\perp} = (B_{m_{2,\perp}} - B_{m_{1,\perp}}) / (m_{2,\perp} - m_{1,\perp}) \quad (4.11)$$

$$g_{\perp} = \bar{\nu}_0 / \mu_B (B_{m_{1,\perp}} - m_{1,\perp} a_{\perp}) \quad (4.12)$$

$$A_{\perp} = a_{\perp} g_{\perp} \mu_B \quad (4.13)$$

where  $\mu_B$  is the Bohr magneton ( $4.6686 \times 10^{-5} \text{ cm}^{-1} \text{ G}^{-1}$ ) and  $A_{\parallel}$  and  $A_{\perp}$  are in  $\text{cm}^{-1}$ . A Fortran code has been developed and used by us for this iterative procedure. Our program takes  $B_{m_{1,\parallel}}$ ,  $B_{m_{2,\parallel}}$ ,  $B_{m_{1,\perp}}$ ,  $B_{m_{2,\perp}}$ ,  $m_{1,\parallel}$ ,  $m_{2,\parallel}$ ,  $m_{1,\perp}$ ,  $m_{2,\perp}$  and  $\bar{\nu}_0$  as inputs and calculates the initial values accordingly from Eqs. 4.8 - 4.13. The iterations are done using Eqs. 4.4 - 4.7. Two or three iterations are needed to achieve 'convergence'. Sample EPR parameters calculated from this method are given in Table 4.4

**Table 4.4** Anisotropic EPR spectroscopic parameters calculated from frozen samples

R	$g_{\parallel}$	$g_{\perp}$	$g_0$	$A_{\parallel}$ ( $10^{-4} \text{ cm}^{-1}$ )	$A_{\perp}$ ( $10^{-4} \text{ cm}^{-1}$ )	$A_0$ ( $10^{-4} \text{ cm}^{-1}$ )
0.50	1.929	1.982	1.964	204.37	77.50	119.79
0.75	1.937	1.983	1.968	205.00	80.00	121.67
1.00	1.938	1.987	1.971	205.00	84.00	124.33
1.25	1.937	1.997	1.977	205.63	80.00	121.88
1.50	1.939	1.986	1.970	204.38	76.25	118.96
1.75	1.938	1.984	1.969	203.75	82.50	122.92
2.00	1.935	1.989	1.971	206.00	80.00	122.00
3.00	1.933	1.990	1.971	205.00	86.00	125.67
4.00	1.934	1.994	1.974	204.00	90.00	128.00
5.00	1.937	1.984	1.968	205.63	82.50	123.54
10.00	1.937	1.984	1.968	206.00	84.00	124.00

### Linewidth analysis

Linewidth is an important parameter which gives us valuable information about the system. The peak-to-peak derivative width  $\Delta B_{m_I}$  of any  $m_I$

line in an EPR spectrum of  $\text{VO}^{2+}$  is given by

$$\Delta B_{m_I} = \Delta B_{-3/2} \left( \frac{h_{-3/2}}{h_{m_I}} \right)^{1/2}. \quad (4.14)$$

Lineshapes are assumed to be Lorentzian. Since  $m_{-3/2}$  is the sharpest line in the room-temperature X-band EPR spectrum of  $\text{VOSO}_4$  (aqueous solution), its width  $\Delta B_{-3/2}$ , and its amplitude or intensity  $h_{-3/2}$ , have been used in this relation to find out the width of any  $m_I$  line.

Moreover, the fact that the linewidths will be used directly in the calculation of parameters describing various physical properties, forced us to do an error analysis at this stage. The basic idea of finding the error associated with each variable in Eq. 4.14 separately, and then summing, has been used. Specifically,

$$\partial[\Delta B_{m_I}]^{\Delta B_{-3/2}} = \left( \frac{h_{-3/2}}{h_{m_I}} \right)^{1/2} \partial[\Delta B_{-3/2}] \quad (4.15)$$

$$\partial[\Delta B_{m_I}]^{h_{-3/2}} = \left[ \frac{\Delta B_{-3/2}}{2} \left( \frac{h_{-3/2}}{h_{m_I}} \right)^{-1/2} \left( \frac{1}{h_{m_I}} \right) \right] \partial h_{-1/2} \quad (4.16)$$

$$\partial[\Delta B_{m_I}]^{h_{m_I}} = \left[ \frac{\Delta B_{-3/2}}{2} \left( \frac{h_{-3/2}}{h_{m_I}} \right)^{-1/2} \left( -\frac{h_{-3/2}}{h_{m_I}^2} \right) \right] \partial h_{m_I} \quad (4.17)$$

where  $\partial[\Delta B_{m_I}]^{\Delta B_{-3/2}}$ ,  $\partial[\Delta B_{m_I}]^{h_{-3/2}}$ , and  $\partial[\Delta B_{m_I}]^{h_{m_I}}$  are the maximum possible errors due to the variables  $\Delta B_{-3/2}$ ,  $h_{-3/2}$ , and  $h_{m_I}$ , respectively. As a test case, we can use the following parameters

$$\left. \begin{aligned} h_{-3/2} &= 9.35 \text{ cm}, h_{-1/2} = 9.05 \text{ cm}, \Delta B_{-3/2} = 16.0 \text{ G} \\ \partial h_{-3/2} &= \pm 0.1 \text{ cm}, \partial h_{-1/2} = \pm 0.1 \text{ cm}, \partial(\Delta B_{-3/2}) = \pm 0.25 \text{ G} \end{aligned} \right\} \quad (4.18)$$

The error in determining or calculating  $\delta(\Delta B_{-1/2})$  due to various uncertainties in measuring variables is found out from Eqs. 4.15 to 4.18, i.e.,

$$\delta[\Delta B_{-1/2}]^{\Delta B_{-3/2}} = 0.254 \text{ G}; \delta[\Delta B_{-1/2}]^{h_{-3/2}} = 0.0870 \text{ G}; \delta[\Delta B_{-1/2}]^{h_{-1/2}} = 0.0899 \text{ G}$$

Then,

$$\delta[\Delta B_{-1/2}]^{\text{Total}} = |0.254| + |0.0870| + |-0.0899| = 0.43 \text{ G} \approx 2.5\%$$

Our error analysis, and previous experience elsewhere,<sup>19</sup> clearly demonstrate that this 'indirect method' can be satisfactorily used in preference to directly measuring linewidths from the EPR spectra. The values calculated from our method (indirect) are shown in Table 4.5.

**Table 4.5 :** Linewidths of the component hyperfine lines of  $\text{VO}^{2+}$  ion in CTAB reverse micelles

R	Experimental Linewidth, $\Delta B_{m_I}$ (Gauss)							
	-7/2	-5/2	-3/2	-1/2	1/2	3/2	5/2	7/2
0.50			50.000	47.891	76.765	101.551	86.103	90.870
0.75			46.000	46.000	73.636	111.551	98.181	88.808
1.00			46.000	46.000	67.823	122.940	122.940	100.380
1.25			40.000	40.000	52.915	83.666	118.322	103.275
1.50	71.402	45.043	34.000	34.300	43.936	66.478	111.476	111.476
1.75	68.133	39.686	30.000	30.632	39.686	68.317	93.915	105.000
2.00	45.473	31.967	26.000	26.000	32.345	44.691	63.202	82.219
3.00	36.073	26.387	22.000	22.170	27.110	44.222	46.805	63.800
4.00	24.660	18.613	16.000	16.334	19.524	25.046	23.246	42.807
5.00	24.162	18.558	16.000	16.263	19.190	24.617	32.616	42.107
10.00	12.728	10.115	9.000	9.210	10.694	13.425	16.926	22.245

The sensitivity of the linewidths of  $\text{VO}^{2+}$  to changes in the water pool size is shown in Fig. 4.6 in which the linewidths are plotted against 'R'. The general trend observed for all the  $m_I$  lines reveals an interesting three-step behavior. When 'R' changes from 10 to 4, there is a slight increase; in the range of  $R = 4$  to  $R = 2$ , this increase is significant, and for R values between 2.0 and 0.5 it is substantial. Again, the width of the broadest line,  $m_I = 7/2$  increases the most with decreasing 'R', while the width of the narrowest, line  $m_I = -3/2$  increases the least. For example, decreasing the water content, R, from 10.0 to 1.75 increases the width of the  $m_I = 7/2$  line by nearly 80.0 G compared to only 21.0 G for the  $m_I = -3/2$  line.

The widths of different  $m_I$  lines calculated for a particular size of the 'water pool' (i.e., a particular R value) are plotted against  $m_I$  values and shown in Fig. 4.7. The least-squares method has been used to fit these experimental linewidth points in Fig. 4.7 to Eq. 4.2, and the best-fitting curves are also shown in Fig. 4.7. The least-squares parameters ( $\alpha$ ,  $\beta$ ,  $\gamma$  and  $\delta$ ) used to get the best-fit are listed in Table 4.6.

Table 4.6 Least-squares parameters used in Eq. 4.2

R	$(\alpha' + \alpha'')$ (G)	$\beta$ (G)	$\gamma$ (G)	$\delta$ (G)
1.5	41.51	15.76	4.43	-0.777
1.75	36.48	13.99	4.43	-0.691
2.00	28.82	6.81	2.89	-0.122
3.00	24.10	4.62	2.10	-0.057
4.00	16.62	2.05	1.42	-0.035
5.00	17.44	3.00	1.29	-0.035
10.00	9.78	1.44	0.62	-0.007

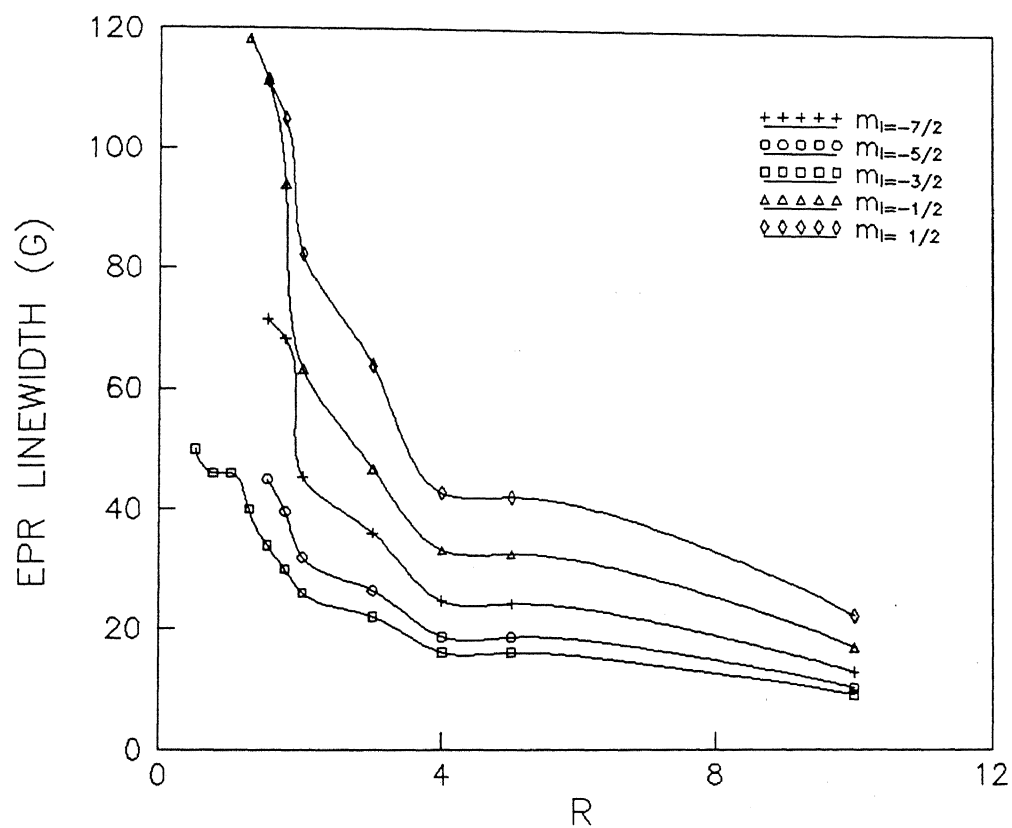


Fig. 4.6 Dependence of the  $m_I$ -dependent  $\text{VO}^{2+}$  EPR linewidths on the water pool size ( $\propto R$ ) of CTAB reverse micelles.

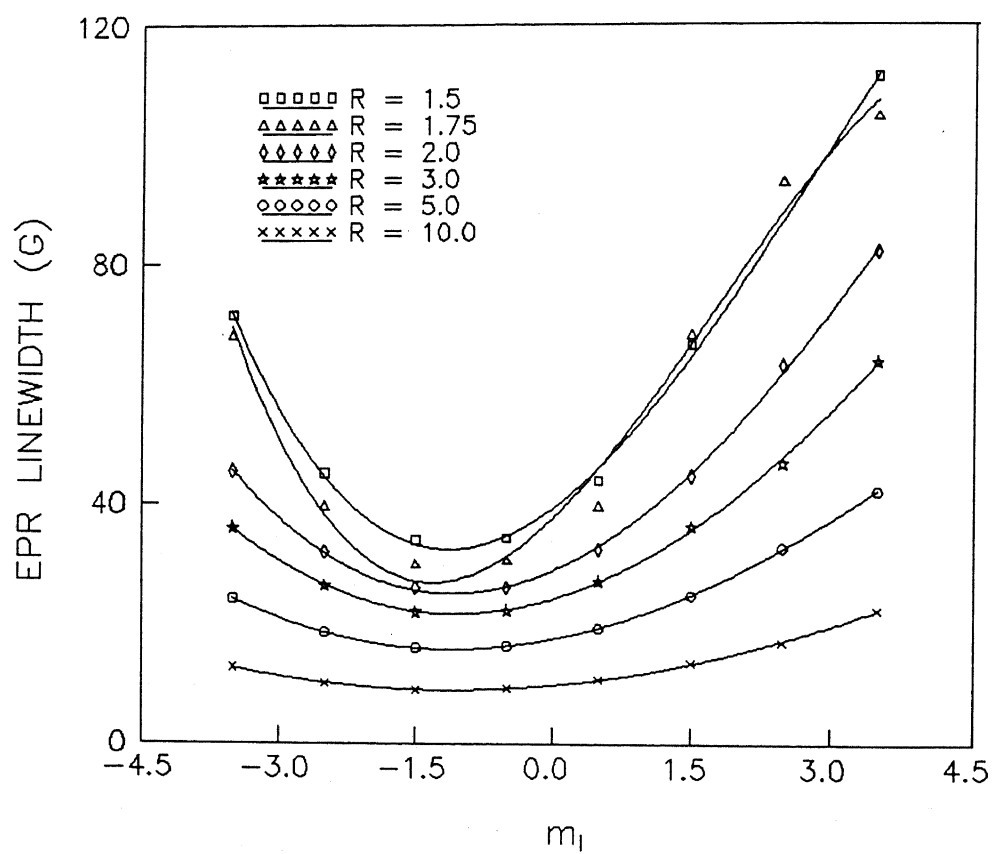


Fig. 4.7 Dependence of the  $\text{VO}^{2+}$  EPR linewidths on  $m_I$  for various 'R' values.



### Rotational correlation time measurement

One of the more direct and fruitful, although less exploited, uses of linewidth variations is the measurement of rotational correlation times,  $\tau$ , which could provide an insight into liquid-state structure. Studying rapid rotational motions of  $\text{VO}^{2+}$  ('fast' motion) characterized by a single  $\tau$  is relatively simpler. All one has to do is solve the polynomial equation (Eq. 4.2), involving the least-squares parameters  $\alpha$ ,  $\beta$ ,  $\gamma$  and  $\delta$ . Given the principal values of  $g$  and  $A$ , from the frozen solution spectrum, we can calculate  $\tau$  from  $\beta$  or  $\gamma$  by the use of lengthy equations.<sup>15</sup> In most cases the coefficient  $\gamma$  is used, because it depends only on the hyperfine tensor components, which are more accurately known than those of  $g$  tensor :

$$\gamma = \frac{2 \hbar \tau}{\sqrt{3} g_o \mu_B} \left[ \frac{b^2}{8} - (7 + 5u + 12uf) \frac{\Delta \gamma b B_o a}{30 \omega_o} + (5fa/\omega_o - 1) \frac{b^2 u}{40} + \frac{C^2}{15} (10 - 2u) \right] \quad (4.19)$$

$$\text{where } B_o = \hbar \omega_o / g_o \mu_B, \quad u = \left[ 1 - \omega_o^2 \tau^2 \right]^{-1}, \quad f = \omega_o^2 \tau^2 u,$$

$$b = (2/3) \left[ (A_z - \frac{1}{2} (A_x + A_y)) \right], \quad c = (A_x - A_y)/4,$$

$$\Delta g = g_z - \frac{(g_x + g_y)}{2}, \quad \Delta \gamma = \mu_B \Delta g / \hbar, \quad a = \frac{A_x + A_y + A_z}{3}$$

$A_x$ ,  $A_y$ ,  $A_z$  and  $\omega_o$  are expressed in  $\text{rad s}^{-1}$  using the least-squares parameters and anisotropic parameters (given in Table 4.6 and Table 4.4, respectively). The correlation times are then calculated for all the samples of reverse micellar solution having different water contents. Some of these values are given in Table 4.7.

Table 4.7 Rotational correlation times of  $\text{VO}^{2+}$  in CTAB reverse micelles

R	$\text{VO}^{2+}$ in water pools $\tau \times 10^{11} \text{ (s rad}^{-1}\text{)}$	Water in water pools <sup>23</sup> $\tau \text{ (water) (s rad}^{-1}\text{)}$ (by NMR techniques)
1.50	25.87	
1.75	25.87	
2.00	16.88	1.561
3.00	12.10	1.35
4.00	8.299	0.813
5.00	7.541	0.548
10.00	3.647	0.424

#### Viscosity measurements

The microviscosity of the medium felt by spin probe is a routinely studied property in reverse micelles having nitroxide spin probes.<sup>22</sup> We have also done this measurement for  $\text{VO}^{2+}$  probe in CTAB micelles.

For a sphere of radius  $r$ , rotating in a fluid medium of viscosity  $\eta$ ,  $\tau$  is given by the Debye relationship,

$$\eta = \frac{3kT\tau}{4\pi r^3} \quad (4.20)$$

In our calculations 'r' is the hydrodynamic radius of  $\text{VO}(\text{H}_2\text{O})_5^{2+}$  ion which is equal to  $3.4 \text{ \AA}$ .<sup>19</sup> The microviscosities are listed in Table 4.8.

The values tabulated in Tables 4.7 and 4.8 are individually plotted against 'R'. These are also shown in Figs. 4.8 and 4.9, respectively.

We shall now discuss the implication of the results presented so far.  $\text{VO}(\text{SO}_4)_2$  is insoluble in dry organic solvents such as  $\text{CHCl}_3$ , octane etc., even

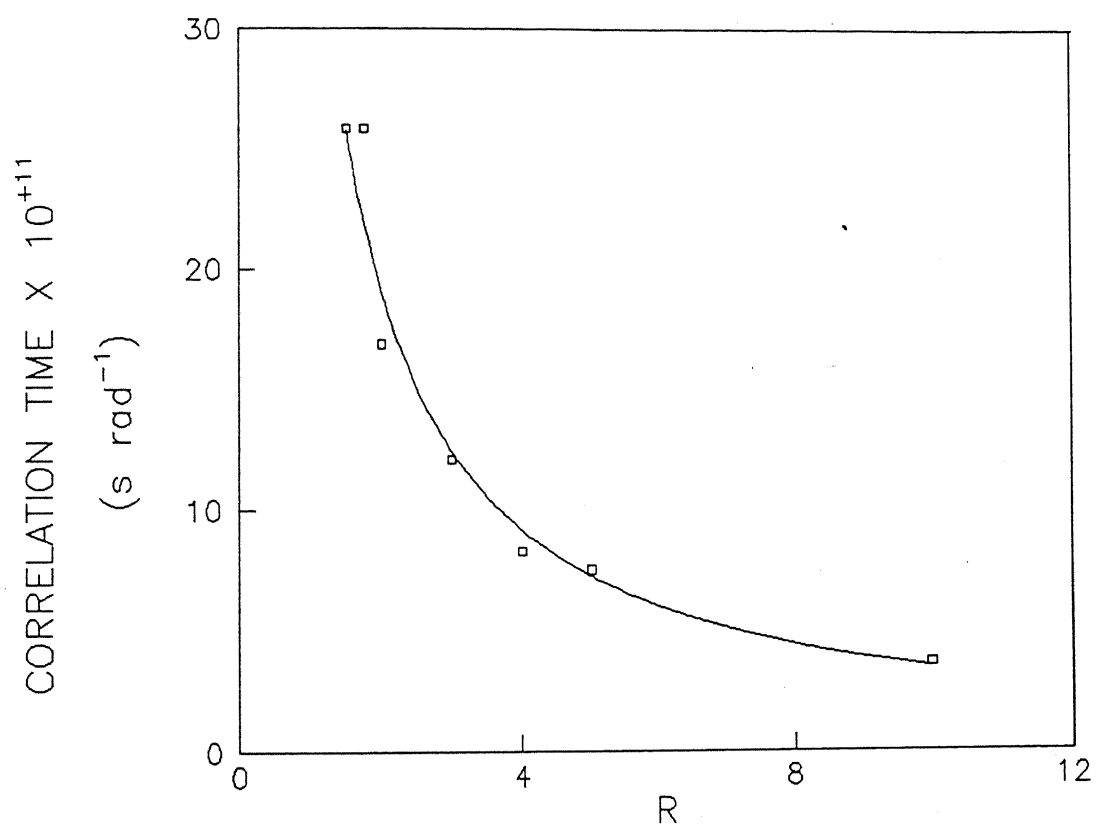


Fig. 4.8 Dependence of  $\text{VO}^{2+}$  rotational correlation times on ' $R$ ' in CTAB reverse micelles.

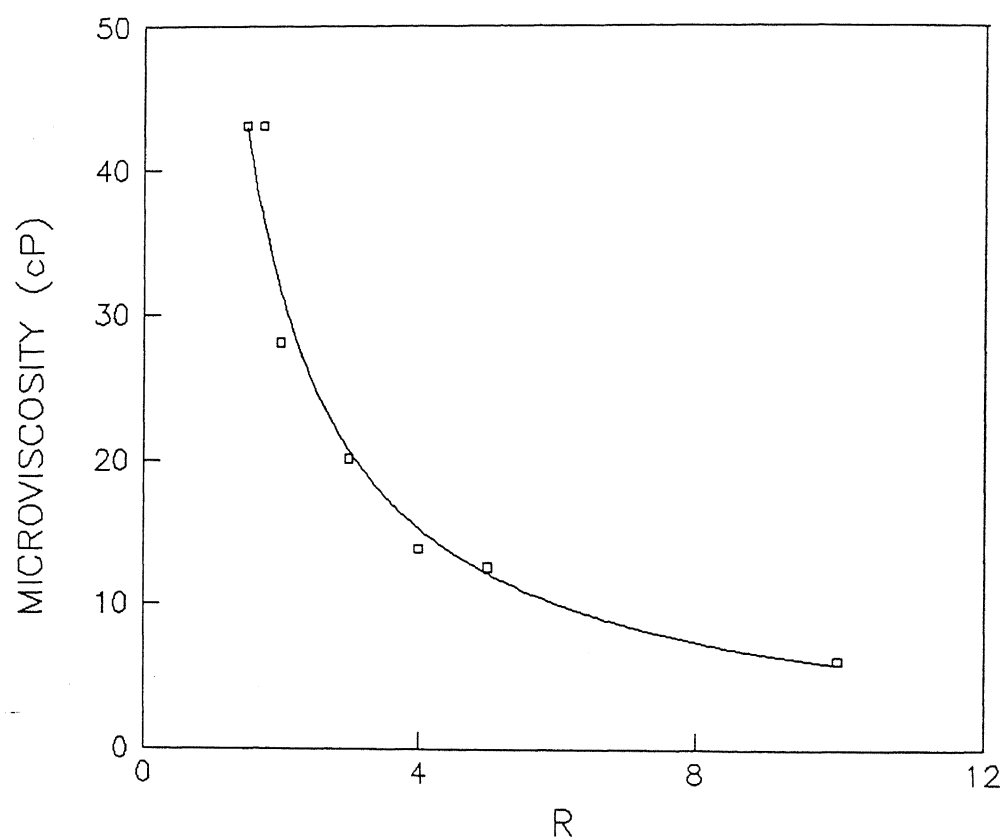


Fig. 4.9 Variation of microviscosity of the water pools of CTAB reverse micelles with size of the pools ( $\propto R$ ).

**Table 4.8 Microviscosities of water pools of various sizes in CTAB reverse micelles, probed by  $\text{VO}^{2+}$**

R	$\text{VO}^{2+}$ in water pools $\eta$ (cP)	Water in water pools <sup>23</sup> $\eta$ (water)(cP)
1.50	43.10	
1.75	43.10	
2.00	28.13	46.77
3.00	20.13	40.35
4.00	13.83	24.36
5.00	12.57	16.44
10.00	6.077	12.72

in the presence of surfactant CTAB. Thus it is safe to conclude that  $\text{VOSO}_4$  is located only in the water pools of CTAB/ $\text{CHCl}_3$ -octane/ $\text{H}_2\text{O}$  reverse micelles. Based on this physical observation, it is expected that whatever changes that take place in the properties of water in the 'water pool' of CTAB reverse micelles due to the micellar structure will be reflected through the dynamics of  $\text{VO}^{2+}$  ion. Recent results obtained from the NMR study carried out in this laboratory on the CTAB reverse micelles<sup>23</sup> could be mentioned here in this context. The rotational correlation times of water calculated from  $^1\text{H}$  NMR  $T_1$  (relaxation time) measurement are included in the last column of Table 4.7. These values indicate that the mobility of water molecules engaged in binding to the polar head groups is significantly reduced at low water content, and that as the water content increases, mobility of the water molecules also increases.

Present EPR studies show that the correlation times of  $\text{VO}^{2+}$  in CTAB

reverse micelles also follow the same trend, i.e., restricted mobility of  $\text{VO}^{2+}$  ion at low R, and freer motion at higher 'R'. As already mentioned in section 4.2.1, at low water content ( $R \leq 3$ ) the 'ordinary' (aquated)  $\text{VO}^{2+}$  ion undergoes incipient slow tumbling motion (intermediate motion), while at higher water content ( $R > 3$ ) it executes 'fast' tumbling motion. Since the  $\text{VO}(\text{H}_2\text{O})_5^{2+}$  ion is bulkier compared to the water molecule, the rotational correlation time of  $\text{VO}^{2+}$  ion is always greater (motion is slower) than that of water at a particular R.

Microviscosity of the water in CTAB reverse micelles as probed by  $\text{VO}^{2+}$  ion and that estimated directly by  $^1\text{H}$  NMR<sup>23</sup> follow the same dependence of water content. The discrepancy in the actual values obtained for a particular 'R' may be due to the different time scales inherent in these two magnetic resonance techniques. The water present at lower water content is more viscous compared to bulk water (normal water).<sup>28</sup>

A clearer picture regarding the dynamics and location of the  $\text{VO}^{2+}$  spin probe using our EPR results of microviscosity and correlation time measurements may be sought as follows. It is normally expected that  $\text{VO}^{2+}$  ion in CTAB reverse micelles should have more mobility ( $10^{-10} \text{ s} > \tau > 10^{-11} \text{ s}$ ) due to electrostatic repulsion between the polar head group  $-\text{N}^+(\text{CH}_3)_3$  of CTAB and  $\text{VO}^{2+}$  ion, unlike the water molecules which are in a 'bound' state. But, contrary to this expectation, the mobility of the  $\text{VO}^{2+}$  ion slows down when the water content of the reverse micelles is minimal ('R' < 3). This is because the nature of the water is 'more viscous' and the size of the 'water pool' is smaller or 'tighter'. Under this condition, electrostatic repulsion is not favored and hence the mobility is decreased by the 'viscous water pool'.

Rationalizing the linewidth variations, we know that the linewidth of the  $\text{VO}^{2+}$  ion largely originates from motional modulation of anisotropic g and nuclear hyperfine tensors. For a Lorentzian line, the total linewidth

parameter  $T_2$  ( s rad<sup>-1</sup>), is related to derivative peak-to-peak separation,  $\Delta B$ , by the equation,

$$\Delta B = (2/\sqrt{3}) (\hbar/T_2 g_o \mu_B) . \quad (4.21)$$

Both spin-lattice relaxation,  $T_1$ , and transverse relaxation,  $T_2$ , contribute significantly to the total linewidth  $1/T_2$ . The  $T_1$  contributions to the linewidth of each of the hyperfine lines of  $\text{VO}(\text{H}_2\text{O})_5^{2+}$ , have been found out, in the past, using dynamic nuclear polarization spectroscopy.<sup>24</sup> We have not attempted any such experiments in this work; rather, the linewidth variations are analyzed using motional narrowing theory only.

When the 'water pool' size is diminished, the water will be unusually viscous. Because of this, the motional averaging of  $g$  and  $A$  tensors is incomplete and this is reflected in the linewidth. As the 'water pool' size increases, the microviscosity of the water would be expected to decrease. Due to this, the motional averaging of  $g$  and  $A$  tensors will be complete and the linewidths narrow down.

A notable point in our linewidth analysis of  $\text{VO}^{2+}$  in CTAB reverse micelles is that the widths of different  $m_I$  lines at 'R' = 10 have reached a value which is smaller than that found for the  $\text{VOSO}_4$  in aqueous solutions. Normally,  $\text{SO}_4^{2-}$  ion has been found to broaden the EPR lines of vanadyl<sup>24</sup> and manganese<sup>25</sup> ion in ordinary aqueous solutions. This contribution is generally small in dilute aqueous solution. Our linewidth analysis indicates, however, that even this small contribution is ruled out in the CTAB reverse micelles. This may be because of the interaction of polar head groups with sulfate ions present in the water pools, whereby separation between  $\text{VO}^{2+}$  ion and sulfate ion is ensured in the water pools of large size (  $R \approx 10$  ).

#### 4.4.2 EPR Studies of $\text{VO}^{2+}$ in Reverse Micelles Containing Anionic Surfactants

The system chosen for this work is AOT/iso-octane/ $\text{H}_2\text{O}$ , at eight R values. Spin probes were prepared as per the composition given in Table 4.2. Water content in the reverse micelles was varied from  $R = 1$  to  $R = 50$ . Recently reported EPR study of  $\text{VO}^{2+}$  in AOT reverse micelles<sup>11a</sup> did not explore the reverse micelles having low water content. In this work, we have done a systematic investigation starting from  $R = 1$ . Before analyzing the EPR spectra, some data may be preferable regarding (i) the size of the water pool, (ii) molar ratio of water to probe, i.e., number of probe molecules present in a micelle and (iii) number of surfactant molecules per cationic probe present in micelle. The necessary information has been collected from previous studies;<sup>29</sup> this, as well as the concentration of various components used in forming reverse micelles, are listed in Table 4.9. For estimating the number of probe molecules present in a micelle, we have used the aggregation number reported for the same system.<sup>11a</sup>

The X-band EPR spectra recorded at room temperature for the AOT reverse micelle samples containing  $\text{VO}^{2+}$  are shown in Figs. 4.10 - 4.12. Spectrometer settings were typically the same as already mentioned in section 4.3.3. Here, again, our EPR lineshapes show a strong dependence on water content. The spectrum obtained for  $R = 1$  is similar to that of  $\text{VO}(\text{acac})_2$  in toluene at  $-99^\circ\text{C}$ .<sup>16</sup> In this spectrum ( $R = 1$  in Fig. 4.10) the parallel and perpendicular features are clearly evident. When the water content is slowly increased (up to  $R = 3$ ), the  $\parallel$  and  $\perp$  regions start merging. This is evident from the peaks, marked with arrows( $\downarrow$ ), in the spectra. When  $R = 4$ , (Fig. 4.10) the merging process is complete. The spectral features for  $R = 5$  to  $R = 10$  (Fig. 4.11) are not symmetrical, and overlapping of lines is observed in the high field region. Symmetrical and well resolved hyperfine lines are, however,



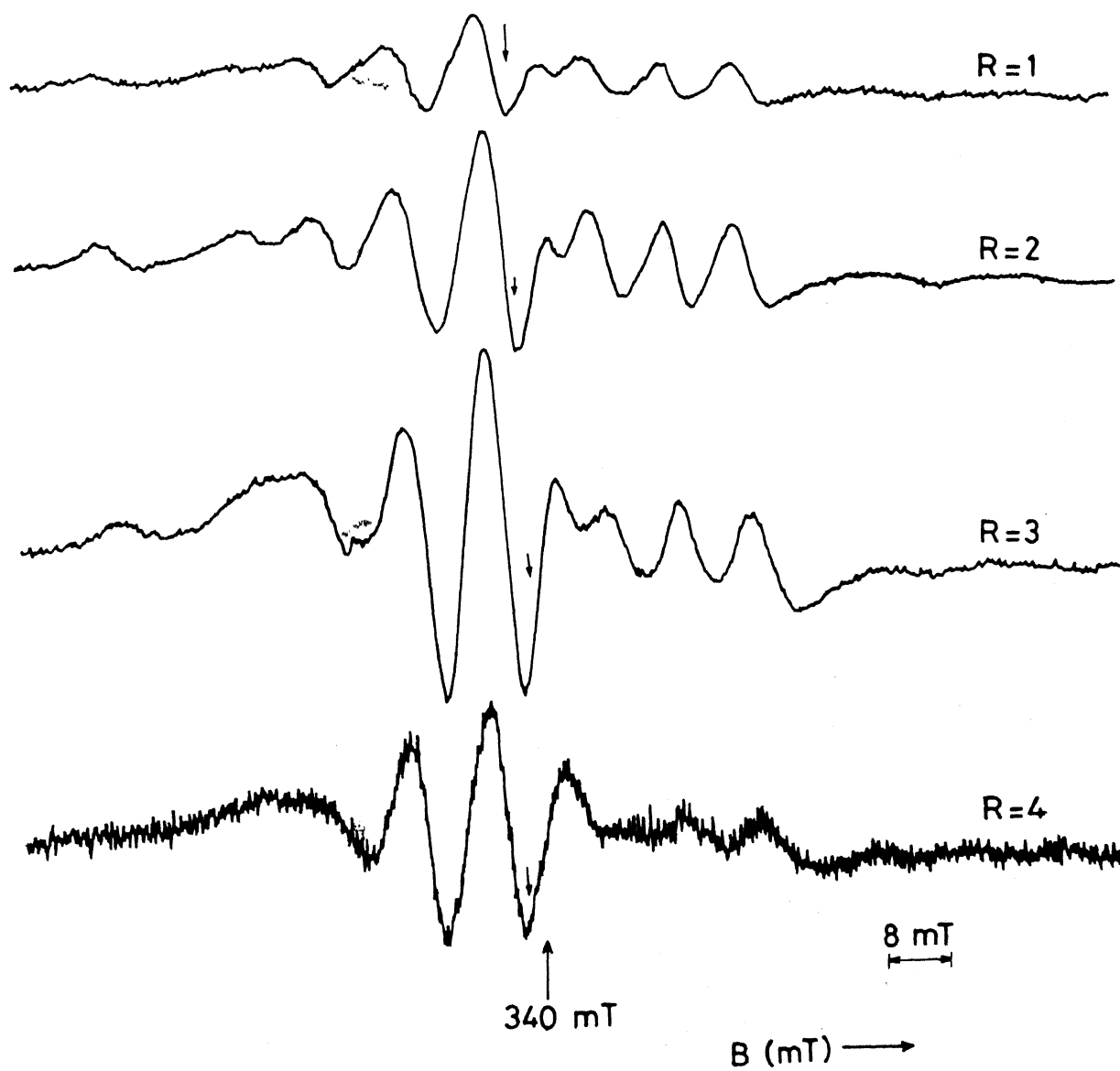


Fig. 4.10 X-band EPR spectra of  $\text{VO}^{2+}$  in AOT/isooctane/ $\text{H}_2\text{O}$  reverse micelles for  $R = 1$  to 4.

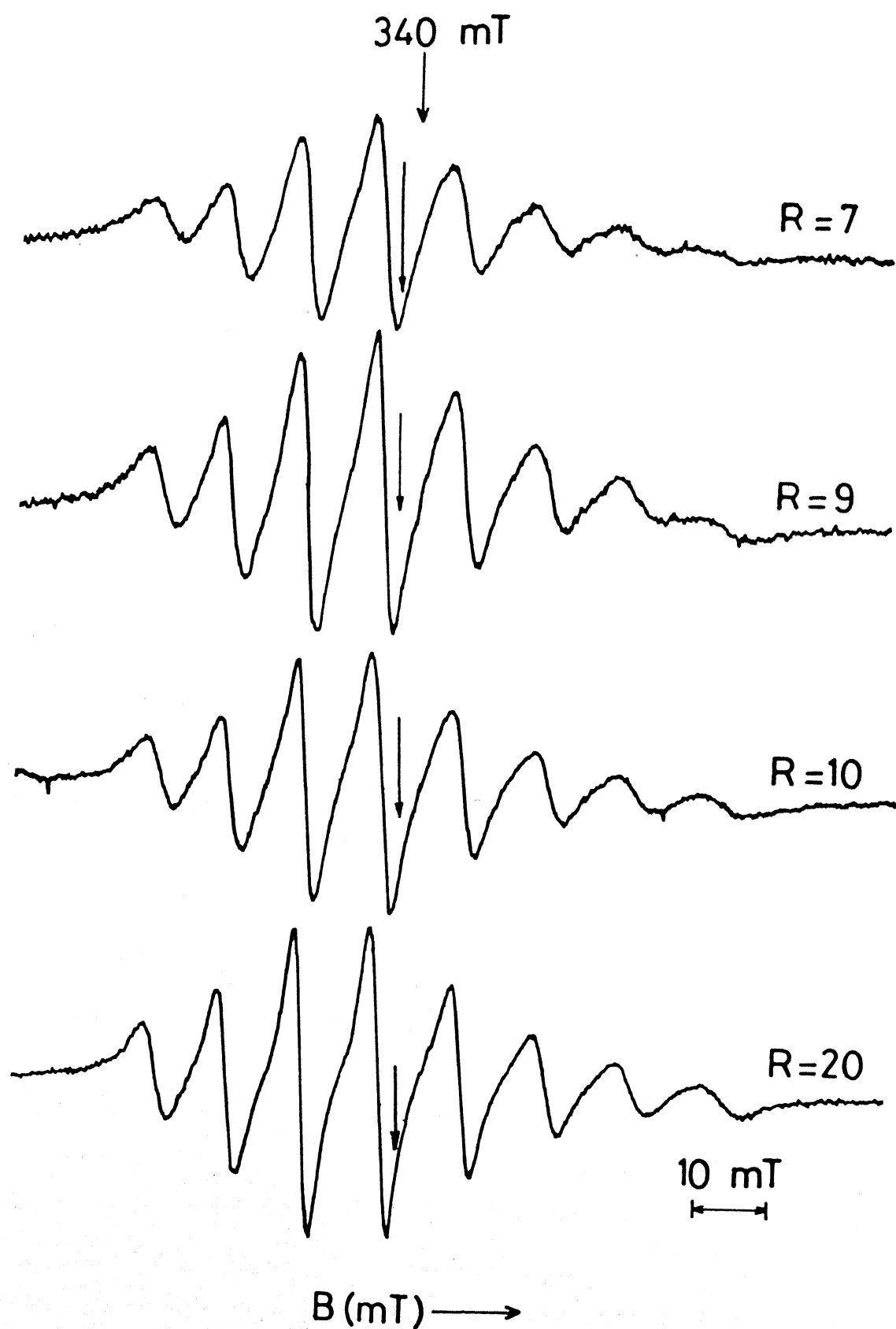


Fig. 4.11 X-band EPR spectra of  $\text{VO}^{2+}$  in AOT/isooctane/ $\text{H}_2\text{O}$  reverse micelles for  $R = 7$  to 20.

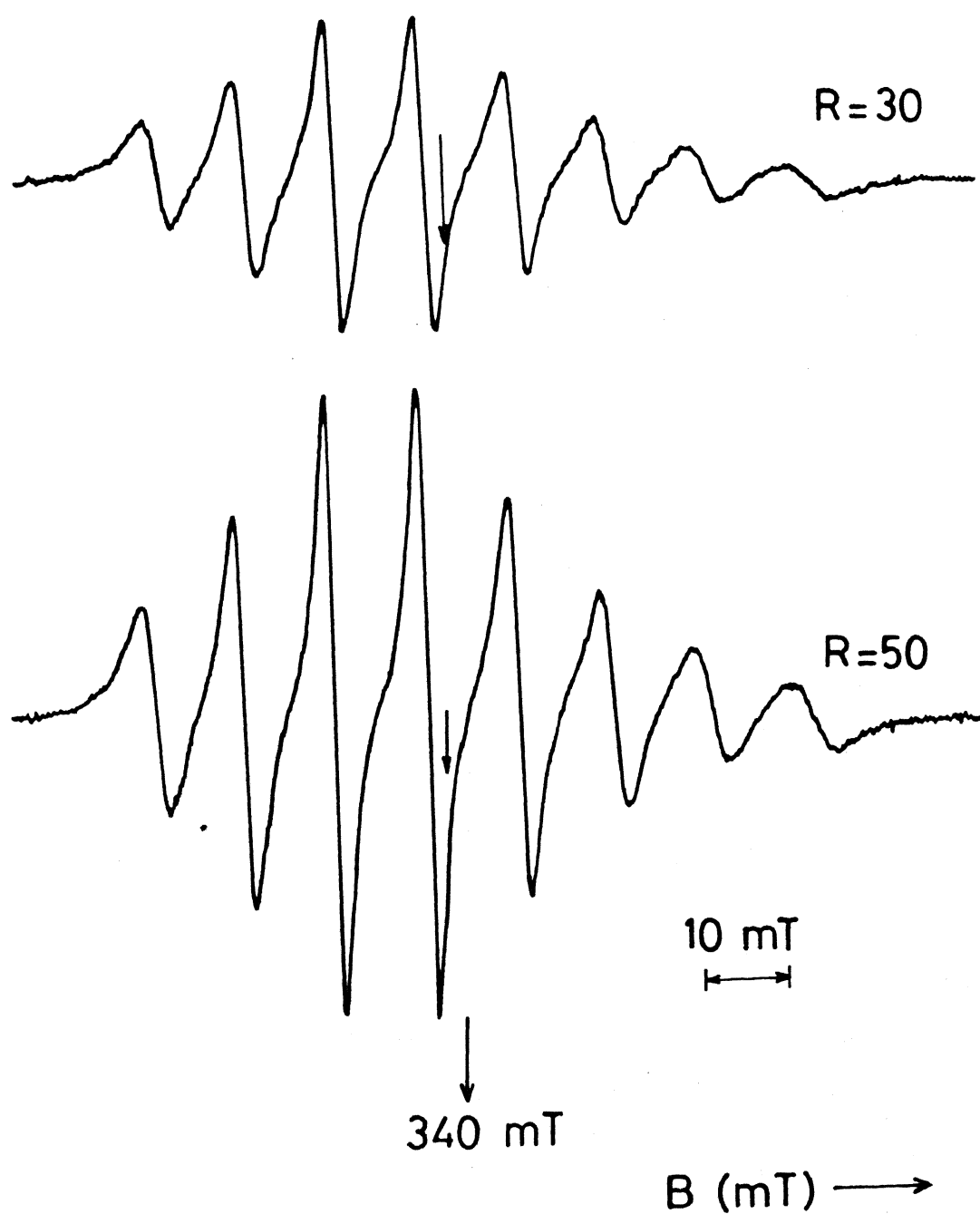


Fig. 4.12 X-band EPR spectra of  $\text{VO}^{2+}$  in AOT/isooctane/ $\text{H}_2\text{O}$  reverse micelles for  $R = 30$  and  $50$ .

Table 4.9 Quantitative data on AOT/H<sub>2</sub>O(VO<sup>2+</sup>) reverse micelles at Various 'R'

[H <sub>2</sub> O/ [AOT]	radius of water pool r (Å) <sup>29</sup>	[H <sub>2</sub> O]/ [probe]	Probe/ micelle *	[H <sub>2</sub> O/ [AOT]	radius of water pool r (Å) <sup>29</sup>	[H <sub>2</sub> O]/ [probe]	Probe/ micelle *
1.0	1.5	82.92	0.033	9.0	13.5	746.28	
2.0	3.0	165.84		10.0	15.0	829.20	0.568
3.0	1.5	248.76		15.0	22.5	1243.80	
4.0	6.0	331.68		20.0	30.0	1658.40	2.278
5.0	7.5	441.60	0.142	25.0	37.5	2073.00	
6.0	9.0	447.52		30.0	45.0	2787.60	5.137
7.0	10.5	580.944		50.0	75.0	4196.60	
8.0	12.0	663.36					

\* The number of AOT molecules per cation probe is 83, fixed for all samples

obtained in the range  $R = 15$  to  $R = 50$  (Fig. 4.12). Another striking, rather unusual, feature in all the spectra shown in Figs. 4.11 and 4.12 is that the sharpest line is due to  $m_I = -1/2$ . Generally, the width of the  $m_I = -3/2$  line will be smaller compared to other lines in the EPR spectrum of VOSO<sub>4</sub> in aqueous solution. Indeed, this trend has been observed for VO<sup>2+</sup> ion in our CTAB reverse micelles ( $m_I = -3/2$  is the sharpest line).

#### Linewidth analysis

The generally used expression to calculate the widths of different  $m_I$  lines of VO<sup>2+</sup> ion has to be modified as shown in Eq. 4.22 because of the abovementioned difference in the pattern of lines observed for VO<sup>2+</sup> in AOT reverse micelles.

$$\Delta B_{m_I} = \Delta B_{-1/2} \left( \frac{h_{-1/2}}{h_{m_I}} \right)^{1/2} \quad (4.22)$$

As has been already mentioned, a detailed lineshape analysis<sup>12</sup> is required to interpret the spectral lineshape features recorded for  $R = 1$  to  $R = 4$  cases. Spectra exhibiting highly resolved hyperfine lines are only considered in the present linewidth analysis. The widths calculated for all the  $m_I$  lines of various 'R' values are tabulated in Table 4.10.

Table 4.10 : Component hyperfine Linewidths of  $\text{VO}^{2+}$  in AOT/iso-octane/ $\text{H}_2\text{O}$  reverse micelles

R	Experimental Linewidth, $\Delta B_{m_I}$ (Gauss)							
	-7/2	-5/2	-3/2	-1/2	1/2	3/2	5/2	7/2
5.0	96.63	57.29	36.47	35.0	53.46	108.03	122.50	187.12
6.0	75.99	49.16	33.70	32.0	46.53	79.37	104.60	161.20
7.0	72.23	46.81	33.44	31.0	44.23	67.56	88.46	125.10
8.0	54.14	37.12	27.82	27.0	36.05	52.49	75.77	104.99
9.0	54.16	37.84	28.51	27.0	35.96	51.14	72.32	100.12
10.0	52.69	37.78	27.81	27.0	36.04	51.98	73.03	95.98
20.0	47.79	34.47	26.49	26.25	33.56	46.44	63.92	82.79
30.0	44.05	32.35	25.26	25.0	31.64	43.82	62.29	78.78
50.0	32.31	23.7	18.94	18.75	23.45	31.52	44.16	56.83

The linewidths of all hyperfine lines thus obtained are fitted to Eq. 4.2 using a least squares method. These 'best-fit' curves are shown passing through the experimental points in Fig. 4.13 for various 'R' values. The least squares parameters ( $\alpha + \alpha''$ ),  $\beta$ ,  $\gamma$  and  $\delta$  used to achieve the best-fit are shown in Table 4.11.

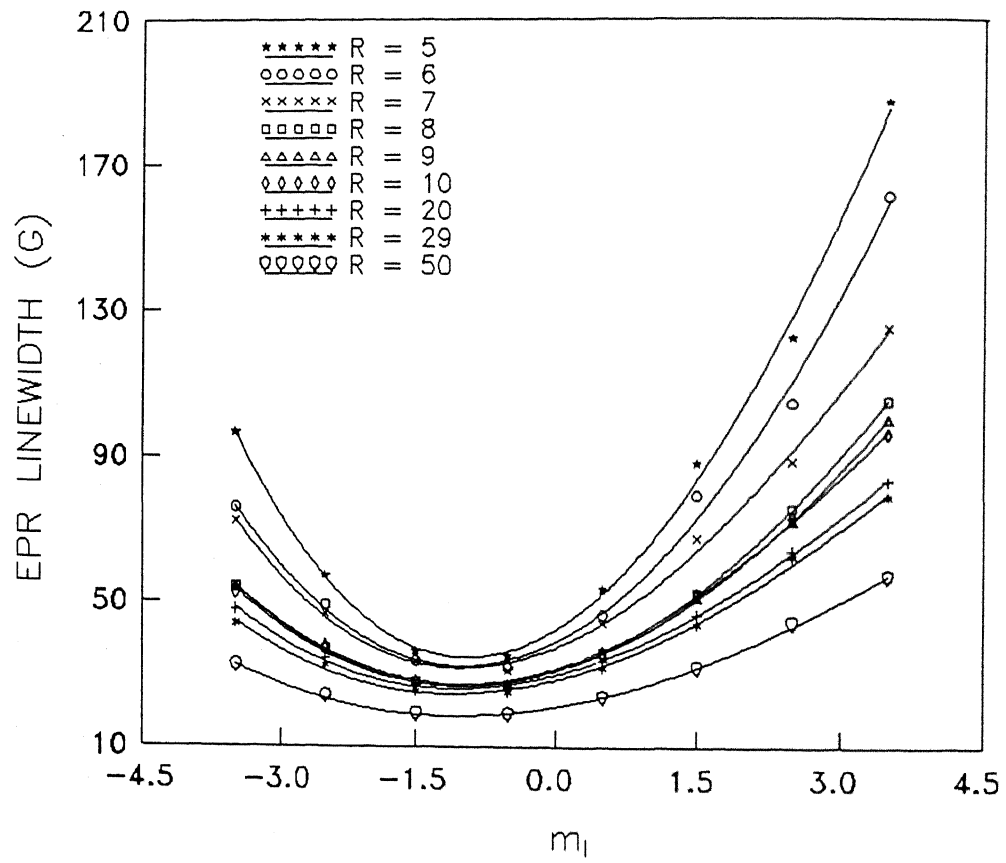


Fig. 4.13 Dependence of the  $\text{VO}^{2+}$  EPR linewidths on  $m_I$  for various 'R' values.

Table 4.11

Least-squares parameters used in Eq. 4.2

R	$(\alpha' + \alpha'')$ (G)	$\beta$ (G)	$\gamma$ (G)	$\delta$ (G)
5.0	42.36	16.02	8.038	-0.2750
6.0	39.00	13.23	6.442	-0.1114
7.0	37.43	11.00	4.985	-0.2947
8.0	30.96	8.39	3.992	-0.0938
9.0	31.00	7.64	3.788	-0.0908
10.0	31.64	8.30	3.550	-0.1756
20.0	29.80	6.98	2.96	-0.1621
30.0	28.40	6.74	2.760	-0.1423
50.0	20.93	4.55	1.959	-0.0846

#### Calculation of dynamical parameters

The rotational correlation times of  $\text{VO}^{2+}$  and the microviscosity felt by the probe in the water pools of AOT reverse micelles of different water contents have been calculated using Eq. 4.19 and Eq. 4.20, respectively. Calculated values of dynamical parameters for different 'water pool' size are listed in Table 4.12. Along with these values are shown the values of rotational correlation time of water, found from  $^1\text{H}$  NMR study<sup>26</sup> (see column 4, Table 4.12). The rotational correlation time ( $\tau$ ) and microviscosity ( $\eta$ ) values are plotted against 'R'; these are shown in Fig. 4.14 and Fig. 4.15, respectively.

It may be determined from Table 4.9 that, on average, only one out of every 30 micelles has the spin probe when  $R = 1$ . An aggregation number of 0.4 M AOT has been used in arriving at this ratio.<sup>11a</sup> Since we have used a much lower concentration [ $\sim 0.138$  M] in our preparation, this ratio could be an overestimate. Nevertheless, we can firmly say that at  $R = 1$  there will be a minimum of 29 unlabeled micelles for every labeled micelle. This ratio is

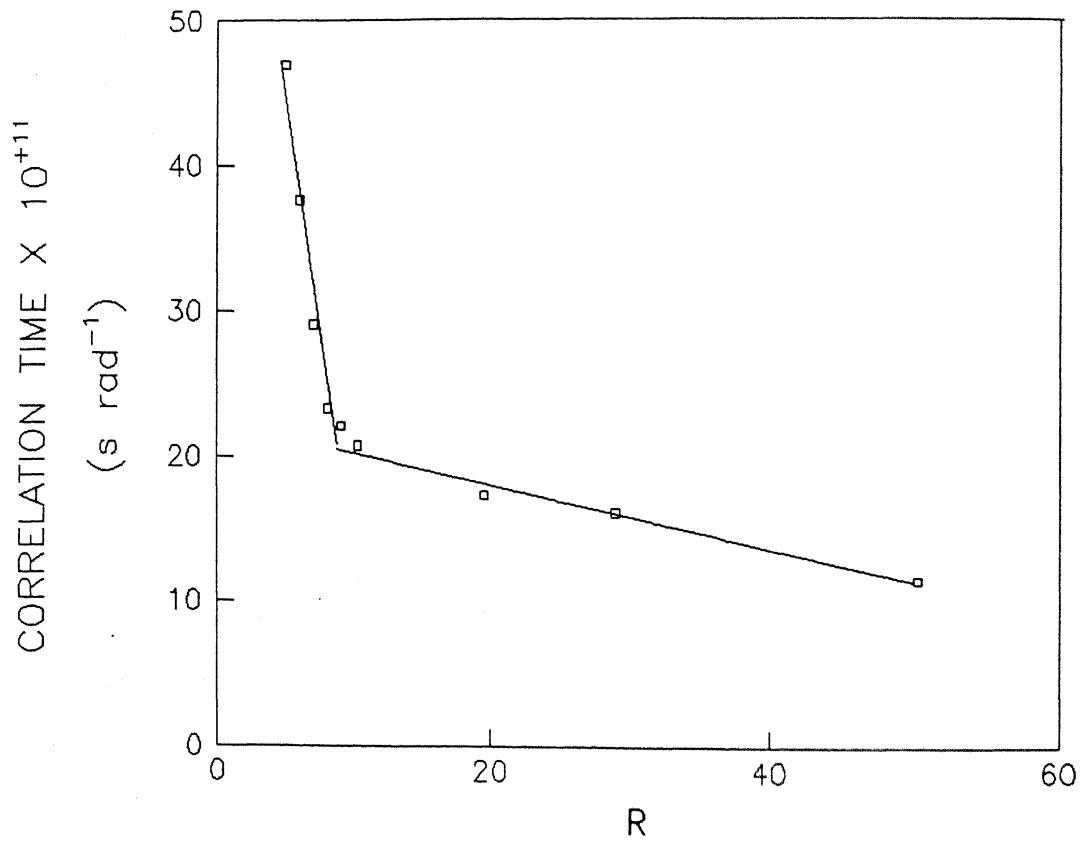


Fig. 4.14 Dependence of  $\text{VO}^{2+}$  correlation time,  $\tau$ , on 'R' in AOT reverse micelles.



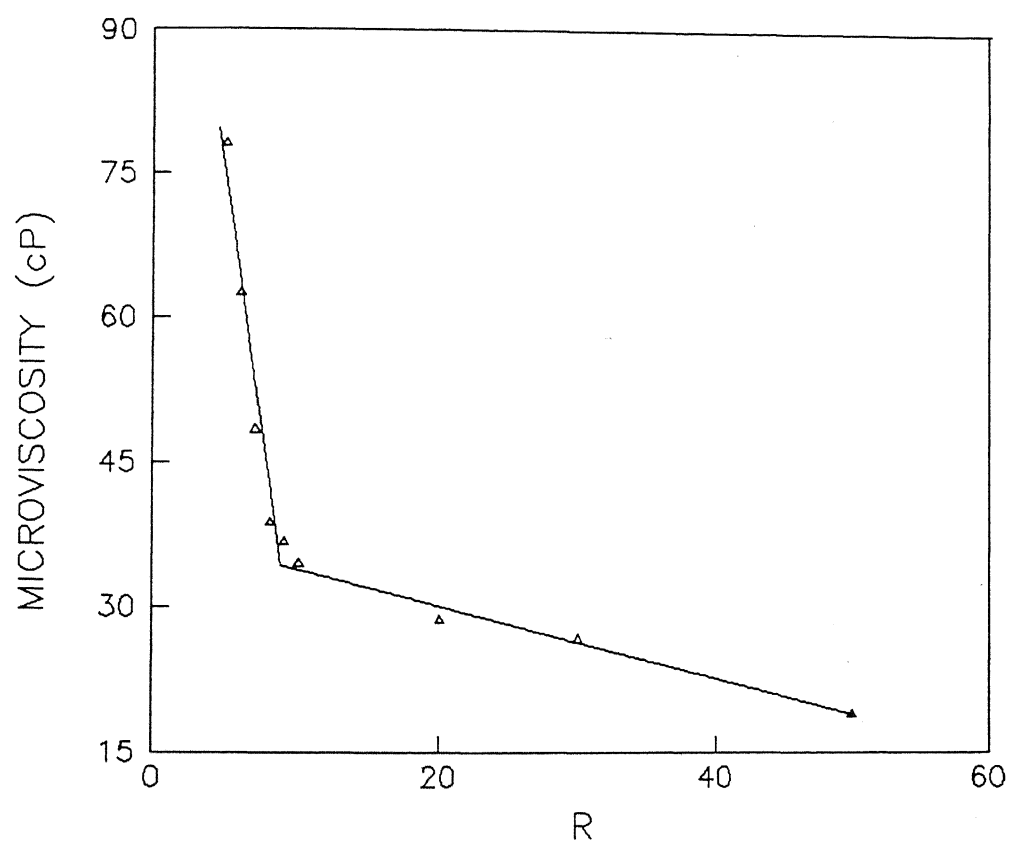


Fig. 4.15 Variation of microviscosity,  $\eta$ , of the water pools of AOT reverse micelles with size of the pools ( $\propto R$ ).

Table 4.12                      Dynamical parameters of  $\text{VO}^{2+}$  in AOT reverse micelles

R	$\text{VO}^{2+}$ in water pools $\tau \times 10^{11} \text{ s}$	Water in water pools <sup>26</sup> $\tau \times 10^{11} \text{ s}$	Microviscosity felt by $\text{VO}^{2+}$ $\eta$ (cP)
5.0	46.94	7.0	78.21
6.0	37.62		62.68
7.0	29.11		48.50
8.0	23.31		38.84
9.0	22.12		36.86
10.0	20.73	2.0	34.54
20.0	17.29	0.8	28.81
30.0	16.12		26.86
50.0	11.44	0.3	19.06

slowly varied when the water content is increased. For example, when  $R = 5$ , the ratio is 7 and, finally, ~5 spin probe molecules will be there in every micelle at  $R = 50$ . Based on this we can rule out the possibility of exchange process taking place within a micelle (i.e. 'intramolecular exchange') and consequent dipolar broadening due to spin-spin interaction. Having ruled out this mechanism, we can then safely say that whatever changes are manifested in EPR lineshapes are only due to the inherent structure of the reverse micelles themselves and due to the peculiar nature of 'reverse micellar' water. Knowledge about the ratios of different components (Table 4.9) facilitates us in interpreting the dynamics of  $\text{VO}^{2+}$  in reverse micelles with the help of collected data.

Careful examination of lineshapes, correlation times and microviscosity over a range of 'R' values demonstrates that  $\text{VO}^{2+}$  in AOT

reverse micelles experiences three different environments. When the 'water pool' size is small ( $R = 1 - 4$ ), EPR spectral profiles approach the 'rigid limit' with parallel and perpendicular features clearly visible. Radii of these small water pools vary from 1.5 - 6.0 Å. In spite of the bigger size of the fully hydrated  $\text{VO}^{2+}$  ion compared with the size of the water pool, when  $R = 1$  and 2, the AOT surfactant molecules seem to adjust themselves in such a way that  $\text{VO}^{2+}$  ion could be just accommodated in the water pools. The fact that AOT reverse micelles show greater affinity towards mono- and di-valent metal cations has already been established.<sup>27</sup> Similarly, ligation of  $\text{Cu}^{2+}$  ion to the sulfonic groups of AOT reverse micelles near  $R = 2$  has also been reported recently.<sup>11a</sup> In the present EPR investigation, the  $\text{VO}^{2+}$  ion strongly binds electrostatically to polar head groups when  $R \leq 4$  and subsequently becomes immobile. 'Rigid limit' spectral responses strongly support our arguments. The much more useful correlation time ( $\tau$ ) measurements could not be carried out in this 'slow motion' region because of the complex lineshapes which certainly deserve a separate analysis.<sup>12</sup>

Gradual increase of the water content induces significant changes in the dynamics of the  $\text{VO}^{2+}$  ion from an initial 'rigid-limit' state. Over the range  $R = 5 - 10$ , vanadyl ion undergoes incipient slow motion. This is supported by correlation time measurements which show that ' $\tau$ ' falls in between  $4.69 \times 10^{-10}$  and  $2.07 \times 10^{-10}$  s  $\text{rad}^{-1}$  as well as by the unsymmetrical lines featuring in the spectra. Correlation time measurements reveal that, even in reverse micelles having fairly larger water pools ( $R = 10$ ,  $r = 15$  Å), the interaction between the anionic probe and the polar head group persists weakly with the probable location for  $\text{VO}^{2+}$  in the interfacial water region.

Finally, the highly resolved hyperfine lines obtained for  $R = 20$  to 50 show that vanadyl ion undergoes fast motion. However, the correlation time

measurements indicate that this motion is slower compared to  $\text{VO}^{2+}$  in aqueous solutions.

### 3 EPR Studies of $\text{VOSO}_4$ in Reverse Micelles Containing Zwitterionic Surfactants

The system chosen for this investigation is lecithin/cyclohexane/ $\text{H}_2\text{O}$ . The samples were prepared as per the composition given in Table 4.3. Approximately 30  $\mu\text{l}$  of methanol was added to all reverse micellar solutions to ensure a thorough solubility of  $\text{VO}^{2+}$  ion in water pool. Details of spectrometer settings are given in section 4.3.3.

X-band EPR spectra were recorded at room temperature for all the samples of varying water content. Spectral responses obtained for all the samples of lecithin reverse micelles are similar in appearance. One such typical EPR spectrum (for  $R = 5$ ) is depicted in Fig. 4.16. Lineshapes of all spectra resemble the one that was obtained for  $\text{VO}^{2+}$  ion in 1.5% (W/V) polar lipids of pH 7.<sup>5</sup> In both cases, i.e., (1)  $\text{VO}^{2+}$  in water pools of lecithin reverse micelles and (2) Vanadyl in polar lipid suspension, the EPR spectra indicate the  $\text{VO}^{2+}$  ions are in a strongly immobilized state. Parallel and perpendicular features are very well resolved and facilitate a fairly accurate determination of anisotropic parameters. Using the method described in section 4.4.1, the calculated EPR anisotropic parameters are listed here.

$$\begin{aligned} A_{\parallel} &= 174.58 \times 10^{-4} \text{ cm}^{-1} , & g_{\parallel} &= 1.9355 \\ A_{\perp} &= 72.69 \times 10^{-4} \text{ cm}^{-1} , & g_{\perp} &= 1.9815 \end{aligned}$$

Apart from these, no other parameter could be extracted, directly, from the EPR spectrum. Determination of rotational correlational time demands detailed lineshape analysis.<sup>12</sup> All we could say, at this moment, is that for  $\text{VO}^{2+}$   $\tau > 10^{-9}$  s in the water pools of reverse micelles.

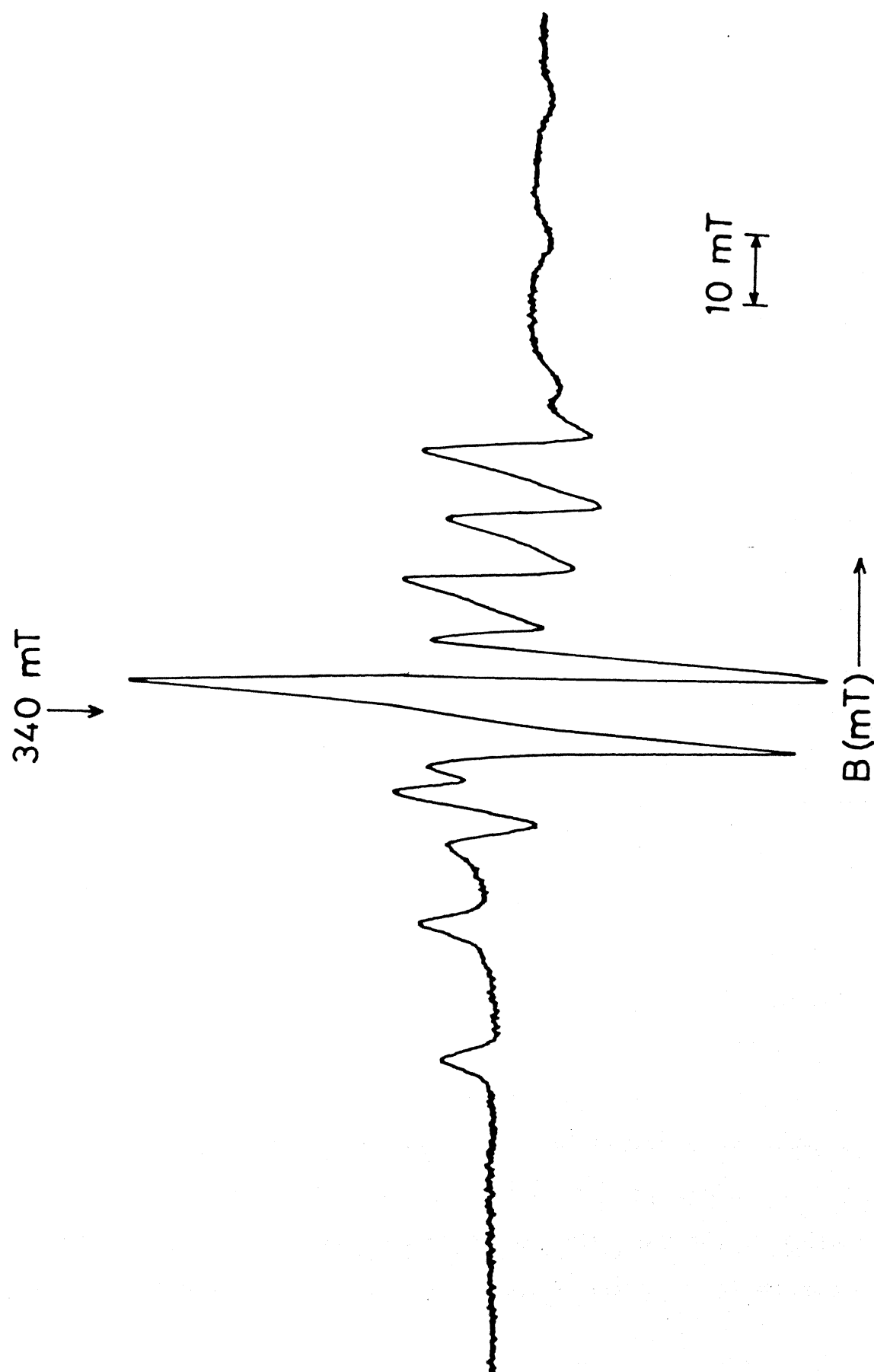


Fig. 4.16 X-band EPR spectra of  $\text{VO}^{2+}$  in lecithin/cyclohexane/ water reverse micelles.

The 'powder-like' EPR spectra obtained for almost all 'R' values suggest that the  $\text{VO}^{2+}$  probe is strongly interacting with the polar head groups of egg yolk lecithin. In all probability, only *coulombic attraction* could favor this kind of binding between phosphate group of lecithin molecules and  $\text{VO}^{2+}$  ion. Unlike in the case of CTAB and AOT, systematic addition of water to the lecithin reverse micelles of low water content, does not have any effect on the room temperature EPR spectrum of vanadyl ion. Addition of a little amount of cosurfactants influence the solubility of  $\text{VO}^{2+}$  in reverse micellar water pool to a certain extent. Methanol, ethanol, iso-butyl alcohol, and tert-butyl alcohol were the cosurfactants added to lecithin reverse micelles. Out of these methanol and tert-butyl alcohol give well resolved and noise free  $\text{VO}^{2+}$  EPR spectra at  $R = 5$ , indicating a high solubility of  $\text{VO}^{2+}$  in presence of the said cosurfactants.

#### 4.5 Conclusions

- 1) In CTAB reverse micelles, the vanadyl spin probe is located at the surfactant water interface when  $R \leq 3$  and is pulled over to the interior of the water pools upon progressive addition of water (i.e.  $R > 3$ ). When the system under study is AOT reverse micelle, the probe is (i) found interacting with the polar head groups when  $R \leq 4$ , (ii) found at the surfactant-water interface when  $5 < R < 10$ , and (iii) found at the interior of the water pools when  $R > 10$ . But in the case of lecithin reverse micelle the probe is strongly bound to the polar head groups of lecithin molecules irrespective of the water content. Thus the location of the  $\text{VO}^{2+}$  spin probe in reverse micelles is strongly influenced by the ionic nature of the surfactant chosen and by the amount of water present in the reverse micelles.

- 2) The vanadyl ion present in the water pools of CTAB reverse micelles undergoes 'incipient slow motion' when the size of the pool is small (say,  $R \leq 3$ ) and rapid rotational motion ('fast' motion) when size is reasonably big, (say,  $R > 3$ ). The same spin probe exhibits 'slow motion' in the small water pools, 'incipient slow motion' in pools of moderate size, and 'fast' motion in the large water pools, as far as AOT reverse micelles are concerned. Because of the strong binding to the phosphate groups of lecithin, the  $\text{VO}^{2+}$  undergoes only 'slow motion' throughout the range of 'R' values studied. Moreover, addition of water does not have any effect on the motion of vanadyl probe.
- 3) The dependence of dynamical parameters (rotational correlation time,  $\tau$ , and microviscosity,  $\eta$ ) on water content estimated from our EPR studies follows the same trend that was observed using  $^1\text{H}$  NMR methods.<sup>23,26</sup>
- 4) The ionic nature of the surfactant affects significantly the widths of all  $m_I$  lines of room temperature  $\text{VO}^{2+}$  EPR spectra obtained at high water content (say,  $R = 10$  for CTAB and  $R = 50$  for AOT reverse micelles). In the case of CTAB reverse micelles, the observed widths of the  $\text{VO}^{2+}$  hyperfine component lines are remarkably **sharper** when compared with the widths in normal aqueous solution; whereas in the case of AOT reverse micelles, the  $\text{VO}^{2+}$  hyperfine linewidths are spectacularly **broad** compared with widths in aqueous  $\text{VO}^{2+}$  solution. These observations are important, since they modify the general belief that the water pools of reverse micelles of higher water content should always behave like normal or 'bulk' water.

## REFERENCES

- 1.a) N. D. Chasteen, R. J. Dekoch, B. Rogers and M. W. Hanna, J. Am. Chem. Soc. **95**, 1301 (1973);  
b) R. J. Dekoch, D. J. West, J. C. Cannon and N. D. Chasteen, Biochemistry **13**, 4347 (1974);  
c) N. D. Chasteen and J. J. Fitzgerald, *ibid.*, **13**, 4338 (1974).
2. W. Snipes and W. Gordy, J. Chem. Phys. **41**, 3661 (1964).
3. B. Lindman and P. Stilbs, J. Colloid Interface Sci. **46**, 177 (1974).
4. R. F. Campbell and M. W. Hanna, J. Phys. Chem. **80**, 1892 (1976).
5. W. Z. Plachy, J. S. Lanyl, and M. Kates, Biochemistry **13**, 4906 (1974).
- 6.a) J. P. Fackler, J. D. Levy and J. A. Smith, J. Am. Chem. Soc. **94**, 2436 (1972);  
b) G. C. Fryburg and E. Gelerinter, J. Chem. Phys. **52**, 3378 (1970);  
c) C. F. Schwerdtfeger and P. Diehl, Mol. Phys. **17**, 417 (1969).
- 7.a) M. B. McBride, Soil Sci. **126**, 200 (1978);  
b) G. D. Templeton and N. D. Chasteen, Geochin. Cosmochin. Acta. **44**, 741 (1980).
8. Y. Yamada, J. Somha, K. Ouchi and Y. Shanada, Chem. Lett. 831 (1976).
9. I. Ravet, A. Gourgue, Z. Gabelica and J. B. Nagy. Proceedings of the eighth international Congress on Catalysis, West Berlin, Germany, Vol. **4**, 1984, p. 871.
10. U. Ilangovan, S. Sharada and P. Raghunathan, Solid state Physics Symposium, India, **34c**, 439 (1991).
- 11a) S. A. Lossia, S. G. Flore, S. Nimmala, H. Li, and S. Sclick, J. Phys. Chem. **96**, 6071 (1992);  
b) P. Brüggeler, J. Phys. Chem. **90**, 1830 (1986).
12. P. Raghunathan and B. B. Das, Chem. Phys. Lett. **160**, 627 (1989).
13. N. D. Chasteen, in Biological Magnetic Resonance, L. J. Berliner (ed.) Vol. **3**, Plenum, 1981; p. 53.
14. G. E. Pake and R. H. Sands, Phys. Rev. **98**, 266(A) (1955).
15. R. Wilson and D. Kivelson, J. Chem. Phys. **44**, 154 (1966).



16. G. V. Bruno, J. K. Harrington and M. P. Eastman, J. Phys. Chem. **81**, 1111 (1977).
17. A. -B. Barelli, Ph.D. Thesis, Basel University, Basel, Switzerland, 1985.
18. R. C. Barklie, O. Girard and O. Braddell, J. Phys. Chem. **92**, 1371 (1988).
19. N. D. Chasteen and M. W. Hanna, J. Phys. Chem. **76**, 3951 (1972).
20. P. T. Manoharan and M. T. Rogers, J. Chem. Phys. **49**, 3912 (1968).
21. B. Bleaney, Phil. Mag., **42**, 441 (1951).
22. Y. Kotake and E. G. Janzen, J. Chem. Phys. **92**, 6357 (1988).
- 23a) S. K. Saxena, M.Sc. Dissertation, Indian Institute of Technology, Kanpur, India (1991).  
  
b) Also V. Govindaraju, S. K. Saxena, and P. Raghunathan (unpublished).
24. D. C. McCain and R. J. Myers, J. Phys. Chem. **71**, 192 (1967).
25. R. G. Hayes and R. J. Myers, J. Chem. Phys. **40**, 877 (1964).
26. M. Wong; J. K. Thomas and T. Nowak, J. Am. Chem. Soc. **99**, 4730 (1977).
27. E. B. Leodidis and T. A. Hatton in : **Structure and reactivity of reverse micelles**, M. P. Pileni (ed.), Elsevier, Amsterdam (1989).
28. V. V. Kumar, C. Kumar and P. Raghunathan, J. Colloid. Interface Sci. **99**, 315 (1984).
29. M. P. Pileni, T. Zemb and C. Petit, Chem. Phys. Lett. **118**, 414 (1985).

## CHAPTER 5

DEVELOPMENT OF NOVEL COMPUTATIONAL PROCEDURES FOR ANALYZING  
NITROXIDE EPR LINESHAPES

## 5.1 Introduction

In recent years, studies of biological systems at the molecular level have been carried out not only to extract valuable information regarding structure and function but also to understand dynamical alterations involved during biological processes. Although many physico-chemical methods have been widely used for these purposes, the advent of EPR spin labelling technique has enabled us to overcome atleast some of the limitations posed by other techniques. Applications of EPR have grown considerably since the original work by McConnell et al.<sup>1,2</sup>

EPR spectroscopy of spin-labeled lipids is widely used for probing the dynamical structure of lipid bilayers and biological membranes. Since the mobility of typical spin labels in fluid lipid membranes is found to be close to the optimum range of motional sensitivity of EPR, the method is widely used to probe the dynamics of these membranes. In principle, the information obtainable from the spectra of spin labels relates to the rate of motion of the labelled group, its amplitude, and the polarity of the environment in which it is situated.

To maximize the information content, it is imperative that the EPR spectra of spin-labeled biomolecules should be analyzed quantitatively by utilizing well known theoretical methods of spectral analysis.<sup>3</sup> The kinds of information available through spectral lineshape analysis are (i) extent of ordering of the labels, (ii) spin label asymmetry, (iii) the rate of rotational reorientation (iv) spin label anisotropy. The rotational rate is a measure of

the fluidity in the mean potential of the surrounding molecules which determines the ordering. Also, the analysis of spectral lineshapes is often the only available approach to the study of conformational changes or biological functions.

In the following sections, the details of the timescale of nitroxide EPR spectroscopy, the types of commonly encountered EPR lineshapes and the effect of motion of spin label on these lineshapes are reviewed. The theory underlying several computational procedures presently available in the literature is then discussed, and the specialized computational procedures developed in this work for simulating EPR spectral lineshapes in 'fast' and 'slow' reorientational limits are documented.

## 5.2 Timescale of Nitroxide EPR Spectroscopy

For a spectroscopist, a proper knowledge of the timescale of the particular spectroscopic technique is, of course, essential. It is possible to define a limiting time-scale,  $\tau_{lim}$ , which represents the slowest molecular motions to which the conventional EPR spectra are sensitive. This time-scale is determined by the spectral anisotropy.  $\Delta [ \approx (A_{zz} - A_{xx}), (g_{xx} - g_{zz}) \beta B ]$ , of the nitroxide group, and is therefore a special characteristic of the spin label method :

$$\tau_{lim} = \frac{\hbar}{\Delta} \approx 6.8 \times 10^{-9} \text{ s.} \quad (5.1)$$

The sensitivity of conventional spin label EPR spectra to molecular motion is determined by transverse relaxation processes ( $T_2$  processes), and is limited by spectral anisotropies to motions faster than  $\approx 10^{-8} - 10^{-7}$  s. This is the timescale involved in conventional EPR studies of rotational motion of spin-labeled lipids in fluid biological membranes.

Motion slower than this range can also be studied, by the saturation transfer EPR spin label method.<sup>4</sup> The optimum motional sensitivity of this method is on the time-scale :  $\tau_{\text{opt}} \text{ (STEPR)} \approx T_1 \approx 10^{-6} - 10^{-3} \text{ s}$ . The saturation transfer EPR timescale is well-suited to studies of rotational motion of spin-labeled integral proteins in membranes.

The fast and slow motional regions of conventional spin label EPR spectroscopy are specified by the correlation time ranges :  $10^{-11} \text{ s} < \tau_R < 10^{-9} \text{ s}$  and  $10^{-9} \text{ s} < T_R < 10^{-7} \text{ s}$ , respectively. In the fast motional regime, the line positions are not dependent on the rate of motion, but only on the amplitude of motion, i.e., on the order parameters. In this regime,  $\tau_R < \tau_{\text{lim}}$ . The spectra may be analyzed using time-dependent perturbation theory, based on the formulation of the spin Hamiltonian given in Eq. 5.2,

$$\mathcal{H}(t) = \langle \mathcal{H}_0 \rangle + [\mathcal{H}(t) - \langle \mathcal{H}_0 \rangle] \quad (5.2)$$

where  $\mathcal{H}(t)$  is the spin Hamiltonian of the nitroxide radicals undergoing random reorientations in liquids and liquid crystals,  $\langle \mathcal{H}_0 \rangle$  represents the time-averaged Zeeman and hyperfine interactions, which also determines line positions and the  $[\mathcal{H}(t) - \langle \mathcal{H}_0 \rangle]$  representing time-dependent fluctuations of these interactions about this average, which determines the linewidth, has been applied to analyzing lipid spectra in highly fluid bilayers. The dependence of the linewidths on the nuclear spin quantum number,  $m_I = 0, \pm 1$ , is given in general by,<sup>5</sup>

$$\Delta B(m_I) = A + B m_I + C m_I^2 \quad (5.3)$$

In the slow motional regime the line positions are not strongly dependent on the amplitude of motion, but rather on the rate of motion. The

line-widths increase with increasing rate of motion in contrast to the fast motion regime where the line-widths decrease with increasing rates of motion. The EPR spectra obtained in slow motional regime can be analyzed using either stochastic Liouville equation or the diffusion-coupled Bloch equations.

### 5.3 Types of Lineshapes and Effect of Motion on EPR Spectral Profiles

The two most commonly encountered lineshapes in EPR absorption are (i) Lorentzian lineshape (ii) Gaussian lineshape. Grossly, the main difference between the two types of lineshapes is that the outer wings of the Lorentzian are larger and drop more slowly than those of the Gaussian (see Fig. 5.1). The two shape functions for a resonance line centered at  $B_0$  can be described by the following expressions,<sup>3</sup>

$$f_L(B) = \frac{2\sqrt{3}}{\pi} \left( \frac{\Delta B_{pp}}{3 \Delta B_{pp}^2 + 4 (B-B_0)^2} \right) \quad \text{for Lorentzian} \quad (5.4)$$

and

$$f_G(B) = \sqrt{\frac{2}{\pi}} \frac{1}{\Delta B_{pp}} \exp \left[ -2 \left( \frac{B-B_0}{\Delta B_{pp}} \right)^2 \right] \quad \text{for Gaussian} \quad (5.5)$$

where ' $\Delta B_{pp}$ ' is the peak-to-peak linewidth of the derivative curve.

#### Isotropic motion

Spherical molecules in isotropic fluids often undergo two distinguishable kinds of isotropic motion:

(i) Under conditions of 'fast' motion, the EPR spectra of the nitroxide spin labels will display g-values ( $g$ ) and  $^{14}\text{N}$  hyperfine splitting ( $a_N$ ) that are the averages of the principal components of the corresponding tensors. The dominant features are described by the  $\langle \mathcal{H}_0 \rangle$  term in Eq. 5.2, and the time-

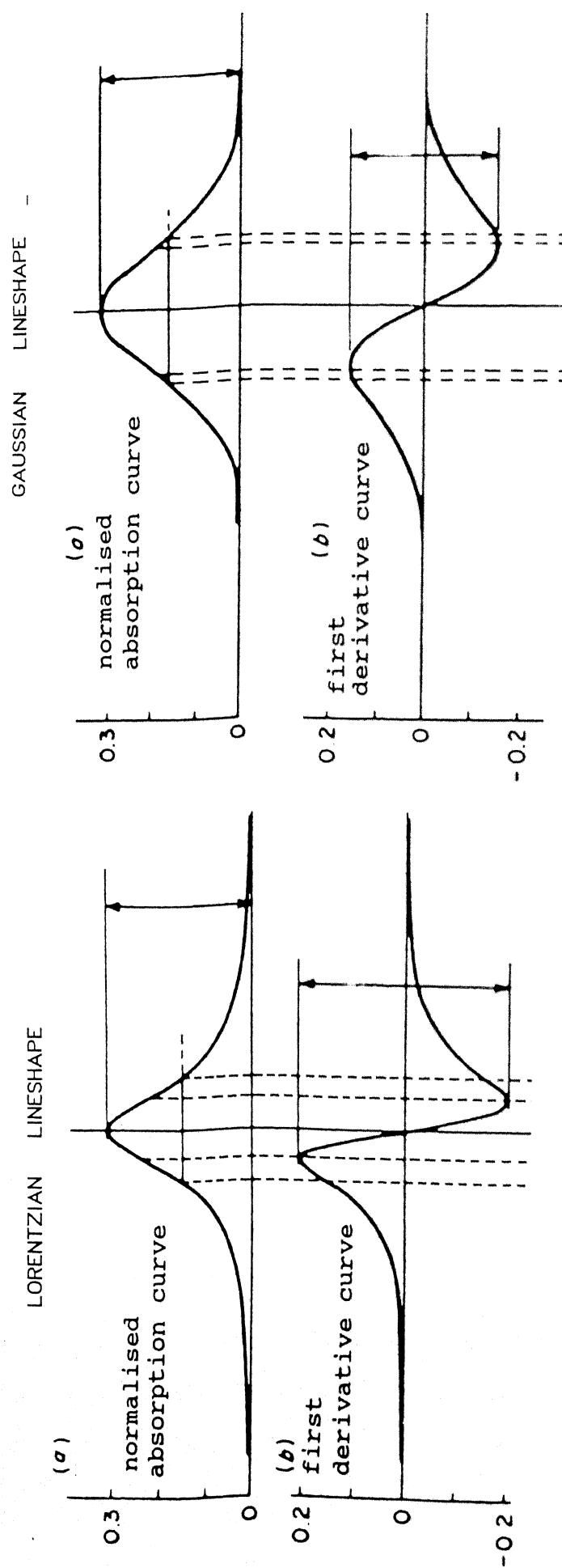


Fig. 5.1 Lineshapes normally encountered in EPR spectroscopy.

dependent terms may be treated as perturbation. Accordingly, a narrow three-line spectrum results, corresponding to the  $m_I = +1, 0, -1$  manifolds of the  $^{14}\text{N}$  nucleus. The linewidths of these lines will be described by Eq. 5.3.

(11) When the motion is slow enough that the rate of averaging of the  $g$ -values and  $^{14}\text{N}$  hyperfine splittings becomes comparable to the spectral anisotropy  $\Delta$ , a complex lineshape results. In the extreme case, when the molecular motion is very slow on the timescale of the experiment ( $\tau \gg \tau_{\text{lim}}$ ), the spectra become the result of the addition of contributions due to molecules with all possible orientations with respect to the magnetic field, similar to those obtained from magnetically dilute powders.

#### Anisotropic motion in isotropic media :

As is evident from the literature, the 'isotropic motion condition' is applied rarely.<sup>6-8</sup> Even small nitroxide molecules in isotropic media may undergo anisotropic motion<sup>6,8</sup> and their EPR spectra must be treated in terms of at least two correlation times, one that characterizes motion about a principal molecular axis ( $\tau_{\parallel}$ ) and another characterizing motion of the molecular axis ( $\tau_{\perp}$ ).<sup>6</sup> Another possible complication for small molecules in isotropic media is non-Brownian motion.<sup>6-8</sup> Different parameters, such as mean jump angle<sup>6,8</sup> or fluctuating torque<sup>7,8</sup> are then needed to characterize this motion. Under this anisotropic motion, the resultant lineshapes will have contribution from unresolved proton hyperfine splitting and conformational interconversion.

#### 5.4 Theory and Computational Procedure Used to Simulate the Lineshapes of Nitroxide Spin Labels Undergoing Slow Motion

Various theories have been developed for simulating EPR spectral lineshapes of nitroxides undergoing slow tumbling.<sup>9-21</sup> Adiabatic approximation has been used in some of these theories. 'Adiabatic' is used here in the

quantum mechanical or Ehrenfest sense. Simply defined, the process takes place in such a way that energy levels of the spin systems are affected, but the populations of the levels are not. Among these, the most used approach for analyzing EPR at arbitrary tumbling rates is that of Freed and coworkers.<sup>9,12</sup> An analysis, in which a variational method is applied to the stochastic Liouville equations, has also been proposed.<sup>12</sup> A comparative treatment of the different theoretical approaches is given by Yoon et. al.<sup>22</sup>

Lee<sup>23</sup> examined a certain characteristic sharp feature for each hyperfine component, called the "parallel-edge line", which was observed at the limit of the EPR rigid powder and slow tumbling spectra associated with those molecules in a liquid which had their symmetry axes oriented nearly parallel to that of the applied magnetic field. It was shown<sup>24</sup> that the difference in parallel edge linewidth of two hyperfine components (as determined from the second derivative spectrum), was a motional broadening effect which depended principally on the rotational modulation of hyperfine and g tensor anisotropic interactions. A theory based on the motional broadening and shifting of these parallel-edge lines has been developed.<sup>24</sup>

Later on, further theoretical investigation<sup>25</sup> has been reported on the general behavior of slow-tumbling, EPR hyperfine centers. The advantages of these approaches<sup>23-25</sup> are the following : (i) relatively simple theory compared with the others which involve cumbersome comprehensive calculations. (ii) inhomogeneous line broadening does not have to be considered. The lineshapes computed using these approaches agree qualitatively with those computed from other theories.

Elsewhere, ensemble averaging based on the solution of an isotropic diffusion equation has been employed<sup>25</sup> to calculate analytical expressions for angular-dependent motional linewidths and shifts in spectral line position of



EPR hyperfine centers. This simple theoretical treatment<sup>24,25</sup> has been adapted and used in our computational procedure, which we shall be described below.

#### 5.4.1 Theory

It is assumed that the molecules initially at a given angle  $\theta'$  reorient very slowly by means of orientational diffusion. This diffusive motion may be described by

$$\frac{\partial W}{\partial t} = D \left( \frac{1}{\sin \theta} \frac{\partial}{\partial \theta} \sin \theta \frac{\partial W}{\partial \theta} \right), \quad (5.6)$$

where  $D$  is the orientational diffusion constant and  $W(\theta, t | \theta', 0) \sin \theta d\theta$  is the conditional probability that if the molecule is oriented at angle  $\theta'$  at  $t = 0$ , its orientation at time 't' will be described by a range of angles between  $\theta$  and  $\theta + d\theta$ . Using spherical harmonics, it can be readily shown that

$$W(\theta, t | \theta', 0) = \frac{1}{2} \sum_l [2l+1] P_l(\theta) P_l(\theta') \exp[-l(l+1)Dt], \quad (5.7)$$

where  $P_l(\theta)$  is the  $l$ th order Legendre polynomial. In the limit of 'fast' motion, each molecule samples all angles in the time characteristic of the experiment, i.e., the spin relaxation time  $T_2$ . However, in the slow motion limit,

$$DT_2^\theta \ll 1, \quad (5.8)$$

and molecules initially at  $\theta'$  sample only a small (restricted) range of angles about  $\theta'$ .

As shown in detail by Kivelson and Lee<sup>24</sup> for isotropic orientational diffusion motion and for axially symmetric paramagnetic centers whose symmetry

axes are oriented at an arbitrary angle  $\theta'$  at  $t = 0$  and reorienting during the characteristic time of EPR measurements (taken as the spin-spin relaxation time  $T_2^{\theta'}$ ), one of the restricted ensemble averages of  $P_l(\theta)$  is

$$\langle P_l(\theta) \rangle_{\theta'} = \int_0^\pi \left[ \int_0^{T_2^{\theta'}} W(\theta, t | \theta', 0) dt / T_2^{\theta'} \right] P_l(\theta) \sin\theta d\theta \quad (5.9)$$

With the help of Eq. 5.7, Eq. 5.9 is calculated to be

$$\langle P_l(\theta) \rangle_{\theta'} = P_l(\theta') \{1 - \exp[-l(l+1) DT_2^{\theta'}]\} [l(l+1) DT_2^{\theta'}]^{-1} \quad (5.10)$$

Since  $DT_2^{\theta'} \ll 1$ , Eq. 5.10 can be expanded as

$$\langle P_l(\theta) \rangle_{\theta'} = P_l(\theta') \sum_{n=0}^{n=\infty} [-l(l+1) DT_2^{\theta'}]^n [(n+1)!]^{-1} \quad (5.11)$$

The first-order terms of the axially symmetric hyperfine spin Hamiltonian, namely,

$$\mathcal{H} = \mu_B [g_{\parallel} S_z B_z + g_{\perp} (S_x B_x + S_y B_y)] + A_{\parallel} S_z I_z + A_{\perp} (S_x I_x + S_y I_y) \quad (5.12)$$

are <sup>(26)</sup>

$$\mathcal{H}(\theta) = g(\theta) \mu_B S_{z'} + A(\theta) S_{z'} I_{z'} \quad (5.13)$$

for which the  $z'$  axis has direction cosines

$$n = [g_{\parallel}/g(\theta)] \cos\theta, \quad (5.14a)$$

$$l = m = [g_{\perp}/g(\theta)] \sin\theta, \quad (5.14b)$$

with respect to the EPR principal z and x or y axes, and z" axis has direction cosines

$$n = [A_{\parallel}g_{\parallel}/A(\theta)g(\theta)] \cos\theta, \quad (5.15a)$$

$$l = m = [A_{\perp}g_{\perp}/A(\theta)g(\theta)] \sin\theta, \quad (5.15b)$$

with respect to the z-and x- or y principal axes, where

$$g(\theta) = (g_{\parallel}^2 \cos^2\theta + g_{\perp}^2 \sin^2\theta)^{1/2}, \quad (5.16)$$

$$A(\theta) = (A_{\parallel}^2 g_{\parallel}^2 \cos^2\theta + A_{\perp}^2 g_{\perp}^2 \sin^2\theta)^{1/2} [g(\theta)]^{-1} \quad (5.17)$$

and  $\theta$  is the angle between B and the principal z axis. The EPR magnetic field value to first order for the M th hyperfine transition  $\Delta m = \pm 1$  and  $\Delta M = 0$ , where  $m = \langle S_{z'} \rangle$ , and  $M = \langle I_{z''} \rangle$  is given by

$$B_H(\theta) = [h\nu_o - MA(\theta)]/[(g(\theta)\mu_B)] \quad (5.18)$$

We shall now consider EPR centers undergoing slow orientational diffusion over a small angular interval. Let  $\theta'$  be the orientation of the EPR center at  $t = 0$ , and let  $\theta$  be the orientation at a later time 't'. Then the first-order spin Hamiltonian of Eq. 5.13 at  $t = t$ , in terms of that at  $t = 0$ , is given by

$$\mathcal{H}(\theta) = \mathcal{H}(\theta') + \int_{\theta'}^{\theta} [\partial \mathcal{H}(\theta)/\partial \theta] d\theta = \mathcal{H}(\theta') + S_{z'} \int_{\theta'}^{\theta} \Delta_H(\theta) \sin\theta \cos\theta d\theta, \quad (5.19)$$

$$\text{with } \Delta_M(\theta) = (g_{\perp}^2 - g_{\parallel}^2) \mu_B B_M(\theta) / g(\theta) + M [A(\theta)(g_{\parallel}^2 - g_{\perp}^2) / g^2(\theta)] \\ + M(g_{\perp}^2 A_{\perp}^2 - g_{\parallel}^2 A_{\parallel}^2) / [A(\theta) g^2(\theta)] \quad (5.20a)$$

where  $I_{Z''}$  is replaced by its eigenvalue  $M$ . If the  $\bar{g}$  anisotropy is small, the above expression is approximated by

$$\Delta_M(\theta) = \left[ (g_{\perp}^2 - g_{\parallel}^2) g^2(\theta) \right] h\nu_0 + M(A_{\perp}^2 - A_{\parallel}^2) / A(\theta) \quad (5.20b)$$

For a small-angle orientational diffusion  $|\theta - \theta'|$  is small, and  $\Delta_M(\theta)$  is assumed to be constant at  $\Delta_M(\theta')$  and hence removed from the integral of Eq. 5.19. Thus,

$$\mathcal{H}(\theta) = \mathcal{H}(\theta') + \frac{1}{3} \Delta_M(\theta') \left[ P_2(\theta') - P_2(\theta) \right] S_z. \quad (5.21)$$

The ensemble average of the above Hamiltonian for the small-angle, orientational diffusion around  $\theta'$  during  $T_2^{\theta'}$  is given by  $\langle \mathcal{H}_{SL}(\theta) \rangle_{\theta'}$ , where  $\langle \rangle_{\theta'}$  represents the averaging process, Eq. 5.11. Then the spin lattice Hamiltonian associated with the motion is

$$\mathcal{H}_{SL}(\theta', \theta, S_z) = \mathcal{H}(\theta) - \langle \mathcal{H}(\theta) \rangle_{\theta'} \\ = (1/3) \Delta_M(\theta') \left[ \langle P_2(\theta) \rangle_{\theta'} - P_2(\theta) \right] S_z. \quad (5.22)$$

The relaxation time  $T_2^{\theta'}(M)$  for the  $M$ th hyperfine component is determined by<sup>27</sup>

$$\left[ 1/T_2^{\theta'}(M) \right] = \int_0^{\infty} \langle h_M(t) h_M(0) \rangle_{\theta'} dt, \quad (5.23)$$

where  $h_M$  is given by

$$h_M(t) = \left[ S_+, \mathcal{H}_{SL}(\theta', \theta, S_{z'}) \right] / \langle |S_+|^2 \rangle_{\theta'}^{1/2}, \quad (5.24)$$

in which  $S_+$  is defined in terms of the components of  $S$  in the (X,Y,Z) laboratory coordinate system with the Z axis along the external magnetic field  $B$ , i.e.,  $S_+ = S_x + iS_y$ .

To evaluate the commutator in Eq. 5.24,  $S_{z'}$  is approximated by  $S_z$  because the  $z'$  axis differs from the Z axis by only a small angle when the  $\bar{g}$  anisotropy is small. Thus, Eq. 5.24 is evaluated as

$$\begin{aligned} \left[ 1/T_2^{\theta'}(M) \right] &= \left[ \frac{8}{35} \langle P_4(\theta) \rangle_{\theta'} + \frac{8}{63} \langle P_2(\theta) \rangle_{\theta'} - \frac{4}{9} (\langle P_2(\theta) \rangle_{\theta'})^2 + \frac{4}{45} \right]^2 \times \\ &\left\{ \left[ \Delta_M(\theta') \right]^2 / (16D) \right\} \left[ \frac{2}{15} + \frac{2}{21} \langle P_2(\theta) \rangle_{\theta'} - \frac{8}{35} \langle P_4(\theta) \rangle_{\theta'} \right]^{-1} \end{aligned} \quad (5.25)$$

By using Eq. 5.11 for  $\langle P_2(\theta) \rangle_{\theta'}$  and  $\langle P_4(\theta) \rangle_{\theta'}$ , Eq. 5.25 is evaluated as

$$\begin{aligned} \left[ 1/T_2^{\theta'}(M) \right] &= \left\{ \left[ \Delta_M(\theta') \right]^2 / (16D) \right\} \left[ 16 \sin^4 \theta' \cos^4 \theta' (DT_2^{\theta'})^2 \right. \\ &+ 8 \sin^2 \theta' \cos^2 \theta' \left( \frac{137}{3} \cos^4 \theta' - 42 \cos^2 \theta' + 3 \right) (DT_2^{\theta'})^3 + \left\{ \left( \frac{137}{3} \cos^4 \theta' \right. \right. \\ &- 42 \cos^2 \theta' + 3 \right\}^2 - 8 \sin^2 \theta' \cos^2 \theta' \left( \frac{838}{3} \cos^4 \theta' - 248 \cos^2 \theta' + 22 \right) \left. \right\} (DT_2^{\theta'})^4 \\ &\times \left[ \sin^2 \theta' \cos^2 \theta' + (10 \cos^4 \theta' - 9 \cos^2 \theta' + 1) (DT_2^{\theta'})^2 \right]^{-1}. \end{aligned} \quad (5.26)$$

In deriving Eq. 5.26, the terms of order higher than  $(DT_2^{\theta'})^4$  are neglected in the numerator, and terms of order higher than  $(DT_2^{\theta'})^2$  are neglected in the

denominator.

For the parallel ( $\theta' = 0^\circ$ ) and perpendicular ( $\theta' = 90^\circ$ ) paramagnetic centers, the  $\sin\theta'\cos\theta'$  terms in Eq. 5.26 vanish, resulting in

$$\left[1/T_2^{0^\circ}(M)\right] = 2^{1/4}(5/36)^{1/2}|\Delta_H(0^\circ)|^{1/2}\tau_2^{-1/2} \text{ (for } \theta' = 0^\circ), \quad (5.27)$$

$$\left[1/T_2^{90^\circ}(M)\right] = 8^{-1/2}|\Delta_H(90^\circ)|^{1/2}\tau_2^{-1/2} \text{ (for } \theta' = 90^\circ) \quad (5.28)$$

where the relation  $D = [1/6\tau_2]$  of  $P_2(\theta)$  has been used. For  $\theta'$  in the vicinity of  $45^\circ$ , the terms  $(DT_2^{\theta'})^3$  and  $(DT_2^{\theta'})^4$  in the numerator and  $(DT_2^{\theta'})$  in the denominator of Eq. 5.26 can be neglected, yielding

$$\left[1/T_2^{45^\circ}(M)\right] = 24^{-1/3}|\Delta_H(45^\circ)|^{2/3}\tau_2^{-1/3} \text{ (for } \theta' = 45^\circ) \quad (5.29)$$

Equations 5.27 - 5.29 can be written in the form of  $[1/T_2(M)] = (a + bM + cM^2)^n$ , where  $a$ ,  $b$  and  $c$  are coefficients depending on the spin Hamiltonian constants and on  $\tau_2$ , and  $n$  is an exponent.

For an arbitrary value of  $\theta'$ ,  $[1/T_2^{\theta'}(M)]$  is determined by the solution of the following equation :

$$\begin{aligned} & 216\sin^2\theta'\cos^2\theta'\tau_2^3[1/T_2^{\theta'}(M)]^5 + 36(10\cos^4\theta' - 9\cos^2\theta' + 1)\tau_2^2[1/T_2^{\theta'}(M)]^4 \\ & - 36[\Delta_H(\theta')]^2\sin^4\theta'\cos^4\theta'\tau_2^2[1/T_2^{\theta'}(M)]^2 \\ & - 3[\Delta_H(\theta')]^2\sin^2\theta'\cos^2\theta'\left(\frac{137}{3}\cos^4\theta' - 42\cos^2\theta' + 3\right)\tau_2[1/T_2^{\theta'}(M)] \\ & - (1/16)[\Delta_H(\theta')]^2\left\{\left(\frac{137}{3}\cos^4\theta' - 42\cos^2\theta' + 3\right)^2 - 8\sin^2\theta'\cos^2\theta'\right. \\ & \left. \times \left(\frac{838}{3}\cos^4\theta' - 248\cos^2\theta' + 22\right)\right\} = 0. \end{aligned} \quad (5.30)$$

When  $\Delta_M(\theta')$  has units of angular frequency,  $[1/T_2^{\theta'}(M)]$  obtained from Eq. 5.30 has units of angular frequency.

If the motional line broadening is Lorentzian in shape, the peak-to-peak linewidth of the first derivative line (in magnetic field units) for  $[1/T_2^{\theta'}(M)]$  obtained by solving Eq. 5.30 is given by

$$\left[ \Delta B_M(\theta') \right]_{pp} = \left\{ h / \left[ \pi 3^{1/2} g(\theta') \mu_B \right] \right\} \left[ 1/T_2^{\theta'}(M) \right] \quad (5.31)$$

The average EPR magnetic field for a spectral line position of the paramagnetic centers as a result of their restricted ensemble average  $\bar{B}_M(\theta')$  is obtained from Eq. 5.21 as

$$\bar{B}_M(\theta') = B_M(\theta') - (1/3) \Delta_M(\theta') \left\{ P_2(\theta') - \langle P_2(\theta) \rangle_{\theta'} \right\} / \left[ g(\theta') \mu_B \right] \quad (5.32)$$

which further simplifies to

$$\bar{B}_M(\theta') = B_M(\theta') - \Delta_M(\theta') (3 \cos^2 \theta' - 1) (h/24\pi\tau_2) T_2^{\theta'}(M) / [g(\theta') \mu_B] \quad (5.33)$$

where  $B_M(\theta')$  is the rigid-limit EPR magnetic field of Eq. 5.18 for  $\theta = \theta'$ . Thus, the spectral line position for the  $M$ th hyperfine component is shifted from the rigid-limit position by

$$\begin{aligned} \left[ \Delta B_M(\theta') \right]_{\text{shift}} &= \bar{B}_M(\theta') - B_M(\theta') \\ &= -\Delta_M(\theta') (3 \cos^2 \theta' - 1) (h/24\pi\tau_2) T_2^{\theta'}(M) / [g(\theta') \mu_B]. \end{aligned} \quad (5.34)$$

By using Eqs. 5.27 and 5.28 for the cases of  $\theta' = 0^\circ$  and  $\theta' = 90^\circ$ , respectively, the above is reduced to

$$\begin{aligned}
\left[ \Delta B_M(0^\circ) \right]_{\text{shift}} &= \bar{B}_M(0^\circ) - B_M(0^\circ) \\
&= -2^{-1/4} (20)^{-1/2} \left\{ h \Delta_M(0^\circ) / \left[ \pi |\Delta_M(0^\circ)|^{1/2} g_{\parallel} \mu_B \right] \right\} \tau_2^{-1/2}
\end{aligned} \quad (5.35)$$

for  $\theta' = 0^\circ$  and

$$\begin{aligned}
\left[ \Delta B_M(90^\circ) \right]_{\text{shift}} &= \bar{B}_M(90^\circ) - B_M(90^\circ) \\
&= (72)^{-1/2} \left\{ h \Delta_M(90^\circ) / \left[ \pi |\Delta_M(90^\circ)|^{1/2} g_{\perp} \mu_B \right] \right\} \tau_2^{-1/2}
\end{aligned} \quad (5.36)$$

for  $\theta' = 90^\circ$ . At the magic angle  $\theta^\circ$  for which  $(3\cos^2\theta^\circ - 1) = 0$ ,

$$\left[ \Delta B_M(\theta^\circ) \right]_{\text{shift}} = 0 \quad (\text{for } \theta' = \theta^\circ) \quad (5.37)$$

The motional shifts can be positive or negative; a positive (negative) shift means that the EPR line position shifts a higher (lower) magnetic field.

Based on the motional linewidth and magnetic field for spectral line position at an arbitrary orientation  $\theta'$ , the  $M$ th EPR hyperfine line in a polycrystalline/amorphous sample, where the paramagnetic centers are assumed to be randomly distributed over a sphere, is determined by the following integral :

$$\begin{aligned}
F_M(B) \propto & \left| \int_0^{\pi/2} N(\theta') \frac{3 \left[ \Delta B_M(\theta') \right]_{pp}^2}{3 \left[ \Delta B_M(\theta') \right]_{pp}^2 + 4 \left[ B - \bar{B}_M(\theta') \right]^2} \right. \\
& \left. \times \sin\theta' d\theta' \right|, \quad (5.38)
\end{aligned}$$



where  $N(\theta')$  is the normalization factor for  $\theta'$ . In the above integral, the factor

$$W(\theta') = \left[ g_{\parallel}^2 + g^2(\theta') \right] / g^2(\theta'), \quad (5.39)$$

representing the angular dependence of the EPR microwave transition probability,<sup>26</sup> is omitted by considering a small  $\bar{g}$  anisotropy. The entire hyperfine spectrum for all hyperfine components is then given by

$$G(B) = \sum_M F_M(B). \quad (5.40)$$

#### 5.4.2 Computational Procedure

To get a good estimation of lineshape for a particular  $M$ th hyperfine line, the main integral given by Eq. 5.38 should be solved with minimum error. The idea of using the Monte Carlo procedure in computing a definite integral is well known.<sup>3,28-31</sup> Let us consider the integral,

$$\bar{z} = \int_S g(x) z(x) dx \quad (5.41)$$

Here,  $z(x)$  is an arbitrary function and  $g(x)$  is a probability density function defined within the integration domain  $S$ . Looking at these definitions from a slightly different viewpoint,  $\bar{z}$  is the expected value of  $z(x)$  with respect to  $g(x)$  in the space  $S$ . Now values can be approximated as mean or the numerical average of the function, and therefore Eq. 5.41 can be written as

$$\bar{z} \approx \hat{z} = \frac{1}{N} \sum_{i=1}^N z(x_i) \quad (5.42)$$

and the  $N$  sample values of  $x_1$  are selected such that their distribution follows the probability function  $g(x)$ . Now let us consider the special case,

$$z_1 = \int_S z(x) dx \quad (5.43)$$

Here  $g(x) = 1$ , implying uniform density function<sup>32</sup> in the space  $S$ .  $z_1$  can be estimated in a manner similar to that given in Eq. 5.42, but the  $x_1$  are now uniformly distributed in  $S$ . In this way, any integral can be estimated as the average of  $N$  values of the integrand determined at  $N$  points distributed uniformly in the integration space.

Now the value of  $\hat{z}$  given by Eq. 5.42 is only an estimate of  $\bar{z}$  and approaches the value of  $\bar{z}$  as  $N$ , the number of sample points, increases. For a one dimensional integral of the kind shown in Eq. 5.43, the convergence in the other routine numerical integration methods such as Simpson's 1/3 rule may be faster and hence better results may be obtained over a shorter computer time. Although our main integral in Eq. 5.38 is also one-dimensional at present, we intend to modify the theory of  $\theta$  and  $\phi$  variation and subsequently the main integral will be two-dimensional. As the number of dimensions in an integral increases, convergence in these regular procedures is achieved only with great difficulty, and it takes less time to estimate the average as given by Eq. 5.42 with less error. The error in  $\hat{z}$  is normally estimated in terms of the variance, which is given by

$$V = \frac{1}{N} \int_S [z(x) - \bar{z}]^2 g(x) dx = \frac{1}{N} [\overline{z^2} - \bar{z}^2]. \quad (5.44)$$

The square root of the variance  $V$  is known as the standard deviation, and denoted by  $\sigma$ . In the general literature, either  $V$  or  $\sigma$  is given as the error

in the estimate. Also, these are the control parameters used in any iterative procedure employed for error reduction.

There are various techniques in minimizing error in the estimation based on Eq. 5.42. These procedures are known collectively as 'variance reduction techniques'. For example, Khan<sup>33</sup> suggests six procedures for the reduction of variance in the estimation. We have followed one of these, known as 'systematic sampling', to estimate the integral given by Eq. 5.38.

In systematic sampling, the integral  $I$  is estimated as follows.

Let

$$I = \iint_S f(y_1, y_2) z(y_1, y_2) dy_1 dy_2 \quad (5.45)$$

where  $f(y_1, y_2)$  is the joint probability density function and  $z(y_1, y_2)$  is any arbitrary function defined in the integral domain  $S$ . Now a common method of picking a sample point  $(y_1, y_2)$  out of a population described by the probability density function  $f(y_1, y_2)$  is to solve the following equation for  $y_{11}$  and  $y_{2j}$ ,

$$\int_{-\infty}^{y_{11}} f_1(y_1) dy_1 = R_1, \quad (5.46)$$

and

$$\int_{-\infty}^{y_{2j}} f_3(y_2/y_{11}) dy_2 = R_2, \quad (5.47)$$

where  $f_1(y_1)$  and  $f_3(y_2/y_{11})$  are, respectively, the marginal and conditional density functions.  $R_1$  and  $R_2$  are independent random numbers uniformly distributed between 0 and 1. Instead of using independent uniform random numbers we can use  $R_1$ 's such that

$$R_{1i} = \frac{(i-1/2)}{N}, \text{ where } i = 1, 2, \dots, N. \quad (5.48)$$

It is easy to see that these deterministic  $R_{1j}$ 's also follow uniform distribution and the estimate will not change very much. However the error in the estimate is reduced, which can be seen if one derives the expression for variance. Similarly, one can use another set of such type of random numbers for  $R_2$ 's in Eq. 5.47 for every  $R_{1j}$  selected.

$$R_{2j} = \frac{(j - 1/2)}{M}, \text{ where } j = 1, 2, \dots, M. \quad (5.49)$$

In this case the error will be further reduced, as seen by the variance expression given by Khan.<sup>33</sup> Finally, the integral estimate is given as

$$I \approx \bar{I} = \frac{1}{N \cdot M} \sum_{i=1}^N \sum_{j=1}^M z(y_{1i}, y_{2j}). \quad (5.50)$$

This procedure is known as 'systematic sampling' because we systematically pick out the mid-points (for example in  $y_1$  direction) of  $N$  intervals defined by

$$\int_{y_{1i}}^{y_{1i+1}} f_1(y_1) dy_1 = \frac{1}{N}. \quad (5.51)$$

We have used the 'systematic sampling' principle in Eq. 5.38, whereby it has been re-cast as follows :

$$f_M(B) \propto \int_0^1 \frac{N(\cos\theta) [\Delta B_M(\cos\theta)]_{pp}^2}{3[\Delta B_M(\cos\theta)]_{pp}^2 + 4[B - \bar{B}(\cos\theta)]^2} d(\cos\theta) \quad (5.52)$$

'n' values of  $\cos\theta$  are then systematically sampled, so that the overall integral is divided into 'n-1' intervals, i.e.,

$$\cos\theta = (1 - 0.5)/n \quad i = 1, 2, \dots, n. \quad (5.53)$$

Note that Eq. 5.53 resembles Eq. 5.48 and 5.49. Then the integral becomes well approximated as

$$f_M(B) \propto \frac{1}{n} \sum_{i=1}^n \frac{N(\cos\theta) [\Delta B_M(\cos\theta)]_{pp}^2}{3[\Delta B_M(\cos\theta)]_{pp}^2 + 4[B - \bar{B}(\cos\theta)]^2} \quad (5.54)$$

The  $\cos\theta$  and subsequent  $\sin\theta$  values sampled using Eq. 5.53 are substituted in Eqs. 5.16 - 5.19, 5.20b and 5.30.

In this work, the analytical expression given in Eq. 5.30 has been solved numerically using the IMSL subroutine DZPORC. The  $1/T_2^{\theta'}(M)$  values obtained thereby are used to calculate the peak-to-peak derivative linewidth and motional shift  $[\Delta B_M(\theta')]_{\text{shift}}$ . The motional shift may then be substituted in Eq. 5.34 to get the average EPR magnetic field for spectral line position of the EPR centers as a result of their restricted ensemble average  $\bar{B}_M(\theta')$ .

The values thus calculated for a particular ' $\cos\theta$ ' are substituted in Eq. 5.54 and the same procedure repeated for ' $n$ '  $\cos\theta$  values. All these values are then summed and an average taken. This average is the lineshape (Lorentzian) function for a particular hyperfine component. The  $F_M(B)$  calculated for three different ' $M$ ' values may be summed and the lineshape function for the entire hyperfine spectrum determined.

This is the required EPR lineshape for, say, a nitroxide spin label undergoing slow orientational diffusion motion. The program listing written in Fortran is given in the Appendix.

#### 5.4.3. Discussion

Since Eq. 5.30 is a polynomial equation of degree 5, the roots

( $1/T_2^{\theta'}$  (M) values) obtained by numerically solving Eq. 5.30 will have 5 values. Since only the positive real values have a physical meaning, they are considered for further computation. If more than one such value are present, the largest among them is chosen.

The following typical nitroxide spin Hamiltonian constants have been used for our model simulation :

$$\begin{aligned}
 S &= 1/2, & I &= 1, & g_{\parallel} &= 2.002, & g_{\perp} &= 2.008 \\
 A_{\parallel}/(g_{\parallel}\mu_B) &= 3.4 \text{ mT}, & A_{\perp}/(g_{\perp}\mu_B) &= 0.5 \text{ mT} \\
 \tau_2 &= 1 \times 10^{-7} \text{ s} & \text{and} & & \nu_o &= 9.5 \text{ GHz}.
 \end{aligned}$$

Complete theoretical EPR spectra computed from Eqs. 5.54 and 5.40 are shown in Figs. 5.2 - 5.4 for various 'n' values. In the case of  $n = 5$  (Fig. 5.2), convergence is not achieved. For the  $n = 10$  case (see Fig. 5.3) convergence is more or less achieved, and when 'n' reaches 25, (see Fig. 5.4) convergence is completed. In the  $n > 25$  case there is virtually no change. Our computational procedure uses only 25 points in the interval 0 to 1, which has been found sufficient to generate a full EPR spectrum with minimum error.

## 5.5 Theory and Computational Procedure Used to Simulate the Lineshapes of Nitroxide Spin Labels Undergoing Fast Motion

The aforementioned computational procedure and the subsequent program developed by us (Section 5.4) could not be used for cases involving 'fast motion' of radicals. The fact that most nitroxide spin probes undergo fast motion in the reverse micellar media has motivated us to develop a second EPR lineshape simulation program using available theories. Search in this direction revealed a novel method<sup>34</sup> which gives a detailed account about

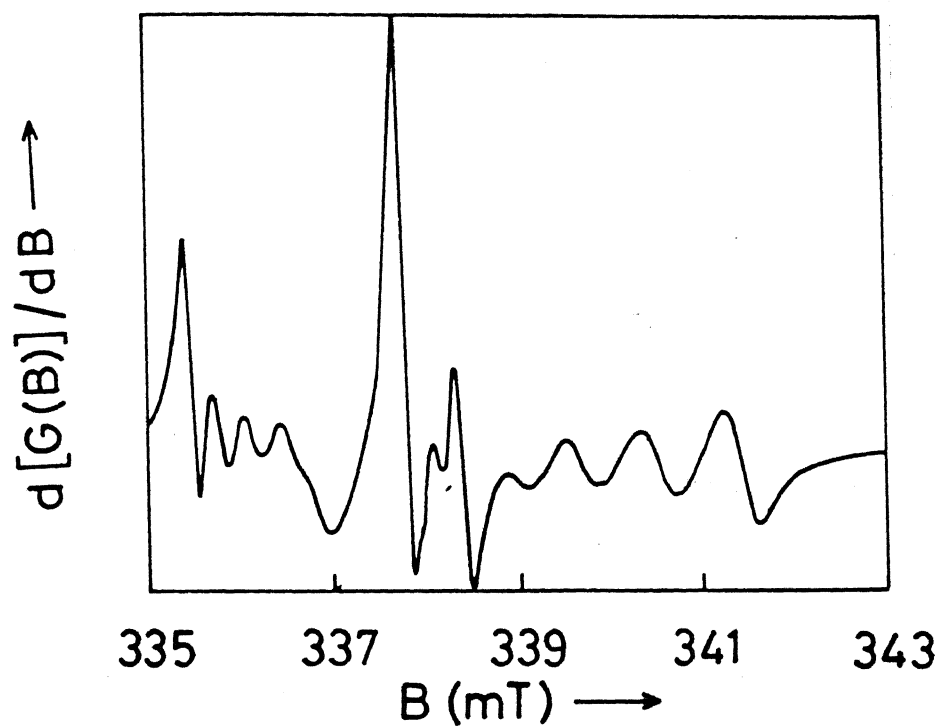


Fig. 5.2 Theoretical EPR lineshapes generated from Eqs. 5.38 and 5.40 at a motional correlation time  $\tau_2 = 1 \times 10^{-7}$  s for the nitroxide center (No. of  $\cos\theta$  values sampled = 5).

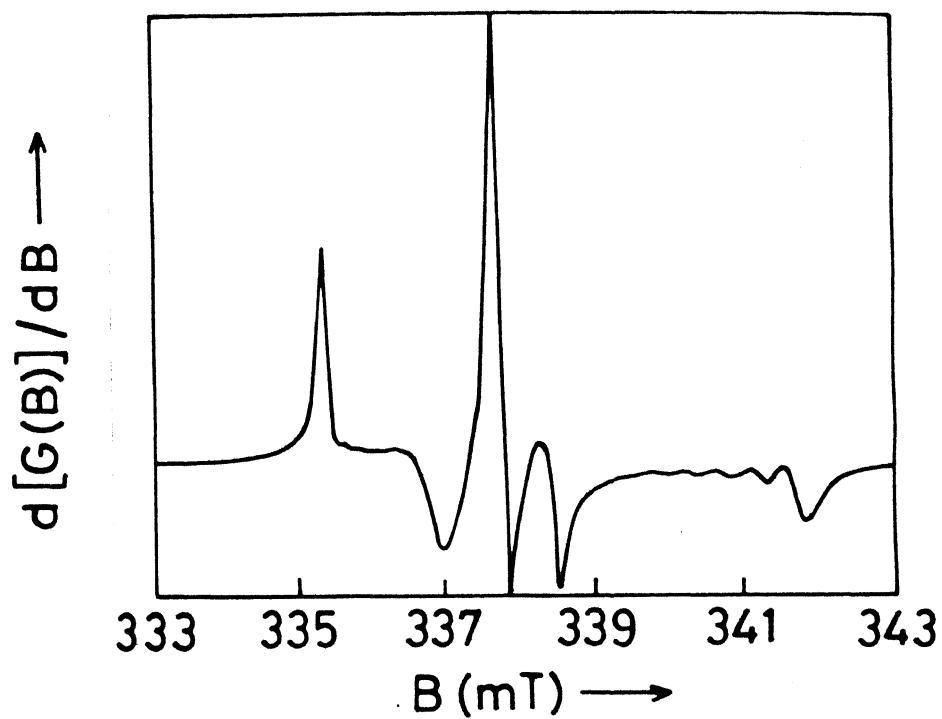


Fig. 5.3 Theoretical EPR lineshapes generated from Eqs. 5.38 and 5.40 at a motional correlation time  $\tau_2 = 1 \times 10^{-7}$  s for the nitroxide center (No. of  $\cos\theta$  values sampled = 10).



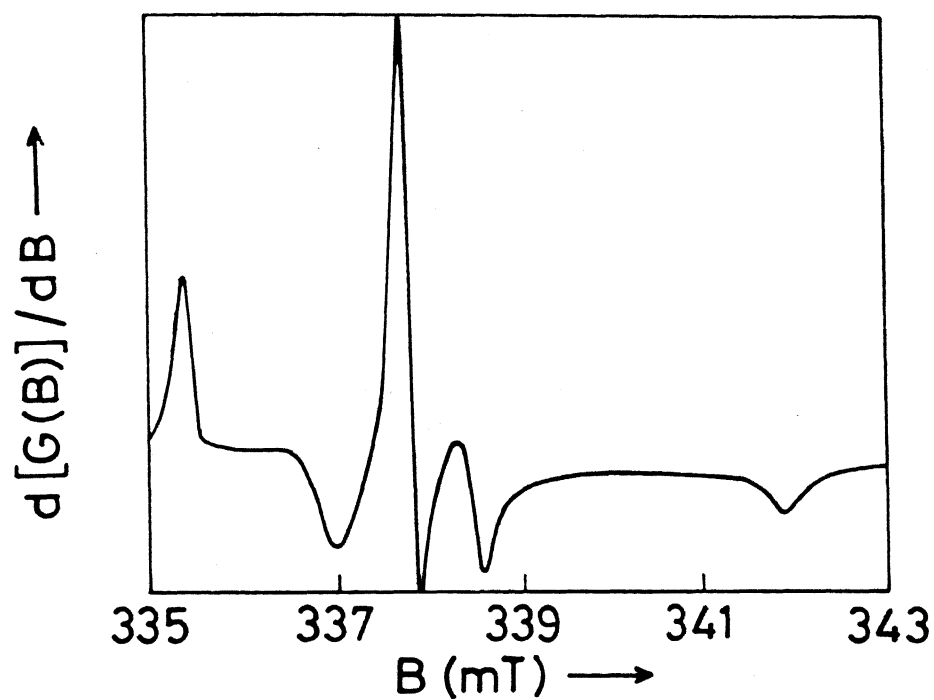


Fig. 5.4 Theoretical EPR lineshapes generated from Eqs. 5.38 and 5.40 at a motional correlation time  $\tau_2 = 1 \times 10^{-7}$  s for the nitroxide center (No. of  $\cos\theta$  values sampled = 25).

calculating the fast orientational-motional correlation time and lineshape function from EPR hyperfine spectra of perdeuterated nitroxides with  $^{15}\text{N}$  ( $I = 1/2$ ). Based on this work,<sup>34</sup> the same authors later on developed a similar method<sup>35</sup> for perdeuterated, normal nitroxide radicals with  $^{14}\text{N}$  ( $I = 1$ ). These theories<sup>34,35</sup> have been used in our work involving normal nitroxide spin probes.

### 5.5.1 Theory

Generally, it is assumed that the total first-derivative peak-to-peak linewidth for the  $M$ th hyperfine component,  $\Delta B_M^T$ , is given by the simple sum

$$\Delta B_M^T = \Delta B_{inh}^{\circ} + \Delta B_M(\tau) \quad (5.55)$$

where  $\Delta B_M(\tau)$  is the first-derivative peak-to-peak Lorentzian motional linewidth and  $\Delta B_{inh}^{\circ}$  is the isotropic inhomogeneous Lorentzian linewidth which is motionally invariant.

However, actual experimental lineshapes of nitroxide hyperfine lines are often not Lorentzian. The reason for this non-Lorentzian experimental lineshape is that the isotropic inhomogeneous line broadening arising from the unresolved superhyperfine interactions with nitroxide intramolecular deuterons and protons is nearly Gaussian rather than Lorentzian in lineshape.

Shetty and Lee<sup>35</sup> have carried out a numerical analysis by convoluting a Gaussian lineshape  $f_G$  having a first-derivative peak-to-peak width of  $\Delta B_G$  over a normalized Lorentzian lineshape  $f_L$  having a first-derivative peak-to-peak width of  $\Delta B_L$ ,

$$F(B) = \int f_L(B-B') f_G(B') dB' = f_L(B) * f_G(B) \quad (5.56)$$

and have found that the total linewidth  $\Delta B_T$  of the resultant lineshape,  $F(B)$ , can be expressed as

$$\Delta B_T = \Delta B_G + \alpha \Delta B_L, \quad (5.57)$$

where  $\alpha$  is the mixing factor which is a smoothly behaving function of  $\Delta B_L/\Delta B_G$  and is different for different hyperfine components. From this relation, the total nitroxide experimental first-derivative peak-to-peak linewidth for the  $M$ th hyperfine components may be written as

$$\Delta B_M^T = \Delta B_{inh}^0 + \alpha_M \Delta B_M(\tau). \quad (5.58)$$

According to Kivelson,<sup>5</sup> the  $\Delta B_M(\tau)$  for the case of nuclear spin  $I = 1$  is given by

$$\begin{aligned} \Delta B_M(\tau) &= [h/\pi\sqrt{3}g_o\mu_B][1/T_2(M)] \\ &= [h/\pi\sqrt{3}g_o\mu_B][(1/15)\Delta A^2 + (4/45)\Delta g^2 + (8/45)\Delta A\Delta gM + (1/18)\Delta A^2M^2]\tau \\ &\equiv G(M)\tau \end{aligned} \quad (5.59a)$$

with

$$\Delta A = (2\pi\mu_B/h) \left\{ [A_z/g_z\mu_B]g_z - 1/2 \left[ [A_x/g_x\mu_B]g_x + [A_y/g_y\mu_B]g_y \right] \right\} \quad (5.59b)$$

$$\Delta g = 2\pi\nu_o \left[ g_z - (1/2)(g_x + g_y) \right] / g_o \quad (5.59c)$$

where  $\Delta g$  and  $\Delta A$  are in units of angular frequency and the nonaxial anisotropy terms such as those depending on  $(g_x - g_y)$  were neglected because of their small contribution. The nonsecular contribution is also neglected in Eq. 5.59(a) as it becomes unimportant in the region where  $\tau \gg 10^{-10}$  s.

Taking sum and difference of the experimental linewidths for the  $M$

and  $M'$  hyperfine components leads to the following expressions,

$$\begin{aligned} |\Delta B_M^T - \Delta B_{M'}^T| &= |\alpha_M \Delta B_M(\tau) - \alpha_{M'} \Delta B_{M'}(\tau)| \\ &= |\alpha_M G(M) - \alpha_{M'} G(M')| \tau \end{aligned} \quad (5.60)$$

and

$$\Delta B_{inh}^\circ = (1/2) \left\{ [\Delta B_M^T + \Delta B_{M'}^T] - [\alpha_M G(M) - \alpha_{M'} G(M')] \tau \right\}. \quad (5.61)$$

The  $\Delta B_M(\tau)$  and  $\Delta B_{inh}^\circ$  thus calculated could be used in Eqs. 5.4 and 5.5, respectively, and the corresponding Lorentzian motional lineshape,  $f_L(B)$ , and Gaussian isotropic inhomogeneous lineshape,  $f_G(B)$ , calculated. By convoluting this Gaussian lineshape  $f_G$  with a normalized Lorentzian lineshape  $f_L$ , the total theoretical lineshape  $F(B)$  is computed as shown in Eq. 5.56.

### 5.5.2 Computational Procedure

In Lee's method,<sup>34</sup> the  $\Delta B_M^T$  values for all the  $M$  hyperfine components were directly measured from the first-derivative experimental EPR spectrum. Then, an iterative procedure was adopted<sup>34</sup> to calculate  $\alpha_M$ ,  $\Delta B_M(\tau)$  and  $\Delta B_{inh}^\circ$  from  $\Delta B_M^T$ . As shown in Fig. 1 of Ref. 34, the average value of the mixing factor for a wide range of  $\Delta B_L/\Delta B_G$  values is approximately 0.6. Accordingly, in our work, we assume a guess value of 0.6 for  $\alpha_M$  and  $\alpha_{M'}$ , and from the measured  $\Delta B_M^T$  and  $\Delta B_{M'}^T$  values, we calculate the initial motional correlation time  $\tau$  using Eq. 5.60. With this initial  $\tau$  value, the motional linewidth  $\Delta B_M(\tau)$  is obtained by using Eq. 5.59a, and the isotropic inhomogeneous linewidth  $\Delta B_{inh}^\circ$  is determined by Eq. 5.61. From the resultant linewidth ratio of  $\Delta B_M(\tau)/\Delta B_{inh}^\circ$ , the corresponding new values are obtained for  $\alpha_M$  and  $\alpha_{M'}$  from

Fig. 1 of Ref. 34. This procedure may be iterated to get accurate experimental  $\alpha_M$  and  $\alpha_{M'}$  at the sample temperature for each hyperfine component.

Using the accurate experimental values of  $\Delta B_M^T$ ,  $\Delta B_{M'}^T$ ,  $\alpha_M$  and  $\alpha_{M'}$ , obtained as above, the associated  $\tau$  value is extracted from Eq. 5.60. This  $\tau$  value is then substituted into Eq. 5.59a, whereby the corresponding motional linewidths for the two hyperfine components  $\Delta B_M(\tau)$  and  $\Delta B_{M'}(\tau)$  could be determined. Finally, with these values of  $\Delta B_M^T$ ,  $\Delta B_{M'}^T$ ,  $\Delta B_M(\tau)$ ,  $\Delta B_{M'}(\tau)$ ,  $\alpha_M$  and  $\alpha_{M'}$ , the isotropic inhomogeneous linewidth  $\Delta B_{inh}^0$  at the sample temperature could be estimated nicely.

The final step of our computation is the convolution of two lineshapes  $f_L$  and  $f_G$  as shown in Eq. 5.56.

Since there is no detail given regarding how the plot shown in Fig. 1 of Ref. 34 was obtained, we have constructed our own plot, as below. Roughly 50 different values of  $(\Delta B_L/\Delta B_G)$  were taken in the range 0.2 to 5.0. These values were obtained by keeping the  $\Delta B_G$  constant and varying  $\Delta B_L$  in steps of 0.05 from 0.1. The  $\Delta B_L$  and  $\Delta B_G$  values were used in Eqs. 5.4 and 5.5 to get appropriate lineshape functions. These two lineshapes were convoluted and the resultant lineshape was obtained. A Fortran program was written to perform all the calculations. The  $\Delta B^T$ 's of the resultant lineshape was accurately measured, as shown in Fig. 5.5, after plotting the second derivative of the EPR spectral lineshapes against magnetic field. Then  $\alpha$ 's for specific  $(\Delta B_L/\Delta B_G)$  values were calculated from Eq. 5.57. The calculated  $\alpha$  values were plotted against the  $(\Delta B_L/\Delta B_G)$  values as shown in Fig. 5.6. The best fit for this curve has been found out to be

$$\alpha = 0.63(\Delta B_L/\Delta B_G)^{0.17} \quad (5.62)$$

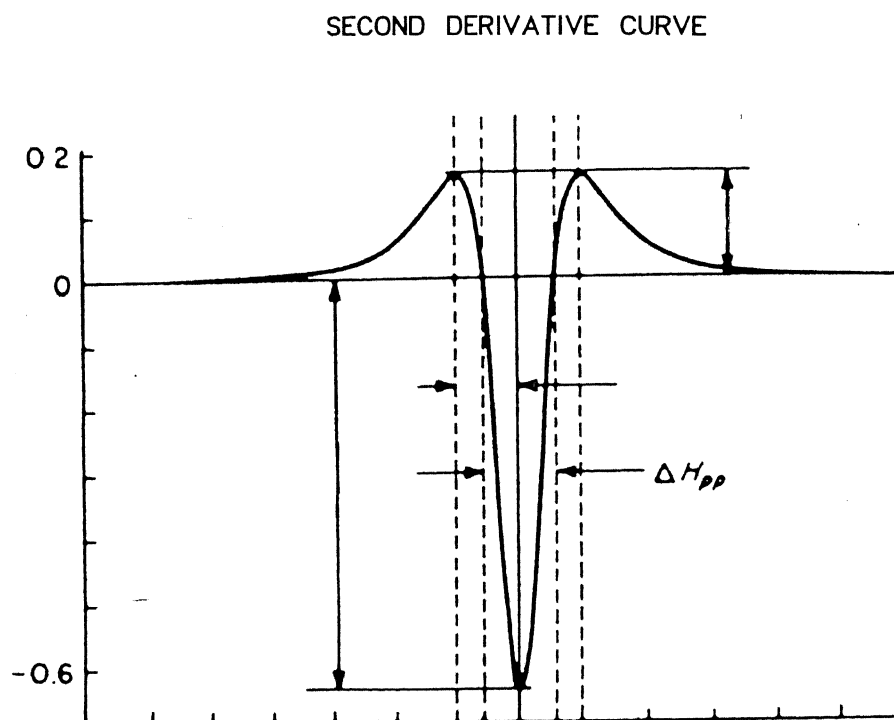


Fig. 5.5 Determination of  $\Delta B_{pp}$  from the second derivative of the absorption curve.

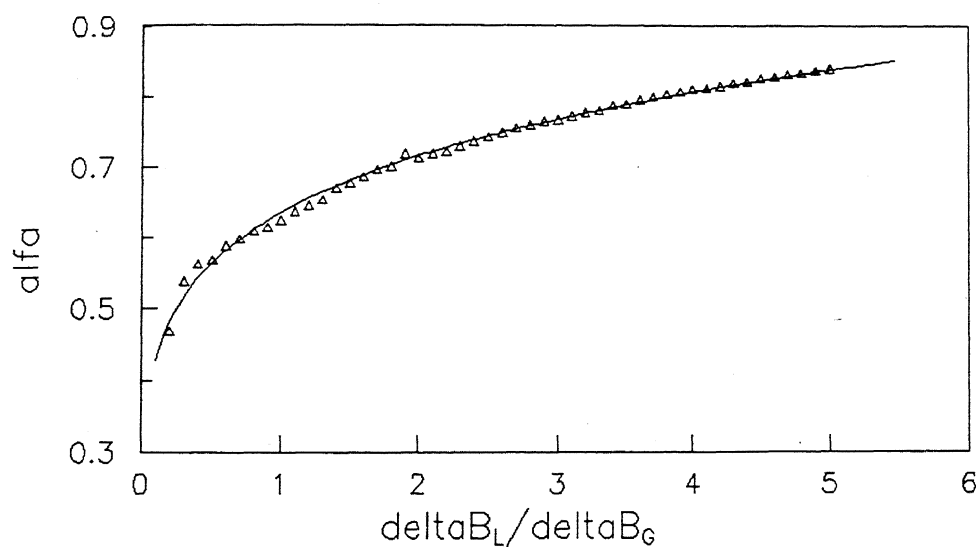


Fig. 5.6 Plot of the mixing factor,  $\alpha$ , of Eq. 5.57 for the total peak-to-peak linewidth  $\Delta B_T$  (resulting from the convolution of a Gaussian envelope of peak-to-peak width  $\Delta B_G$  over a Lorentzian envelope of peak-to-peak width  $\Delta B_L$ ) as a function of  $\Delta B_L / \Delta B_G$ .

In our method, Eqs. 5.59-5.62 have been used to perform the iterations. The Fortran program used to simulate experimental EPR lineshapes using our procedure is given in the Appendix.

### 5.5.3 Discussion

The performance of our computer program developed to analyze the lineshapes of fast motional spectra was tested with certain experimental EPR spectra recorded at room temperature. For this purpose, EPR spectra were recorded by dissolving Tempol spin probe in the water pools of lecithin/cyclohexane/H<sub>2</sub>O reverse micelles. Since there are no significant changes in  $g_0$  and  $A_0$  values (directly measured from the spectra) when going from low 'R' to high 'R', the same  $g$  and  $A$  tensor components were used as input parameters throughout this simulation process, the component values of the tensors being<sup>36</sup>

$$\left. \begin{array}{ll} g_{xx} = 2.0095 & (A_{xx}/g_{xx}\mu_B) = 0.655 \text{ mT} \\ g_{yy} = 2.0064 & (A_{yy}/g_{yy}\mu_B) = 0.655 \text{ mT} \\ g_{zz} = 2.0022 & (A_{zz}/g_{zz}\mu_B) = 3.370 \text{ mT} \end{array} \right\} \quad (5.63)$$

Apart from these, the linewidths of hyperfine components of the Tempol spin probe measured at different 'R' values were also used as input parameters in the program. These are listed in the Table 5.1. The parameters given in Eq. 5.63 and Table 5.1 have been successfully used in our 'fast motion program' to get satisfactory fits for the experimentally observed spectral responses. These theoretically computed spectra are shown with the experimental lineshape in Figs. 5.7(a-d). The agreement, as evident from Figs. 5.7(a-d) between simulated and experimental curves is very satisfactory.



Table 5.1 Input parameters used in the program

R	$\Delta B_{+1}^T$ (mT)	$\Delta B_0^T$ (mT)	$\Delta B_{-1}^T$ (mT)
6	0.200	0.244	0.313
7	0.175	0.188	0.222
8	0.188	0.188	0.219
9	0.181	0.188	0.219
10	0.179	0.175	0.206

Having obtained computer simulated spectra which match the experimental profiles, we shift our focus to discuss the implication of results obtained in terms of (1) motional linewidths (2) inhomogeneous broadening and (3) the mixing factors. These output parameters  $\Delta B_M(\tau)$ ,  $\Delta B_{inh}$ ,  $\alpha$  and  $\tau$  for various 'R' values are calculated in the program. Fig. 5.8 shows the dependence of motional linewidths, obtained from our program, on 'R' for all the three  $^{14}\text{N}$  hyperfine components. The trends of variation for different hyperfine components with 'R' are similar in nature. However, the magnitude of variation of  $\Delta B_{M=-1}(\tau)$  is more compared to  $\Delta B_{M=0}(\tau)$  and  $\Delta B_{M=+1}(\tau)$  at all 'R'.

In Table 5.2 the inhomogeneous broadening and mixing factors are shown with corresponding correlation times for Tempol spin probe in reverse micelles at different 'R'. For comparison,  $\tau$ 's obtained from our program are listed along with the values from other conventional methods in Table 5.2. Clearly,  $\tau$ 's from the conventional method which uses first derivative intensities disagree with the  $\tau$  values obtained from our program. This is due to the fact that the conventional method contains isotropic inhomogeneous broadening as Lorentzian in nature, while in our method this is Gaussian.

Based on the observations above it may be reliably concluded that the motional correlation times calculated using our program are more accurate. Our

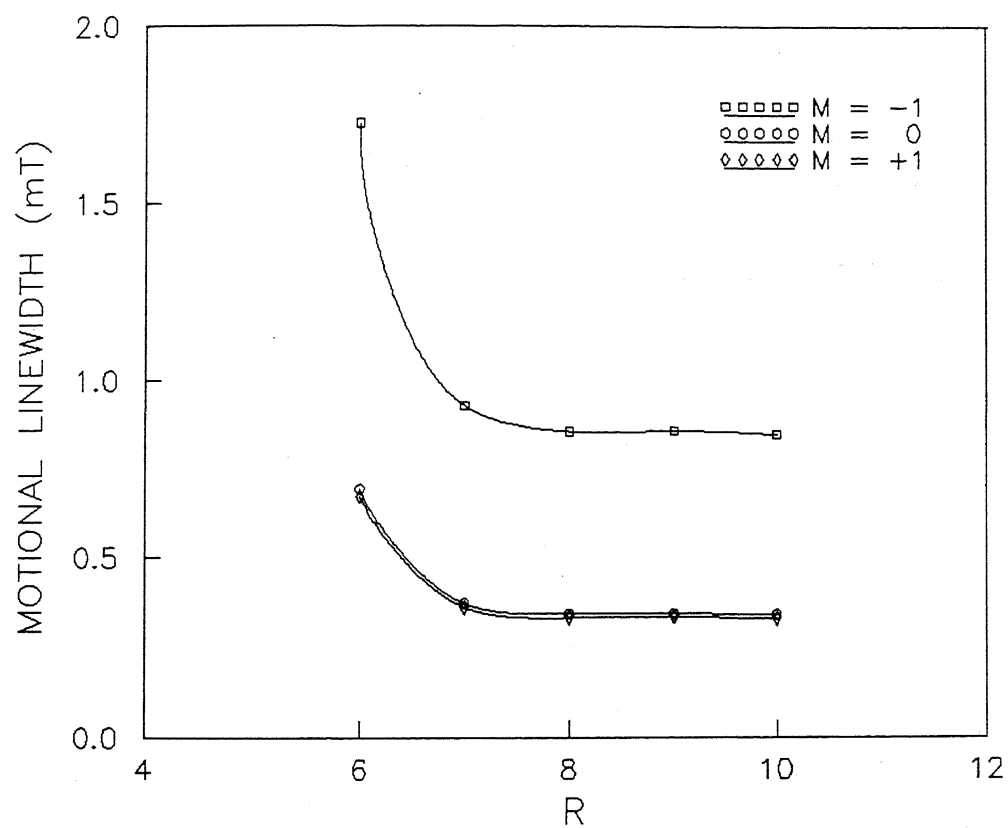


Fig. 5.8 Dependence of motional linewidths  $\Delta B_M(\tau)$  on 'R'.

**Table 5.2**      Various spectral parameters derived using our computer program

R	$\Delta B_{inh}^o$ (mT)	$\alpha_{+1}$	$\alpha_o$	$\alpha_{-1}$	$\tau \times 10^{10}$ (s)	$\tau \times 10^{10*}$ (s)
6	2.070	0.607	0.519	0.526	6.086	5.90
7	1.695	0.565	0.483	0.484	3.268	3.64
8	1.712	0.556	0.476	0.473	3.025	4.11
9	1.711	0.556	0.476	0.475	3.017	3.72
10	1.587	0.563	0.481	0.479	2.992	3.48

\* from conventional method.

conclusion that the isotropic inhomogeneous linewidths from normal nitroxides are essentially Gaussian has been supported by a recent report<sup>37</sup> on EPR studies of some aqueous micelles.

## 5.6 Conclusions

The computational methods developed for 'slow motional spectra' of nitroxides (section 5.4.2) should enable us to investigate the general behavior of EPR hyperfine spectra under isotropic orientational diffusion motion in polycrystalline/amorphous substances at room temperature and liquid samples (nitroxides in reverse micellar solution) at low temperature. The algorithm developed for the abovementioned purpose is a very simple and fast one. The 'systematic sampling' technique enables us to reduce the error normally occurring in lineshape computations. Further, we have clearly demonstrated that only 25 sampling points ( $\cos\theta$  values in the range 0-1) are needed to achieve required convergence. Finally, our computational procedure is capable of handling multidimensional integrals with minimum error.

We have also developed a second computer program which expedites the lineshape analysis of the EPR spectra of nitroxide spin probes undergoing fast motion. The program also facilitates an assessment of the contributions from motional (Lorentzian) and inhomogeneous (Gaussian) broadenings to the total experimental linewidths. The total theoretical lineshapes computed by convoluting the inhomogeneous Gaussian lineshape having width of  $\Delta B_{inh}^{\circ}$  over the motional Lorentzian lineshape having width  $\Delta B(\tau)$  are in good agreement with corresponding lineshapes [Figs. 5.7(a-d)]. Finally, it is demonstrated that our computations lead to more accurate evaluation of correlation times than has been possible heretofore in 'fast motion' limit experiments.

## REFERENCES

1. S. Ohnishi and H. M. McConnell, J. Am. Chem. Soc. **87**, 2293 (1965).
2. T. J. Stone, T. Buckman, P. L. Nordio and H. M. McConnell, Proc. Nat. Acad. Sci. (USA) **54**, 1010 (1965).
3. P. Raghunathan, in : **Electron Magnetic Resonance of the Solid State**, J. Weil (ed.) Can. Soc. Chem., Ottawa, 1987, Chap. 3.
4. J. S. Hyde, L. R. Dalton, Chem. Phys. Lett. **16**, 568 (1972).
5. D. Kivelson, J. Chem. Phys. **33**, 1094 (1960).
6. S. A. Goldman, G. V. Bruno, C. F. Polnaszek and J. H. Freed, J. Chem. Phys. **56**, 716 (1972).
7. C. F. Polnaszek, S. Schreier, K. W. Butler and I. C. P. Smith, J. Am. Chem. Soc. **100**, 8223 (1978).
8. J. S. Hwang, R. P. Mason, L. P. Hwang and J. H. Freed, J. Phys. Chem. **79**, 489 (1975).
9. J. H. Freed, G. V. Bruno and C. F. Polnaszek, J. Phys. Chem. **75**, 30 (1971).
10. H. Sillescu and D. Kivelson, J. Chem. Phys. **48**, 3493 (1968).
11. R. G. Gordon and T. Messenger, in : **Electron Spin Relaxation in Liquids**, L. T. Muus and P. W. Atkins (eds.), Plenum, New York, 1972, p.341.
12. A. E. Stillman, G. P. Zientara and J. H. Freed, J. Chem. Phys. **71**, (1979).
13. P. W. Anderson, J. Phys. Soc. Japan **9**, 316 (1954).
14. a) M. S. Itzkowitz, J. Chem. Phys. **46**, 3048 (1967).  
b) M. Fixman, J. Chem. Phys. **48**, 223 (1968).  
c) M. Saunders and C. S. Johnson, J. Chem. Phys. **48**, 534 (1968).
15. a) J. R. Norris and S. I. Weissmann, J. Phys. Chem. **73**, 3119 (1969).  
b) N. N. Korst and A. V. Lazarev, Mol. Phys. **17**, 481 (1969).
16. I. V. Alexandrov, A. N. Ivanova, N. N. Korst, A. V. Lazarev, A. Prinkhozhenko and V. B. Stryukov, Mol. Phys. **18**, 681 (1970).
17. J. B. Pederson, J. Chem. Phys. **57**, 2680 (1972).
18. R. C. McCalley, E. J. Shimshick and H. M. McConnell, Chem. Phys. Lett. **13**, 115 (1972).
19. C. S. Johnson, Jr., J. Chem. Phys. **41**, 3277 (1964).
20. a) J. H. Freed J. Chem. Phys. **49**, 376 (1968).  
b) A. Baram, Z. Luz and S. Alexander, J. Chem. Phys. **58**, 4558. (1973).

21. J. H. Freed, in : **Electron Spin Relaxation in Liquids**, L. T. Muus and P. W. Atkins, (eds), Plenum, New York, 1972, p. 387.
22. B. Yoon, J. M. Deutch and J. H. Freed, *J. Chem. Phys.* **62**, 4687 (1975).
23. S. Lee, *Phys. Rev. B* **23**, 6151 (1981).
24. D. Kivelson and S. Lee, *J. Chem. Phys.* **76**, 5746 (1982).
25. S. Lee and D. P. Ames, *J. Chem. Phys.* **80**, 1766 (1984).
26. A. Abragam and B. Bleaney, **Electron Paramagnetic Resonance of Transition Ions**, Oxford University, London, 1970.
27. A. G. Redfield, *IBM J. Res. Dev.* **1**, 19 (1957); *Adv. Magn. Reson.* **1**, 1 (1965).
28. S. C. Sivasubramanian, Ph.D. Thesis, Indian Institute of Technology, Kanpur, India (1989).
29. P. Raghunathan and S. C. Sivasubramanian, *J. Phys. Chem.* **95**, 6346 (1991).
30. P. Raghunathan and S. C. Sivasubramanian, *J. Non-Crystalline Solids* **136**, 14 (1991).
31. J. M. Hammersley and D. C. Handscomb, **Monte Carlo Methods**, Methuen, London 1967.
32. A. Papoulis, **Probability, Random Variables and Stochastic Processes**, McGraw-Hill, Inc., New York, 1965.
33. H. Khan, in : **Symposium on Monte Carlo Methods**, H. A. Meyer (ed.), John Wiley & Sons, New York, 1956.
34. S. Lee and A. Shetty, *J. Chem. Phys.* **83**, 499 (1985).
35. A. Shetty and S. Lee, *J. Chem. Phys.* **83**, 6150 (1985).
36. **Spin Labeling : Theory and Applications**, L. J. Berliner (ed.), Academic, New York, (1976), p 565.
37. B. L. Bales and C. Stenland, *J. Phys. Chem.* **97**, 3418 (1993).

## CHAPTER 6

## CONSTRUCTION OF A PC-EPR SPECTROMETER INTERFACE

## 6.1 Motivation

In Electron Paramagnetic Resonance spectroscopy, either cost considerations or technical reasons force us to use only a moderate concentration of paramagnetic species. This situation arises quite commonly in EPR spin labeling studies of enzymes, peptides, reverse micelles, and other biomembranes. Since EPR spectral intensity is directly proportional to the concentration of paramagnetic species used (until the electron 'exchange narrowing' mechanism distorts the spectrum), we often get spectra with poor 'signal-to-noise ratio' (S/N). It is very difficult either to analyze or to match these lineshapes with the ones already reported or theoretically simulated. It often becomes very essential to improve the S/N of the EPR spectral lineshapes before doing any meaningful analysis.

There are two techniques<sup>1</sup> for improving the S/N by signal averaging, namely,

- (i) *usual manipulation of time-constant and spectral band width settings of the EPR spectrometer,*
- (ii) *interfacing a computer with the spectrometer.*

The first technique involves filtering the output of the phase-sensitive-detector by the use of a resistive-capacitive filter network (see Fig. 6.1).

The product  $RC$  of this filter has units in seconds if the resistance  $R$  is expressed in megaohms and the capacitance  $C$  in microfarads. The filter attenuates noise components with a frequency greater than  $\sim (RC)^{-1}$ . However,

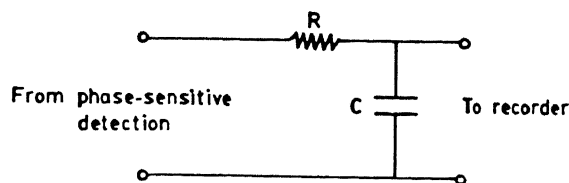


Fig. 6.1 Resistive-capacitive filter network.

use of the filter restricts the rate at which a line may be scanned. A good working rule is to adjust the scan rate such that the time ' $\tau$ ' required to go from peak to peak on a derivative line is such that  $\tau > 10 \times RC$ . Scan times less than this will distort the line. It is desirable to have a large range of RC combinations (e.g.  $10^{-3}$  s to 100 s) depending on the signal-to-noise ratio required and the rate at which the spectrum is to be scanned.

The use of an RC filter improves the S/N ratio in proportion to  $\sqrt{RC}$ , since the effective bandwidth of the spectrometer is usually governed by the time constant of the output filter i.e.,  $b = (RC)^{-1}$ . However, there are practical considerations that limit the magnitude of the product RC which can be used. These usually include (1) the limited life time of a paramagnetic specie and (2) instrumental instability (base line drift, drift of klystron frequency, or power output).

The second technique for signal averaging involves performing repeated scans, and adding spectral intensities at various magnetic fields. This is accomplished by dividing the spectrum into equal intervals (typically 512 or 1024 or 4096 digital points). Each portion is stored in a separate channel of a time-averaging computer. The coherent signal in each channel will build up in proportion to ' $n$ ', the number of scans. However, due to its randomness, a noise signal will tend to cancel; in fact, it will increase in proportion to  $\sqrt{n}$ . Thus there will be an improvement in S/N proportional to



$\sqrt{n}$ . The resulting spectrum can then be plotted out at any time either on an external recorder or on the spectrometer recorder itself.

## 6.2 Advantages of Interfacing a Computer<sup>2</sup>

Experimental spectra often require operations such as baseline correction, integration, differentiation, sum, difference and simulation. These are easily achieved when the spectral data can be analyzed in digital form. Interfacing a computer provides us the digital data needed for these kinds of operations. Some of the advantages are explained below.

One simple application that is routinely found advantageous is the scaling of experimental spectra. This is illustrated in Fig. 6.2, where these spectra were collected using the same sample. The instrumental variables of scan range, gain and phase reversal contribute to the apparent differences in the experimental spectra (left column, Fig. 6.2). In the right column these spectra have been replotted to the same horizontal scale and normalized to an arbitrary vertical scale. This procedure will help us in revealing (or finding 'frequently disappearing small apparent differences' in spin labeling EPR spectra. This procedure will also help to compare experimental spectra to computationally generated theoretical lineshapes. In principle, the calculated lineshapes can be scaled individually to each experimental spectrum. In practice, however, it is simpler to scale the experimental spectra to the calculated ones. A typical example is given in Fig. 6.3.

Integrating once yields the absorption spectra, analogous to the familiar spectra of optical absorption or NMR spectroscopy (middle row of Fig. 6.4). A second integration (i.e., integrating the absorption spectrum) is often performed to determine relative concentrations, and the results are shown in the top portion of Fig. 6.4. The bottom row of Fig. 6.4 consists of

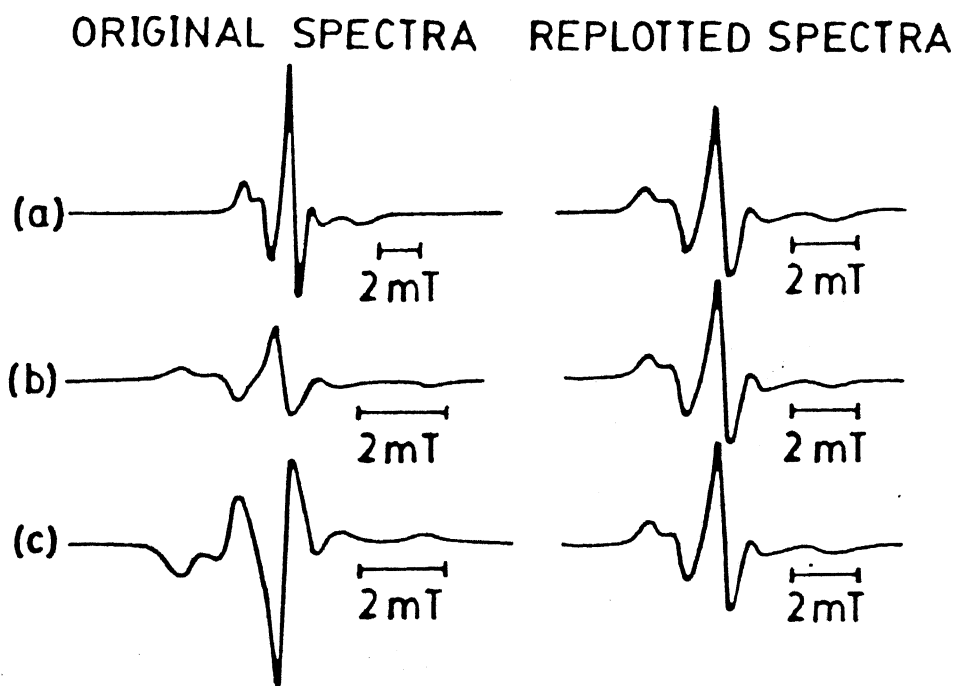


Fig. 6.2 Horizontal and vertical scaling of first derivative spectra. (a) spectrum recorded with a scan range of 20 mT. Spectra (b) and (c) were recorded with a scan range of 10 mT, with spectrum (c) recorded with reverse phase, and spectrum (b) recorded using a lower gain setting. Each of the original spectra has been replotted on the right to have the same horizontal and vertical dimension, (from Ref. 2).

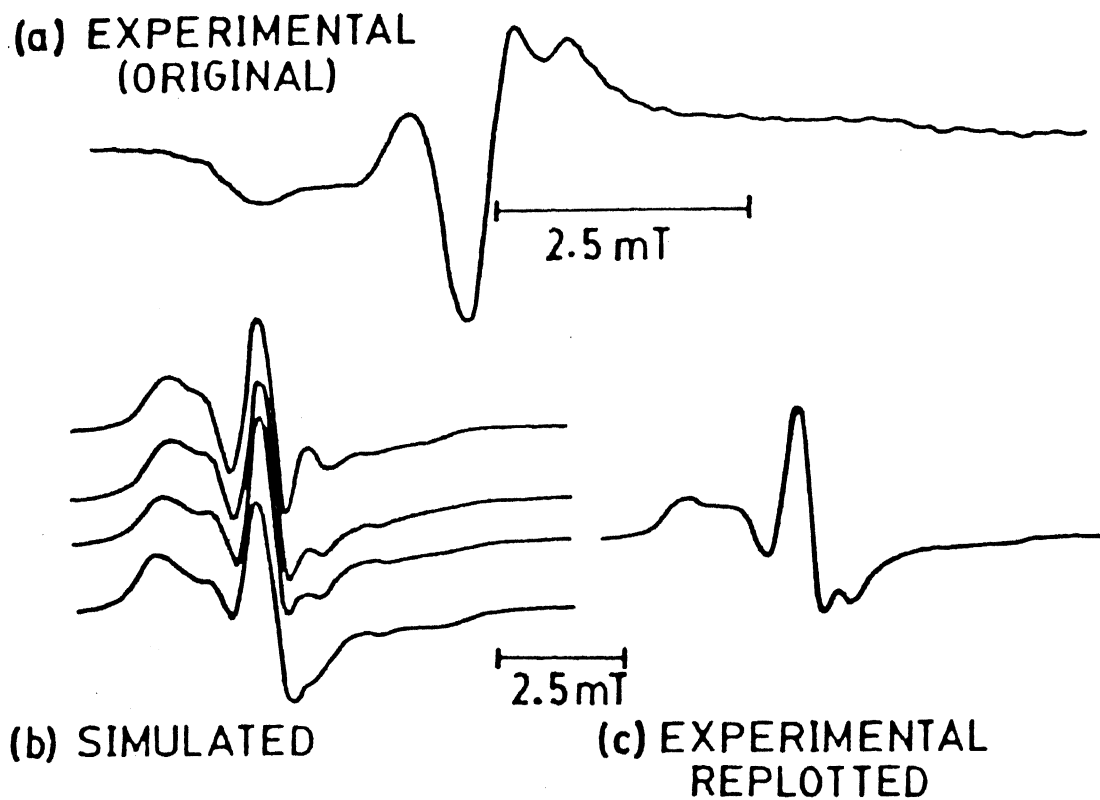


Fig. 6.3 Replotting experimental data. (a) the original experimental spectrum from a dehydrated oriented lecithin preparation containing 5-doxylstearic acid; (b) simulations from large computer to be compared; (c) experimental spectrum (a) replotted to match horizontal and vertical scales and phase of spectra both splittings and lineshape (from Ref. 2).

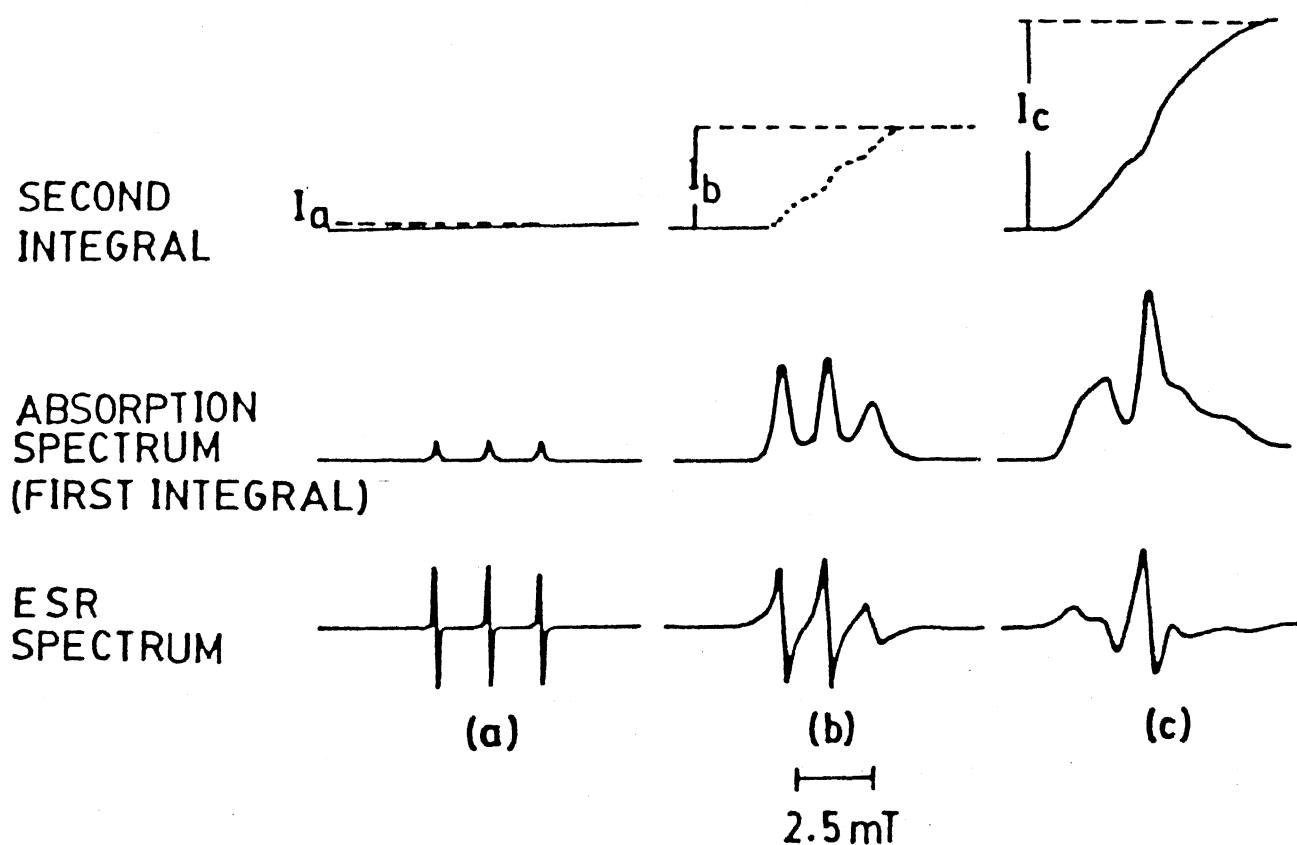


Fig. 6.4 Integration by computer. (a) freely tumbling nitroxide : the same sample as for Fig. 3; (b) moderately immobilized nitroxide: 16-doxylstearic acid in an aqueous dispersion of lecithin; (c) strongly immobilized nitroxide : 5-doxyl stearic acid in an aqueous dispersion of lecithin : cholesterol, molar ratio 2:1. All spectra were recorded at room temperature. The middle line of all three first derivative EPR spectra are of same height.

the familiar first derivative EPR spectra. The heights  $I_a$ ,  $I_b$  and  $I_c$  are proportional to the concentration of the probe, and  $I_a : I_b : I_c$  is approximately 1:19:40. For purposes of illustration, the middle line of each of the first derivative spectra in Fig. 6.4 has been arbitrarily adjusted to the same height before integration. When this height is held constant, the relationship between the EPR linewidth and the radical concentration is dramatically evident. A small concentration of freely tumbling nitroxide has a relatively large first derivative peak height. From Fig. 6.4 one readily appreciates the interesting fact that quite a low concentration of unbound spin label in the presence of bound label may dominate the composite spectrum obtained.

Whenever a nitroxide spin label partitions between two or more environments, the resultant spectrum will be a complex spectrum. To analyze these kinds of composite spectra, storing the digital data of the respective spectra would be a very desirable procedure. If the data are digitized, combinations of spectral subtraction and subsequent double integration can be used to determine the relative concentration of label in the two environments. It is necessary to obtain or simulate the spectrum of at least one component. The next necessary step may be to adjust the spectra for slanting baseline and offset so that the baseline value is zero. The spectra are then shifted horizontally relative to each other so that they are in register. Finally, incremental subtractions are carried out until an obvious endpoint is reached (e.g. negative baseline or phase reversal of peaks). Such an example is given in Fig. 6.5.

The above arguments illustrate that computer interfacing often proves to be a powerful tool in many ways. When we tried to carry out a detailed EPR lineshape study on the enzymes incorporated in the water pools of reverse micelles, we happened to come across an example in the literature<sup>3</sup>

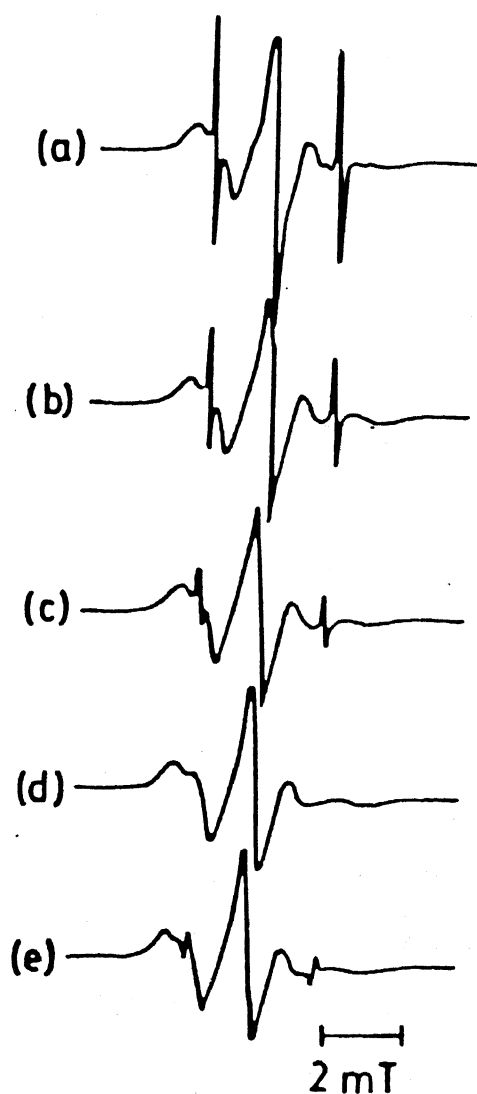


Fig. 6.5 Spectral subtraction by computer. (a) Is a room temperature composite spectrum. Two capillary tubes were placed in the cavity, one containing an aqueous dispersion of  $1.5 \times 10^{-3}$  M 5-doxylstearic acid in lecithin, the second containing  $5 \times 10^{-5}$  M piperidone nitroxide in water. (b) - (e) Are traces produced by subtracting increasing amounts of the sharp three-line spectrum from the composite spectrum, with total subtraction occurring in spectrum (d). In spectrum (c), too much of the sharp three-line spectrum has been subtracted (note three sharp lines of this spectrum are phase-reversed) (from Ref. 2).

where the authors have recorded a very poor EPR signal for lysine-labeled tryptophanase in a reverse micellar environment. Had a computer interfacing been employed with EPR spectrometer, it would have been possible for the authors to get a much better signal for analysis. In this study, the concentration of the spin labeled enzymes could not be increased, however, since the tiny water pool was not able to 'accommodate' all of the label. Such examples, as well as some of our own initial experiments, have prompted us to do a computer interfacing to our EPR spectrometer.

### 6.3 Survey of Existing Interfacing Methods for EPR Spectrometer

So far, there is no single universally accepted method for interfacing a computer with EPR spectrometer. The level of sophistication and the number of limitations do vary with different methods. Van Camp *et al*<sup>4</sup> have given an extensive review of all the methods up to 1980. Goldberg<sup>5</sup> *et al* have shown how an EPR spectrometer can be controlled by computer. Digital data acquisition has also been done very elegantly by Herring<sup>6</sup> *et al*. Posener,<sup>7a-c</sup> has also shown how signal averaging can be done. Though an early method due to Ernst<sup>8</sup> is for NMR, it can be used for detecting and processing EPR signals also. Resolution enhancement of EPR signals by the FT technique<sup>9-12</sup> has also proved to be a generally good method.

On-line EPR data collection systems involving direct connection to a central mainframe computer<sup>13</sup> or mini computer<sup>5,14</sup> have been shown to be more convenient and efficient than on-line EPR data storage using paper<sup>7a,15</sup> or magnetic tape<sup>16</sup> for later processing at a computer installation. Some of the EPR data acquisition systems reported in the literature are either microprocessor based<sup>6,17-19</sup> or dedicated to a specific computer.<sup>20,21</sup> All these data collecting systems, except the one mentioned in Ref. 20, use interfaces design-

ed to operate only in 'talk' mode, which prevents active communication from the host computer to the EPR spectrometer. A versatile computer interface system has been presented by Quine *et al.*,<sup>22</sup> operating in the listen/talk mode through either the RS232 or the IEEE-488 communication bus. These workers also had to provide the Varian E-203 magnetic field controller with extensive electronic modification to permit computer control of the magnetic field. Recently Giugliarelli *et al.*, have reported a method<sup>23</sup> which is versatile in many respects. But the problem with their method is, that, the construction of the hardware will be a laborious task.

#### 6.4 Design Criteria

Having gone through the literature available in this area, we have chosen the following important design criteria to be incorporated in our proposed interface.

- (i) the interface should not be both spectrometer and computer specific, as in most previous cases;<sup>6,7a,13,14</sup>
- (ii) it should be able to operate in the listen/talk mode to facilitate active communication with the host computer. If this is taken care of, then the X-Y recorder of our EPR spectrometer will itself be in a position to operate both for normal spectral tracings and for recording any theoretically generated spectral lineshapes;
- (iii) the interface should control the magnetic field scanning EXTERNALLY without moving the recorder arm;
- (iv) finally, the interface should use inexpensive and readily available electronic components.

Throughout this work, we have followed the method of Trousson *et al.*<sup>20</sup> with some significant modifications. Fig. 6.6 shows the block diagram



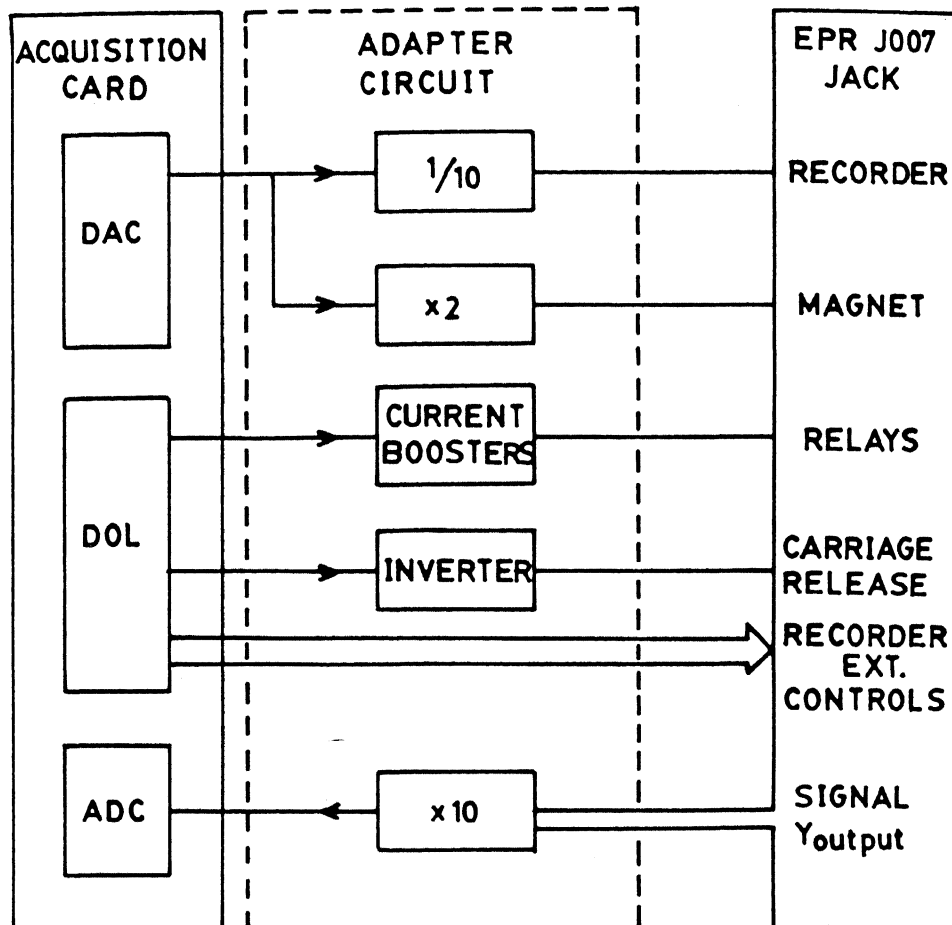


Fig. 6.6 Block diagram of EPR data acquisition system (DAS).

of our EPR data acquisition system. The scan time and number of points to be acquired will be controlled by the computer, while the rest of the settings will be selected from the console of our EPR spectrometer. In the Varian E-109 spectrometer, the field sweep is driven by a voltage ramp (-10 V to +10 V) generated by an electromechanical potentiometer placed on the step-motor axis devoted to the scanning of the recorder. We have planned to generate this voltage ramp using DAC (Digital-to-Analog Converter). To acquire digital EPR signal data an ADC (Analog-to-Digital Converter) is used, whose detailed functions are elaborated in the subsection 6.5.2.1. Recording of the signal thus stored can be done using the same DAC. This recording is also controlled by the computer.

ADC and DAC sections of the interface are connected through the PC data bus. The interface adapter is also linked to the PC through the data bus.

## 6.5 Hardware

The block diagram of the whole data acquisition system (DAS) has been shown in Fig. 6.6. This DAS can be divided into four parts, namely,

- (1) the IBM compatible PC-AT,
- (2) the acquisition card,
- (3) the adapter circuit, and
- (4) the EPR J007 input/output jack in the EPR spectrometer console for two-way communication with the adapter circuit.

Further detailed specifications of these parts shall be given below.

### 6.5.1 Specifications

#### 6.5.1.1 The IBM-Compatible PC-AT

The PC-AT which has been used in our DAS has the following specifications:

- (a) One Mbyte memory,
- (b) a monochrome monitor,
- (c) keyboard,
- (d) 41 Mbyte hard disk
- (e) 1.2 Mbyte  $5\frac{1}{4}$ " floppy disk single drive,
- (f) operating system version DOS 5.0,
- (g) 2 serial and 1 parallel ports,
- (h) 80286 microprocessor (12 MHz),
- (i) 80287 math co-processor.

The above PC has a couple of 31-pin jacks for purposes of upgradability, and we have used one of these for installing our acquisition card.

#### 6.5.1.2 Acquisition Card

In our acquisition card, we intended to have an analog-to-digital converter (ADC), a digital-to-analog converter (DAC), and 16 digital output lines (DOL). A suitable card having the above specifications was custom built and supplied by Vinytics Peripherals Pvt. Ltd (India). This acquisition card has a 12-bit ADC, with 16 channels for receiving analog input. Two multiplexers (MUX AD 7503) are also present before the signal reaches the ADC. LF 398 sample and hold (S/H) circuit is also used in the ADC part of the circuit. The DAC part of the acquisition card consists of AD7521 IC, 12-bit, 500 nsec current setting time and 0.02% non-linearity. Both the ADC and DAC work with bipolar input/output signals. The DAC also consists of two 74LS374 ICs (octal D flip-flop tristate). See Fig. 6.7.

#### 6.5.1.3 Adapter Circuit

The acquisition card described above is versatile which can ensure link to almost any instrument. But, adapter circuit is the important part of

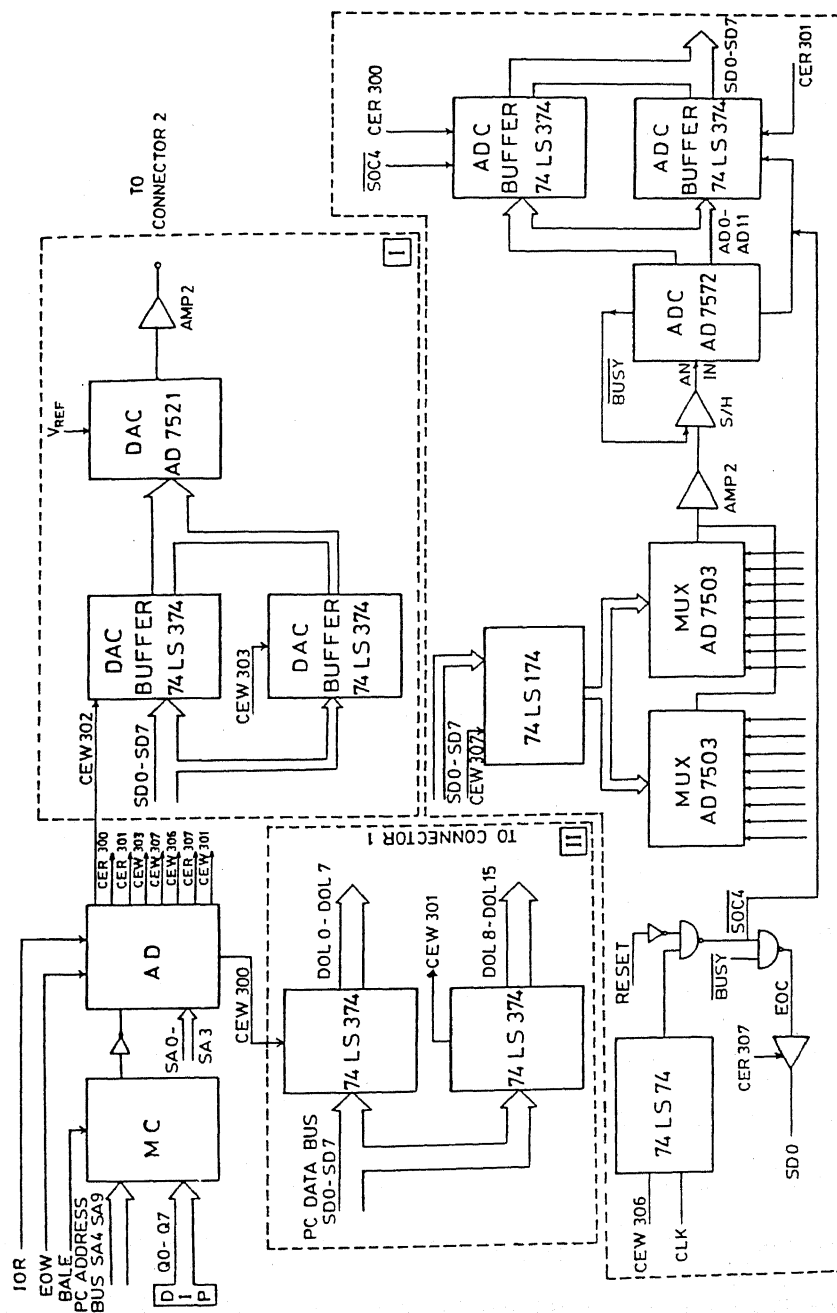


Fig. 6.7 Layout of the acquisition card.

the DAS in the sense that it is specifically designed to establish interface between the PC and EPR spectrometer. The method reported by Trousson *et al.*<sup>20</sup> has been followed in designing this circuit, which is designed to match the  $\pm 5$  V requirement of DAC,  $\pm 1$  V requirement of ADC, as well as the TTL (transistor-transistor logic) level requirements of DOL, and 20 mA current sink requirement of EPR control relays. The circuit is shown in detail in Fig. 6.8. The components used in designing the adapter circuit are one IC 7404 inverter, four operational amplifiers (741), and two BC 147B transistors. All these components are rather easily available in the market.

#### 6.5.1.4 EPR Jack J007

The rear panel of the E-006D operator's console of our E-109 spectrometer has a J007 data input/output jack, which provides all the necessary connections from and to the spectrometer. The jack comprises 34 pins. Sixteen out of these 34 pins have been selected for our interfacing purposes. The necessary connection from and to the jack are shown in Table 6.1.

### 6.5.2 Functional Details of the Hardware

#### 6.5.2.1 Acquisition Card

First of all, 30xh (where x varies from 0 to F) address is set in the DIP switch (refer to Fig. 6.7). This will be one of the two inputs needed for magnitude comparator (MC) IC. The other input comes from the Address Bus of the PC-AT (SA4-SA9). When MC receives a valid address and AEN input, it compares PCAB (PC-address Bus) and DIP switch. If both are equal it gives an output which will be inverted and sent to Address Decoder (AD) ICs. AD also receives PCAB (SA0-SA3) and IOR and IOW signals (PC control signals). Depending upon whether the IOR or IOW signal is received, AD will generate Chip

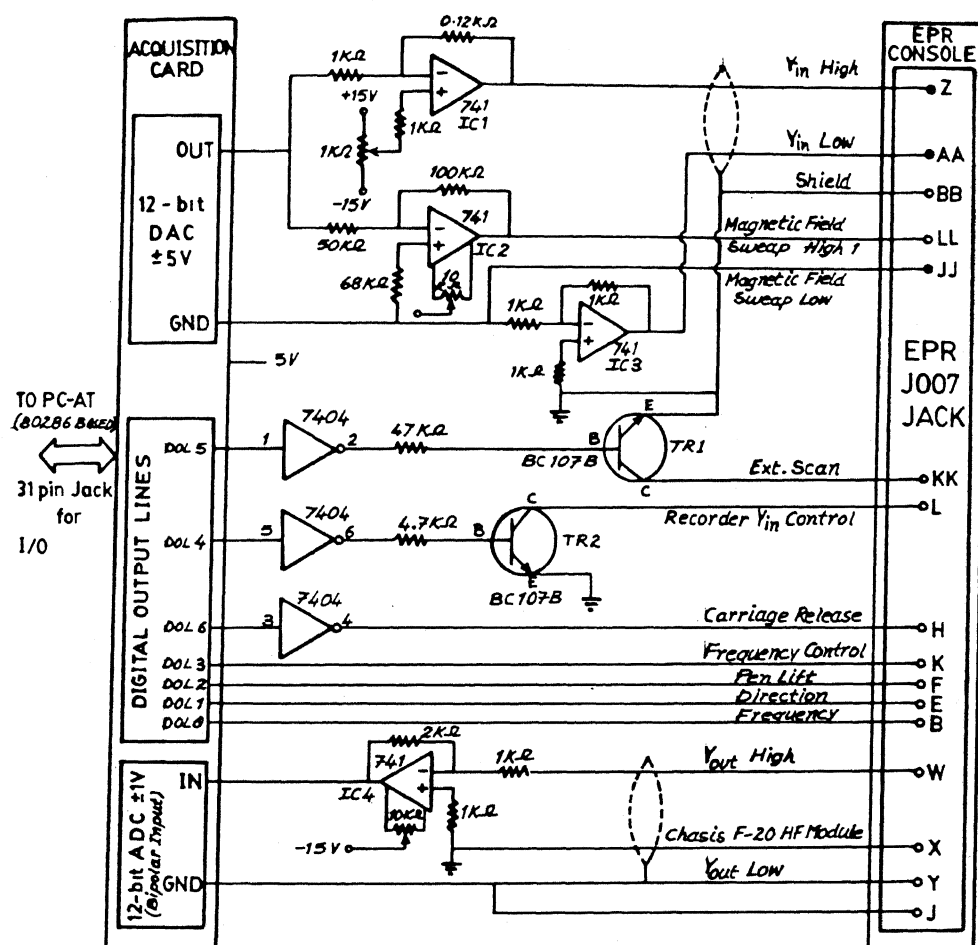


Fig. 6.8 Circuit diagram of the adapter circuit.

**Table 6.1**                      **Details of the connections between the EPR J007 jack and the interfaces**

EPR J007 JACK PINS			ADC/DAC/ Digital output lines	PC/AT Memory Address
K	Remote override : to be grounded for remote control of the X-scan,		DOL3	300h-I/O write signal
L	Remote Y-input enable : to be grounded for an external Y-Sig nal input		DOL4	-do-
B(X-drive)	External Frequency in put for the step motor (0.0175 to 883 Hz)		DOL0	-do-
E	External direction In put (H-Right) (L-left )		DOL1	-do-
F	Pen lift input (H-up L-down)		DOL2	-do-
H	Carriage Release		DOL6	-do-
Input (Y-Signal)				
Z	External Signal ( $\pm 1/2$ V)	High lead	DAC Ch#1	304h-I/O Write Signal
AA		Low lead	DAC GRND	
BB	Shield			
KK	EXT. Scan # 2 enable		DOL5	304h-I/O Write Signal
LL	EXT. Scan # 2 input		DAC CH#1	
JJ			DAC GRND	
Output (Y-Signal)				
W	EPR Signal ( $\pm 1/2$ V)	High Lead	ADC Ch#1	307h I/O write for channel selection
X		Low Lead	ADC GRND	306h I/O write for start of conversion (SOC)
Y	Shield			307h I/O read to read end of conversion (EOC)
J	Shield			300h I/O read to read analog voltages

Enable Read (CER) and Chip Enable Write (CEW) for different devices in the circuit. The signals will be used appropriately at specific places for specific purposes.

The DAC section of the acquisition card comprises (1) DAC buffers (74LS374) (2) DAC IC and (3) Amplifier ICs. The DAC buffers will get inputs from the PC-Data bus (PCDB) (SD0-SD7), CEW302 and CEW303. The buffers will allow the digital data only when 'enable' signal is sent by CEW302 and CEW303. The DAC IC (AD7527) converts 12-bit offset binary code into analog voltage. The lower 8 bits receive data from DAC buffer 1 (74LS374), while the upper 4 bits receive data from DAC buffer 2 (74LS324). After digital-to-analog conversion, DAC IC sends the signal to an operational amplifier (A1) and the amplified signal eventually goes to the connector 2.

The Digital Output Lines (DOL) contain two tristate octal D flip-flop ICs. The inputs for the ICs come from PCDB (SD0-SD7), CEW300 and CEW302. The function of these two flip-flops is similar to that of DAC buffers, except that both of these ICs give output of 8 bits each to make a total of 16-bit output (DOL0-DOL15).

The ADC section of the acquisition card contains (1) a channel selector (74LS174) (2) two multiplexers (MUX-AD 7503), (3) an amplifier (A2), (4) a sample and hold (S/H) circuit, (5) ADC IC (MAX162), (6) two ADC buffers (74LS374), (7) start of conversion (SOC) flip-flop (74LS74) and (8) end of conversion (EOC) buffers.

The channel selector buffer gets its input from PCDB (SD0-SD3) as well as from CEW307. Buffered output can be sent to multiplexers as CO-C3 only when they receive 'enable' from CEW307.

Each multiplexer IC has eight analog input channels and one output channel. Depending upon the code received from CO-C3, one of these two MUX ICs



will be selected, and input from one of the eight channels will be allowed to come out as output, i.e., one analog input signal out of sixteen will be selected by the multiplexers. This selected analog signal voltage will be amplified by A2 and fed to S/H circuit.

The ADC needs a finite time (say, 9  $\mu$ sec) to convert any analog voltage to digital data. It is noticed that the analog input voltage changes markedly within this 9  $\mu$ sec 'conversion time'. In order to overcome this problem, a S/H circuit is included. This device will 'sample' the analog signal and then 'hold' the value constant for the duration of the analog to digital conversion. The ADC sends out a  $\overline{\text{BUSY}}$  signal when it is performing 'analog-to-digital conversion'.

The SOC flip-flop IC receives input from CEW306 and CLK. The response to CEW306 and CLK will be sent as SOC command. As soon as the ADC IC (MAX162) receives this  $\overline{\text{SOC}}$  command, it sends out a  $\overline{\text{BUSY}}$  signal and starts doing conversion (digitizing) of analog voltage present at its input.  $\overline{\text{BUSY}}$  and  $\overline{\text{SOC}}$  signals are ANDed to generate the EOC signal which will be read by PC data bit SD0 by sending CER307. As soon as this conversion is over, 12-bit output will be present at the output bus and the  $\overline{\text{BUSY}}$  signal will be lifted. 12-bit ADC output will be split up into 4 most significant bits (MSB) and 8 least significant bit (LSB) and sent to the respective ADC buffers. These ADC buffers will send the digital data 'out' only when they receive 'enable' from CER300 and CER301.

#### 6.5.2.2 Adapter Circuit

##### Data Acquisition

To acquire the EPR signal in PC in digitized form, the magnetic field sweep in the EPR instrument should be switched over to EXT.SCAN position. This will be achieved by using DOL5. The output coming from DOL5 will be inverted

by 7404 inverter IC and passed on to the Transistor TR1, which will then switch on the relay (50mA current) in the EPR console to put it on the 'External Scan' mode.

In EPR, generally, -10 V to +10 V ramp signal will be used for the magnetic field sweep. However, the DAC generates only to -5 V to +5 V ramp signal for this purpose. To meet the EPR instrument requirement, this  $\pm 5$  V ramp will have to be amplified. This task will be performed by the IC2.

The analog EPR signal at the output of the spectrometer has a range of -0.5 V to +0.5 V. Since each channel of the ADC accepts voltages in the range of -5 V to +5 V, the EPR signal will be fed to IC4 with an amplification factor or gain of 10. This  $\pm 5$  V analog signal will be used as input by ADC.

#### Recording of Spectra

DOL0 to DOL3 and DOL6 lines are directly connected to the EPR console to be used, respectively, as frequency drive, direction, pen lift, frequency controls and carriage release for recording purposes. DOL4 will be inverted by 7404 inverter IC and the output will be passed on to the transistor (TR2). The TR2 switches on the relay (50 mA current) in EPR recorder to put it on EXTERNAL  $Y_{input}$  mode. The -5 V to +5 V recorder analog output from DAC is sent to IC1 and attenuated by a factor 10, and the resulting  $\pm 0.5$  V output is given to  $Y_{in}$  high. The DAC GND is connected to an emitter follower IC3 and its output is sent to  $Y_{in}$  low. Shielded cables should be used for recorder input ( $Y_{in}$  high and  $Y_{in}$  low) and EPR output ( $Y_{out}$  high and  $Y_{out}$  low).

#### 6.6 Software

In our attempt to perform digital data acquisition and subsequent recording, we have decided to control our DAS (Hardware) using appropriate software. For this purpose we have written three MASM assembly language

programs, namely, (1) ACQN.ASM, (2) RECR.ASM and (3) DSPL.ASM. These programs, which can be assembled and run using Microsoft Macro Assembler, are briefly described below.

#### 6.6.1 ACQN.ASM

This is the acquisition program (main) of ~ 5 kbytes. This main program uses the following subroutines : SCR, STRG, BRNG, HXBD, BDHX, DELAY, CMM, COLLECT and WRITE. First of all, when the ACQN.ASM program is executed after assembling and linking, it displays the 'menu' and the 'prompt' on the screen and waits for the operator to enter a single letter (only alphabet) command. The received command will be compared with the ASCII code stored in data segment, and upon finding the corresponding character it jumps to an appropriate subroutine. For example if 'n' or 't' is keyed in after the program prompt, the default values stored in data segment for number of scans or scan time will appear. Instead, if 'g' is keyed in, control will be transferred to the 'GCOLL' subroutine which subsequently calls the 'COLLECT' and 'WRITE' subroutines. 'q' can be pressed if we wish to quit.

##### 6.6.1.1 Functions of Subroutines

- SCR : It displays on screen that character whose ASCII code is in 'dl' register.
- STRG : It displays value in 'ax' register on screen in 4 digits.
- BRNG : It waits for the operator to enter the numerical values and stores them in data segment. The allowed number of digits will be 4 or less.
- HXBD : This converts the 4-digit hexadecimal numbers stored in data segment into binary coded decimal numbers and stores them back in data

segment.

BDHX : This subroutine does exactly the reverse of HXBD.

DELAY : Scan time 't' is multiplied by predefined factor stored in 'dc' to convert 't' into seconds and stored in 'cx' register. To achieve 't' second delay, count down is performed on 'cx' register till it reaches zero. This gives desired delay.

CMM : It displays corresponding parameters in 4 digit decimal form and allows the operator to enter a new decimal value, (maximum 4 digits) and for this purpose it uses HXBD, STRG, BRNG and BDHX subroutines.

COLLECT : It sends the appropriate code to set the 'EXTERNAL SCAN' mode in the EPR spectrometer. It selects Ch #0 out of the 16 channels available for ADC. It initializes 'di' register with number of scans, 'bx' register with address of data storage block, and 'cx' register with number of steps for ramp. It initializes the 'si' register to zero to indicate first location of data storage block. After all these initialization operations have been performed, a loop will be started to generate the ramp for field sweep. Before entering loop we initialize 'ax' register with zero and 'output' it to DAC. This will generate -5 V at the output of DAC. In the loop the 'ax' register value will be incremented, which is then output to DAC to generate a ramp. After each increment, we read the EPR spectrometer analog signal through ADC. For this reading purpose Start of Conversion (SOC) command is given to ADC, End of Conversion (EOC) tested and the value is read in 'ax' register. This is converted into '2's complement' form and added in data storage block in respective location pointed by 'si' register. Then the 'si' register is

incremented twice. Number of steps stored in 'cx' register is stepped down, until it becomes zero. Till then the loop is continued for generating higher voltage. Within the loop, the DELAY subroutine is called to get the required scan time. This whole operation is repeated for the number of scans required. In case of memory overflow during this process, the loop will be terminated with the message of 'memory full'.

WRITE : This creates an output file (EPR) in the hard disk. The data generated by 'COLLECT' subroutine will be stored in the file and finally 'file' will be closed.

#### 6.6.2 RECR.ASM

Except BGN, LIN and PULSE, all other subroutines used in this program have analogous names and functions to those used in ACQN.ASM. As a starting point, the 'EPR' file already generated by ACQN.ASM is opened and the data loaded in storage block in data segment. The menu is then displayed for our further action. It takes the parameters and commands from the operator. When 't' is pressed, the recording time can be set; similarly 'p' is keyed in for upward shift, 'm' for downward shift, 'a' for attenuation and 'g' to start recording the spectrum acquired by ACQN.ASM.

##### 6.6.2.1 Functions of Subroutines

BGN : Depending on the 'p' and 'm' entries, the constants to shift the spectrum in 'y' direction are calculated and stored in MNS1 (memory). Appropriate codes are sent through DOL (1) to energize the carriage motor, (2) to place logic circuit in remote mode, (3) to set the recorder arm in 'right' direction and (4) pen down. The codes sent

to recorder are also stored in data segment as 'PEN' (memory). 'si' register is initialized to zero to indicate first memory in first data storage block. The EPR recorder arm requires 6676 pulses to travel from left limit to right limit. During this time interval, 4096 data points have to be sent to the recorder, i.e., 163 pulses for 100 data points. To achieve this we have written a code for distributing 8 motor drive pulses for 5 data points. The code is repeated twenty times and three extra pulses are given to X to make the ratio 163/100. After sending each data, a check is made to verify whether data pointer 'si' register's value has reached the maximum limit ( $2 \times 4096 = 8192$  points). This section of the program has been put in a loop, so that all the 4096 data points can be sent to the EPR recorder. Then proper code is sent through DOL to switch over the recorder to 'INTERNAL MODE'.

PULSE : The LSB of the DOL is connected to the X-axis frequency drive for convenience. In this subroutine the status of the DOL is read from 'PEN' memory. Then it is incremented and output to DOL. This makes LSB 'high'. After providing some delay, the code is decremented and again output to DOL. After some delay, the subroutine returns the control back to the main program, by providing a pulse whose period depends on the delay. This pulse is sent to X-axis drive of the recorder through DOL.

YAX : In this, the data to Y-axis drive of the recorder is sent through DAC. Data is read from the data storage block pointed (indicated) by 'si' register. Sum of 'Up shift' and 'Down shift' constants calculated earlier is added to every data points. Data pointer 'si' is incremented twice. Data is divided by attenuation factor 'a'.

The 2's complement number is converted to offset binary code and output to recorder through DAC. The 'si' register is compared with 'set value' for raising zero flag. In this subroutine 'cx' register pushed in stack.

LIN : The value in 'ax' is output to DOL and stored in temporary location 'PEN' memory.

### 6.6.3 DSPL.ASM

The file (EPR) created already by ACQN.ASM is opened first and placed in data storage block. Each word of the EPR file is converted into 4 ASCII codes and stored in data block ST2. For this conversion each 4 bit nibble of data word is added either with 30h or 37h depending on whether it's value is 0-9 or 10-16, respectively. These ASCII data points are saved in a file, named ASC, in the hard disk .

### 6.6.4 HEX.FOR

These converted ASCII codes are in turn converted into decimal numbers and saved in ASC.M file using the FORTRAN program. This ASC.M file is used as input file to plot the spectrum on the PC screen. Commercial package MATLAB is used for plotting purposes.

For convenience the executable file names of DSPL.ASM and HEX.FOR are (i.e. files with .EXE extension) dumped in a batch file called DIS.BAT and the batch file is subsequently executed.

## 6.7 Self Test on Hardware and Software

This test was devised to test our software, acquisition card and adapter circuit as a whole before connecting our DAS (Data Acquisition System)

to the EPR spectrometer.

As the first step of the self-test, the  $Y_{in}$  high and  $Y_{out}$  high pins are shorted, followed by placing (or) touching the oscilloscope probe at magnetic field sweep pins (LL). After this, ACQN.EXE is run. The -10 V to +10 V ramp is observed on the oscilloscope when the command 'g' is given after choosing proper number of scans and scan time. During the period the voltage at the base of TR1 (transistor) is 0.5 V, the generated ramp signal is stored in 'EPR' file. The data in this EPR file can be plotted by running DIS.BAT file. After generating a proper ramp, the abovementioned shorts may be disconnected.

The waveforms shown in Fig. 6.9 are observed in the oscilloscope when RECR.EXE is run. Appearance of proper ramp indicates our DAS is functioning properly.

## 6.8 Improvement in Software

Towards the final phase of this work, we wished to improve our software capabilities which consisted only of programs written in MASM assembly language. Since this language still remains unfamiliar to many, we thought that it would be appropriate to make it interactive with other familiar high level languages such as FORTRAN, BASIC, PASCAL and C. We have written a Fortran program (NM.FOR) which is capable of calling all the assembly language subroutines used in the ACQN.ASM, RECR.ASM. The parameters needed in the ACQN.ASM and RECR.ASM, such as the number of scans, scan time, etc., can be passed through the Fortran program arguments. This Fortran program needs only COLLECT, DELAY and WRITE subroutines for the acquisition purpose. For the recording purpose BGN, DELAY, PULSE, YAX, LIN, STRG subroutines of RECR.ASM are needed. These subroutines are clubbed in separate files and suitable changes are made so that proper linking is achieved with Fortran programs.



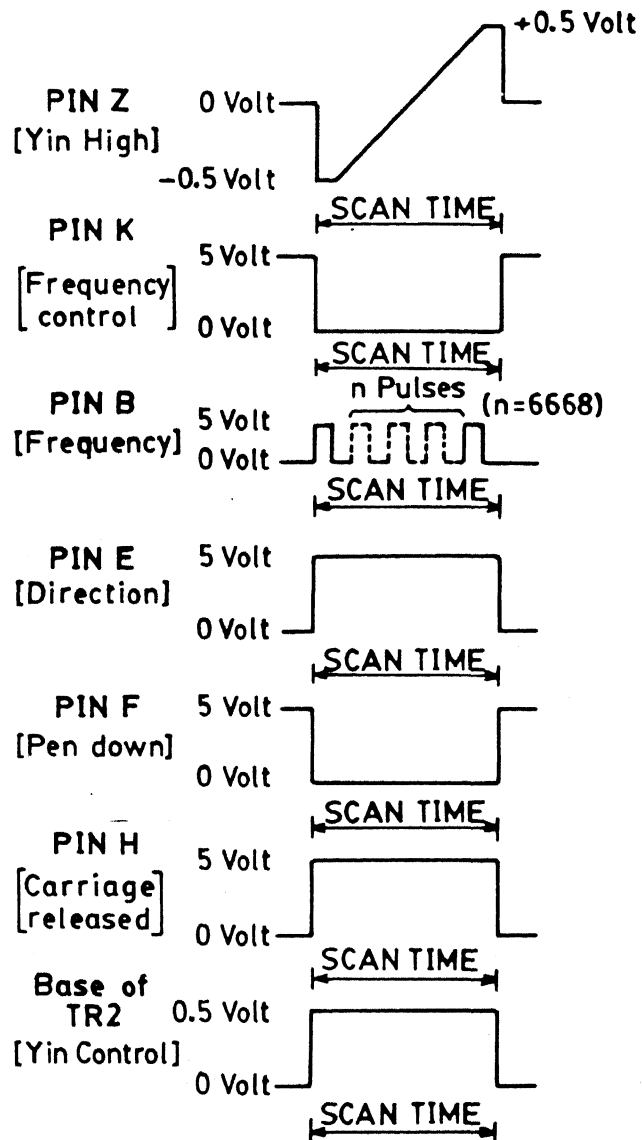


Fig. 6.9 Wave forms as a result of self test.

## 6.9 Working Details of Software

Before the digital data acquisition starts, all the programs should be compiled and the corresponding .EXE files should be created. The ACQN.ASM and RECR.ASM programs are assembled and linked using Microsoft Macro Assembler. This is done as shown below :

C:\MASM>masm ACQN.ASM ← (or) C:\MASM>masm RECR.ASM ← ⇒ will create corresponding file.OBJ files.

After successful completion of this assembling, linking is done according to the following steps.

C:\MASM> link file.ASM ← ; by these commands, file.EXE files will be created.

The HEX.FOR and NM.FOR files are compiled using Microsoft Fortran compiler.

C:\MSFORBIN> fl file.for ← ⇒ ensures creation of file.EXE. files.  
After these operations have been completed, we should make sure that all the connection between the PC, acquisition card, adapter circuit and EPR instrument have been properly done.

Now we have two options, namely,

### (1) Running Acquisition Program directly

If ACQN.EXE is run, the following message will appear on the screen :

\*q = quit t = scan time n = # of scans g = go c = continue

Default values for t and n are 2 and 1 respectively. If 't' or 'n' is to be changed, the appropriate letter can be pressed, whereby the default value will be echoed on the screen. After this a new value can be given. After coming to \* prompt 'g' can be pressed to start the acquisition. If the specified number of scans is over, the number of completed scans is echoed,

followed by the \* prompt. By pressing 'q' the execution of the acquisition program can be terminated.

At this stage 'EPR' file must have been created, but the data will be in 2's complement form. DSPL.EXE will convert this 'EPR' to 'ASC'. The data in ASC will be as 'hexadecimal' numbers. They are converted into decimal numbers by hex.EXE and then written on file ASC.M. Finally, this ASC.M file can be loaded in 'MATLAB' where it can be viewed as an X-Y plot. This plot can be saved in a file which can be fed into any printer or plotter to get the final hard copy of the EPR spectrum.

## (2) Data Acquisition using Fortran

For this option, the ACQN.OBJ and NM.FOR files should be linked together. This can be achieved by the following command,

C:\MSFORBIN> fl NM.FOR ACQN.OBJ <|. This creates NM.EXE file. When this file is run, computer asks for various parameters, viz., central magnetic field, scan range, modulation amplitude, gain, time constant, number of scans needed, scan time, and number of steps. After all these input parameters have been received, the 'COLLECT' subroutine (used in ACQN.ASM) is called by our Fortran program for receiving our collected data as input and for subsequent execution.

## 6.10 Salient Features of our Data Acquisition System (DAS)

Although the method of Trousson *et al*<sup>20</sup> has been adapted in its basic form for our design, our DAS has some superior features. These are discussed in this section.

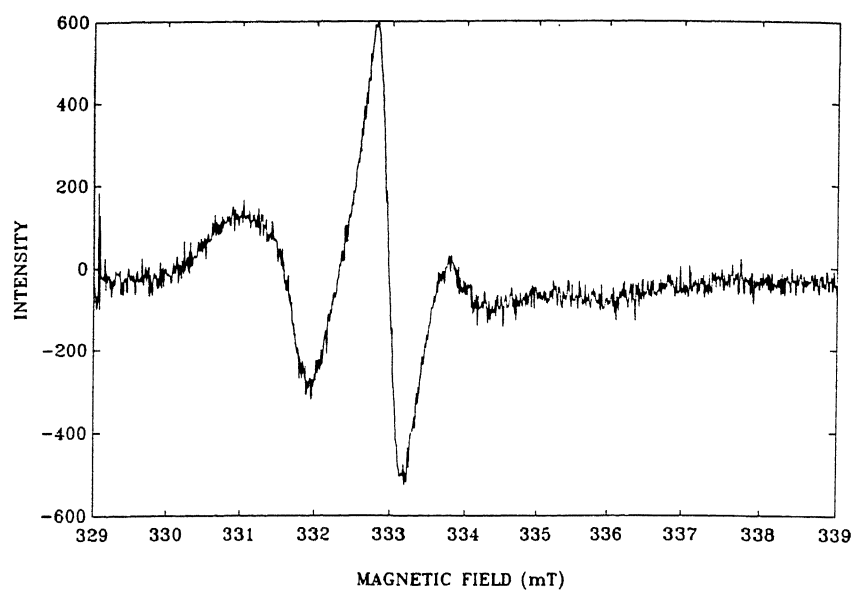
- (1) Whenever multiscanning experiments are performed to time-average noisy spectra, in many respects it will be disadvantageous to use the recorder arm for sweeping the magnetic field. Trousson *et al*<sup>20</sup> have used the

recorder arm for this purpose (i.e., scanning the magnetic field internally). In our design, this problem has been overcome by sweeping the magnetic field externally by means of a computer generated ramp.

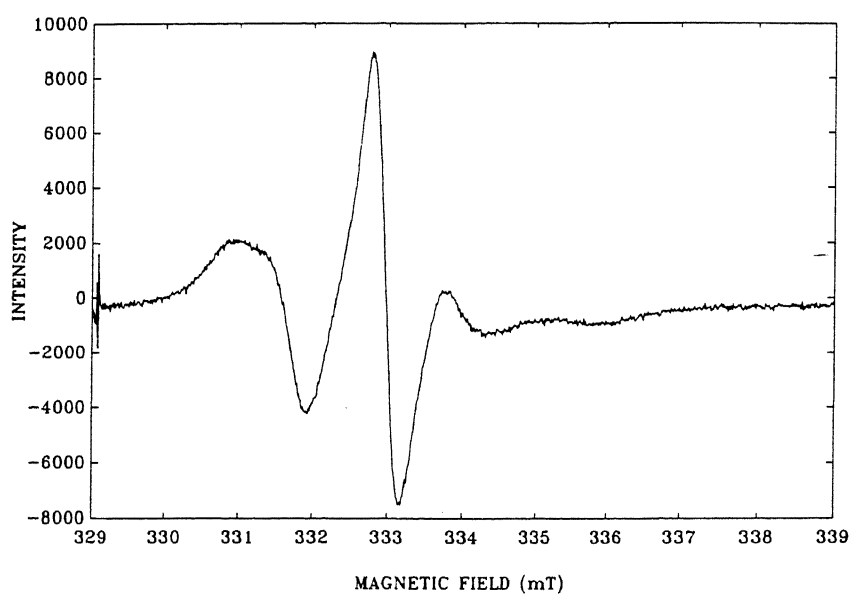
- (ii) The ADC used by Trousson *et al*<sup>20</sup> has only an 8-bit resolution. We have used a 12-bit ADC in our DAS. ADCs having a resolution of 8-bit will be able to produce only 256 ( $2^8$ ) digitized values, and 12-bit will be able to produce 4096 ( $2^{12}$ ) digitized values. Whereas there was a change of each digital value for a voltage change of 39 mV in the earlier design, in our case each digital point was acquired for a change of just 2.5 mV of our sweep ramp. This leads to a relative precision of 0.02% in our work, compared with a corresponding value of 0.39% in the earlier work.<sup>20</sup>
- (iii) For a noise-free spectrum the number of scans that can be added before 'memory overflow' occurs depends on N, the resolution of the ADC, and W, the word-length of the computer.<sup>22</sup> The maximum number of scans possible is given by  $2^{W-N}$ , which is equivalent to  $(2^{16-12}) = 16$  scans in our DAS as opposed to only  $(2^{8-8}) = 1$  scan in the earlier system.<sup>20</sup>
- (iv) Any IBM-Compatible PC can be used as a part of our DAS. Whereas the earlier version<sup>20</sup> has been dedicated to a specific computer (Apple II microcomputer).

## 6.11 Performance and Discussion

To check the performance of the DAS, we have carried out three different experiments. The system taken up for our study has been 5-doxyl stearic acid spin label dissolved in the 'water pools' of lecithin/cyclohexane/ $H_2O$  reverse micelles. The parameters adjusted in the spectrometer are listed in Table 6.2. We performed a single scan acquisition for this sample. The acquired spectrum is shown in Fig. 6.10(a). In Fig.



(a)



(b)

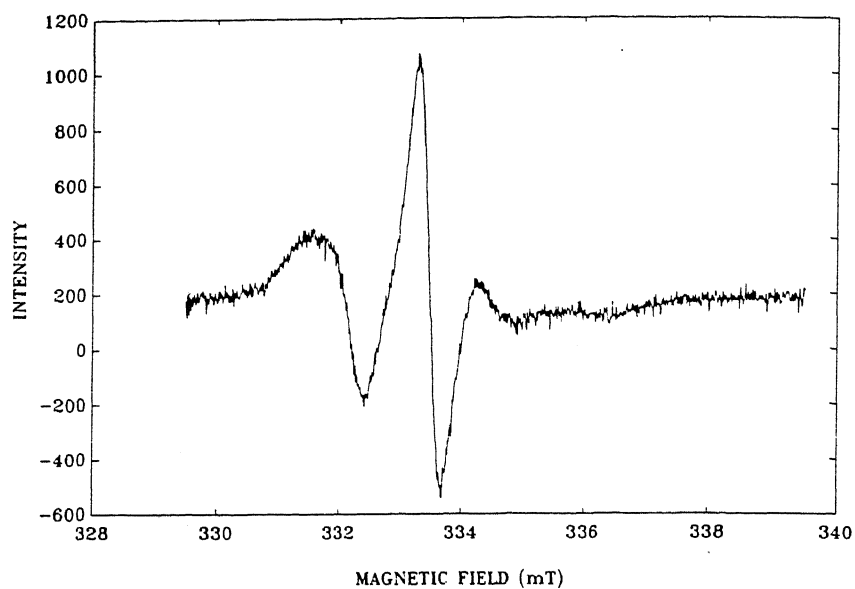
Fig. 6.10 (a) EPR spectrum obtained for 5-doxylstearic acid in lecithin reverse micelles with single scan.

(b) EPR spectrum obtained for 5-doxylstearic acid in lecithin reverse micelles with No. of scans = 10.

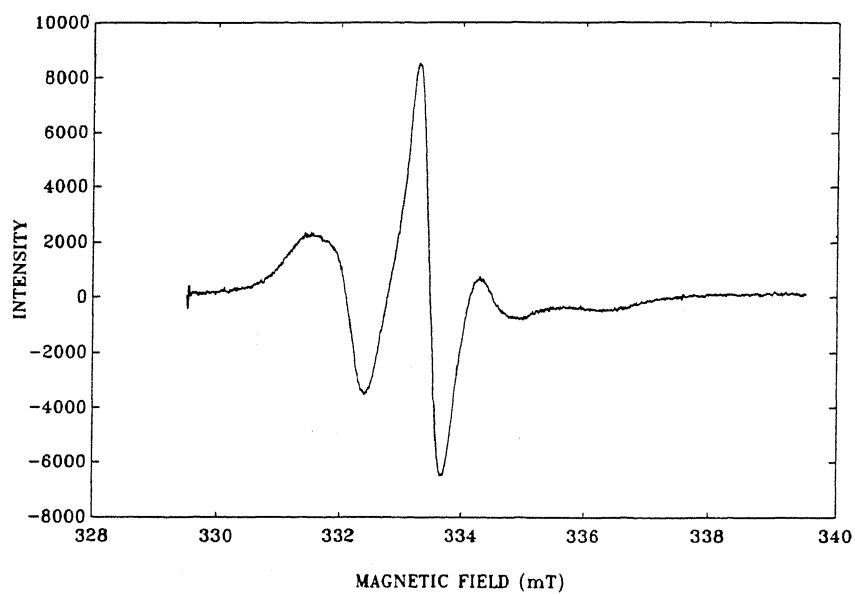
6.10(b), the spectrum of the same sample, obtained after 15 scans, Figs. 6.11(a) and 6.11(b) show the spectra of the same sample with 'R' value, obtained after 1 scan and 10 scans, respectively. Figs. 6.11 clearly demonstrate how effectively the multiscanning experiment helped us in getting noise-free spectrum.

Another very important point shall also be highlighted. position of the poorly resolved peaks at the 'outer extrema' often play a crucial role in accurately determining the 'parallel' feature of the tensor, which in turn will be used to calculate the order parameter of the system under study. The order parameters calculated from the Fig. 6.11 will not be so accurate. Our attempts to signal average the spectrum with even larger number of scans failed after 16 scans because of memory overflow. We have therefore decided to record the high field portion of the spectrum which is shown in Fig. 6.12(a). The parameters used to acquire this spectrum are shown in Table 6.2. One ends up with enormous error if he calculates  $A_{||}$  and S from the Fig. 6.12(a). The same spectrum was time averaged using 15 scans, and the resulting spectrum is shown in Fig. 6.12(b). In this figure the high field part of the outer extrema are well resolved. Calculating  $A_{||}$  and S from this spectrum will be simpler and more accurate than from the Fig. 6.12(a).

Fig. 6.13(a) shows the EPR spectrum recorded in the normal scan mode (without using our DAS). A dilute aqueous solution of the  $^{13}\text{C}$ -labeled sodium dodecyl sulfate was used to record this spectrum. High gain ( $10 \times 10^4$ ) and modulation amplitude (1.0x1.0 G) have been used to record this spectrum. The signal is poorly resolved and the S/N ratio is also poor. The spectrum of the same sample, acquired after 40 scans, is shown in Fig. 6.13(b).



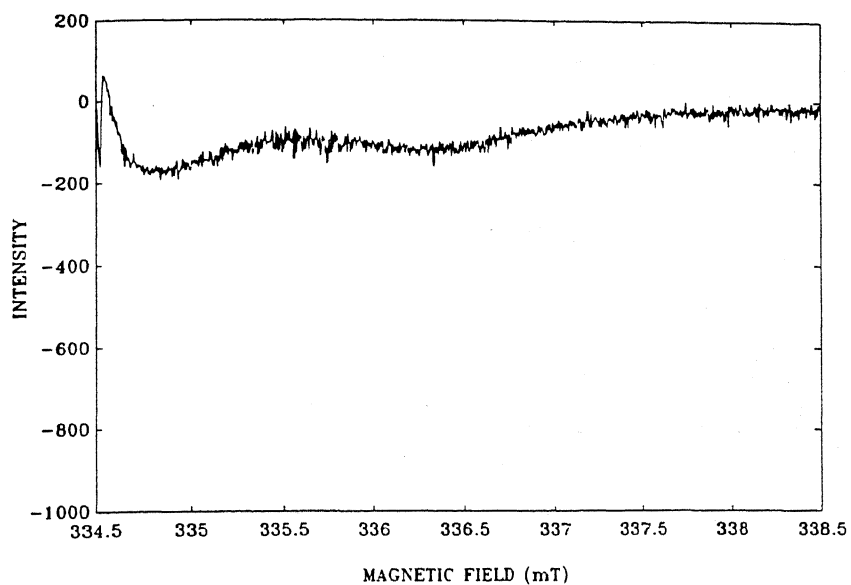
(a)



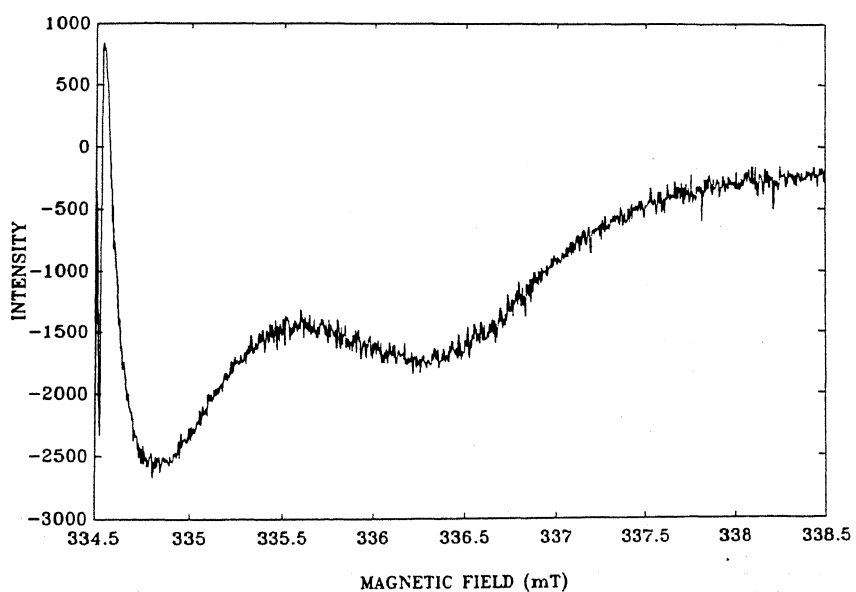
(b)

Fig. 6.11 (a) EPR spectrum obtained for 5-doxylstearic acid in lecithin reverse micelles with single scan.

(b) EPR spectrum obtained for 5-doxylstearic acid in lecithin reverse micelles with No. of scans = 10.



(a)



(b)

Fig. 6.12 (a) EPR spectrum obtained for 5-doxylstearic acid in lecithin reverse micelles with single scan.

(b) EPR spectrum obtained for 5-doxylstearic acid in lecithin reverse micelles with No. of scans = 10.



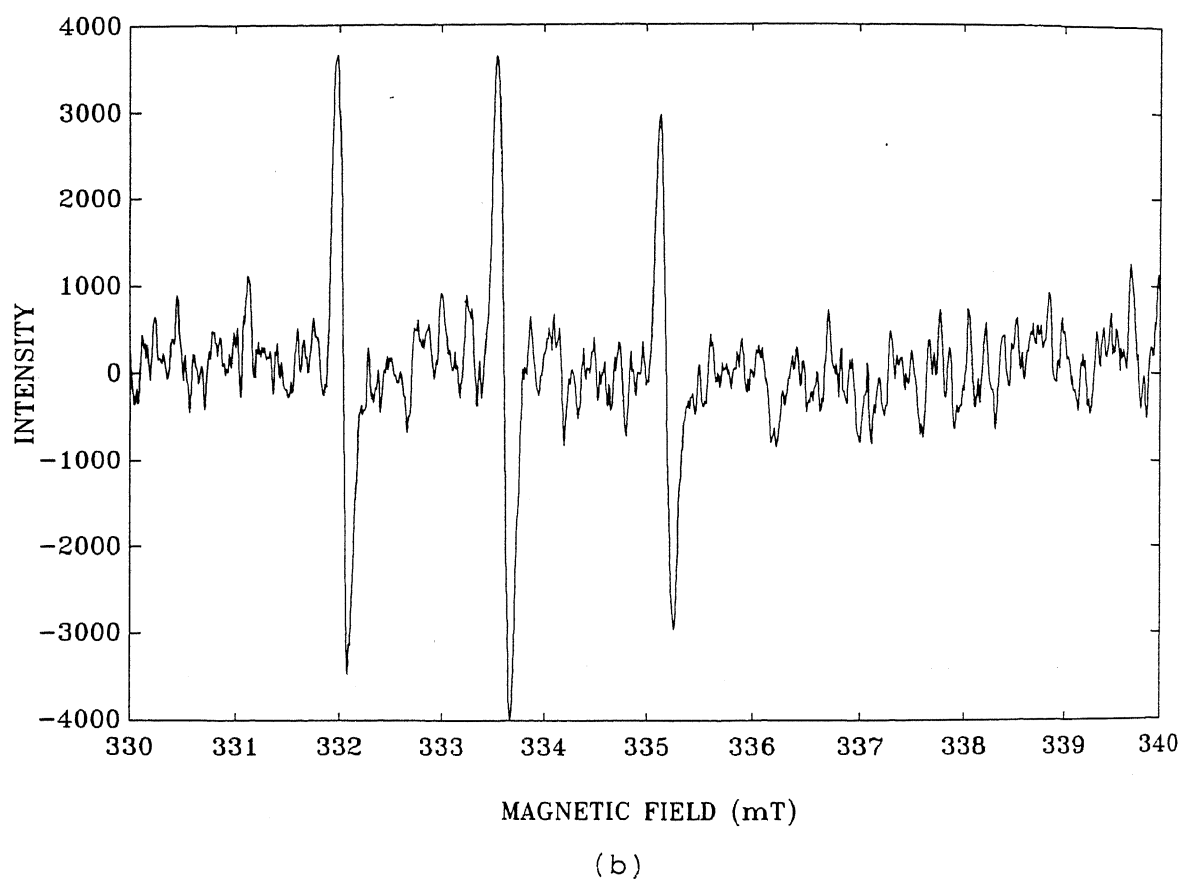
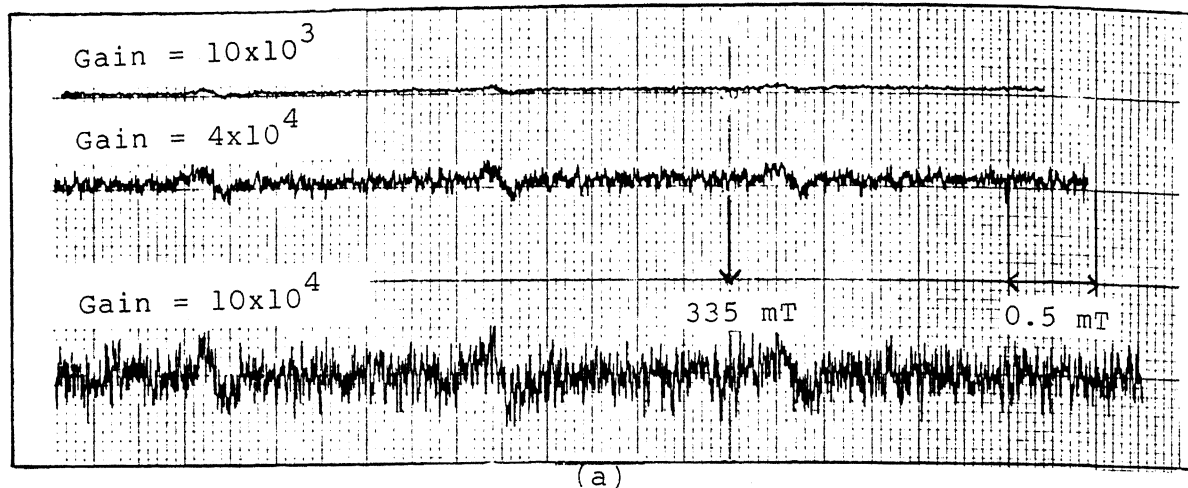


Fig. 6.13 (a) EPR spectrum obtained for 5-doxylstearic acid in lecithin reverse micelles with single scan.

(b) EPR spectrum obtained for 5-doxylstearic acid in lecithin reverse micelles with No. of scans = 15. (computer plots)

**Table 6.2** Parameters used to acquire spectra shown in Fig. 6.10 to 6.13 using our DAS

Figure No.	Parameters supplied from computer		Spectrometer Settings					
	No. of Scans	Sweep Time [Sec]	Central Field [G]	Scan Range [G]	Modulation Amplitude [G]	Time Constant [Sec]	Gain	Power [mW]
6.10(a)	1	2	3340	100	0.5	0.004	$10 \times 10^3$	2
6.10(b)	15	2	3340	100	0.5	0.004	$10 \times 10^3$	2
6.11(a)	1	33	3345	100	0.5	0.004	$6.3 \times 10^3$	5
6.11(b)	10	33	3345	100	0.5	0.004	$6.3 \times 10^3$	5
6.12(a)	1	15	3365	40	0.5	0.004	$10 \times 10^3$	5
6.12(b)	15	15	3365	40	0.5	0.004	$10 \times 10^3$	5
6.13(a)		240*	3350	100	1.0	0.032	$10 \times 10^4$	2
6.13(b)	40	15	3350	100	1.0	0.032	$10 \times 10^4$	2

Except for Fig. 6.13(a), all other figures shown in this section are the plots of the spectrum displayed by the computer which are obtained using our DAS. Fig. 6.14(a) shows the spectrum obtained using our ACQN.ASM and retransferred to the X-Y recorder using RECR.ASM. Fig. 6.14(b) was obtained after attenuating the spectrum shown in Fig. 6.14(a). Figs. 6.15(a) and 6.15(b) show the spectra obtained or recorded using 2 minutes of recording time. Table 6.3 shows the parameters used for recording spectra shown in Figs. 6.14 and 6.15.

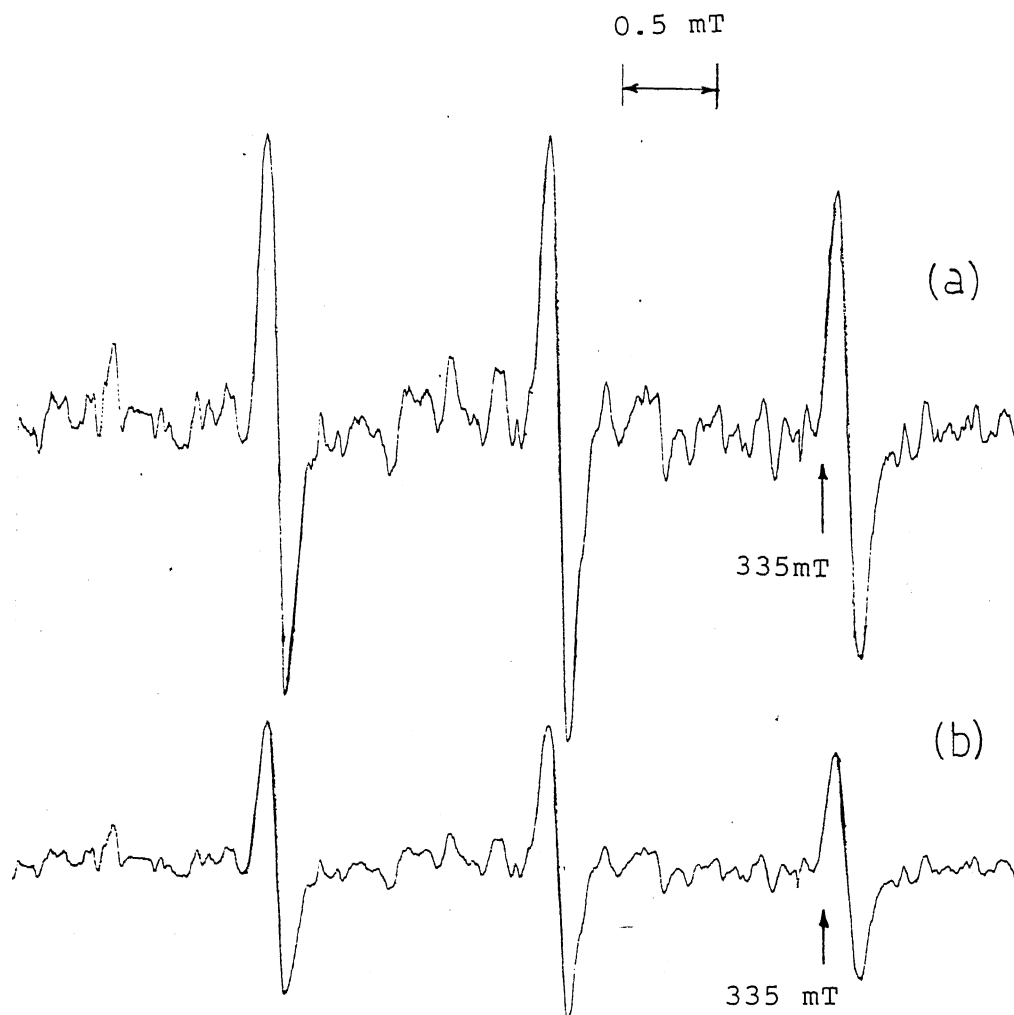


Fig. 6.14 (a) EPR spectrum obtained for 5-doxylstearic acid in lecithin reverse micelles with No. of scans = 40, recording time = 30 s and attenuation = 4. (recorded using X-Y recorder).

(b) EPR spectrum obtained for 5-doxylstearic acid in lecithin reverse micelles with No. of scans = 40, recording time = 30 s and attenuation = 8. (recorded using X-Y recorder).

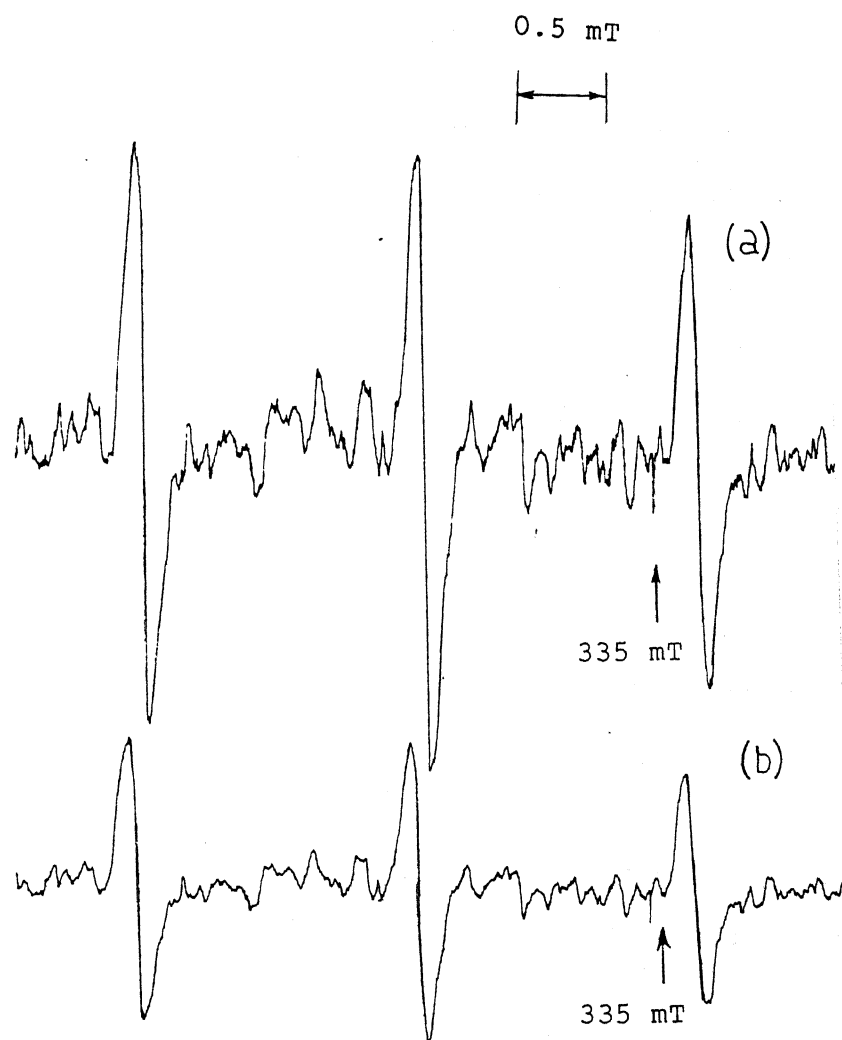


Fig. 6.15 (a) EPR spectrum obtained for 5-doxylstearic acid in lecithin reverse micelles with No. of scans = 40, recording time = 120 s and attenuation = 4. (recorded using X-Y recorder).

(b) EPR spectrum obtained for 5-doxylstearic acid in lecithin reverse micelles with No. of scans = 40, recording time = 120 s and attenuation = 80. (recorded using X-Y recorder).

Table 6.3                      Parameters used for recording spectra shown in  
Figs. 6.14 and 6.15

Figure No.	Number of Scans	Sweep Time [Sec]	Recording Time [Sec]	Attenuation	Spectrometer Settings
6.14(a)	40	15	30	4	Same as in Fig.6.13(a)
6.14(b)	40	15	30	8	-do-
6.15(a)	40	15	120	4	-do-
6.15(b)	40	15	120	8	-do-

## 6.12 Conclusion

- (i) We have demonstrated the successful construction of a Data Acquisition System which can be interfaced to an EPR spectrometer, capable of acquiring digital spectral data, and retransferring this digital data to the X-Y recorder.
- (ii) We have shown how important EPR spectral parameters such as  $A_{||}$  could be calculated accurately using our DAS, and how the S/N can be improved considerably to get a noise-free spectrum.

## REFERENCES

1. J. E. Wertz and J. R. Bolton, **Electron Spin Resonance : Elementary theory And Practical Applications**, McCraw -Hill, New York (1972).
2. **Spin Labeling : Theory and Applications**, L. J. Berliner (ed), Academic, New York, (1976).
3. D. S. Clark, L. Creagh, P. Skerker, M. Guinn, J. Prusnitz and H. Blanch In **Biocatalysis and Biomimetics**, J. D. Burrington and D. S. Clark (eds.) (ACS Symposium Series 392) , American Chemical Society, Washington, D.C., (1989).
4. H. L. Van Camp and A. H. Heiss, *Magn. Res. Rev.* **7**,1 (1981).
5. I. B. Goldberg, H. R. Crowe and R. S. Carpenter II, *J. Magn. Reson.* **18**, 84 (1975).
6. F. G. Herring, J. Mayo and P. S. Philips *J. Magn. Reson.* **34**,413 (1979).
7. a) D. W. Posener *J. Magn. Reson.* **13**, 102 (1974).  
b) D. W. Posener *J. Magn. Reson.* **14**, 121 (1974).  
c) D. W. Posener *J. Magn. Reson.* **14**, 129 (1974).
8. R. R. Ernst *Adv. Magn. Res* **2**, 1 (1966).
9. H. Twilfer, K. Gersonde and M. Christahl *J. Magn. Reson.* **44**, 470 (1981).
10. W. R. Hagen, D. O. Hearshen, L. J. Harding and W. R. Dunhsm *J. Magn. Reson.* **61**, 233 (1985).
11. J. Tang, C. P. Lin, M. K. Bowman and J. R. Norris *J. Magn. Reson.* **62**, 167 (1985).
12. K. Roth and B. Kirste *J. Magn. Reson.* **63**, 360 (1985).
13. T. E. Gough and R. G. Hacker *J. Magn. Reson.* **6**, 129 (1972).
14. J. S. Hwang, R. P. Mason, L-P. Hwang and J. H. Freed *J. Phys. Chem.* **79**, 489 (1975).
15. T. O. Seim, T. B. Melo and S. Prydz, *J. Magn. Reson.* **9**,175 (1973).
16. A. Bauder and R. J. Myers, *J. Molec. Spectroc.* **27**, 110 (1968).
17. R. Schultz, G. Hurst, T. E. Thieret and R. W. Kreilick, *J. Magn. Reson.* **53**, 303 (1983).
18. P. N. T. Lindsay and B. M. Peake *J. Magn. Reson.* **47**, 365 (1982).
19. S. R. Maple and J. P. Hensel, *J. Magn. Reson.* **66**, 445 (1986).
20. P. Trousson and M. Rinne *Rev. Sci. Instrum.* **55**, 1989 (1984).

21. R. W. Quine, G. R. Eaton and S. S. Eaton, J. Magn. Reson. 66, 164 (1986).
22. J.C. Lindon and A.G. Ferrige, Prog. in NMR Spectroscopy 14, 27 (1980).
23. G. Giugliarelli, P. Tancini and S. Connistraro, J. Phys. E : Sci. Instrum. 22, 702 (1989).

## CHAPTER 7

## SUMMARY AND FURTHER PROSPECTS

In this thesis we have reported extensive EPR investigations carried out on lecithin reverse micelles using three nitroxide spin labels as well as the  $\text{VO}^{2+}$  probe, along with lineshape studies and construction of a spectrometer interface.

The major findings of this work may be summarized as follows :

- (1) Spin labeling studies of PIX and SL-SHS in EYL/cyclohexane/ $\text{H}_2\text{O}$  reverse micelles have been performed, and the results obtained could be explained with the help of the "two-site" and "cage" models. Our results have enabled us to characterize different reverse micellar compartments. EPR study of 5-DSA in lecithin reverse micelles provides evidence for the segmental motion of phosphate (polar head) group of EYL molecules in reverse micelles.
- (2) Cholesterol addition causes significant effects on the interfacial region of the EYL/cyclohexane/ $\text{H}_2\text{O}$  reverse micelles. Beyond values of  $R = 4$ , cholesterol addition speeds up the motion of the added spin label, TEMPOL ; for values of  $R > 4$ , cholesterol slows down the motion of the spin label. A peculiar relation between the polarity and the high field line splitting has been found using our cholesterol studies.
- (3)  $\text{VO}^{2+}$  spin probe study on reverse micelles reveals that the location and motion of the probe are strongly influenced by the ionic nature of the surfactant chosen to form the reverse micelle as well as the size of the water pool. Our  $\text{VO}^{2+}$  EPR studies in anionic (AOT), cationic (CTAB) and zwitterionic (EYL) reverse micellar systems together lead to the interest-



ing finding that the water pools of reverse micelles of high water content need not always behave like 'normal' or 'bulk' water.

- (4) Two computer programs, one for 'slow motion' and another for 'fast motion' have been developed based on existing theory. 'Systematic sampling' technique used in the 'slow motion' program has not only facilitated us to reduce the error occurring in lineshape computations, but has also led to a very rapid computation. The 'fast motion' program enabled us to have an assessment of contributions from motional and inhomogeneous broadenings to the total experimental linewidth. It leads, finally, to more accurate evaluation of motional correlation times.
- (4) The construction of the spectrometer interface, DAS, has enabled us to acquire digital data in a convenient form for further processing. It has also been demonstrated that some important spectral parameters can be calculated accurately and easily using DAS.

Possible extension of the work presented in this thesis may be summarized as below: \_

- (1) Direct spin-labeling of the polar head group and hydrocarbon tail group of EYL and other surfactants can be done, and further EPR studies with such labelled surfactants in reverse micelles, may lead to a better understanding of the dynamics of the 'head' and 'tail' segments of surfactants in reverse micelles.
- (2) Apart from 5-DSA, which we have used in probing the motion of the phosphate segment of EYL molecule, other spin labels such as 7-DSA, 10-DSA, 12-DSA and 16-DSA can also be used to probe the motion of the other segments of the EYL molecules in reverse micellar media.

- (3) Nitroxide biradicals may provide a better choice for studying the inter compartmental exchange of spin labels in EYL reverse micelles, as has been demonstrated in several biological systems.
- (4) Since rotational correlation times of spin-labeled enzymes in reverse micellar water pools can be related to the 'activity' of the enzymes, carrying out further well-planned EPR studies on reverse micellar system may prove useful.
- (5) There is scope for further detailed EPR lineshape simulation studies of  $\text{VO}^{2+}$  in lecithin reverse micelles.
- (6) Regarding EPR instrumentation, we have proposed to make further improvements to the software of DAS with 'window based menus'.

# APPENDIX I

---

```
#           #   #   #   #####   #   #   #           #####
#           #   ##  #   #           #   #   #           #
#           #   # #  #   #####  #####  #           #####
#           #   #  #  #           #  #   #   #   ###  #
#           #   #   ##  #   #   #   #   #   #   ###  #
#####      #   #   #   #####  #   #   #   #   ###  #
```

This Program Calculates Lineshape of All hyperfine components:

---

```
implicit double precision(a-h,o-z)
double precision miu,niu
double complex xyz(5)
dimension a(6),xz(5),yz(5)
dimension field(501),signal(501),isort(501)
dimension deriv(501),dbderv(501)
data ninp,nout/21,22/
open(unit=ninp,file='lin.inp')
open(unit=nout,file='lin1.out')
open(unit=24,file='t21.out')
open(unit=7,file='plot.inp')
```

---

reading data ; see explanation below.

---

```
read(ninp,*)gpar,gper
read(ninp,*)apar,aper
read(ninp,*)niu
read(ninp,*)tau
read(ninp,*)nn,n,nsp
read(ninp,*)cf,sr
close(unit=ninp)
```

---

gpar,gper are parallel and perpendicular g values.  
apar,aper are parallel and perpendicular a values.(in Gauss)  
miu is the electronic magnetic moment in erg/Gauss  
niu is the microwave frequency in Hertz.  
tau should be in seconds  
nn is the number of cos(theta) values used for averaging.  
n is the degree of the polynomial(in our case it is 6)  
actually in imsl case n = 5 is used . this is done internally  
in the program. so there is no change in the input for either  
linshn.f or linshi.f programs.  
cf is the central mag.field(in Gauss).sr is the scan range.  
nsp is the number of the spectral points to be generated.  
nsp .le. 501 at present.  
h is the Plank's constant in erg.sec.

---

```
write(nout,*)gpar,gper
write(nout,*)apar,aper
write(nout,*)niu
write(nout,*)tau
write(nout,*)nn,n,nsp
write(nout,*)cf,sr
n=n-1
bi=cf-(sr/2.)
binc=sr/nsp
miu = 9.2841e-21
h = 6.62618e-27
aparz=apar
aperxy=aper
apar = apar*gpar*miu
aper = aper*gper*miu
gpar2 = gpar*gpar
gper2 = gper*gper
apar2 = apar*apar
aper2 = aper*aper
gdiff2 = gper2-gpar2
adiff2 = aper2-apar2
```

```

agpar = apar*gpar
agper = aper*gper
agpar2 = agpar*agpar
agper2 = agper*agper
agdif2 = agper2-agpar2
pi = 4.*atan(1.)
tol =x02ajf()
b = bi
check = 1.0e-30
a(4) = 0.0
do 90 ii = 1,nsp
signal(ii)=0.0d0
field(ii)=b
b=b+binc
continue
do 120 i = 1,nn
type*,i-
c1 = (i-0.5)/nn
c2 = c1*c1
s2 = 1.-c2
s1 = dsqrt(s2)
gtheta = dsqrt(gpar2*c2+gper2*s2)
gthet2 = gtheta*gtheta
atheta = (dsqrt(apar2*gpar2*c2+aper2*gper2*s2))/gtheta
c4 = c2*c2
s4 = s2*s2
dum1 = 10.*c4-9.*c2+1.
dum2 = (137./3.)*c4-42.*c2+3.
dum3 = dum2*dum2
dum4 = (838./3.)*c4-248*c2+22.
a(6) = 216.*s2*c2*(tau**3)
a(5) = 36.*dum1*(tau*tau)
      do 110 j = 1,3
      m = j-2
      btheta = (h*niu-m*atheta)/(gtheta*miu)
      del=niu*gdifff2/gthet2+m*adiff2/(atheta*h)
      del=del*2.0*pi

```

```

del=niu*gdif2/gthet2+m*agdif2/(atheta*h*gthet2)
del=del-2.*m*atheta*gdif2/(gthet2*h)
del=del*2.*pi
del2 = del*del
a(3) = -36.*s4*c4*del2*(tau*tau)
a(2) = -3.*s2*c2*dum2*del2*tau
a(1) = (-(1./16.)*(dum3-8*s2*c2*dum4)*del2)
ran = del*tau
c      type*,ran,del
call dzporc(n,a,xyz)
do 95 ik=1,5
xz(ik)=real(xyz(ik))
yz(ik)=imag(xyz(ik))
write(24,*) c1,m,xz(ik)
95      continue
big = 0.0d0
do 98 kk = 1,n
if(dabs(yz(kk)) .gt. check) go to 98
if(xz(kk).gt.big) big = xz(kk)
98      continue
c      type*,big,c1
t2 = 1./big
delbpp = h/(pi*sqrt(3.)*gtheta*miu*t2)
delbsh = -del*(3.*c2-1.)*(h/(24.*pi*tau))*t2/(gtheta*miu)
do 100 ii = 1,nsp
b = field(ii)
f = delbpp**2/(3.*delbpp**2+4*(b-btheta-delbsh)**2)
signal(ii) = signal(ii)+3.*f
100      continue
110      continue
120      continue
do 125 ii = 1,nsp
signal(ii) = signal(ii)/nn
125      continue
call differ(field,signal,deriv,binc,nsp)
call differ(field,deriv,dbderv,binc,nsp)
do 140 i=1,nsp

```

```

write(nout,130)i,field(i),signal(i),deriv(i),dbderv(i)
write(7,199)field(i),signal(i),deriv(i),dbderv(i)
format(1x,i4,4x,4(5x,e15.7))
format(4(5x,e15.7))
continue
open(unit=6,file='pl.ot')
write(6,160)gpar,gper
format(//1x,'g-parallel = ',f10.8,' g-perpendicular = ',f10.8)
write(6,170)aparz,aperxy
format(1x,'hyperfine values in Gauss :',5x,
      'a-parallel = ',e15.7,2x,'a-perpendicular = ',e15.7)
write(6,180)apar,aper
format(1x,'hyperfine values in ergs :',5x,
      'a-parallel = ',e15.7,2x,'a-perpendicular = ',e15.7)
write(6,190)niu
format(1x,'microwave frequency = ',e15.7,1x,'Hz')
write(6,200)tau
format(1x,'correlation time (tau) = ',e15.7,1x,'sec')
write(6,210)nn,n,nsp
format(1x,'No. of theta points sampled = ',i4/1x,
      'degree of the polynomial involved = ',i4/1x,
      'No. of spectral points scanned = ',i4)
write(6,220)cf,sr
format(1x,'central field = ',f8.2,'Gauss',2x,'scan ',
      'range = ',f8.2,'Gauss')
if (iset .eq. 1) go to 240
if (iset .eq. 2) go to 260
write(6,230)
format(//40x,'field vs absorption plot follows')
call g01agf(field,signal,nsp,isort,110,46,1)
iset=1
go to 150
write(6,250)
format(//1x,'field vs first derivative plot follows')
call g01agf(field,deriv,nsp,isort,110,46,1)
iset=2
go to 150

```

```

260      write(6,270)
270      format(/1x,'field vs second derivative plot follows'/)
        call g01agf(field,dbderv,nsp,isort,110,46,1)
        close(unit=6)
        close(unit=nout)
        stop
        end

c      -----
c      subroutine differ(x,y,dybdx,xinc,nsp)
c      this subroutine finds out the derivative of a given x y data.
c      -----

        implicit double precision (a-h,o-z)
        dimension x(nsp),y(nsp),dybdx(nsp)
        d2=xinc+xinc
        d4=d2+d2
        dybdx(1)=(-3.0*y(1)+4.0*y(2)-y(3))/d2
        dybdx(2)=(-y(1)+y(3))/d2
        nspm1=nsp-1
        nspm2=nsp-2
        do 100 i=3,nspm2
            der=(-y(i-1)+y(i+1))/d2
            der2=(-y(i-2)+y(i+2))/d4
100      dybdx(i)=der+((der-der2)/3.0)
        dybdx(nspm1)=(-y(nspm2)+y(nsp))/d2
        dybdx(nsp)=(y(nspm2)-4.0*y(nspm1)+3.0*y(nsp))/d2
        return
        end

```



## APPENDIX II

```
C*****
C      PROGRAM TO SIMULATE EPR LINESHAPES OF NITROXIDES      *
C      UNDERGOING FAST MOTION      *
C*****
C      this is the modified version of the program fast1.f
C      modified on mar 15, & mar 26 , 1993
      implicit double precision (a-h,o-z)
      character*12 file1,file2,file3,file4
      double precision m , niu0 , miu , inhlw(2),motlw(3)
      dimension fieldl(9999),siglor(9999),isort(9999),siggas(9999),
1 dvtlor(9999),dvtgas(9999),alfa(3),alfain(3),alfafi(3),ratio(31),
1 alpha(31),ratio1(3),delhpp(3),tau(2),g(3),totwid(3),totdif(2),
1 work(9999),sigcon(9999),fieldc(9999),signal(9999),dvtcon(9999),
1 fieldg(9999),flwlor(3),flwgas(3),npts(3),field1(3,9999),
1 dvtsig(3,9999),field(9999),xval(15000),yval(15000)
      common /worksp/ rwksp
      real rwksp(262642)
      call iwkin(262642)
      type *, 'give the input file name'
      read (5,*) file1
      type *, 'give the output file which will be needed by program'
      read (5,*) file2
      type *, 'give the output data file name for the plot'
      read (5,*) file3
      type *, 'give the output data file name for reference'
      read (5,*) file4
      open (unit = 20 , file = file1)
      open (unit = 21 , file = file2)
      open (unit = 22 , file = file3)
      open (unit = 23 , file = file4)
      read (20,*) axg,ayg,azg,gx,gy,gz
      read (20,*) niu0,spin,sr,cf,itrano,bstep
      read (20,*) totwid(1),totwid(2),totwid(3)
      read (20,*) alfain(1),alfain(2),alfain(3)
      read (20,*) parlor, pargas
      miu = 9.2841e-21
      pi = 4.0*atan(1.0)
      h = 6.62618e-27
      bi = cf - (sr/2.0)
      ax = axg*gx*miu
      ay = ayg*gy*miu
      az = azg*gz*miu
      a0 = (ax+ay+az)/3.0
```

```

      do 80 j = 1,nsamp
        dvtsig(i,j) = dvtcon(j)
        write(21,3) fieldc(j),dvtcon(j)
80      continue
      else
        do 89 j = 1,nsamp
          dvtsig(i,j) = dvtcon(j)
          write(21,6) fieldc(j),dvtcon(j)
89      continue
      endif
      3      format (f7.2,1x,e15.6)
      6      format (f7.1,1x,e15.6)
c      call g01agf (fieldl,siglor,nsplor,isort,110,62,1)
c      call g01agf (fieldg,siggas,nspgas,isort,110,62,1)
c      call g01agf (fieldc,dvtcon,nsamp,isort,110,62,1)
      20      continue
      rewind 21
      ntpt = npts(1)+npts(2)+npts(3)
c      type *, ntpt
      do 999 k = 1,ntpt
        read(21,3) xval(k),yval(k)
999      continue
      no = 1
      do 998 i = 3,1,-1
c      type *, npts(i)
      do 997 j = 1,npts(i)
        field1(i,j) = xval(no)
        no = no +1
997      continue
998      continue
      call adjust (npts,field1,dvtsig,signal,field,nspt,bstep)
      call normal (signal,nspt)
      do 996 kkk = 1,nspt
        write (22,3) field(kkk),signal(kkk)
c        write (22,3) field(kkk),dvtsig(2,kkk)
996      continue
c      call g01agf (field,signal,nspt,isort,110,62,1)
      write (23,*) axg,ayg,azg,gx,gy,gz
      write (23,*) niu0,spin,sr,cf,itrano,bstep
      write (23,*) totwid(1),totwid(2),totwid(3)
      write (23,*) alfain(1),alfain(2),alfain(3)
      write (23,*) parlor, pargas
140      stop
      end
c      -----

```

```
subroutine differ(x,y,dybdx,xinc,nsp)
this subroutine finds out the derivative of a given x y data.
```

```
-----
implicit double precision (a-h,o-z)
dimension x(nsp),y(nsp),dybdx(nsp)
d2=xinc+xinc
d4=d2+d2
dybdx(1)=(-3.0*y(1)+4.0*y(2)-y(3))/d2
dybdx(2)=(-y(1)+y(3))/d2
nspm1=nsp-1
nspm2=nsp-2
do 100 i=3,nspm2
der=(-y(i-1)+y(i+1))/d2
der2=(-y(i-2)+y(i+2))/d4
dybdx(i)=der+((der-der2)/3.0)
dybdx(nspm1)=(-y(nspm2)+y(nsp))/d2
dybdx(nsp)=(y(nspm2)-4.0*y(nspm1)+3.0*y(nsp))/d2
return
end
```

```
-----
subroutine normal (signal,number)
double precision signal(number)
dimension signal(number)
sigmax = 0.0
do 10 j = 1,number
if (signal(j).gt.sigmax)sigmax = signal(j)
continue
do 20 k = 1,number
signal(k) = signal (k)/sigmax
type * , k
continue
return
end
```

```
-----
subroutine adjust (npts,field1,dvtsig,signal,field,nspt,bstep)
implicit double precision (a-h,o-z)
dimension npts(3), field1(3,9999), dvtsig(3,9999),field(9999),
1 signal(9999)
xmin = field1(3,1)
xmax = field1(1,npts(1))
nspt = 1 + (xmax -xmin)/bstep
ndiff1 = nspt - npts(1)
type *, xmin,xmax,nspt,ndiff1,npts,field1(2,1)
do 111 mm = npts(1),1,-1
dvtsig(1,ndiff1+mm) = dvtsig(1,mm)
```

```
111      continue
      do 222 k = 1,nspt
      field(k) = field1(3,1) + (k - 1) * bstep
      signal(k) = 0.0
      if (k .gt. npts(3)) dvtsig(3,k) = dvtsig(3,npts(3))
      if (field(k) .lt. field1(1,1)) dvtsig(1,k) = dvtsig(1,1)
      if (abs(field1(2,1)- field(k)).lt.1.0e-4) liml = k
      if (abs(field1(2,npts(2))- field(k)).lt.1.0e-4) limr = k
222      continue
c      type *, liml,limr
      do 333 n = npts(2),1,-1
      dvtsig(2,liml+n-1) = dvtsig(2,n)
333      continue
      do 444 m = 1,nspt
      if (m.lt.liml)dvtsig(2,m) = dvtsig(2,1)
      if (m.gt.limr)dvtsig(2,m) = dvtsig(2,npts(2)+liml-1)
444      continue
      do 555 l = 1,nspt
      do 666 n = 3,1,-1
      signal (l) = signal(l) + dvtsig (n,l)
666      continue
555      continue
      return
      end
```